



DOVILĖ RUBINAITĖ

**TWO-STAGE
SYNTHESIS
OF CALCIUM
SULFOALUMINATES,
THEIR STRUCTURE,
PROPERTIES AND
APPLICATION**

DOCTORAL DISSERTATION

K a u n a s
2 0 2 4

KAUNAS UNIVERSITY OF TECHNOLOGY

DOVILĖ RUBINAITĖ

TWO-STAGE SYNTHESIS OF CALCIUM
SULFOALUMINATES, THEIR STRUCTURE,
PROPERTIES AND APPLICATION

Doctoral dissertation
Technological Sciences, Chemical Engineering (T 005)

2024, Kaunas

This doctoral dissertation was prepared at Kaunas University of Technology, Faculty of Chemical Technology, Department of Silicate Technology during the period of 2020–2024. The studies were supported by the Research Council of Lithuania.

Research supervisor:

Prof. Dr. Raimundas ŠIAUČIŪNAS (Kaunas University of Technology, Technological Sciences, Chemical Engineering, T 005).

Research consultant:

Assoc. Prof. Dr. Tadas DAMBRAUSKAS (Kaunas University of Technology, Technological Sciences, Chemical Engineering, T 005).

Edited by: English language editor Dr. Armandas Rumšas (Publishing House *Technologija*), Lithuanian language editor Rita Malikėnienė (Publishing House *Technologija*).

Dissertation Defence Board of Chemical Engineering Science Field:

Prof. Dr. Rimvydas KAMINSKAS (Kaunas University of Technology, Technological Sciences, Chemical Engineering, T 005) – **chairperson**;

Assoc. Prof. Dr. Jonas BALTRUŠAITIS (Lehigh University, United States of America, Technological Sciences, Chemical Engineering, T 005);

Assoc. Prof. Dr. Irmantas BARAUSKAS (Kaunas University of Technology, Technological Sciences, Chemical Engineering, T 005);

Prof. Dr. Ramūnas SKAUDŽIUS (Vilnius University, Natural Sciences, Chemistry, N 003);

Prof. Dr. Virgilijus VALEIKA (Kaunas University of Technology, Technological Sciences, Chemical Engineering, T 005).

The dissertation defence will be held on 13 September 2024, at 10 a.m. in a public meeting of the Dissertation Defence Board of the Chemical Engineering science field in the Rectorate Hall at Kaunas University of Technology.

Address: K. Donelaičio 73-402, LT-44249 Kaunas, Lithuania.

Phone (+370) 608 28 527; e-mail doktorantura@ktu.lt

The dissertation was sent out on 13 August, 2024.

The doctoral dissertation is available on <http://ktu.edu> and at the library of Kaunas University of Technology (Gedimino 50, LT-44239 Kaunas, Lithuania).

KAUNO TECHNOLOGIJOS UNIVERSITETAS

DOVILĖ RUBINAITĖ

KALCIO SULFOALIUMINATŲ DVIEJŲ
STADIJŲ SINTEZĖ, JŲ STRUKTŪRA,
SAVYBĖS IR TAIKYMAS

Daktaro disertacija
Technologijos mokslai, chemijos inžinerija (T 005)

2024, Kaunas

Disertacija rengta 2020–2024 metais Kauno technologijos universiteto Cheminės technologijos fakultete, Silikatų technologijos katedroje. Mokslinius tyrimus rėmė Lietuvos mokslo taryba.

Mokslinis vadovas:

prof. dr. Raimundas ŠIAUČIŪNAS (Kauno technologijos universitetas, technologijos mokslai, chemijos inžinerija, T 005).

Mokslinis konsultantas:

doc. dr. Tadas DAMBRAUSKAS (Kauno technologijos universitetas, technologijos mokslai, chemijos inžinerija, T 005).

Redagavo: anglų kalbos redaktorius dr. Armandas Rumšas (leidykla „Technologija“), lietuvių kalbos redaktorė Rita Malikėnienė (leidykla „Technologija“).

Chemijos inžinerijos mokslo krypties disertacijos gynimo taryba:

prof. dr. Rimvydas KAMINSKAS (Kauno technologijos universitetas, technologijos mokslai, chemijos inžinerija, T 005) – **pirmininkas**;

doc. dr. Jonas BALTRUŠAITIS (Lehajaus universitetas, Jungtinės Amerikos Valstijos, technologijos mokslai, chemijos inžinerija, T 005);

doc. dr. Irmantas BARAUSKAS (Kauno technologijos universitetas, technologijos mokslai, chemijos inžinerija, T 005);

prof. dr. Ramūnas SKAUDŽIUS (Vilniaus universitetas, gamtos mokslai, chemija, N 003);

prof. dr. Virgilijus VALEIKA (Kauno technologijos universitetas, technologijos mokslai, chemijos inžinerija, T 005).

Disertacija bus ginama viešame Chemijos inžinerijos mokslo krypties disertacijos gynimo tarybos posėdyje 2024 m. rugsėjo 13 d. 10 val. Kauno technologijos universiteto Rektorato salėje.

Adresas: K. Donelaičio g. 73-402, LT-44249 Kaunas, Lietuva.

Tel. (+370) 608 28 527; el. paštas doktorantura@ktu.lt

Disertacija išsiųsta 2024 m. rugpjūčio 13 d.

Su disertacija galima susipažinti interneto svetainėje <http://ktu.edu> ir Kauno technologijos universiteto bibliotekoje (Gedimino g. 50, LT-44239 Kaunas, Lietuva).

TABLE OF CONTENTS

LIST OF TABLES	7
LIST OF FIGURES	9
LIST OF ABBREVIATIONS AND TERMS	14
INTRODUCTION	17
1. LITERATURE REVIEW	20
1.1. Demand for Research on Cementitious Building Materials.....	20
1.2. Calcium Sulfoaluminate (CSA) Cements.....	22
1.2.1. CO ₂ footprint reduction in the production process of CSA cements	22
1.2.2. Mineralogical composition and classification of CSA cements	23
1.3. Ye'elimite	25
1.3.1. The crystal structure of ye'elimite.....	25
1.3.2. The synthesis methods of ye'elimite	26
1.3.3. Hydration mechanism of ye'elimite	31
1.4. Structure and Properties of Calcium Sulfoaluminate Hydrates.....	34
1.4.1. Calcium trisulfoaluminate hydrate (ettringite)	34
1.4.2. Calcium monosulfoaluminate hydrate	35
1.5. Hydrothermal-Calcination Synthesis Method for Cementitious Materials ...	38
2. MATERIALS AND METHODS.....	42
2.1. Materials.....	42
2.2. Methods.....	45
2.2.1. Preparation of the initial mixtures	45
2.2.2. Hydrothermal synthesis	46
2.2.3. Study of the impact of water vapour pressure on stability.....	48
2.2.4. Thermal stability assessment	48
2.2.5. Investigation of early hydration.....	49
2.2.6. Methods of testing ternary blended cement.....	50
2.2.7. Synthesis of belite-ye'elimite-ferrite cement	50
2.2.8. Curing procedures for belite-ye'elimite-ferrite cement.....	52
2.2.9. Characterization methods	53
2.2.10. Thermodynamic calculations.....	57
2.2.11. Apparent kinetic parameter calculations.....	58
2.2.12. Modeling of the calcium monosulfoaluminate 12-hydrate synthesis process.....	60
3. RESULTS AND DISCUSSION.....	61
3.1. Hydrothermal Synthesis of Calcium Monosulfoaluminate 12-hydrate.....	61
3.1.1. Characterization of the obtained samples	61
3.1.2. Thermodynamic calculations.....	70
3.2. Technological Recommendations for the Hydrothermal Synthesis of Calcium Monosulfoaluminate 12-hydrate.....	73
3.3. Influence of Water Vapour Pressure on the Stability of Calcium Monosulfoaluminate 12-hydrate in the Presence of Environment CO ₂	80

3.3.1. Characterization of the phase transitions	80
3.3.2. Carbonation mechanism	87
3.4. Investigation of the Thermal Transition Mechanism from Calcium Monosulfoaluminate 12-hydrate to Ye'elimate	90
3.4.1. Investigation by in-situ X-ray diffraction method at 25–1250 °C	90
3.4.2. Investigation by <i>ex-situ</i> X-ray diffraction method at 750–1250 °C.....	95
3.5. Reactivity and Early Hydration Mechanism of Synthetic Ye'elimate	100
3.6. Fly Ash Effect on the Hydration and Properties of Synthetic Ye'elimate.....	105
3.6.1. Kinetics of the initial hydration	105
3.5.2. Characterization of hydration products.....	108
3.7. Effect of Synthetic Ye'elimate on the Hardening Process of Ordinary Portland – Fly Ash Blended Cement.....	111
3.7.1. Setting time and compressive strength	112
3.7.2. Characterization of hydration products.....	114
3.8. Ye'elimate Formation during High-Temperature Sintering of Belite-Ye'elimate-Ferrite Clinker and the Properties of the Obtained Cement.....	120
4. CONCLUSIONS	129
5. SANTRAUKA.....	131
5.1. Įvadas	131
5.2. Medžiagos ir metodai	134
5.2.1. Naudotos medžiagos.....	134
5.2.2. Taikyti metodai.....	135
5.3. Rezultatai ir aptarimas.....	141
5.3.1. Kalcio monosulfoaliuminato 12-hidrato hidroterminė sintezė	141
5.3.2. Dalinio vandens garų slėgio įtaka kalcio monosulfoaliuminato 12-hidrato stabilumui esant aplinkos CO ₂	144
5.3.2. Terminio skilimo iš kalcio monosulfoaliuminato 12-hidrato į jelimitą mechanizmo tyrimas.....	146
5.3.3. Sintetinio jelimito ankstyvosios hidratacijos tyrimas	148
5.3.4. Lakiųjų pelenų įtaka sintetinio jelimito ankstyvajai hidratacijai	150
5.3.5. Jelimito priedo įtaka pelenų portlandcemenčio kietėjimo savybėms.....	152
5.3.6. Jelimito susidarymas belitinio-jelimitinio-feritinio cemento sintezės metu ir paruošto cemento mechaninių savybių tyrimas.....	155
5.4. Išvados.....	159
REFERENCES	161
CURRICULUM VITAE.....	179
LIST OF SCIENTIFIC PUBLICATIONS:	180
ACKNOWLEDGEMENTS.....	182
APPENDICES	183

LIST OF TABLES

Table 1.1. Classification of cements containing ye'elimite [26].....	24
Table 1.2. Summary of synthesis procedures for high purity ye'elimite employed in prior studies	27
Table 2.1. Water vapour pressure equilibrium over H ₂ SO ₄ solutions of different concentrations at 20 °C.....	48
Table 2.2. Targeted phase composition of BYF clinker, dosages of raw materials, and oxide composition of the initial mixture (excluding H ₂ O and CO ₂).....	51
Table 2.3. Standard thermodynamic properties at 25 °C (298 K) and 1 bar	57
Table 3.1. Assignments of the FTIR spectrum absorption bands of the formed synthesis products at 130 °C for 8 h [105,166]	69
Table 3.2. Simulated stream parameters of the thermal decomposition of Al(OH) ₃	75
Table 3.3. Simulated stream parameters in the cyclone from the thermal decomposition of Al(OH) ₃	75
Table 3.4. Simulated stream parameters of the thermal decomposition of CaCO ₃	76
Table 3.5. Simulated stream parameters in the air cleaning system from the thermal decomposition of CaCO ₃	76
Table 3.6. Solid particle size distribution in the streams	77
Table 3.7. Properties of the materials composing the autoclave	78
Table 3.8. Simulated stream parameters in the precursor drying system	80
Table 3.9. Apparent kinetic reaction constants of carbonated CaO during the carbonation of samples at different p/p_0 conditions calculated by with different kinetic models.....	88
Table 3.10. Thermal stability of different hydration states of calcium monosulfoaluminate	92
Table 3.11. Quantitative phase analysis of the precursor samples calcinated from 950 °C to 1250 °C for 1 h	97
Table 3.12. Changes in the intensities of the main diffraction peaks during the hydration (W/S 1.1) of synthetic ye'elimite.....	102
Table 3.13. Compositions of extracted and prepared pore solutions by ICP–OES	108
Table 3.14. Changes in the main diffraction peaks after 72 h of hydration in various ye'elimite-fly ash blends.....	110
Table 3.15. Strength development of BYF cement mortars cured in water environment.....	124

It is worth observing that, due to the diverse phase composition of the synthesized BYF clinker, other compounds could also form during the hydration of mortar samples, including hydrogarnet (C₃AFSH₄), monosulfoaluminate, portlandite (CH), aluminium hydroxide (AH₃), calcite (CaCO₃), and so forth. However, they cannot be clearly distinguished in the XRD patterns, likely due to their low crystallinity and/or small quantities.

Table 3.16. Changes in the main diffraction peaks of compounds during the curing of BYF mortar samples.....	125
--	-----

Table 3.17. Strength development of BYF cement mortar samples cured in hydrothermal environment at different temperatures with an isothermal time of 24 h	127
5.1 lentelė. Pradinio mišinio sudėtis BYF klinkeriui paruošti	137
5.2 lentelė. Hidroterminės sintezės produktų masės nuostoliai, kai S2 bandinys apdorojamas 110 °C temperatūroje skirtingomis izoterminio išlaikymo trukmėmis.....	143
5.3 lentelė. Kiekybinės RSDA analizės rezultatai, atlikus prekursoriaus terminį apdorojimą 950–1250 °C temperatūroje, kai išlaikymo trukmė – 1 h.....	147
5.4 lentelė. Pagrindinių difrakcijos smailių pokyčiai po 72 h hidratacijos įvairiuose jelimitinių ir lakiųjų pelenų mišiniuose	152
5.5 lentelė. Paruoštų cemento tešlų rišimosi pradžios ir pabaigos trukmės	153
5.6 lentelė. Paruoštų skiedinio bandinių gniuždymo stiprio priklausomybė nuo hidratacijos trukmės.....	153
5.7 lentelė. Vandens aplinkoje kietintų BJK cemento skiedinio bandinių gniuždymo ir lenkimo stiprio vertės	157
5.8 lentelė. Hidroterminėje aplinkoje kietintų BJK cementų skiedinio gniuždymo ir lenkimo stiprio vertės, kai izoterminio išlaikymo trukmė – 24 h	158

LIST OF FIGURES

Fig. 1.1. Correlation between the emission of CO ₂ and the components of concrete. *The taken cement composition corresponds to the current average ratio of overall cement types in the EU.....	21
Fig. 1.2. CaO-SiO ₂ -Al ₂ O ₃ phase diagram (a) showing two regions of cementitious phase, Ordinary Portland cement and calcium sulfoaluminate cements, and CO ₂ released and energy requirement (b) during the formation of cement phases [23,24]	23
Fig. 1.3. Calculated crystal structures of ye'elimite phases: a – cubic (I43m); b – tetragonal (I4); and c – orthorhombic (Pcc2). Ca is denoted within the dark-blue prisms, Al is within the light-blue tetrahedra, S is within the yellow tetrahedra, and O is red. CaO bonds are omitted in (c) for clarity [31]	26
Fig. 1.4. Simplified schematic representation of the reaction product layers emerging during ye'elimite formation [56].....	29
Fig. 1.5. Schematic representation of the lamellar structure in AFm phase [107] ...	36
Fig. 2.1. XRD pattern of fly ash. Indexes: i – mullite, h – hematite, Q – quartz, an – anatase, M – magnesium oxide, co – calcium oxide, mg – magnetite.....	42
Fig. 2.2. XRD pattern of OPC. Indexes: â – alite, β – belite, B – brownmillerite, g – gypsum, k – tricalcium aluminate, M – magnesium oxide.....	43
Fig. 2.3. XRD pattern of silica gel waste. Indexes: G – gibbsite, r – aluminium trifluoride trihydrate, f – aluminium hydroxide fluoride hydrate	44
Fig. 2.4. XRD pattern of granite cutting waste. Indexes: An – annite, Ac – actinolite, z – microcline, x – albite, Q – quartz, n – anorthite, l – labradorite	44
Fig. 2.5. XRD patterns of the homogenized initial mixture (1; Sample S1) and mechanochemically treated initial mixture at different stages (2 – after 10 min, 3 – after 20 min, and 4 – after 30 min [Sample S2]). Indexes: g – gypsum, p – portlandite, co – calcium oxide, A – anhydrite, s – bassanite.....	46
Fig. 2.6. XRD patterns of Sample S2, after hydrothermal synthesis at 110 °C for 8 h, dried at different RH conditions. Indexes: Ms – calcium monosulfoaluminate (the number shows the water content), Cê – calcium carbonate.....	47
Fig. 3.1. XRD patterns of S1 and S2 samples products after hydrothermal synthesis. Indexes: Ms12 – monosulfoaluminate 12-hydrate, Et – ettringite, g – gypsum, K – katoite, Cê – calcium carbonate, b – boehmite, G – gibbsite, p – portlandite	62
Fig. 3.2. TGA plots (a – TG; b – DTG) of Sample S2 after hydrothermal synthesis at 110 °C for varying durations	64
Fig. 3.3. FTIR spectrum of Sample S2 synthesized at 110 °C for varying durations	65
Fig. 3.4. SEM image and EDS elemental maps of Sample S2 after hydrothermal synthesis at 110 °C for 8 h.....	66
Fig. 3.5. Quantitative phase analysis refinement plot (a) and ²⁷ Al NMR spectrum (b) of Sample S2 after hydrothermal synthesis at 110 °C for 8 h	67
Fig. 3.6. TGA curves (1 – TG, 2 – DTG) of Sample S2 after hydrothermal synthesis at 130 °C for 8 h	68

Fig. 3.7. ^{27}Al NMR spectrum (a) and FTIR spectrum (b) of Sample S2 after hydrothermal synthesis at 130 °C for 8 h	68
Fig. 3.8. SEM micrographs of Sample S2 after hydrothermal synthesis at 130 °C for 8 h	69
Fig. 3.9. Sequences of crystalline product formation in the $\text{CaO-Al}_2\text{O}_3\text{-SO}_4\text{-H}_2\text{O}$ system under hydrothermal conditions.....	70
Fig. 3.10. Temperature dependence of Gibbs free energy based on Equations 3.1–3.16	72
Fig. 3.11. The preparation scheme of the initial mixture, modeled by <i>Aspen Plus</i> . Here: FBA, FBC – fluidized bed reactor; C–A, C–C – compressor; AIR–A, AIR–C – ambient air; AIR–IN–A, AIR–IN–C – compressed air; AIROUT–A, AIROUT–C – outgoing air stream; CIK–A, CIK–C – cyclone; TOP–A, TOP–C – cleaned air stream; BOT–A, BOT–C – separated solid particles; ST–A ($\text{Al}(\text{OH})_3$), ST–C (CaCO_3), ST–G ($\text{CaSO}_4 \cdot 2\text{H}_2\text{O}$) – initial material stream; PR–A1, PR–C1 – product; PR–A2, PR–C2 – cooled product; CO–A1, CO–A1, CO–C1, CO–C2 – cooler; S1,S2 – cooled air stream; MI – mixer; MIX – initial mixture stream (resulting mixture of CaO , Al_2O_3 and gypsum); MIL – mill; MIL–MIX – milled initial mixture stream.....	74
Fig. 3.12. The process scheme of precursor synthesis, modeled by <i>Aspen HYSYS</i> ..	78
Fig. 3.13. Dependence of energy losses (a) and the autoclave’s surface temperature (b) on the thickness of the insulating layer during temperature rise (2 h) and the dwell period (8 h)	79
Fig. 3.14. The process scheme of the precursor drying, modeled by <i>Aspen Plus</i>	79
Fig. 3.15. Mass change of Sample S2 synthesized at 130 °C for 8 h, depending on the duration at different p/p_0 values (the error bars represent standard deviation).....	81
Fig. 3.16. XRD patterns (left) and TGA plots (right) (a – TG, b – DTG) of Sample S2 hydrothermally treated at 130 °C for 8 h exposed at different p/p_0 and durations. Indexes: Ms – monosulfoaluminate (the number shows the water content), Hc – hemicarboaluminate, Et – ettringite, b – boehmite, G – gibbsite, C \hat{c} – calcium carbonate, s – bassanite, a – aragonite, v – vaterite, g – gypsum	82
Fig. 3.17. Relationship of the carbonation degree of CaO in the samples and the exposure duration at different p/p_0 values. The dashed line – the linear trendline (the error bars represent standard deviation)	87
Fig. 3.18. Plots of the Jander model (a) and the Avrami model (b) applied for the carbonated CaO during the carbonation of samples under different p/p_0 conditions	89
Fig. 3.19. <i>In-situ</i> XRD patterns of the precursor with the calcination temperature varying within 25–1250 °C range. Indexes: Ms – calcium monosulfoaluminate (the number shows the water content), C \hat{c} – calcium carbonate, CO – calcium oxide, A – anhydrite, CA – calcium aluminate, Y – ye’elimite.....	91
Fig. 3.20. TG (a), DTG (b) and DSC (c) curves of the precursor	93
Fig. 3.21. Ranges of crystalline phases developing in the heating process of the precursor detected by <i>in-situ</i> X-ray diffraction. Indexes: Ms – calcium monosulfoaluminate hydrate (the number shows the water content), C \hat{c} – calcium	

carbonate, CO – calcium oxide, A – anhydrite, CA – calcium aluminate, Y – ye'elimite	95
Fig. 3.22. Dependence of LOI on the calcination temperature maintained for 1 h ..	96
Fig. 3.23. XRD patterns of precursor sintered at different temperatures for 1 h. Indexes: Y – ye'elimite, m – mayenite, A – anhydrite, CA – calcium aluminate, co – calcium oxide.....	97
Fig. 3.24. Effect of the calcination temperature (dwell for 1 h) on the crystallite size of the synthesized ye'elimite (the error bars represent standard deviation).....	98
Fig. 3.25. XRD patterns of the precursor calcinated for varying durations at 1150 °C (a), and the change in the main diffraction peak of ye'elimite ($d = 0.375$ nm) depending on the duration of calcination (b). Indexes: Y – ye'elimite, A – anhydrite, co – calcium oxide	99
Fig. 3.26. Calorimetric curves measured during isothermal hydration (W/S=1.1) of synthetic ye'elimite (Roman numerals represent the hydration stages).....	101
Fig. 3.27. Results of conductivity and pH measurements (W/S=40) of the hydration solution	101
Fig. 3.28. XRD patterns (left) and TGA plots (right) (a – TG, b – DTG) of ye'elimite hydration (W/S=1.1) at different durations (1 – 12 min, 2 – 6 h, 3 – 12 h, 4 – 14 h 45 min, 5 – 16 h, 6 – 24 h). Indexes: Y – ye'elimite, A – anhydrite.....	102
Ms – calcium monosulfoaluminate hydrate, Et – ettringite, AH – aluminium hydroxide.....	102
Fig. 3.29. SEM images during the hydration (W/S=1.1) of synthetic ye'elimite at different durations	103
Fig. 3.30. Calorimetric curves obtained during isothermal hydration (W/S=1.1) of various ye'elimite–fly ash blends.....	106
Fig. 3.31. Calorimetric curves measured during isothermal hydration of blends containing ye'elimite-fly ash and ye'elimite-limestone when using different solutions.....	108
Fig. 3.32. Degree of ye'elimite reaction (left) and XRD patterns (right) of different ye'elimite-fly ash blends after 72 h of hydration. Indexes: Y – ye'elimite, Ms – monosulfoaluminate, Et – ettringite, AH – aluminium hydroxide, i – mullite, Q – quartz	109
Fig. 3.33. TGA plots (left) and the amount of bound water (right) of different ye'elimite-fly ash blends after 72 h of hydration	111
Fig. 3.34. The setting time of paste (a) and the compressive strength of mortars (b) prepared by using OPC–FA blends	113
Fig. 3.35. Setting times of the prepared OPC–FA–Y paste samples.....	113
Fig. 3.36. Compressive strength of the prepared OPC–FA–Y mortar samples.....	114
Fig. 3.37. XRD patterns of different OPC–FA–Y samples after 2 days (a) and 28 days (b) of curing (1 – OPC, 2 – 80P20FA, 3 – 80P19.5FA0.5Y, 4 – 79.5P20FA0.5Y, 5 – 80P19FA1Y, 6 – 79P20FA1Y). Indexes: p – portlandite, Et – ettringite, Hc – hemicarboaluminate, Mc – monocarboaluminate, \hat{a} – alite, β – belite, B –	

brownmillerite, i – mullite, Q – quartz, C \hat{c} – calcium carbonate, k – tricalcium aluminate	115
Fig. 3.38. Reaction degree of alite during the curing of different OPC–FA–Y samples	117
Fig. 3.39. DTG curves of the prepared OPC–FA–Y samples after 28 days of curing. Samples: 1 – OPC, 2 – 80P20FA, 3 – 80P19.5FA0.5Y, 4 – 79.5P20FA0.5Y, 5 – 80P19FA1Y, 6 – 79P20FA1Y	118
Fig. 3.40. Mass loss of samples within the temperature range of 50–400 °C (a) and the formed amount of portlandite (b) at various curing ages relative to the binder content. Samples: 1 – OPC, 2 – 80P20FA, 3 – 80P19.5FA0.5Y, 4 – 79.5P20FA0.5Y, 5 – 80P19FA1Y, 6 – 79P20FA1Y (error bars represent the standard deviation)	119
Fig. 3.41. XRD patterns of BYF clinker sintered at different temperatures for 1 h. Indexes: Q – quartz, S – srebrodolskite; m – mayenite, β – belite (β -C $_2$ S), γ – dicalcium silicate (γ -C $_2$ S), M – magnesium oxide, Y – ye'elimite, B – brownmillerite.....	121
Fig. 3.42. XRD pattern of BYF clinker sample sintered at 1150 °C for 2 h. Indexes: β – belite (β -C $_2$ S), m – mayenite, M – magnesium oxide, Y – ye'elimite, S – srebrodolskite, Ge – gehlenite	122
Fig. 3.43. Heat flow curves of BYF cement samples with different gypsum additive	123
Fig. 3.44. XRD patterns of mortar samples after different durations of curing in water environment. Indexes: β – belite (β -C $_2$ S), M – magnesium oxide, et – ettringite, st – stratlingite, K – katoite, C – CAH $_{10}$, C $_2$ – C $_2$ AH $_8$, F – ferro-actinolite, C \hat{c} – calcium carbonate.....	124
Fig. 3.45. STA curves (a – DSC, b – TG) of mortar samples after different durations of curing.....	125
5.1 pav. S1 ir S2 bandinių hidroterminės sintezės produktų RSDA kreivės: Ms12 – kalcio monosulfoaliuminato 12–hidratas; Et – etringitas; g – gipsas; K – katoitas; C \hat{c} – kalcio karbonatas; b – bemitas; G – gibsitas; p – portlanditas.....	141
5.2 pav. Hidroterminės sintezės produktų masės išvestinės kreivės (DTG), kai S2 bandinys apdorojamas 110 °C temperatūroje skirtingomis izoterminio išlaikymo trukmėmis	143
5.3 pav. Kristalinių produktų susidarymo sekos hidroterminėmis sąlygomis CaO–Al $_2$ O $_3$ –SO $_4$ –H $_2$ O sistemoje	144
5.4 pav. S2 bandinio, hidrotermiškai apdoroto 130 °C 8 h, RSDA kreivės, esant skirtingai p/p_0 aplinkai skirtingomis išlaikymo trukmėmis: Ms – kalcio monosulfoaliuminato hidratas (skaičius rodo vandens kiekį); Hc – hemikarbonatas; Et – etringitas; b – bemitas; G – gibsitas; C \hat{c} – kalcio karbonatas; s – basanitas; a – aragonitas; v – vateritas; g – gipsas	145
5.5 pav. Bandinių karbonizacijos laipsnio priklausomybė nuo išlaikymo trukmės esant skirtingam p/p_0 (paklaidų juostos rodo standartinį nuokrypį)	146
5.6 pav. Kalcio monosulfoaliuminato 12-hidrato <i>in situ</i> RSDA analizės kreivės atlikus terminį apdorojimą 25–1250 °C temperatūros intervale: Ms –	

monosulfoaliuminatas (skaičius rodo vandens kiekį); C \hat{c} – kalcio karbonatas; CO – kalcio oksidas; A – anhidritas; CA – kalcio aliuminatas; Y – jelimitas	147
5.7 pav. Kalorimetrinės kreivės, išmatuotos sintetinio jelimito izoterminės hidratacijos metu	148
5.8 pav. Sintetinio jelimito hidratacijos produktų RSDA kreivės (a) ir TGA kreivės (b) skirtingomis hidratacijos trukmėmis (1 – 12 min, 2 – 6 h, 3 – 12 h, 4 – 14 h 45 min, 5 – 16 h, 6 – 24 h): Y – jelimitas; Ms – monosulfoaliuminatas; Et – etringitas; AH – aliuminio hidroksidas; A – anhidritas	149
5.9 pav. Kalorimetrinės kreivės, išmatuotos įvairių jelimito ir lakiųjų pelenų mišinių izoterminės hidratacijos metu	150
5.10 pav. Kalorimetrinės kreivės, išmatuotos jelimito ir lakiųjų pelenų bei jelimito ir klinties miltelių mišinių izoterminės hidratacijos metu	151
5.11 pav. Bandinių RSDA kreivės po 2 (a) ir 28 (b) hidratacijos parų (1 – OPC, 2 – 80P20FA, 3 – 80P19.5FA0.5Y, 4 – 79.5P20FA0.5Y, 5 – 80P19FA1Y, 6 – 79P20FA1Y): p – portlanditas; Et – etringitas; Hc – hemikarboaliuminatas; Mc – monokarboaliuminatas; \hat{a} – alitas; β – belitas; B – braunmileritas; i – mulitas; Q – kvarcas; C \hat{c} – kalcio karbonatas; k – trikalcio aliuminatas	154
5.12 pav. Bandinių masės nuostoliai 50–400 °C temperatūroje (a) ir susidaręs portlandito kiekis (b) įvairiu kietėjimo laikotarpiu, normalizuoti pagal rišamosios medžiagos kiekį: 1 – OPC; 2 – 80P20FA; 3 – 80P19.5FA0.5Y; 4 – 79.5P20FA0.5Y; 5 – 80P19FA1Y; 6 – 79P20FA1Y	155
5.13 pav. BJT klinkerio, degto įvairiose temperatūrose 1 h, RSDA kreivės: Q – kvarcas; S – srebrodolskitas; m – majenitas; β – belitas (β -C $_2$ S); γ – dikalcio silikatas (γ -C $_2$ S); M – magnio oksidas; Y – jelimitas; B – braunmileritas	156
5.14 pav. BJT skiedinio bandinių XRD kreivės skirtingomis kietėjimo trukmėmis vandens aplinkoje: β – belitas; M – magnio oksidas; Et – etringitas; st – stratlingitas; K – katoitas; C – CAH $_{10}$; C $_2$ – C $_2$ AH $_8$; F – geležies aktinolitas; C \hat{c} – kalcio karbonatas	157

LIST OF ABBREVIATIONS AND TERMS

Cementitious symbols

Symbol	Chemical formula	Name
A	Al_2O_3	Aluminium oxide
C	CaO	Calcium oxide
\hat{c}	CO_2	Carbon dioxide
F	Fe_2O_3	Iron oxide
H	H_2O	Water
S	SiO_2	Silicium oxide
\hat{S}	SO_3	Sulfur trioxide

Cementitious phases

Symbol	Chemical formula	Name
C_3S	$3\text{CaO}\cdot\text{SiO}_2$	Tricalcium silicate, Alite
C_2S	$2\text{CaO}\cdot\text{SiO}_2$	Dicalcium silicate, Belite
C_3A	$3\text{CaO}\cdot\text{Al}_2\text{O}_3$	Tricalcium aluminate, Celite
C_4AF	$4\text{CaO}\cdot\text{Al}_2\text{O}_3\cdot\text{Fe}_2\text{O}_3$	Tetracalcium aluminoferrite, Ferrite, brownmillerite
$\text{C}\hat{\text{S}}$	CaSO_4	Anhydrite
$\text{C}\hat{\text{S}}\text{H}_{0.5}$	$\text{CaSO}_4\cdot 0.5\text{H}_2\text{O}$	Bassanite
$\text{C}\hat{\text{S}}\text{H}_2$	$\text{CaSO}_4\cdot 2\text{H}_2\text{O}$	Gypsum
CA	$\text{CaO}\cdot\text{Al}_2\text{O}_3$	Calcium Aluminate, Krotite
CA_2	$\text{CaO}\cdot 2\text{Al}_2\text{O}_3$	Calcium Dialuminate, Grossite
C_{12}A_7	$12\text{CaO}\cdot 7\text{Al}_2\text{O}_3$	Dodecacalcium hepta- aluminate, Mayenite
$\text{C}_4\text{A}_3\hat{\text{S}}$	$4\text{CaO}\cdot 3\text{Al}_2\text{O}_3\cdot\text{SO}_3$	Calcium sulfoaluminate, Ye'elimitite
$\text{C}\hat{c}$	$\text{CaO}\cdot\text{CO}_2$	Calcium carbonate, Calcite
AH_3	$\text{Al}_2\text{O}_3\cdot 3\text{H}_2\text{O}$	Aluminium hydroxide, Gibbsite
CH	$\text{Ca}(\text{OH})_2$	Calcium hydroxide, Portlandite
CAH_{10}	$\text{CaO}\cdot\text{Al}_2\text{O}_3\cdot 10\text{H}_2\text{O}$	Dodeca hydrated calcium aluminate
C_2AH_8	$2\text{CaO}\cdot\text{Al}_2\text{O}_3\cdot 8\text{H}_2\text{O}$	Octa-hydrated dicalcium aluminate
$\text{C}_4\text{A}\hat{\text{C}}\text{H}_{11}$	$4\text{CaO}\cdot\text{Al}_2\text{O}_3\cdot\text{CO}_3\cdot 11\text{H}_2\text{O}$	Monocarboaluminate
$\text{C}_4\text{A}\hat{\text{C}}_{0.5}\text{H}_{12}$	$4\text{CaO}\cdot\text{Al}_2\text{O}_3\cdot 0.5\text{CO}_3\cdot 11\text{H}_2\text{O}$	Hemicarboaluminate
$\text{C}_4\text{A}\hat{\text{S}}\text{H}_{12}$	$3\text{CaO}\cdot\text{Al}_2\text{O}_3\cdot\text{CaSO}_4\cdot 12\text{H}_2\text{O}$	Calcium monosulfoaluminate hydrate
$\text{C}_6\text{A}\hat{\text{S}}\text{H}_{32}$	$3\text{CaO}\cdot\text{Al}_2\text{O}_3\cdot 3\text{CaSO}_4\cdot 32\text{H}_2\text{O}$	Ettringite

Terms:

^{27}Al NMR – ^{27}Al solid-state nuclear magnetic resonance spectroscopic

BCSA – belite calcium sulfoaluminate cement

BYF – belite-ye'elimite-ferrite cement

CAC – calcium aluminate cement

C_p – specific heat capacity

CSA – calcium sulfoaluminate cement

$D_{\text{crystallite}}$ – average crystallite sizes

DSC – differential scanning calorimetry

EDS – energy-dispersive X-ray spectroscopy

FA – fly ash;

FTIR – Fourier transform infrared spectroscopy

ICP-OES – inductively plasma optical emission spectroscopy

LOI – loss on ignition

OPC/P – Ordinary Portland cement

p/p_0 – water vapour pressure

PS – artificial pore solution

PSD – particle size distribution

QPA – quantitative phase analysis

RH – relative humidity

S_a – specific surface area

SCM – supplementary cementitious materials

SEM – scanning electron microscopy

STA – simultaneous thermal analysis

TG – thermogravimetry

TGA – thermogravimetric analysis

W/B – water to binder ratio

W/C – water to cement (binder) ratio

W/S – water to solid ratio

XRD – X-ray diffraction analysis

XRF – X-ray fluorescence spectroscopy

Indices in the X-ray powder diffraction patterns:

\hat{a} – alite

A – anhydrite

a – aragonite

Ac – actinolite

AH – aluminium hydroxide

an – anatase

An – annite

b – boehmite

B – brownmillerite

C – CAH_{10}

K – katoite

k – tricalcium aluminate

l – labradorite

M – magnesium oxide

m – mayenite

Mc – Monocarboaluminate

mg – magnetite

Ms – calcium monosulfoaluminate (the number with this index shows the water content)

n – anorthite

p – portlandite

C2 – C₂AH₈
CA – calcium aluminate
co – calcium oxide
Et – ettringite
f – aluminium hydroxide fluoride hydrate
F – ferro-actinolite
G – gibbsite
g – gypsum
Ge – gehlenite
h – hematite
Hc – hemicarboaluminate
i – mullite

Q – quartz
r – aluminium trifluoride trihydrate,
s – bassanite
S – srebrodolskite
st – stratlingite
v – vaterite
x – albite
Y – ye'elimite
z – microcline
β – belite (β-C₂S)
γ – dicalcium silicate (γ-C₂S)

INTRODUCTION

Currently, due to the rapidly progressing urbanization and industrialization, the annual consumption of concrete has soared to a staggering 30 billion tons. As a result of the substantial need for construction materials, the cement industry is responsible for around 8% of worldwide anthropogenic greenhouse gas emissions. Considering the climate crisis and international agreements, such as the *Paris Agreement* and the *European Green Deal*, the cement industry must pursue significant transformations aimed at reducing its CO₂ footprint. Over the past decades, numerous solutions have been deployed to mitigate the negative impacts of the cement production on the environment. However, while the adoption of supplementary cementitious materials, of the transfer towards alternative fuels, and the introduction of new production technologies and processes represent three highly positive steps in the right direction, they still only partially address the issue. Therefore, the building materials industry and the scientific community are facing a significant challenge in developing new binder types that can minimize the environmental impact while retaining similar operational properties and costs as the conventional cement.

Cements containing ye'elimite represent an appealing category of low-carbon binders. These types of cement require a lower CaO/SiO₂ ratio and a calcination temperature of ~200 °C compared to the widely used ordinary Portland cement. This results in a 25–35% reduction in the CO₂ footprint triggered in the course of the production. Ye'elimite is calcium sulfoaluminate (4CaO·3Al₂O₃·SO₃). It plays a crucial role in defining the initial hydration characteristics and the final properties of concrete. Consequently, numerous scientists have shown interest in studying its synthesis and properties. Two methods are currently commonly employed to produce high-purity ye'elimite: 1) the solid-state reaction method involves the use of limestone, alumina, and gypsum as the starting materials, with the prepared mixture then sintered at 1250–1350 °C. It is of importance to note that this method necessitates multiple cycles of milling, pelleting, and sintering to synthesize high-purity ye'elimite powder. Additionally, the instability of ye'elimite and anhydrite at high temperatures (>1300 °C) challenges the synthesis. Meanwhile, 2) the sol-gel method (the chemical routes) involves the preparation of gel by mixing inorganic metal salts (Ca(NO₃)₂·4H₂O, Al(NO₃)₃·9H₂O and Al₂(SO₄)₃·16H₂O) with polymer precursors as the starting materials, which are then sintered at 1250 °C. However, this method suffers from the drawback of being time-consuming and requiring expensive materials and equipment. Another advanced two-stage method applied to produce high-purity phases (such as β-C₂S, C₃A, C₁₂A₇, etc.) involves the hydrothermal synthesis of cementitious hydrates and the calcination of the obtained precursors. This method is appealing due to its capacity to reduce the final calcination temperature, it results in compounds with high reactivity, while also enabling easy control of the key physical parameters, such as the specific surface area, crystallinity, particle size, and other highly relevant aspects during the synthesis process.

The scientific literature still lacks data on the two-stage synthesis of high-purity ye'elimite. In terms of this synthesis method, the desired properties of the target

product depend on various factors, including the preparation of raw materials, the specifics of hydrothermal synthesis (such as the temperature and duration), precursor stability, high-temperature sintering conditions (in terms of both the temperature and duration), as well as other related parameters. It is likely that this method of synthesis would facilitate a reduction in the calcination temperature and would give more insights into the mechanism behind the ye'elimite formation. Furthermore, the resulting product could serve as an effective additive in cement blends, thereby enhancing their binding properties, and the proposed methodology could be applied in the production of cements containing ye'elimite.

The aim of the dissertation

To investigate the formation of ye'elimite by the two-stage method, which includes the hydrothermal synthesis of a precursor with the corresponding composition and its calcination, to study the formation sequence and the hydration properties of the resulting compounds, as well as to propose the potential application of the obtained product.

The objectives of the dissertation

1. To determine the influence of the mechanochemical activation of the initial mixture and hydrothermal synthesis parameters on the formation processes of calcium monosulfoaluminate 12-hydrate.
2. To investigate the impact of water vapour pressure on calcium monosulfoaluminate 12-hydrate composition alterations in the presence of environment CO₂.
3. To examine the influence of the sintering conditions on the stability of calcium monosulfoaluminate hydrates and the formation mechanism of ye'elimite.
4. To investigate the hydration properties of synthetic ye'elimite and assess the influence of siliceous fly ash (F class) on its hydration.
5. To evaluate the influence of ye'elimite blended into ash Portland cement and formed in belite-ye'elimite-ferrite cement on their hardening process, hydration, the mineral composition of the resulting hydration products and strength properties.

Statements presented for the defence

1. Mechanochemical activation of the initial mixture promotes the formation of the targeted hydrothermal synthesis product – calcium monosulfoaluminate 12-hydrate.
2. Water vapour pressure regulates the carbonation rate of calcium monosulfoaluminate 12-hydrate and influences the formation of the intermediate phases and the final products.

Scientific novelty of the research

1. It has been proven that the mechanochemical activation (three 10 min on-off cycles at 900 rpm) and the two-stage method (hydrothermal synthesis at 110 °C

for 8 h and calcination at 1150 °C for 1 h) allow reducing the sintering temperature by 150 °C and produce high purity (~97%) ye'elimate.

2. It has been determined that the substitution of ye'elimate with fly ash accelerates its hydration due to an increased alkalinity content in the system (the strongest influence), the supply of additional nucleation sites (the filler effect), and a higher water-to-binder ratio.

Practical significance of the scientific research

1. The addition of ye'elimate (0.5–1%) can be used as an accelerator for Ordinary Portland-fly ash cement pastes, as it reduces the initial and final setting times of the prepared pastes by ~1.7 times.
2. The hydrothermal curing of belite-ye'elimate-ferrite cement mortars positively affects their strength development, and the obtained compressive strength values of the produced samples cured at 200 °C for 24 h meet the values defined by the relevant standards for masonry products (EN 771-2).

Approval and publication of the research results

The results obtained in the course of this PhD research have been presented in 5 scientific publications cited in the *Clarivate Analytics Web of Science* database. Based on the work results, one application (No. LT2024 002) has been prepared and submitted to the *Lithuanian Patent Office*, and the results have been presented at 6 international scientific conferences.

Contribution of the author of the thesis and the co-authors of the publications

The author carried out the two-step synthesis, investigated the stability of monosulfoaluminate, the hydration properties of synthetic ye'elimate, and the curing properties of ternary blended cement. The author also performed the theoretical calculations described in this thesis. Prof. Dr. Raimundas Šiaučiūnas advised on the progress of the experiments that were carried out at Kaunas University of Technology and on the preparation of the manuscripts. Assoc. Prof. Dr. Tadas Dambrauskas consulted on the experiments and theoretical calculations. Prof. Dr. Kęstutis Baltakys advised on the progress of the experiment and the preparation of the manuscripts. Assoc. Prof. Dr. Anatolijus Eisinis advised on kinetical calculations. Prof. Dr. Alisa Machner and Dr. Anne Heisig advised on the progress of the experiments that were carried out at the Technical University of Munich. Dr. Harald Hilbig consulted on the results of ²⁷Al nuclear magnetic resonance spectroscopic analysis.

Structure and content of the dissertation

The dissertation consists of an introduction, literature review, experimental part, results and discussion, conclusions, a list of references, a list of publications on the topic of the dissertation, and an appendix. The list of references includes 212 bibliographic sources. The main results are discussed in 182 pages and illustrated in 25 tables, 59 figures, and 1 appendix.

1. LITERATURE REVIEW

1.1. Demand for Research on Cementitious Building Materials

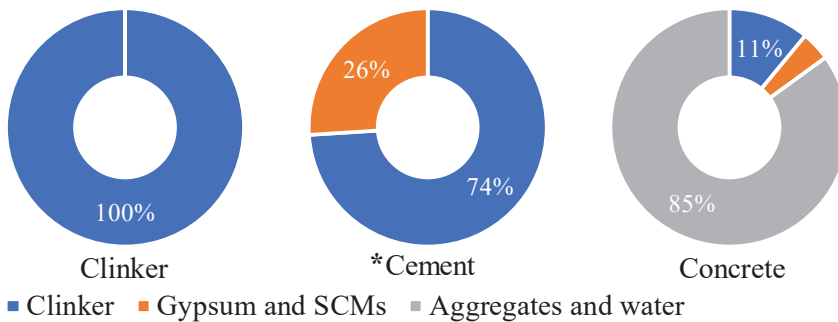
One of the main challenges of the 21st century is climate change which is primarily caused by human activity. According to scientists, this issue is driven by the escalation of greenhouse gases (GHGs), such as carbon dioxide (CO₂), methane (CH₄), nitrous oxide (N₂O), and chlorofluorocarbons (CCl₂F₂), accumulating in the atmosphere[1]. As a result of the industrial revolution, the concentration of CO₂ increased from ~280 to ~420 parts per million (ppm) by volume between the mid-1700s and 2023, thereby establishing a new record high value based on the annual report from *NOAA's Global Monitoring Lab*. Referring to this enormous growth (150%), CO₂ is considered one of the most influential gases among the various greenhouse gases. Thus, these gases directly contribute to global warming, which can lead to many severe environmental alterations, change precipitation patterns, increase risks of droughts and floods, threaten biodiversity, and eventually impact human health [2,3]. To tackle the climate change and mitigate its adverse effects, various international agreements have been established. The *Paris Agreement* (adopted in 2015) aims to limit the global temperature increase to 2 °C this century by reducing global greenhouse gas emissions in the long term [4]. Meanwhile, the *European Commission* approved the *European Green Deal* in 2020, while aiming to make Europe a climate-neutral continent by the year 2050 [5]. To achieve these goals, significant changes are required in various industrial sectors.

Today, concrete is the second most consumed substance after water, with 30 billion tonnes used annually, which is equivalent to ~3.7 tonnes per person on Earth [6]. Houses, skyscrapers, roads, freeways, bridges, sidewalks, water systems, dams, etc. rely on concrete for its superior strength, durability, versatility, and a low cost. While building structures improving our daily lives are essential, the construction and building industry currently accounts for 39% of the global carbon emissions [7]. Considering the urgency of addressing the climate concerns and aligning with the previously mentioned international agreements, the *European Cement Association* (CEMBUREAU) has established a comprehensive framework. This strategic approach, known as *the 5C approach*, covers five chain elements: clinker, cement, concrete, construction, and carbonation [8]. This framework underscores *CEMBUREAU's* commitment to advancing sustainable practices across the entire lifecycle of construction and building sector-related processes and structures, while fostering a strategy to mitigate the climate change.

Looking at one of the elements of the chain, in terms of cement alone, its production accounts for ~8% of the global anthropogenic CO₂ emissions [9,10]. Cement is the essential ingredient of concrete and can be referred to as the 'glue' that binds aggregates of various sizes together when it reacts with water to form a rocklike mass – concrete. Although cement only constitutes 10–15% of the concrete mix by volume, 90% of concrete CO₂ emissions originate from the cement production process (Fig. 1.1). Currently, ~99.8% of clinker produced globally is based on *Ordinary*

Portland cement (OPC) clinker [9,10]. The main constituents of OPC clinker are 60–37% tricalcium silicate (alite, Ca_3SiO_5), 37–15% dicalcium silicate (belite, Ca_2SiO_4), 15–6% tricalcium aluminate ($\text{Ca}_3\text{Al}_2\text{O}_6$), and 18–10% tetracalcium aluminoferrite (ferrite, $\text{Ca}_4\text{Al}_2\text{Fe}_2\text{O}_{10}$) [11]. To produce OPC cement, the prepared clinker is blended with 3–5% gypsum. This addition enables the control of cement mineral hydration and classifies the cement as *CEM I* type [12]. Meanwhile, other OPC cement types include the usage of *supplementary cementitious materials* (SCMs). From an environmental standpoint, OPC has a pretty low carbon footprint. It is estimated that, on average, the production of 1 kg of OPC clinker releases ~0.8 kg of CO_2 . In comparison, cotton textiles produce 11.17–34.90 kgCO_2/kg , steelmaking triggers 2.2 kgCO_2/kg , whereas plastics contributes to the emission of 3.43–5.42 kgCO_2/kg [13–15]. The essential problem is the enormous demand for cement, without which people cannot imagine their lives. It is forecasted that the demand for cement is expected to increase by approximately 45% by 2050 [16].

Percentage of total mass



Percentage of total CO_2 emissions

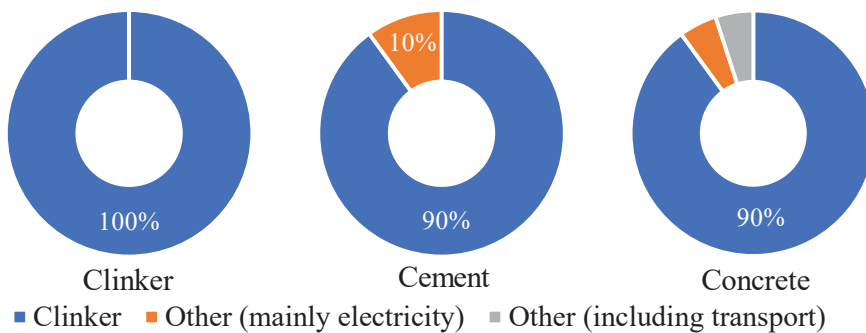


Fig. 1.1. Correlation between the emission of CO_2 and the components of concrete.
*The taken cement composition corresponds to the current average ratio of overall cement types in the EU

Looking at the cement manufacturing process, CO_2 is emitted in different production stages:

- The highest carbon emissions, about 54% of the total, come from the calcination of limestone ($\text{CaCO}_3 \rightarrow \text{CaO} + \text{CO}_2$) [17]. The rotary kiln is at the heart of the manufacturing process, where raw materials are heated, and limestone is decarbonized through a chemical reaction referred to as calcination. Commonly, the initial mixture consists of 65% lime when producing OPC cement.
- 40% of the carbon dioxide emissions from cement plants result from the combustion of fossil fuels to operate the kiln. Cement production is an energy-intensive process associated with a high calcination temperature of ~ 1450 °C, which is required to form the main phase of OPC cement – alite (C_3S), and for the clinker grinding processes. It is worth noting that the cement industry is responsible for about 2–3% of the world’s energy consumption [18].
- The remaining 6% of CO_2 emissions are due to indirect factors, such as the transportation of the finished products and the front-end production processes [19].

Thus, in order to implement international agreements and create a sustainable future, the cement industry must redesign its clinker factor and the quantities of raw materials with a high focus on energy savings and a significant reduction of the CO_2 footprint. As the primary sources of CO_2 emissions derive from the decarbonization of limestone and the calcination of clinker, modifications in these areas offer a significant potential for mitigating the adverse environmental impact.

1.2. Calcium Sulfoaluminate (CSA) Cements

Regarding the previously mentioned issue of cement production, a great number of scientists have been concentrating on researching environmentally friendly types of cement (also known as *Green cement*) in recent decades [19,20]. One of the attractive groups of low-carbon binders is *calcium sulfoaluminate* (CSA) cements. This type of cement is considered a green cement because its production releases less carbon dioxide into the environment. The invention of CSA cement was initiated by Alexander Klein in the late 1950s, mainly for shrinkage compensation in OPC-based concrete, which resulted in the creation of *Type K* cement (ASTM C845–04) [21]. Meanwhile, CSA cement, called ‘the third cement series’, was for the first time industrially manufactured in 1970 in China [22]. Until now, CSA cements have been produced and used in the special cement markets to develop fast-setting mortars, shrinkage compensation, and expansive concretes, which are used in constructing airport runways, freeway pavements, bridges, etc.

1.2.1. CO_2 footprint reduction in the production process of CSA cements

There are several reasons why the CSA cement production process emits lower CO_2 quantities than OPC. One aspect is related to the fact that the mineralogical composition of CSA cements differs from OPC (Fig. 1.2.a). Depending on the initial design of the raw materials, the CSA binders may have a quite variable composition

that contains phases such as ye'elimite ($C_4A_3\hat{S}$), belite ($\beta-C_2S$), tetracalcium alumino ferrite (C_4AF) and calcium aluminates (CA , $C_{12}A_7$, and C_3A) [23]. The majority of the presently listed phases require a lesser quantity of $CaCO_3$ for their formation when compared to alite, the most abundant phase in OPC, which necessitates 3 moles of $CaCO_3$. For instance, the production of pure belite, krotite (CA) and ye'elimite emits approximately 12%, 52%, and 62% less CO_2 than alite, respectively (Fig. 1.2.b).

The second aspect is that the required formation energy of CSA phases is lower than that of alite (Fig. 1.2.b) [24]. For instance, ye'elimite and belite, the primary phases in CSA cement, necessitate $\sim 56\%$ and $\sim 28\%$ less energy, respectively, to form when compared to alite. Due to this reason, CSA clinkers are manufactured at a $\sim 200^\circ C$ lower temperature than required for OPC clinker production. This enables a decrease in the necessary consumption of fossil fuels for clinker combustion, leading to reduced CO_2 emissions associated with fuel combustion. In addition, this type of clinker is softer and easier to crush, which allows the reduction of the energy costs related to clinker grinding. Combining the reduced amount of limestone (20–30%) and energy savings during the CSA cement production enables cutting the CO_2 footprint by 25–35% compared to OPC.

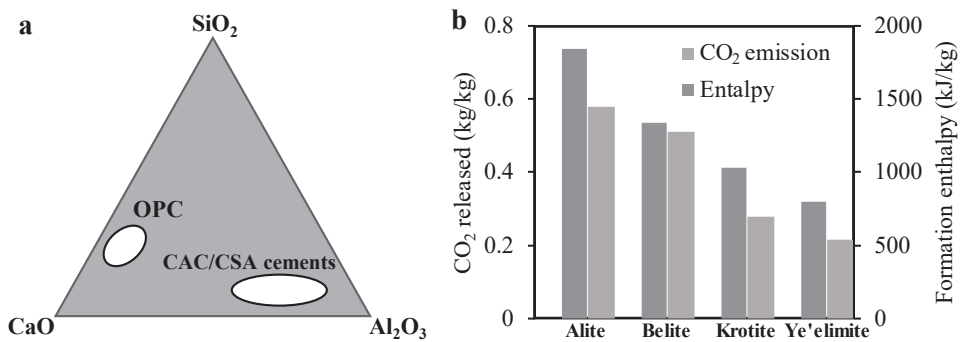


Fig. 1.2. $CaO-SiO_2-Al_2O_3$ phase diagram (a) showing two regions of cementitious phase, Ordinary Portland cement and calcium sulfoaluminate cements, and CO_2 released and energy requirement (b) during the formation of cement phases [23,24]

1.2.2. Mineralogical composition and classification of CSA cements

CSA cements are produced using by limestone as the main raw material, just like OPC, but in lower quantities. Meanwhile, the necessary secondary raw materials must include relatively considered sources of aluminium (bauxite) and sulfur (gypsum). The proportions of these compounds to be used depend on the target composition of the CSA clinker [23,25]. The broader production and application of ye'elimite-based cement faces challenges due to the requirement for expensive raw materials with a high alumina content, such as bauxite. Consequently, this leads to higher costs for CSA cement compared to OPC (to the extent of ~ 6 times). However, studies have shown that it is possible to synthesize ye'elimite-containing cements by

using industrial by-products, or waste materials such as bauxite waste, fly ash, blast furnace slag, and dam sludge [25]. This approach allows for the use of cheaper raw materials, while also reducing the cost of the final product by implementing a circular economy action plan. It is worth noting that industrial by-product integration into the production of CSA cement is currently executed on only a pilot scale.

Depending on the used raw material batch, CSA clinker can contain different cementitious phases, such as ye'elinite as the characteristic and main phase, belite, krotite, grossite (CA_2), tricalcium aluminate (C_3A), brownmillerite, mayenite, and also minor phases like gehlenite (C_2AS) and others [26,27]. Referring to these phases (also covering alite), cements containing ye'elinite are categorized based on the quantitative distribution of the abundant crystalline components within the cement composition. They are distributed into four classes of cements [26]: *calcium sulfoaluminate cement* (CSA; abundant phase – ye'elinite), *belite calcium sulfoaluminate cement* (BCSA; abundant phase – belite), *belite ye'elinite ferrite cement* (BYF; abundant phases – belite and ferrite), and *alite calcium sulfoaluminate cement* (ACSA, alite and ye'elinite) (Table 1.1). It is worth emphasizing that the chemical and mineralogical composition of the presently discussed cements can be very diverse and used in different areas.

Table 1.1. Classification of cements containing ye'elinite [26]

Classification	Abbreviation	Abundant phase	Other phases
Calcium sulfoaluminate cement; Sulfoaluminate cement	CSA	50–80% of $C_4A_3\hat{S}$	C_2S , C_4AF , $C\hat{S}$, $C_{12}A_7$
Belite calcium sulfoaluminate cement; Belite sulfoaluminate cement	BCSA	>50% of C_2S and 20–30% of $C_4A_3\hat{S}$	$C_{12}A_7$, C_4AF , others
Belite-ye'elinite-ferrite cement	BYF	>40% of C_2S , $C_4A_3\hat{S}$ and C_4AF	CA , $C_{12}A_7$, others
Alite calcium sulfoaluminate cement; Alite-ye'elinite cement	ACSA	C_3S and $C_4A_3\hat{S}$	C_2S , CA , others

It is worth emphasizing that CSA cements find frequent application in ternary blended cement systems featuring combinations such as CSA-OPC-anhydrite and CSA-OPC-Fly ash (alternatively, by utilizing silica fume and slag instead of fly ash) [28,29]. These ternary mixtures have a significant practical value, for example, for floor mortars or tile adhesives, because such amalgamations combine the advantages of CSA cement, such as the rapid hardening of the cement paste, a high early strength and a good volume stability, with the benefits provided by Ordinary Portland cement, such as an extremely high compressive strength and durability. Therefore, such systems offer high expectations for the broader application of binders.

1.3. Ye'elimite

Ye'elimite is the main reacting cementitious mineral in CSA cement, and the second most influential phase in BCSA cement. Many properties of concrete made with these types of cement depend on the reaction of ye'elimite with water, including its hydration characteristics and final properties. Ye'elimite is also known as Klein's compound, which was named in honour of Alexander Klein [21]. The mineral's title, 'Ye'elimite', originally comes from the geographic region 'Hill Har Ye'elim' in Israel, where this mineral was discovered in nature for the first time [30]. It is worth highlighting that ye'elimite minerals occur extremely rarely in the nature, in high-temperature combustion metamorphic rocks. The chemical composition of naturally occurring ye'elimite slightly differs from pure ye'elimite. It commonly features 46.49–48.10 wt.% Al_2O_3 , 35.46–36.57 wt.% CaO , and 12.89–13.11 wt.% SO_3 . Other impurities may be present, including SiO_2 (0.43–0.85 wt.%), Fe_2O_3 (1.15–2.79 wt.%), and SrO (0.32–0.58 wt.%). Occasionally, it may also contain small amounts of BaO (up to 0.77 wt.%), K_2O (up to 0.32 wt.%), P_2O_5 (up to 0.24 wt.%), or Na_2O (up to 0.19 wt.%). Notably, no traces of fluorine or chlorine have been detected in naturally occurring ye'elimite.

Recently, many authors have become interested in studying the synthesis and structural features of this mineral on a laboratory scale. The goal of such studies is to understand the unique hydration properties of this mineral which significantly contribute to the final CSA concrete properties. Section 1.3 presents a literature review of the crystallographic structures of ye'elimite, along with the current knowledge of the synthesis methods and the hydration mechanism of ye'elimite.

1.3.1. The crystal structure of ye'elimite

Ye'elimite is attributed to the sodalite mineral family, which has a tetrahedral framework and is built from all-corner-connected tetrahedra [31]. The general composition of sodalite-type structures is expressed as $\text{M}_8(\text{T}_{12}\text{O}_{24})\text{Y}_2$, where M represents a relatively low-charged cage cation (such as Ca^{2+} , Sr^{2+} , K^+ , Na^+ , etc.), T is tetrahedrally coordinated with oxygen as Si^{4+} or Al^{3+} , constituting the framework, and Y is the caged anion, which can either be a single atom anion, such as Cl^- , or a tetrahedrally shaped oxyanion, like XO_4^{2-} . In the case of ye'elimite, it can be described as sodalite with $\text{M} = \text{Ca}$, $\text{T} = \text{Al}$, and $\text{Y} = \text{SO}_4$, crystallizing as a tectoaluminosilicate sodalite structure.

To date, three different crystallographic polymorphs of stoichiometric ye'elimite have been reported in the literature: cubic, tetragonal, and orthorhombic (Fig. 1.3) [32–34]. It is worth emphasizing that only cubic (I43m) and orthorhombic (Pcc2) structures are stable. Based on the results of the powder diffraction and atomistic calculations [31], the structure of orthorhombic ye'elimite is energetically more stable than the cubic structure, which is related to a longer average Al–Ca distance. Therefore, stoichiometric ye'elimite in the cubic structure does not exist in ambient temperatures and can only be present at elevated temperatures. Kurokawa et al. established the reversible transformation temperatures from orthorhombic to cubic

phases, observed at ~ 438 °C upon heating and ~ 469 °C during cooling [35]. Moreover, studies demonstrate that minor elements, such as iron, form a solid solution with ye'elimite. This leads to the partial substitution of Al^{3+} with Fe^{3+} ions in the ye'elimite structure, promoting the stabilization of cubic ye'elimite ($\text{Ca}_4\text{Al}_{2.7}\text{Fe}_{0.3}\hat{\text{S}}$) [36]. Other authors also investigated solid solutions of ye'elimite by adding Na^+ , Si^{4+} , and Fe^{3+} [37–39]. The findings validated the partial substitution of Ca^{2+} ions by Na^+ ions and the substitution of Al^{3+} ions by Fe^{3+} and Si^{4+} ions, which resulted in the formation of a cubic structure of ye'elimite with the chemical formula $\text{Ca}_{3.8}\text{Na}_{0.2}\text{Al}_{5.6}\text{Fe}_{0.2}\text{Si}_{0.2}\text{O}_{12}\text{SO}_4$.

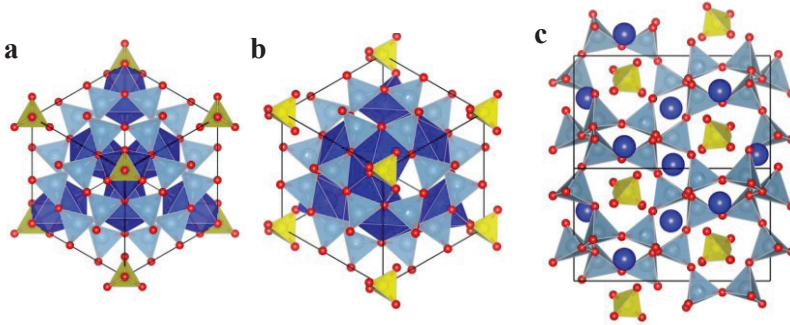


Fig. 1.3. Calculated crystal structures of ye'elimite phases: a – cubic (I43m); b – tetragonal (I4); and c – orthorhombic (Pcc2). Ca is denoted within the dark-blue prisms, Al is within the light-blue tetrahedra, S is within the yellow tetrahedra, and O is red. CaO bonds are omitted in (c) for clarity [31]

1.3.2. The synthesis methods of ye'elimite

All methods currently used for synthesizing ye'elimite can be divided into two main methods: 1) the solid-state reaction method, and 2) the sol-gel method (the chemical routes). The diverse protocols outlined in the literature for the laboratory-scale synthesis of ye'elimite are summarized in Table 1.2. The solid-state reaction method, also known as the conventional synthesis, is the most widely applied. Commonly, the stoichiometric ye'elimite composition ratios of limestone ($\text{C}\hat{\text{C}}$), alumina (A), and gypsum ($\text{C}\hat{\text{S}}\text{H}_2$) are used as raw materials. Other authors also included the pre-firing step, where gypsum is dehydrated into anhydrite ($\text{C}\hat{\text{S}}$), and limestone is decarbonated into lime (C) (Table 1.2). Afterwards, the powder is homogenized or milled, followed by powder or compressed pellets (for moisturizing, water or ethanol is used) firing cycles at 1250–1350 °C. Both powder milling and pelleting are employed to reduce the void space and to enhance the formation of ye'elimite during the solid-state reactions (Table 1.2). It is of importance to note that, when using the solid-state reactions method, multiple cycles of milling, pelleting, and sintering are required to synthesize a high-purity ye'elimite powder. Additionally, the problematic aspect of the synthesis is the instability of ye'elimite and anhydrite at high temperatures [52]. Upon sintering at temperatures above 1300 °C, ye'elimite begins

to decompose into aluminate phases (CA and $C_{12}A_7$), calcium oxide, sulfur dioxide, and oxygen. On the other hand, during the synthesis of ye'elimite at temperatures below 1300 °C, minor phases such as CA, CA_2 , and $C_{12}A_7$ are formed in the final products. Therefore, as a remedy for sulphur evaporation, some authors utilized non-stoichiometric blends with an excess of 10–20 wt.% calcium sulphate.

Table 1.2. Summary of synthesis procedures for high purity ye'elimite employed in prior studies

Raw materials	Preparation of raw materials	Sintering conditions	Products	Reference
$C\hat{S}H_2/A/C\hat{C}$	Pre-fired 1000 °C	1350 °C 4–12 h	$C_4A_3\hat{S}$, C, C_3A	Halstead and Moore (1962) [40]
?	Pre-fired 1000 °C + Pellets	800–1400 °C 12–14 h	–	Saalfeld and Depmeier (1972) [41]
$Ca(NO_3)_2$, $(NH_4)_2SO_4$, $Al(NO_3)_3$	Mix in water + Pre-fired (597 °C) + Pellets	0.25 h / 0.5 h / 1h /2 h / 4 h 1100–1125–1150– 1175 °C	$C_{12}A_7$, CA, CA_2	Hanic et al. (1986) [42]
$C\hat{S}/CA$	Pellets	0.25 h / 0.5 h / 1 h /2 h / 4 h 1160–1180–1190– 1200 °C		
$C\hat{S}H_2/A/C\hat{C}$	Crushed and mixed	3 h 1350 °C	–	Krstanovića et al. (1992) [43]
$C\hat{S}H_2/AH_3/C\hat{C}$	Homogenized	1320 °C 1 h	–	Peixing et al. (1992) [44]
$C\hat{S}/A/C\hat{C}$	Crushed (<63 μm) + pellets	1100–1200–1250– 1300–1325 °C 0.5–4 h	$C_4A_3\hat{S}$, CA	Ali et al. (1994) [45]
$C\hat{S}/A/C\hat{C}$	Pre-dried	6 h 800 °C, then 4 h 900 °C, and then 1300 °C	–	Andac and F.P. Glasser (1994) [46]
$C\hat{S}H_2/A/C\hat{C}$	Gypsum pre-fired at 1000 °C, mixed in ethanol during 10 h	9h 1300 °C	$C_4A_3\hat{S}$	Ikeda et al. (1996) [47]
$C\hat{S}H_2/A/C\hat{C}$	–	1h 1350 °C	$C_4A_3\hat{S}$, CA, $C_{12}A_7$, CA_2	Song and Young (2002) [48]
$Ca(NO_3)_2$, 4H ₂ / $Al(NO_3)_3 \cdot 9H_2O$ / $Al_2(SO_4)_3$,		12 h 105 °C, then		

14–18H ₂ O	Mixed in polyvinyl alcohol	1 h 500–1300 °C		
CŜH ₂ /A /CĈ	Mixed in water + Pellets	4 h 1300 °C	C ₄ A ₃ Ŝ	Winnefeld and Barlag (2009) [49]
CŜH ₂ /A/CĈ	Mix in water + Pellets	4 h 1300 °C, slow cooling	C ₄ A ₃ Ŝ, CA, C ₃ A, C ₁₂ A ₇	A. Cuesta et al. (2013/2014) [31,50]
CŜ/A/ CĈ	–	2 h 1300 °C, slow cooling	C ₄ A ₃ Ŝ, CA	Kurokawa et al. (2014) [35]
CŜH ₂ /A/ CĈ	A and CĈ dried at 105 °C, CŜH ₂ at 40 °C. The prepared mixture was mixed with acetone (20 min 500 rpm) and dried at 40 °C for 24 h	3 h 1200 °C	C ₄ A ₃ Ŝ, CŜ, A, C	Mokra et al. (2016) [51]
CŜH ₂ /A/CĈ	Mixture homogenized for 15 min, then ground for 1 h (120 rpm) + pressed tablets	0.5–4 h 1000–1350 °C (Optimal: 3 h 1300 °C)	C ₄ A ₃ Ŝ C ₁₂ A ₇ , CA, CA ₂ , CŜ	El Khessaimi et al. (2018) [52]
Ca(NO ₃) _{2.4} H ₂ O Al(NO ₃) _{2.9} H ₂ O Al ₂ (SO ₄) _{3.16} H ₂ O Deionized H ₂ O Citric acid Ethylene glycol PVA 22000 (5 wt.% aqueous sol.)	Pechini synthesis, Organic steric entrapment synthesis, Self-propagating combustion synthesis	400–1290 °C 1 h (Optimal: 1 h 1250 °C)	C ₄ A ₃ Ŝ, CA, CA ₂ ,	El Khessaimi et al. (2019) [53]
CŜH ₂ /A	Homogenized for 0.5 h by using ethanol	900–1350 °C 30 min	C ₄ A ₃ Ŝ, CA, A, CA ₆	Wu et al. (2023) [54]
CŜH ₂ /A PbCl ₂	Molten salt method	1250 °C 0.5–4 h	C ₄ A ₃ Ŝ, CA, A, CŜ	

Unfortunately, many papers (especially the older ones) vaguely describe the applied processes and lack essential details about the methods used for the synthesis and the prepared quantity of ye'elimitite. Recently, a comprehensive study on ye'elimitite

synthesis through the solid-state reaction method was reported by El Khessaimi et al. [52]. This work used a stoichiometric mixture corresponding to $C_4A_3\bar{S}$, which was prepared from reagent-grade $C\hat{C}$, A, and $C\hat{S}H_2$. The mixture was homogenized (15 min), which was followed by milling at 120 rpm for 1 h ($d_{50} = 14.6 \mu\text{m}$). The prepared mixture was then pelleted (form diameter: 20 mm, load: 1 tonne) and sintered at 1000–1350 °C (heating rate: 5 °C/min) with the dwell duration varying from 0.5 to 4 h. The examination demonstrated that ye'elinite formation begins at 1000 °C with the interaction between $C\hat{C}$, A and $C\hat{S}H_2$ and continues until 1300 °C through the reaction between the minor calcium aluminate phases ($C_{12}A_7$, CA, CA_2) and $C\hat{S}$. Investigations of the sintering temperature and duration confirmed that 1300 °C for 3 h is required to maximize the ye'elinite formation ($84.5 \pm 1.5 \text{ wt.}\%$). Meanwhile, when exceeding 1300 °C, the testing led to the decomposition of ye'elinite into calcium aluminate phases, SO_2 , and O_2 gas. Additionally, it was identified that high-purity ye'elinite ($\sim 98\%$) can be achieved by using a second firing cycle (at 1300 °C for 3 h) with a slight excess of $CaSO_4$ (10 wt.%) in the sample. It is worth emphasizing that the observation identified by El Khessaimi et al. corresponds well with the studies of other authors [35,42,55].

In another study, El Khessaimi et al. [56] summarized the possible solid-state diffusion mechanism during ye'elinite formation, while referring to the kinetic results obtained by Li et al. [57]. They recognized that the diffusive ions in the formation of ye'elinite are Ca^{2+} and SO_4^{2-} . During the sintering process, Ca^{2+} ions emerge from C which diffuses through calcium aluminates. These ions subsequently react with alumina, thus inducing the formation of CA_2 around the A/ CA_2 contact region. Further, Ca^{2+} ions reach CA_2 and react to produce CA. Alternatively, CA can decompose into C, thus producing Ca^{2+} ions and CA_2 , which results in the growth of CA_2 grains and a decrease in CA. It is worth highlighting that a similar formation mechanism of calcium aluminates has also been identified by other authors [58–60]. Meanwhile, the growth of the $C_4A_3\bar{S}$ phase depends on the contact of CA and CA_2 with the $C\hat{S}$ phase, i.e., Ca^{2+} and SO_4^{2-} diffuse from $C\hat{S}$ through the $C_4A_3\bar{S}/CA$ contact region, thereby inducing the formation of $C_4A_3\bar{S}$. The simplified schematic model of the reaction-product layers forming during the ye'elinite synthesis is presented in Fig. 1.4.

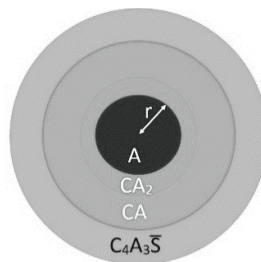


Fig. 1.4. Simplified schematic representation of the reaction product layers emerging during ye'elinite formation [56]

To summarize, the formation of ye'elimite can be described in a two-step process. In the first stage (a short duration and low temperatures), the reaction between C, A and C \hat{S} takes place, inducing the formation of calcium aluminate layers and some ye'elimite, which is controlled by interface processes (chemical reaction, nucleation, and product growth). During the second step (a high temperature and long durations), calcium and sulfate (either free or combined) diffuse into calcium aluminate phases, leading to the formation of C $_4$ A $_3\hat{S}$, where the diffusion rate is the governing factor for the reactions.

The second widely applied group of synthesis for cementitious phases is the sol-gel method, also known as the chemical routes method. Different sol-gel methods include mixing inorganic metal salts or organic metal compounds as the starting materials with polymer precursors (citric acid, ethylene glycol, or polyvinyl alcohol). The initial materials are used to prepare a colloidal suspension (sol), which undergoes gelation with ageing and drying, during which, a three-dimensional network (gel) is formed. Afterwards, the gel is dried until foam is created, which is then crushed until powder, and used as a precursor in the sintering process to produce the final products (cementitious phases) [61]. The rate of the reactants depends on several factors, including pH, the concentration, the solvent type, and the temperature.

Researchers have been showing an increasing interest in applying the sol-gel technology in cement in recent decades for several reasons. The sol-gel technique imparts a significant degree of homogeneity to the colloidal gel, thus making it conducive for producing minerals of high purity at lower processing temperatures than the solid-state reaction method [62,63]. Additionally, the sol-gel conditions (the starting precursors, the water content, the catalyst, and the synthesis temperature) are easy to modify, and the synthesis is easy to replicate. Other advantages of this method are that it provides the opportunity to obtain materials with properties such as a low particle size (a high specific surface area), a high reactivity, and the formation of sub-micronic or nanometric crystallite structures [64].

Various high-purity cementitious phases, such as C $_3$ S, C $_2$ S, C $_3$ A and CA, etc., have been synthesized by using the sol-gel method in the past [65–67]. In the case of the synthesis of ye'elimite, only two works have been published which would deal with ye'elimite production by applying the chemical methods. Song and Young used a PVA (Poly Vinyl Alcohol)-based chemical method, where the stoichiometric mixture of calcium nitrate, aluminium nitrate and aluminium sulfate was mixed in a 5 wt.% PVA solution [48]. The prepared suspension was dried at 105 °C for 12 h, and the resulting gel was calcinated at 500–1300 °C for 1 h. The results indicated that, by applying this method, C $_4$ A $_3\hat{S}$ formation begins at 900 °C, its content increases up to 1300 °C, where it is already identified as the only crystalline phase. The study did not investigate the multiscale size characterization or the effect of the organic precursors on the synthesis of ye'elimite, nor did it quantify the formed ye'elimite.

El Khessaimi et al. [53] synthesized ye'elimite by applying three different polymer precursor methods: the *Pechini* method (Pech), the *Organic Steric Entrapment* method (OSE), and the *Self-Propagating Combustion* (SPC). For all of

these methods, $\text{Ca}(\text{NO}_3)_2 \cdot 4\text{H}_2\text{O}$, $\text{Al}(\text{NO}_3)_3 \cdot 9\text{H}_2\text{O}$ and $\text{Al}_2(\text{SO}_4)_3 \cdot 16\text{H}_2\text{O}$ were used as the starting materials in stoichiometric amounts corresponding to ye'elimite. The difference in the applied sol-gel methods is that different liquid mediums were used: for Pech – citric acid, ethylene glycol, and deionized water; for OSE – an aqueous solution of PVA 22000 and deionized water; for SPC – citric acid and deionized water. The prepared aqueous solutions were stirred at 80 °C for 8 h, which resulted in the formation of a viscous gel. Subsequently, the gels were dried at 150 °C for 8 h, and the crushed-and-prepared powders were calcinated at 400–1290 °C for 1 h. The findings demonstrated that the employment of these methods allows for producing high-purity ye'elimite at 1250 °C sustained for 1 hour. Specifically, the Pech, OSE, and SPC methods resulted in ye'elimite purities of 95.8 wt%, 97.9 wt%, and 98.3 wt%, respectively. According to Rietveld analysis results, CA and CA₂ were the only intermediate crystalline phases, which, with an increasing sintering temperature, were consumed for the formation of ye'elimite. Additionally, the prevailing crystallite size varied from 51 nm to 57 nm, with the average particle size ranging between 136 nm and 175 nm.

Although the sol-gel synthesis method has the potential to produce high-purity ye'elimite, this synthesis method also incurs several drawbacks. The sol-gel method can be a time-consuming process because it often requires long ageing times or multiple heating and drying steps. Additionally, the use of expensive precursors, catalysts, and solvents, as well as the need for specialized equipment, such as controlled atmosphere systems, significantly increases the overall cost of this synthesis. Further, the sol-gel method often produces purification and/or degradation by-products, such as CO₂ and NO_x, along with large amounts of solvents used for the synthesis, which require additional technologies and facilities for utilization.

1.3.3. Hydration mechanism of ye'elimite

The hydration process of cement is a complex process due to its multi-mineralogical composition. It proceeds through dissolution and precipitation processes, leading to the formation of various hydrates [68]. Additionally, it is widely known that the process of cement hydration can be affected by various factors. For instance, the presence of extra ions within cement minerals, the polydispersity and granulometric composition of the cement particles, the water-cement ratio (W/C), the ambient temperature, and the usage of additives to adjust the properties of the cement paste, as well as the inclusion of supplementary cementitious materials, can all have an impact [69]. A straightforward approach towards investigating the factors of different cementitious phases is to analyze the hydration of the primary reactive cementitious phase under conditions of controlled hydration.

Regardless of the CSA cement type, once water has been added to cement, ye'elimite is one of the first reacting phases (along with calcium aluminates, if present). In the presence of a soluble calcium sulphate source (gypsum, bassanite [$\text{CaSO}_4 \cdot 0.5\text{H}_2\text{O}$], or anhydrite), ye'elimite undergoes hydration, thus giving rise to the formation of ettringite ($\text{C}_6\text{A}\hat{\text{S}}_3\text{H}_{32}$) and aluminium hydroxide (AH_3) (both amorphous

and microcrystalline) (Eq. 1.1) [49,70,71]. In the case of pure ye'elimite interacting with water, such reactions lead to the formation of monosulfoaluminate ($C_4A\hat{S}H_{12}$) and AH_3 (Eq. 1.2) [49,70,71]. It is worth emphasizing that even without sulphate in the system, a small quantity of ettringite and amorphous/microcrystalline aluminium hydroxide is always observed.



The amount of soluble calcium sulphate plays a crucial role in controlling the hydration of ye'elimite and the final performance of CSA pastes/concrete/mortars. The addition of a calcium sulphate source not only promotes the formation of ettringite, but also accelerates the hydration rate of ye'elimite, which depends on the calcium sulphate type [72,73]. The different sulfate sources have diverse dissolution rates (bassanite>gypsum>anhydrite), whereas the optimal variety is the commonly chosen gypsum. It is also important to highlight that the formation of ettringite from the hydration reactions of ye'elimite with calcium sulphate can cause an expansion in the hardening cement system [74]. It has been suggested that if most of the ettringite forms before hardening, then, non-expansive and rapidly hardening CSA cement can be achieved, but the significant formation of ettringite after hardening can cause expansion and cracking. Therefore, it is essential to determine the optimal calcium sulfate additions (its type and quantities) to obtain the required performance of the cementitious material.

There have been several attempts to investigate the hydration mechanisms of two ye'elimite polymorphs. Cuesta et al. [75] studied the hydration mechanisms of orthorhombic ye'elimite ($Ca_4Al_6O_{12}SO_4$) and cubic ye'elimite ($Ca_{3.8}Na_{0.2}Al_{5.6}Fe_{0.2}Si_{0.2}O_{12}SO_4$) as a function of ye'elimite polymorphism, along with the water content as well as the type and content of the sulfate source. The results indicated that, without gypsum, cubic ye'elimite reacts faster than orthorhombic ye'elimite, where monosulfoaluminate was observed as the major crystalline hydrate. In the meantime, the hydration rate of orthorhombic ye'elimite becomes higher than cubic ye'elimite when gypsum is used alongside.

Jansen et al. [76] studied the impact of calcium sulphates on the hydration mechanisms of orthorhombic ye'elimite and iron-containing cubic ye'elimite ($C_4Al_{2.7}F_{0.3}\hat{S}$) by means of isothermal calorimetry. They also confirmed that, in the absence of calcium sulphate, the hydration rate of orthorhombic ye'elimite is slower than that of cubic ye'elimite. To the contrary, the addition of gypsum leads to highly similar reactions. Additionally, it was identified that, during the hydration of both ye'elimite polymorphs with gypsum, ettringite precipitates in two steps. In the first step, the interaction between ye'elimite, gypsum and water takes place, which promotes the formation of ettringite and a highly hydrated AH_x . Meanwhile, in the second step, ettringite precipitation is supported by only ye'elimite dissolution, i.e., no more gypsum is dissolved in the second stage. The understanding of the second step still remains limited. However, it might be explained by the sulphate incorporation in

the amorphous AH_3 gel, and the presence of calcium ions in the amorphous phase, which are precursors for the second formation of ettringite.

In contrast, Irissi et al. [77] and Chen et al. [78] demonstrated that the hydration of cubic (iron-rich) ye'elimite is slower than that of orthorhombic ye'elimite. Other authors also confirmed the same hydration tendency with lower levels of iron substitution ($C_4A_{3-x}F_x\hat{S}$, x of 0.05–0.08) [79]. Meanwhile, a substantial acceleration in the cubic ye'elimite hydration rate was identified with higher iron substitutions (x of 0.2–0.4). Bullerjahn et al. [80] concluded that ye'elimite polymorphism (alone) could not explain the observed differences in the hydration kinetics. To verify this statement, they added ground synthetic mayenite to orthorhombic ye'elimite. With this experiment, they obtained faster initial reactions, altered the calcium/aluminium (Ca/Al) ratio in the solutions, and achieved high pH values, which were also observed during the initial hydration period of cubic ye'elimite. It was determined that adding 1% of mayenite is sufficient to reproduce the hydration pattern of cubic ye'elimite. It is of importance to note that the addition of iron accelerates the formation of cubic ye'elimite, which also leads to a faster decomposition of ye'elimite, along with sulphur volatilization. As a result, mayenite is formed, thereby altering the hydration kinetics of cubic ye'elimite. Thus, it appears that the presence of small amounts of mayenite, rather than polymorphism, is responsible for the different kinetics of ye'elimite.

Researchers have also studied the impact of other compounds on the ye'elimite hydration mechanism. Hargis et al. [81] examined the impact of calcium carbonates (calcite and vaterite), both with and without gypsum, on the hydration of ye'elimite. The examination confirmed that both calcite and vaterite accelerate the hydration rate of ye'elimite due to the filler effect, i.e., fine calcium carbonate provides additional nucleation sites. Additionally, both calcite and vaterite reacted with monosulfoaluminate to give monocarboaluminate and ettringite, with vaterite being more reactive, whereas gypsum lowered the reactivity of both carbonates.

Further, the impact of an alkaline environment on the early-age hydration of ye'elimite is also acknowledged in the literature. The studies point out that a higher pH value (with 0.1 M, 1 M, 2 M NaOH) enhances the dissolution of ye'elimite and the subsequent formation of hydrates (ettringite and AH_3) [82–84]. At high alkalinities (4 M and 8 M), retardation in the hydration kinetics is observed. This is linked to the instability of ettringite and the precipitation of other hydrates (CAH_{10} , C_3AH_6 , and thenardite). Furthermore, it should be noted that aluminium hydroxide displays greater crystallinity at higher pH levels.

Investigation of the use of retarders (additives, superplasticizers) in cement hydration is essential to achieve well-controlled and workable concrete mixes, thereby ensuring the construction efficiency, and meeting the specific requirements of diverse construction scenarios. Hydroxylic organic compounds, such as sugars or citric, tartaric or gluconic acids and their respective salts, serve as potent retarders in CSA cements [82,83]. Citric acid is the primary carboxylic acid used to retard CSA cement setting. The mechanism by which citric acid solutions modify the hydration of high-purity ye'elimite has been investigated in detail by Y. El Khessaimi et al. [85]. Their

study demonstrated that the presence of citric acid at concentrations of 0.5 wt.% and 1 wt.% leads to a retarding effect on the dissolution of ye'elimite grains. Additionally, it has been observed that citric acid reduces the formation of hydrates, especially ettringite. The reason why citric acid causes a delay in the reaction can be explained by the fact that citrate molecules form chemical complexes (known as chelates) with calcium on the surface of ye'elimite. This interference with ye'elimite dissolution hinders the reaction, as citrate molecules also form chelates with calcium ions which are already present in the solution. This makes them less available for the hydration reactions of ye'elimite.

1.4. Structure and Properties of Calcium Sulfoaluminate Hydrates

It is recognized that, in the $\text{CaO}-\text{Al}_2\text{O}_3-\text{CaSO}_4-\text{H}_2\text{O}$ system, two main phases may occur – ettringite and calcium monosulfoaluminate hydrate. These phases are detected not only during the hydration of calcium sulfoaluminate/aluminate-containing binders, but also in Portland cement [86,87]. As mentioned previously, a sufficient amount of additional calcium sulphate is needed for ettringite formation. Meanwhile, the deficiency of calcium sulphates results in the formation of monosulfoaluminate. In addition, ettringite can convert to monosulfoaluminate when sulphate is consumed, and *vice versa*. Regarding the stability of these phases, it is essential to comprehend their behaviour in given conditions for concrete sustainability and durability. Section 1.4 provides a review of the literature on the crystallographic structures of ettringite and monosulfoaluminate, together with the current knowledge of the synthesis methods and their stability.

1.4.1. Calcium trisulfoaluminate hydrate (ettringite)

Ettringite is one of the most important members of the calcium trisulfoaluminate hydrate (AFt) mineral group which is rarely found in the nature but is widespread in the mineralogy of hydrated cements. Ettringite has a general formula of $[\text{Ca}_3\text{Al}(\text{OH})_6 \cdot 12\text{H}_2\text{O}]_2 \cdot \text{X}_3 \cdot n\text{H}_2\text{O}$, where n is usually ≤ 2 , whereas X represents the corresponding anion. In the case of ettringite, the anion is typically SO_4^{2-} , but, due to its flexible structure, other anions, such as Cl^- , CO_3^{2-} and CrO_4^{2-} , can be intercalated [88]. The structure of ettringite is based on the column structure ($[\text{Ca}_6[\text{Al}(\text{OH})_6]_2 \cdot 24\text{H}_2\text{O}]^{6+}$) running parallel to the c axis and the channel components (SO_4^{2-} and H_2O) in the inter-column channels joining the whole structure together by a network of hydrogen bonds [89]. Due to this structure, it has a lower density ($\sim 1770 \text{ kg/m}^3$) and a higher water content (32 mol; 46%) than other cement-based hydrates. Ettringite crystals are hexagonal prisms, often elongated with different shapes: needle-like (most commonly), lath-like, or rod-like.

The most widely used synthesis of pure ettringite is based on precipitation from the solutions. For this method, analytical grade $\text{Ca}(\text{OH})_2$ and $\text{Al}_2(\text{SO}_4)_3 \cdot \text{XH}_2\text{O}$ are used as the starting materials. The two reaction solutions are mixed with $\text{CaO}/\text{Al}_2\text{O}_3$ at a molar ratio of 6:1 for 3h and stored at room temperature for 2 days to precipitate ettringite crystals. Afterwards, the suspension is filtered and dried over a saturated CaCl_2 solution (35% RH) [90–92]. This conversion method of the solution allows the

synthesis of high-purity ettringite, and only small impurities of calcium carbonate and monosulfoaluminate were detected. Other authors also employed cementitious phases as the precursors for the synthesis of ettringite. For this approach, phases like CA, C₃A, C₁₂A₇ and C₄A₃S̄ are mixed with the required amount of gypsum and water, where the prepared suspension ages for a couple of days [93–95]. Although the use of a cementitious precursor to synthesize ettringite is a slow process which can take up to 10 days, it results in a highly pure product and effectively eliminates the formation of other potential mineral impurities.

Moreover, to synthesize the ettringite (and also monosulfoaluminate), the technique used for free water removal from the sample must be considered. According to the literature, AFt and AFm phases are highly sensitive. Techniques such as oven-drying (105 °C), vacuum drying, and freeze-drying remove not only the free water but also structural water from the structures, resulting in the microstructure alteration [96,97]. Therefore, it is recommended to adopt milder methods such as solvent exchange, or use isopropanol over other solvents. It has been proven that the application of isopropanol for a limited time has the lowest damaging effect on the microstructure of ettringite and monosulfoaluminate compared to that of methanol, ethanol, and acetone [98,99].

Regarding the stability of AFt and AFm, it is essential to comprehend their behaviour under given conditions for concrete sustainability and durability. Several authors have reported a similar ettringite decomposition process, while separating it into three steps [100,101]. It has been identified that the first 23 molecules of water (33% of mass loss) are lost in the temperature between 40 °C and 180 °C, with the main TGA peak at ~110 °C. The following three molecules undergo dehydration in the temperature range of 200–280 °C, while the remaining three molecules dehydrate between 280 °C and 500 °C. Looking at the mineralogical changes, the gradual drying of ettringite reduces its crystallinity, and its structure degrades to metaettringite (i.e., ettringite with 10–13 H₂O molecules) at 55–95 °C, and, finally, to monosulfoaluminate and bassanite (CaSO₄·0.5H₂O) at 114–116 °C temperature [102]. Moreover, ettringite has been reported to persist in aqueous solutions even at elevated temperatures (90 °C) due to its limited solubility in water. Similarly, when exposed to saturated steam (100% RH), ettringite exhibited greater resistance compared to dry conditions. The conversion into monosulfoaluminate and bassanite was only observed at a temperature as high as ~149 °C [103]. Recently, the practical stability of ettringite under different temperatures and relative humidity was modeled by Baquerizo et al. [93]. Experimental and theoretical results also confirmed that the stability of ettringite correlates with RH, i.e., a higher relative humidity increases the ettringite stability.

1.4.2. Calcium monosulfoaluminate hydrate

Calcium monosulfoaluminate hydrate (Ms) is categorized within the group of hydrated minerals known as tetracalcium aluminate-ferrite-mono (AFm) phases, which are part of the layered double hydroxide family (LDH-type) [104]. LDHs are

also known as hydrotalcite-like compounds due to their resemblance to hydrotalcite with the general formula $[\text{MII}_{1-x}\text{MIII}_x(\text{OH})_2]^{x+} [\text{A}^{n-} \cdot y\text{H}_2\text{O}]^{x-}$, where MII and MIII represent divalent (Ca^{2+} , Mg^{2+} , Zn^{2+} , etc.) and trivalent (Al^{3+} , Fe^{3+} , Cr^{3+} , etc.) metal cations, respectively, and A^{n-} is an n -valent anion (OH^- , NO_3^- , SO_4^{2-} , CO_3^{2-} , etc.) [105]. Looking at the structure of Ms, it contains positively charged main layers $[\text{Ca}_2(\text{Al,Fe})(\text{OH})_6]^+$ and negatively charged interlayers $[\text{SO}_4 \cdot n\text{H}_2\text{O}]^{2-}$ (Fig. 1.5) [106]. Referring to previous works [107,108], the interlayer content can vary from 2 to 10 molecules, displaying different hydration states, i.e., Ms9, Ms10.5, Ms12, Ms14, Ms16 (the layer thickness varies from 7.96 Å to 9.57 Å), where the number indicates the amount of water present in the compound. Calcium monosulfoaluminate 12-hydrate (Ms12) is the most abundant hydration state in cement hydrate systems. It is worth noting that it has a naturally occurring structure analogue – mineral kuzelite ($\text{C}_4\text{A}\hat{\text{S}}\text{H}_{12}$), whose structure was characterized by R. Allmann [109].

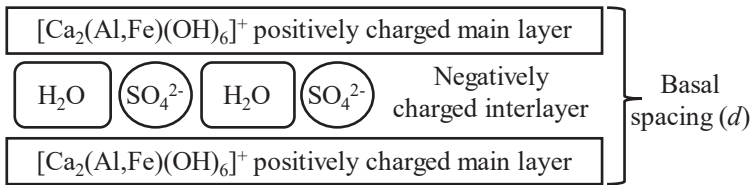


Fig. 1.5. Schematic representation of the lamellar structure in AFm phase [107]

The lab-scale production of calcium monosulfoaluminate can be performed by applying various approaches. The first synthesis of calcium monosulfoaluminate was carried out by Kuzel in 1965 [98]. He used a stoichiometric mixture of tricalcium aluminate and gypsum which was hydrothermally treated at 150 °C for 4 days. The purity of the synthesized monosulfoaluminate was not identified in this work. There have also been attempts to produce Ms through the hydrothermal decomposition of ettringite at ~115 °C [110]. It should be specified that this approach complicates the synthesis process, and impurities (bassanite) in the final products were identified. Over the last few decades, a commonly utilized approach for synthesizing Ms includes the preparation of a suspension from C_3A and CaSO_4 in a 1:1 molar ratio, which was heated and stirred periodically at 85 °C for 7 days to 3 months, depending on the specific approach used by the authors [111–113]. It is worth noting that there is no literature on monosulfoaluminate synthesis from non-stoichiometric mixtures.

When striving to produce individual hydration states of monosulfoaluminate, it is also essential to evaluate the environmental aspects. It is acknowledged that the temperature and *relative humidity* (RH) regulate which hydration state of Ms will occur in the $\text{CaO}-\text{Al}_2\text{O}_3-\text{CaSO}_4-\text{H}_2\text{O}$ system. When assessing the Ms stability in an aqueous medium, Damdot and Glasser determined that monosulfoaluminate becomes more stable with an increasing temperature (>45 °C) at the expense of ettringite [114]. Additionally, several studies have been carried out on the stability of the hydration states of synthetic monosulfoaluminate (powder) as a function of the temperature and relative humidity [108,111,115]. The most recent study was done by Luis G.

Baquerizo et al., in which the researchers also addressed the thermodynamic properties associated with these changes [107,112]. The obtained results indicated that Ms16 is stable only at lower temperatures (5–18 °C) at a given high relative humidity (>92%). At room temperature (25 °C), Ms14 is only stable in the presence of high RH (>97%). Below this RH value (<97%), Ms14 dehydrates to Ms12 and remains stable until the RH level drops to 23% (Ms12 → Ms10.5). Meanwhile, Ms9 was observed to exist only at low RH (<2%). Additionally, it was determined that rehydration of Ms12→Ms14 does not occur at room temperature, and that it requires elevated temperatures, for instance, 50 °C and >90% RH.

To date, the thermal decomposition of monosulfoaluminate has been reported in several studies, which identified the phenomenon of multiple transformations accompanied by a mass change. Pöllmann (1984) [106] reported that the loss of the six interlayer water molecules proceeds between 43–200 °C. Meanwhile, the six remaining water molecules from the main layers are lost between 200 and 300 °C. Other authors have suggested that the crystalline water from the octahedral layer is lost at slightly higher temperatures (250–300 °C) [116–118]. Accordingly, the remaining mass loss beyond this temperature is associated with the dehydration of the main layers. However, most of the previous studies dealing with the stability of monosulfoaluminate were mainly validated by thermal analysis (DSC/TG) and *ex-situ* XRD experimental results. These results do not demonstrate the precise mechanism and kinetics of the degradation reactions of monosulfoaluminate, thus leaving not-well-resolved questions about the decomposition of monosulfoaluminate. In addition, there is a lack of elaboration on the obtained results, such as the beginning and the end temperatures of the transitional phases, i.e., different hydration states of monosulfoaluminate.

Another essential stability factor of Ms is the carbonation resistance. It is known that the carbonation of cementitious hydrate phases is one of the crucial factors driving the deterioration of concrete structures. Comprehending the carbonation of individual cement hydrates allows us to improve the cement composition and predict the durability of concrete. When reviewing the carbonation of monosulfoaluminate, it is observed that most of the studies were performed on the mortar samples, and only a few attempts were made on pure monosulfoaluminate [119–121]. Studies report that monosulfoaluminate is one of the earliest phases to react as soon as CO₂ is available in the concrete system [122,123]. It is known that the final disintegration products of monosulfoaluminate are the same as for ettringite: calcium carbonate, aluminium hydroxide, gypsum, and water. Additionally, investigations [124] confirmed the formation of intermediate reaction products, such as hemicarboaluminate (C₄A \hat{c} _{0.5}H_{11.5}), monocarboaluminate (C₄A \hat{c} H₁₁), and ettringite. However, questions regarding the carbonation of monosulfoaluminate and the impact of the reaction kinetics on the formation of various intermediate products still persist.

1.5. Hydrothermal-Calcination Synthesis Method for Cementitious Materials

A higher interest in the hydrothermal technology for the synthesis of materials started to be observed in the 20th century, particularly in the fields of hydrometallurgy and single-crystal growth [125]. In recent years, there has been a renewed commercial interest in hydrothermal synthesis, attributable to the emergence of an expanding family of materials, predominantly ceramic powders, which can be prepared under relatively mild conditions ($T < 350\text{ }^{\circ}\text{C}$, $P < 100\text{ MPa}$). The term ‘hydrothermal’ typically denotes any heterogeneous reaction occurring in the presence of aqueous solvents or mineralizers under elevated pressure and temperature conditions. This facilitates the dissolution and recrystallization (recovery) of the materials that are generally insoluble under the ordinary conditions. Synthesis is usually conducted inside a pressure vessel, also known as an autoclave. In terms of producing ceramic powder, the process involves fewer time-consuming and energy-intensive steps because the high-temperature calcination, mixing, and milling steps are either no more needed, or else they are minimized. Additionally, the ability to precipitate already crystallized powders directly from a solution helps regulate the rate and uniformity of the nucleation, growth, and ageing. As a result, it is possible to better control the size and morphology of crystallite and significantly reduce the aggregation levels, which is not possible with many other synthesis processes [126].

Hydrothermal-calcination synthesis is another method used for synthesizing cementitious phases, allowing the reduction of the energy needed for final calcination. This synthesis typically involves two stages. In the first stage, the initial mixture undergoes hydrothermal treatment (alternatively, microwave synthesis can be applied), which results in the formation of cementitious hydrates as the final products. In the following stage, the formed hydrates undergo calcination at the necessary temperature, thereby stabilizing anhydrous cement phases. It is worth highlighting that the initial materials in use can be the same as for the solid-state synthesis, and that no expensive substances are required.

In terms of producing pure cementitious phases, this technology has been extensively studied for the synthesis of high-purity β - C_2S , C_3A and C_{12}A_7 . Ishida and co-authors [127] thoroughly investigated the preparation and hydration of reactive β -dicalcium silicate obtained by the thermal decomposition of hydrothermally obtained calcium silicate hydrates. They demonstrated that highly reactive β - C_2S can be produced by using an initial mixture of reagent-grade calcium oxide and quartz, with hydrothermal treatment at $250\text{ }^{\circ}\text{C}$ for 20 h and calcination at $600\text{ }^{\circ}\text{C}$ for 1 h. Meanwhile, Nakshatra et al. [128] synthesized calcium silicate through a hydrothermal reaction involving calcium oxide and silica (featuring the calcium/silicon (Ca/SiO_2) ratio of 2.0). The reaction occurred at temperatures between $205\text{ }^{\circ}\text{C}$ and $215\text{ }^{\circ}\text{C}$, accompanied by a pressure of 17–19 bar. The subsequent decomposition at $900\text{ }^{\circ}\text{C}$ yielded highly reactive β -dicalcium silicate with a specific surface area of $45500\text{ m}^2/\text{kg}$. However, this product was found to be contaminated with trace amounts of wollastonite as an impurity.

Several studies have also been conducted to investigate the formation of mayenite through the hydrothermal-calcination method [129,130]. For this, the initial materials (featuring the stoichiometric ratio of $\text{Ca}(\text{OH})_2$ and $\text{Al}(\text{OH})_3$ of 1:1) were hydrothermally treated at 150 °C for 5 h and calcinated at 200–1000 °C. The results indicated that C_3A formation proceeds at 300 °C, while the formation of C_{12}A_7 begins at 350–400 °C. Furthermore, it has been verified that mayenite with a high BET surface area (70000 m^2/kg) can be synthesized through hydrothermal treatment followed by comparatively low-temperature calcination at around 600 °C. This stands in contrast to the conventional method (the solid-state reaction) requiring temperatures exceeding 1000 °C to achieve the formation of the same phase. It is worth noting that there is no literature on ye'elimite synthesis by applying the hydrothermal-calcination synthesis method.

In the context of ye'elimite-containing cements, scientists are trying to incorporate industrial by-products or waste materials into its production. This approach not only allows for the recycling of industrial waste, but also reduces the final cement cost. There is literature addressing the application of the hydrothermal-calcination technology in synthesizing belite and BCSA cements, including the utilization of industrial waste as the initial material. For instance, Mazouzi and co-authors [131] synthesized belite cement with starting materials from aluminosilicate wastes (oil well-drilling mud and hydraulic dam sludge) and hydraulic lime dust recovered from bagging workshops. The hydrothermal treatment of the raw mixture was performed in an alkaline KOH (0.6 M) solution (so that to promote hydrate formation), at a temperature of 100 °C for 4 h under atmospheric pressure and continuous agitation. The calcination of the hydrothermal mixture at 1000 °C for 1 h produced reactive belite cements containing between 79% and 86% of C_2S (α'_L and/or β -polymorphs), the rest being C_{12}A_7 (5–8%), C_4AF (7–11%), and free lime (2%). These findings demonstrated the fast formation of hydrates, including C–S–H/C–A–S–H, calcium aluminate hydrates, and portlandite. This resulted in a rapid setting time being attributed to the reaction of C_{12}A_7 . The compressive strength evolution categorized these cements as belonging to the 32.5 MPa category according to EN 197–1.

Several researchers have managed to produce belite cements by hydrothermally treating blends containing fly ash and lime, followed by calcination at temperatures below 1000 °C [132–135]. Mostly, slurries of fly ash and lime with high water/solid ratios were autoclaved for 4 h at 180–200 °C under continuous stirring, and the synthesized precursors were dried and calcined at 750–900 °C. The main hydraulic minerals of the clinkers consisted of β - C_2S (or α'_L - C_2S) and C_{12}A_7 . The hydrothermal treatment of the slurry provides favourable conditions for the reaction between fly ash and water. This process yields increased quantities of hydrated calcium silicates and hydrated calcium aluminates in the synthesized precursors, thereby resulting in elevated proportions of hydraulic minerals in the clinkers.

Unfortunately, there is less research available on the hydrothermal calcination synthesis of BCSA clinkers. For the preparation, Bouha et al. [136] used hydraulic

dam sludge, slaked lime dust, iron ore, gypsum ore, and pure aluminium oxide as the initial materials. The hydrothermal treatment was carried out in a stirring suspension autoclave at 100 °C for 4 h (W/S = 7), which was followed by calcination at 1100–1300 °C for 30 min. The highest hydration degree was determined for the sample calcined at 1200 °C, featuring a composition of β -C₂S (56.6%), C₄A₃S̄ (24.2%), C₄AF (11.6%), C₁₂A₇ (6.2%), and MgO (1.4%). Meanwhile, the developed compressive strength after 28 days of hydration was ~42 MPa.

Rungchet et al. [137] produced BCSA from fly ash, Al-rich sludge and flue gas desulfurization gypsum. The prepared slurry (featuring a water-to-solid ratio = 7) was hydrothermally treated at 130 °C for 1 h, 3 h, 6 h, and 9 h, filtered, dried at 60 °C for 24 h, and calcinated at temperatures ranging from 750 to 1150 °C. The results showed that BCSA cement can be optimally synthesized by hydrothermal treatment for 3 h and by calcination at 1050 °C for 1 h. The resulting cement exhibited rapid setting, by achieving the final setting within 31 min, and attained a satisfactory compressive strength of ~30 MPa after 28 days of curing.

The hydrothermal-calcination synthesis method shows the capability to reduce the calcination temperature during the synthesis of cementitious materials. However, the knowledge pertaining to the application of this method and the impact of its conditions on the formation of ye'elimite is scarce. Such studies assist in understanding and optimizing the production of environmentally friendly binders and in controlling the ongoing mineralogical changes.

To summarize, concrete is the most-consumed artificial substance on the planet, with ~30 million tonnes annually. The production of a fundamental ingredient – cement, which binds the aggregates and provides the strength for concrete – is responsible for ~8% of the global anthropogenic CO₂ emissions. In alignment with the *Paris Agreement* and the *European Green Deal* to reduce the global greenhouse gas (including CO₂) emissions in the long term, substantial changes must be implemented in the cement production sector. Looking at the production process of the most globally manufactured (~99.8%) *Ordinary Portland cement*, the highest carbon emissions come from the calcination of limestone and the combustion of fossil fuels to operate the kiln (contributing to 90% of the full extent). Additionally, due to a high calcination temperature (~1450 °C), its production accounts for about 2–3% of the world's energy consumption. Hence, extensive research is underway to redesign the clinker composition and the raw material usage, with a focus on reducing CO₂ emissions and minimizing the energy consumption in cement production.

In recent decades, researchers have been increasingly focusing on environmentally friendly types of cement containing ye'elimite which offer several advantages: 1) production enables cutting down the CO₂ footprint by 25–35% (due to requiring less limestone and mitigating the energy usage); 2) potential utilization of the industrial waste as raw materials; and 3) an enhanced performance of concrete (rapid hardening and high early strength). Ye'elimite stands as the pivotal mineral

dictating the hydration characteristics as well as the initial and final properties of concrete. Therefore, an increasing number of authors have recently concentrated on exploring the synthesis, chemical and physical characteristics, and the hydration mechanism of this mineral on a laboratory scale.

According to the literature, the most widely used synthesis approaches for ye'elimite are the solid-state reaction and the sol-gel methods. The synthesis of high-purity ye'elimite powder by solid-state reactions is an energy-intensive process (1300 °C for 3 h); it also requires multiple milling, pelleting, and firing cycles. Meanwhile, the sol-gel methods enable a reduction in the energy consumption (1250 °C for 1 h), but necessitate expensive raw materials and solvents. Hydrothermal-calcination synthesis is another energy-saving pathway allowing the synthesis of clinker or high-purity cementitious phases such as β -C₂S, C₃A, C₁₂A₇, etc. To the best of the knowledge of the author of this thesis, this two-stage method demonstrates the potential to produce high-purity ye'elimite, which has not been reported in the literature before. To achieve this, it is crucial to examine the influence of both hydrothermal and calcination conditions on the formation of synthetic ye'elimite and its properties, as well as the possible applications of the obtained product.

2. MATERIALS AND METHODS

2.1. Materials

1) **Calcium carbonate** (CaCO_3 , *Eksparas*, Lithuania), purity ≥ 99.0 wt.%. For the initial mixture, CaCO_3 was calcined (in an electric muffle furnace *SNOL 8.2/1100* (*UAB SnolTherm*, Lithuania)) at 950 °C temperature for 1 h (LOI 42.98%; free CaO ~ 98.1 wt.%). The obtained CaO density was 3340 kg/m^3 , and the particle distribution varied from 0.1 μm to 28 μm , $d_{50} = 3.93$ μm .

2) **Aluminium hydroxide** ($\text{Al}(\text{OH})_3$, *Honeywell*, Germany) with purity ≥ 99.0 wt.%. $\text{Al}(\text{OH})_3$ was thermally treated at 475 °C temperature for 4 h (LOI 34.28%). The density of the obtained Al_2O_3 was 2340 kg/m^3 , and the particle distribution varied from 0.1 μm to 6 μm , $d_{50} = 1.44$ μm .

3) **Gypsum** ($\text{CaSO}_4 \cdot 2\text{H}_2\text{O}$, *Lach-Ner*, Poland), with purity ≥ 99.0 wt.% of $\text{CaSO}_4 \cdot 2\text{H}_2\text{O}$. The density was 2490 kg/m^3 , and the particle distribution varied from 0.05 μm to 30 μm , $d_{50} = 5.24$ μm .

4) Hard coal **fly ash** (*SAFAMENT*, Germany). Based on the XRF results, fly ash consists of 46.6% SiO_2 , 29.2% Al_2O_3 , 5.9% Fe_2O_3 , 7.3% CaO, 2.0% TiO_2 , 1.5% K_2O , 0.28% NaO, 0.69% SO_3 , 0.12% MgO, and other oxides. According to the determined chemical composition and EN 451-1 Standard, this ash can be assigned to Class F (siliceous) fly ashes. Rietveld analysis demonstrated that fly ash contained 24.9% mullite ($\text{Al}(\text{Al}_{0.8}\text{Si}_{1.08}\text{O}_{4.85})$, PDF No. 01-089-2645), 8.9% quartz (SiO_2 , PDF No. 00-005-0490), 0.9% hematite (Fe_2O_3 , PDF No. 01-076-9683), 0.7% magnetite (Fe_3O_4 , PDF No. 00-065-0731), calcium oxide 0.2% (CaO, PDF No. 01-077-2010), 0.1% anatase (TiO_2 , PDF No. 01-070-6826), 0.2% magnesium oxide (MgO, PDF No. 00-045-0946), and 64.1% amorphous phase (Fig. 2.1). The determined density was 2770 kg/m^3 , and the particle distribution varied from 0.5 μm to 211 μm , $d_{50} = 24.09$ μm . The pozzolanic activity was determined by the NF P 18-513 Standard [138]. The obtained value was 350 mg CaO/g, which can be attributed to the low pozzolanic activity value.

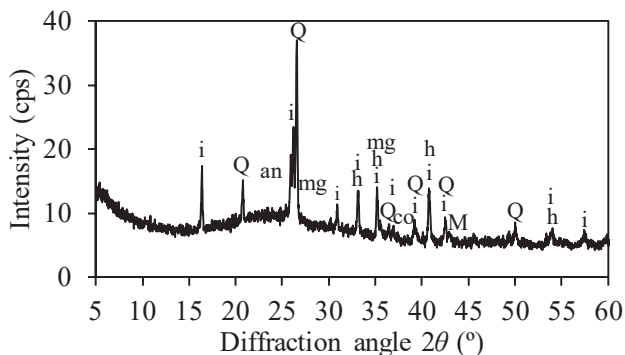


Fig. 2.1. XRD pattern of fly ash. Indexes: i – mullite, h – hematite, Q – quartz, an – anatase, M – magnesium oxide, co – calcium oxide, mg – magnetite

5) **Limestone powder (LS)** (*Max Bögl Stiftung und Co. KG*, Wiesenhofen, Germany). The density was 2890 kg/m^3 , and the particle distribution varied from $0.46 \text{ }\mu\text{m}$ to $163 \text{ }\mu\text{m}$, $d_{50} = 17.57 \text{ }\mu\text{m}$. It was determined by XRF analysis that LS consisted of 55.12% CaO and contained a low content (with a total of <1.4%) of other oxides (LOI ~43.3%). The main crystalline phases included calcium carbonate (97.1%) (CaCO_3 , PDF No. 01-080-2793) and calcium oxide (CaO , PDF No. 00-037-1497).

6) **Portland cement (CEM I 42.5N)**, (*Akmenės cementas*, Lithuania). The following minerals in OPC were determined: alite (Ca_3SiO_5 , PDF No. 04-018-9702), belite (Ca_2SiO_4 , PDF No. 00-033-0302), brownmillerite ($\text{Ca}_2\text{FeAlO}_5$, PDF No. 01-072-7995), tricalcium aluminate ($\text{Ca}_3\text{Al}_2\text{O}_6$, PDF No. 00-006-0495), gypsum ($\text{CaSO}_4 \cdot 2\text{H}_2\text{O}$, PDF No. 04-010-9409) and magnesium oxide (Fig. 2.2). The determined density was 3100 kg/m^3 , and the particle distribution varied from $0.1 \text{ }\mu\text{m}$ to $70 \text{ }\mu\text{m}$, $d_{50} = 8.0 \text{ }\mu\text{m}$.

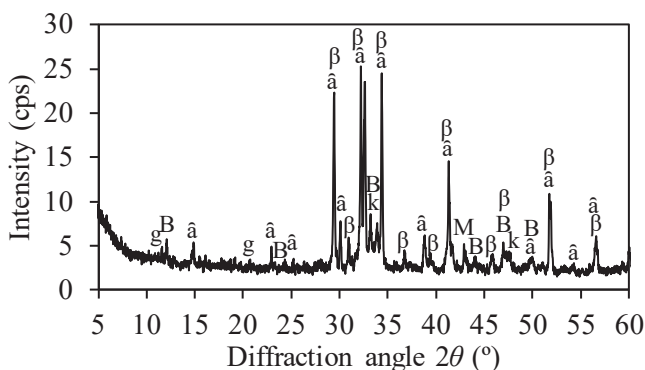


Fig. 2.2. XRD pattern of OPC. Indexes: $\hat{\alpha}$ – alite, β – belite, B – brownmillerite, g – gypsum, k – tricalcium aluminate, M – magnesium oxide

7) **Standard sand** CEN EN 196–1 (*Normensand*, Germany). Standard sand has a silica content of no less than 98% and a moisture content of no more than 0.2%. The particle size distribution varied between 0.08 and 2.00 mm.

8) **Limestone** (*JSC Naujasis kalcitas*, Lithuania), with a purity of ~92.8 wt.% of CaCO_3 . The density was 2537 kg/m^3 , and the particle distribution varied from $0.05 \text{ }\mu\text{m}$ to $83 \text{ }\mu\text{m}$, $d_{50} = 5.16 \text{ }\mu\text{m}$.

9) **Silica gel waste**, the by-product of the aluminium fluoride production at the plant *JSC Lifosa* (Kėdainiai, Lithuania). It was determined that the presently employed silica gel consisted of gibbsite ($\text{Al}(\text{OH})_3$, PDF No. 04-011-1369), aluminium trifluoride trihydrate ($\text{AlF}_3 \cdot 3\text{H}_2\text{O}$, PDF No. 00-035-0627), aluminium hydroxide fluoride hydrate ($\text{AlF}_{1.5}(\text{OH})_{1.5}(\text{H}_2\text{O})_{0.375}$, PDF No. 01-074-0940) and amorphous silicon dioxide (a broad basal reflection within the $18\text{--}37^\circ$ diffraction angle range) (Fig. 2.3). XRF and chemical analysis revealed that silicon, aluminium and fluorine are the dominant components in the silica gel waste: SiO_2 – 81.2 wt.%, F – 8.4 wt.%, Al_2O_3 – 7.5 wt.%, along with other minor constituents. The density was

determined as 2598 kg/m³, and the particle distribution varied from 0.03 μm to 170 μm, d₅₀ = 29.57 μm.

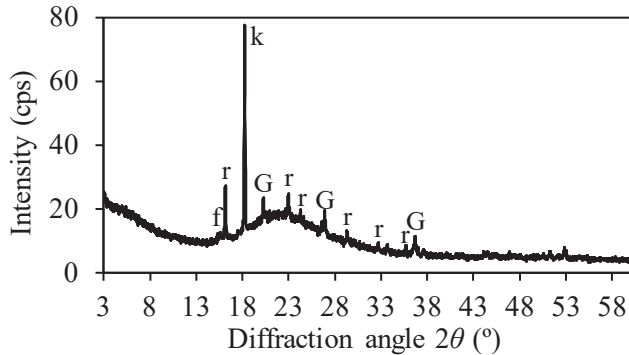


Fig. 2.3. XRD pattern of silica gel waste. Indexes: G – gibbsite, r – aluminium trifluoride trihydrate, f – aluminium hydroxide fluoride hydrate

10) **Granite cutting waste**, the by-product of granite production in the plant of *JSC Granitas* (Kaunas, Lithuania). After the examination of the mineral composition of granite cutting waste, the following compounds were identified: quartz, microcline (KAlSi₃O₈, PDF No. 04-008-1783), annite-1 M (KFe₂(Si,Al)₄O₁₀(OH)₂, PDF No. 00-042-1413), anorthite (CaAl₂Si₂O₈, PDF No. 00-041-1486), actinolite (Na_{0.08}Ca_{1.76}Mn_{0.16}Mg_{1.88}Fe_{2.72}Fe_{0.32}Al_{0.32}Si_{7.68}O₂₂(OH)₂, PDF No. 00-073-2339), albite ((Na,Ca)Al(Si,Al)₃O₈, PDF No. 00-041-1480) and labradorite (Ca_{0.64}Na_{0.35}(Al_{1.63}Si_{2.37}O₈), PDF No. 00-083-1371) (Fig. 2.4). X-ray fluorescence analysis showed that granite cutting waste consisted of 59.2 wt.% of SiO₂, 6.79 wt.% of Fe₂O₃, 14.7 wt.% of Al₂O₃, 3.92 wt.% of K₂O, 3.41 wt.% of Na₂O, 4.15 wt.% of CaO, 2.59 wt.% of MgO, and a minor fraction of other elements, such as Ti, P, Ba, and Mn. The density was established as 2589 kg/m³, and the particle distribution varied from 0.05 μm to 48 μm, d₅₀ = 3.99 μm.

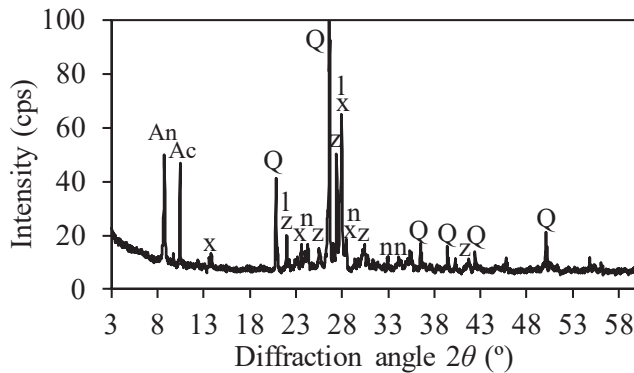


Fig. 2.4. XRD pattern of granite cutting waste. Indexes: An – annite, Ac – actinolite, z – microcline, x – albite, Q – quartz, n – anorthite, l – labradorite

11) **Calcium sulfate hemihydrate** ($\text{CaSO}_4 \cdot 0.5\text{H}_2\text{O}$, *Knauf*, Germany) which consisted of 22.8 wt.% of Ca, 18.47 wt.% of S, 1.54 wt.% of Si and other elements. The density was established as 2642 kg/m^3 , and the particle distribution varied from $0.5 \mu\text{m}$ to $160 \mu\text{m}$, $d_{50} = 21.97 \mu\text{m}$.

12) **Iron (III) oxide** ($\text{Fe}_2\text{O}_3 \geq 97.0 \text{ wt.}\%$, *Honeywell*, Germany).

13) **Sodium hydroxide** ($\text{NaOH} \geq 99.0 \text{ wt.}\%$) (*Honeywell Riedel-de-Haën*TM, Germany).

14) **Potassium hydroxide** ($\text{KOH} \geq 86.0 \text{ wt.}\%$) (*Carl Roth*, Germany).

15) **Isopropyl alcohol** (2-propanol $\geq 99.0\%$) (*Reachem*, Slovakia).

16) **Nitric acid** ($\text{HNO}_3 \text{ 65}\%$) (*Reachem*, Slovakia).

2.2. Methods

2.2.1. Preparation of the initial mixtures

For the experiments, the initial composition for two specimens, named *Sample 1* (S1) and *Sample 2* (S2), was prepared referring to the stoichiometry of ye'elimite ($\text{Ca}_4(\text{Al}_2\text{O}_3)_3\text{SO}_4$; $\text{CaO}/\text{Al}_2\text{O}_3 = 1.33$). For Sample S1, the initial compounds (CaO , Al_2O_3 and $\text{CaSO}_4 \cdot 2\text{H}_2\text{O}$) were weighed, poured into a plastic container with three grinding bodies (to ensure the homogenization quality), sealed and homogenized for 45 minutes at 34 rpm by using a *TURBULA TYPE T2F* (*Willy A Bachofen AG*, MuttENZ, Switzerland) homogenizer. The obtained mixture density was 2513 kg/m^3 , $d_{50} = 4.79 \mu\text{m}$. Figure 2.5 illustrates the mineralogical composition of the prepared mixture, where the identified compounds were gypsum, anhydrite (CaSO_4 , PDF No. 00-037-1496), portlandite ($\text{Ca}(\text{OH})_2$, PDF No. 00-044-1481), and calcium oxide. The presence of portlandite in the mixture indicates that freshly prepared CaO reacted with water vapour present in the atmosphere during the homogenization process. Based on the literature data [139,140], the preparation of Al_2O_3 by dehydrating $\text{Al}(\text{OH})_3$ at $475 \text{ }^\circ\text{C}$ boosts the amorphous structure. Thus, Al_2O_3 was not detected in the XRD patterns.

It is acknowledged that mechanochemical treatment promotes intense mixing, breaks down particle agglomerates, and creates high-energy interfaces, leading to accelerated and more complete reactions of the reactants [141]. Therefore, in order to enhance the formation of the precursor, the initial mixture of Sample S2 was treated mechanochemically. With this objective in mind, the weighed initial materials (of the same composition as in Sample S1) were ground in a high-energy vibrating cup mill *Pulverisette 9* (*FRITSCH*, Germany) with three 10 min on-off cycles at 900 rpm. The obtained mixture density was 3290 kg/m^3 , $d_{50} = 1.57 \mu\text{m}$. The application of mechanochemical treatment was found to induce significant alterations in the mineralogical composition of the initial mixture, which was confirmed by XRD analysis (Fig. 2.5). The results show that, within the first 10 min of milling, the mechanochemical treatment induces the decomposition of gypsum, i.e., a significant decrease in the diffraction peaks characteristic of gypsum was observed [142]. Additionally, due to partial water evaporation out of the gypsum structure, bassanite ($\text{CaSO}_4 \cdot 0.5\text{H}_2\text{O}$, PDF No. 00-033-0310) was detected in the XRD patterns. At the same time, the prepared calcium oxide reacts with water from the gypsum structure

(also, possibly, from air), resulting in the formation of portlandite. Meanwhile, mechanochemical milling induces damage in the crystalline structure of anhydrite (which was already present in the raw material), which led to the reduction of the diffraction peaks in its reflections. This tendency is manifested in further milling (up to 30 min) for almost all the diffraction peaks of the compounds in the initial mixture. It is evident that mechanochemical treatment induces the disintegration of the structure of the crystalline phases. The exception is observed only for calcium oxide, whose reflections increase with the increasing duration of milling due to the dehydration of portlandite.

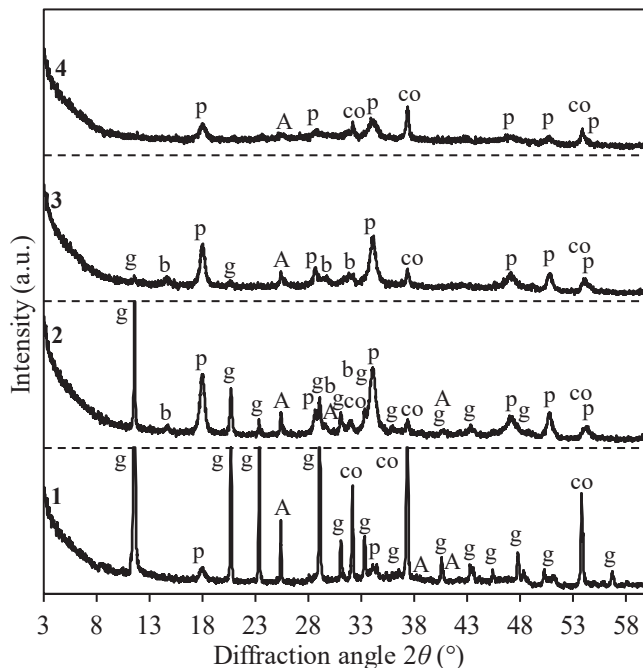


Fig. 2.5. XRD patterns of the homogenized initial mixture (1; Sample S1) and mechanochemically treated initial mixture at different stages (2 – after 10 min, 3 – after 20 min, and 4 – after 30 min [Sample S2]). Indexes: g – gypsum, p – portlandite, co – calcium oxide, A – anhydrite, s – bassanite

2.2.2. Hydrothermal synthesis

Hydrothermal synthesis was used to produce a precursor (calcium monosulfoaluminate 12-hydrate), which was performed in an unstirred suspension autoclave *Parr Instruments 4621* (*Parr Instrument Company*, USA). The treatment of the samples was carried out by using 25 ml PTFE cells, where the produced powders (Samples S1 and S2) (2 g) were mixed with distilled water (in a water-to-solid ratio (W/S) of 10) by using a laboratory spatula (stirred for ~1 min). Afterwards, the cells

were placed in the autoclave and treated at 100 °C, 110 °C and 130 °C for 1 h, 4 h, 8 h, 12 h, 24 h and 48 h, where the dwell temperature was reached within 2 h. After hydrothermal treatment, the sample suspensions were decanted, rinsed with isopropanol (~5 min), filtered (filter paper thickness – size 4), and dried at 50±0.2 °C for 24 h at RH of 35%. Finally, the dried samples were manually ground, sieved through an 80 µm sieve to ensure the uniform particle distribution, and used for instrumental analysis. In order to produce higher amounts of the precursors, 60 g of the initial mixture was mixed with 600 ml of water, and the prepared suspension was placed in a 1-liter autoclave (*Parr Instruments 4621, Parr Instrument Company, USA*). Following the hydrothermal synthesis, the treated suspension underwent a process of decantation, rinsing, and drying under identical conditions as those specified above.

To improve the synthesis of Ms12, two essential steps of synthesis have to be taken into consideration:

- After the isothermal treatment, the autoclave must be cooled to 60–70 °C (following the work safety requirements). Removal of the cells below 60 °C was found to induce the destabilization of Ms12, leading to its partial conversion into ettringite.

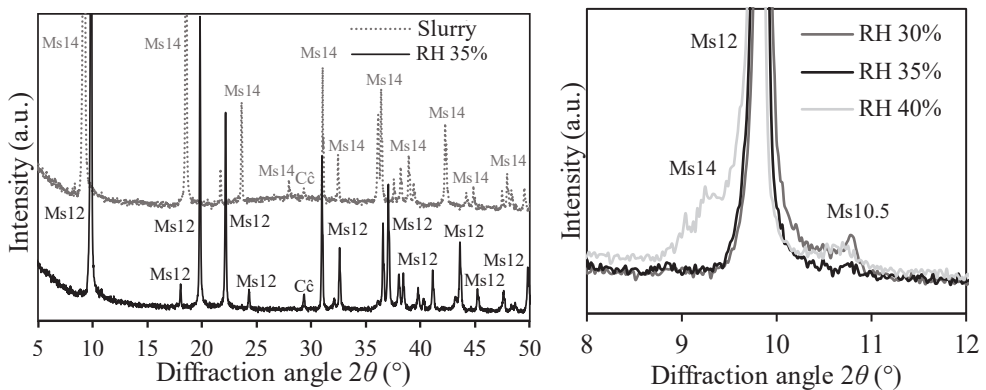


Fig. 2.6. XRD patterns of Sample S2, after hydrothermal synthesis at 110 °C for 8 h, dried at different RH conditions. Indexes: Ms – calcium monosulfoaluminate (the number shows the water content), Cc – calcium carbonate

- Stabilization of the hydration state of Ms12 requires rigorous drying conditions. It has been determined that monosulfoaluminate with 14 molecules of water forms under hydrothermal conditions (Fig. 2.6, slurry). In this work, the observed optimal drying conditions were at an RH of 35% at 50 °C (drying was performed by using a humidity and temperature test chamber *CB-CS Series, Italy*). Drying the slurry at a lower relative humidity (~30%) leads to the formation of a lower hydration state of monosulfoaluminate (Ms10.5; $d = 0.814$ nm) (Fig. 2.6). Meanwhile, the higher relative humidity (40%) is insufficient to convert Ms14 ($d = 0.957$ nm) into

Ms12 completely. It is noteworthy that, despite strict drying conditions, the minor formation of Ms10.5 was observed in the samples, with this occurrence being more pronounced at elevated synthesis temperatures. These findings suggest that higher synthesis temperatures might contribute to the destabilization of Ms12 during the drying process.

2.2.3. Study of the impact of water vapour pressure on stability

The prepared sample was examined in the presence of the environment CO₂ concentration (668±4 ppm) (monitored by using *IAQ-Calc Indoor Air Quality Meters 7545*, *TSI's IAQ-Calc™*, USA) over varying relative water vapour pressure (p/p_0) (from 0.355 to 1.0). The corresponding p/p_0 was maintained in 5 separate desiccators while using various sulfuric acid solution concentrations (see Table 2.1) [143]. For every measurement, 1 gram of the sample was weighed, and the powder was evenly spread on a porcelain plate (layer thickness ~ 4 mm), thereby ensuring sufficient exposure of the samples to the water vapour. Afterwards, 3 plates with the samples were stored in desiccators under above-outlined different p/p_0 environments, without allowing contact with the acid solution. The experiment was carried out at a temperature of 20±0.5 °C for up to 90 days. The samples were taken out of the desiccators every week or two to monitor the development of the mass change of the samples and alterations in the phase composition throughout the duration of the experiment. The samples were weighed immediately after being removed from the desiccator so that to minimize the experimental error, and then placed back to continue the experiment.

Table 2.1. Water vapour pressure equilibrium over H₂SO₄ solutions of different concentrations at 20 °C

No.	Concentration of H ₂ SO ₄ (wt.%)	Water vapour pressure
1	0	1.0
2	20	0.877
3	30	0.753
4	40	0.565
5	50	0.355

2.2.4. Thermal stability assessment

First, the thermal stability of the synthesized precursor (hydrothermally produced at 110 °C for 8 h) was investigated by applying the XRD *in-situ* method with the *MTC-HIGHTEMP* chamber (*Bruker AXS*, Germany). The samples for the measurement were prepared by mixing the powder (~0.2 g) with 2–3 drops of ethanol (96%) until the viscous consistency had been reached. Afterwards, the thin suspension layer was placed on the heating strip. The experiments were performed in the temperature range of 25–1250 °C, with 50 °C/min, in an air atmosphere. The XRD patterns were recorded after equilibration of 2 min at the desired temperature within

the range $2\theta = 8\text{--}38^\circ$ with steps of $\sim 0.02^\circ 2\theta$ and 0.2 s counting the time per step. In total, 78 patterns were recorded within ~ 11.5 h.

Second, solid-phase sintering was performed by using a synthetic precursor by applying the calcination method (an *ex-situ* method). After hydrothermal synthesis and drying, the sample was sieved through a $315\ \mu\text{m}$ sieve to ensure particle distribution. Calcination was carried out at a high-temperature furnace (*Nabertherm HTC 03/16*, *Nabertherm GmbH*, Germany) when using 4 g of the sample. The required temperature ($700\text{--}1250\ ^\circ\text{C}$) was reached at a heating rate of $10\ ^\circ\text{C}/\text{min}$, and then samples were maintained for different durations (0–3 h). After the calcination, the obtained samples were kept in the furnace until they cooled to $300\ ^\circ\text{C}$, and then they were taken out, cooled to room temperature and sieved through a sieve with a mesh width of $80\ \mu\text{m}$ and used for further investigations. All the samples were stored in a desiccator to avoid the moisture and CO_2 available in the air. For the production of a higher amount of synthetic ye'elimite, an even layer of 60 grams of the precursor powder was distributed across a ceramic plate with a thickness of 4 mm and calcinated at the required temperatures.

2.2.5. Investigation of early hydration

Isothermal calorimetry analysis was performed by using an eight-channel *TAM Air III* isothermal calorimeter (*TA Instruments*, USA) so that to investigate the reactivity and heat released during the hydration of the synthesized ye'elimite and ye'elimite-fly ash blended samples. The measurements were done by applying two methodologies: 1) the admix ampoule experiment (internal mixing), and 2) the sealed ampoule experiment (external mixing). According to the first strategy, glass ampoules (20 ml) were filled with 1.80 g of the dry sample, whereas the syringes were filled with water equivalent to a water/solid ratio of 1.1. After the thermal equilibration, the water was injected into the ampoules and mixed inside the calorimeter with the dry material for 20 s (at a frequency of 1–2 times per sec). Based on the second technique, the same water/solid ratio was maintained the same, but the sample mixing was performed outside of the calorimeter, i.e., in a plastic container. To guarantee proper mixing, for the first 15 sec, the sample was mixed with a spatula, and, for 1 minute 45 sec, with an electric mixer (1700 rpm. /min). Once the paste had been prepared, it was transferred to glass ampoules (~ 3.8 g of paste) and placed into the calorimeter. All the measurements were taken at $25\ ^\circ\text{C}$ temperature and measured over a period of 72 h. Repetition of the measurements demonstrated deviations in total heat below 3%.

The influence of fly ash on the hydration of synthetic ye'elimite was examined by substituting the weight portions of ye'elimite. Abbreviations were employed to facilitate the easy identification of each sample. For instance, the sample with 100 wt.% of synthetic ye'elimite was named *Y*, whereas the sample with 90 wt.% of ye'elimite and 10% of fly ash was titled *YFA10*. Synthetic ye'elimite was replaced with 5 wt.%, 10 wt.%, 20 wt.%, and 40 wt.% of fly ash. The required component portions were weighed and homogenized for 45 min at 34 rpm by using *TURBULA TYPE T2F*. The prepared samples were used for the required investigations. It is worth

emphasizing that the isothermal calorimetry data was normalized to the initial synthetic ye'elimite content of each sample.

To investigate the phase composition of the formed hydrates, the prepared samples were mixed with water ($W/S = 1.1$), placed in sealed containers and cured for the required durations at 25 °C. The hydration stoppage of the samples was performed by employing the following technique: the taken sample was crushed in an agate mortar by hand, rinsed in isopropanol, and oven-dried at 40 °C for 24 h. Afterwards, the samples were sieved through a mesh width of 80 μm .

2.2.6. Methods of testing ternary blended cement

The possible application of synthetic ye'elimite as an accelerator for Ordinary Portland – fly ash blended cement pastes was investigated by preparing different ternary mix compositions. In the blends, the quantity of OPC ranged from 78 wt.% to 80 wt.%, siliceous fly ash (F class) from 18 wt.% to 20 wt.%, and synthetic ye'elimite from 0.5 wt.% to 2 wt.%. For the preparation of different blends, the required component portions were weighed and homogenized for 45 min at 34 rpm by using *TURBULA TYPE T2F*. The prepared blends were used for further investigations. Additionally, abbreviations were employed to make the identification of the prepared blends easier. For instance, the sample which contained 80 wt.% OPC, 19 wt.% fly ash and 1 wt.% synthetic ye'elimite, was titled *80P19FA1Y*. Accordingly, other blends were also given specific abbreviations.

The standard consistency and setting time tests of the prepared cement pastes were determined according to Standard EN 196-3 (E) by using an automatic *Vicat* apparatus *EO44N (MATEST, Italy)*. The standard consistency was determined according to the scale reading, i.e., the distance between the plunger and base plate needed to be 6 ± 2 mm. Meanwhile, the setting time was determined by penetrating the paste every 5 min.

Mortar cubes (30x30x30 mm) were prepared with a water-to-binder (W/B) ratio of 0.50 and the cement blend/standard sand portions of 1:3 (by following the Standard EN 196-1:2016 (E)). Immediately after the preparation of the mortar, the samples were moulded and pre-cured in a room environment (20 ± 1 °C) for 24 h. Afterwards, the cubes were de-moulded, submerged in sealed containers with distilled water, and cured for 2, 7, and 28 days. After curing, the compressive strength of the samples was determined by using a compression and bending testing machine *MEGA 10-400-50 (FORM+TEST Seidner & Co. GmbH, Germany)* at a rate of 2.4 kN/s. The compressive strength values are presented by using the average of 3 samples. To analyze the phase composition of the resulting hydration products, cement pastes were separately prepared with a water-to-binder ratio of 0.5 and stored in sealed plastic vessels at 20 ± 1 °C for the required durations. Hydration stoppage of the samples was performed according to the procedure outlined above.

2.2.7. Synthesis of belite-ye'elimite-ferrite cement

According to the literature [24], belite-ye'elimite-ferrite (BYF) cement does not have a standardized phase composition. The main criteria include only the amount of

belite in the clinker (>50%). Considering the hydraulic reactivity of the phases, the following phase composition of belite clinker was selected: 60% of $2\text{CaO}\cdot\text{SiO}_2$, 20% of $4\text{CaO}\cdot 3\text{Al}_2\text{O}_3\cdot\text{SO}_3$, and 20% of $4\text{CaO}\cdot 3\text{Al}_2\text{O}_3\cdot\text{Fe}_2\text{O}_3$. Based on the identified oxide composition of the raw materials and the prospective phase composition of BYF clinker, a system of equations was created to estimate the required mix proportions for the initial mixture. The composition of the oxides within each compound was considered, while ensuring that the raw material batch contained less than 0.04% of F^- ions. Table 2.2 demonstrates the prospective chemical composition of BYF clinker and the calculated mix portions of the initial batch.

Table 2.2. Targeted phase composition of BYF clinker, dosages of raw materials, and oxide composition of the initial mixture (excluding H_2O and CO_2)

Targeted composition, wt.%	
$2\text{CaO}\cdot\text{SiO}_2$	60
$4\text{CaO}\cdot 3\text{Al}_2\text{O}_3\cdot\text{SO}_3$	20
$4\text{CaO}\cdot 3\text{Al}_2\text{O}_3\cdot\text{Fe}_2\text{O}_3$	20
Oxide composition, %	
CaO	55.63
SiO_2	20.93
Al_2O_3	14.23
SO_3	2.62
Fe_2O_3	6.58
Raw material, wt %	
Limestone	66.67
Calcium sulfate hemihydrate	3.17
Granite cutting waste	14.35
Iron (III) oxide	2.50
Aluminium hydroxide	9.47
Silica gel waste	3.81

To prepare the initial mixtures for investigating the influence of the sintering temperature on the BYF clinker phase development, the raw materials were weighed, poured into sealed plastic containers with 2 grinding bodies (to ensure the homogenization quality), and homogenized for 45 min at 34 rpm by using a homogenizer *TURBULA TYPE T2F*. To ensure the required fineness of the reactants, the homogenized initial mixture was ground for 3 min at 850 rpm in a laboratory vibrating disc mill *Pulverisette 9*. Afterwards, the tablets were first prepared and subsequently sintered to synthesize belite clinker. For the tablet formation, when the initial batch was 20 g, the resulting mixture was moistened with 2 ml of distilled water to achieve the desired material stickiness. The moistened mixture was then poured into a 36 mm diameter cylinder and compressed (at 10 MPa for 60 s) with a loading rate of 0.5 MPa/s. The initial tablets (of a height of 11 mm) were sintered in five steps in a high-temperature furnace (*Nabertherm HTC 03/16*, *Nabertherm GmbH*, Germany): 1) the temperature was raised to 900 °C by using a 5 °C/min heating rate,

2) maintained for 30 min at 900 °C, and then 3) the temperature was increased from 900 °C to the required temperature (varied from 1000 to 1250 °C) by using a 2 °C/min heating rate, where 4) the temperature was maintained for 1 h, and, lastly, 5) the tablet was taken out hot (~1000 °C), where simultaneous shredding and (quick) cooling followed. The sintering method was selected considering the thermal stability of CaCO₃ (800–900 °C) and the characteristic transition of β-C₂S to γ-C₂S within the slow cooling stage [38].

To produce the high quantity of BYF clinker (7 kg), the raw materials were weighed and poured into a plastic container (20 l) with five grinding bodies, sealed and homogenized by using a laboratory roll ball mill. The homogenization was performed for 1 h at a spinning rate of 120 rpm, where grinding bodies were used to ensure the homogenization quality. Afterwards, the initial mixture was transferred to a laboratory triangular ball mill, in which 25 grinding bodies were added and ground for 4 h at 60 rpm ($S_a = 525 \text{ m}^2/\text{kg}$). Later, 500 g of the produced mixture was moisturized with 50 ml of distilled water, placed in a square press form (100×100×40 mm), and compressed by following the previously mentioned conditions. The prepared tablets (~29 mm in height) were sintered by following the same five sintering steps when the calcination temperature was 1150 °C, and the dwell duration was 2 h.

It is known that gypsum is added to control the initial hydration of various types of cement [27,70]. Therefore, an isothermal calorimetric analysis was performed to determine the required amount of the gypsum additive for the produced BYF clinker. For this, the BYF clinker was replaced with 5%, 7.5%, and 10% gypsum, poured into plastic containers, and homogenized. The obtained samples were analyzed by using an eight-channel *TAM Air III* isothermal calorimeter (*TA Instruments*, USA). The experiments were conducted by using the admix ampoule method, containing 3 g of the dry sample with a W/S ratio of 0.5. The investigation was performed for 72 h at 25 °C. Lastly, to produce a high quantity of BYF cement, the produced clinker was blended with 7.5% gypsum (determined by calorimetric analysis), and milled for 2 h in a ball mill ($S_a = 350\text{--}400 \text{ m}^2/\text{kg}$).

2.2.8. Curing procedures for belite-ye'elinite-ferrite cement

The compressive strength test of the BYF mortar samples was applied by following the Standard EN 196–1. Mortar prisms (40×40×160 mm) were prepared by mixing the produced belite cement with standard sand (with the cement/sand ratio being equal to 1:3) and water (W/B – 0.67). The curing of the prepared mortars was conducted by using two methodologies. Following the first one, the fresh mortar was cast into sealed metal moulds and then pre-cured at 20±1 °C for 24 h. After the initial curing, the samples were demoulded and transferred into distilled water and stored for 3, 7, 14, 28, 56, and 90 days at 20±1 °C. According to the second methodology, the fresh mortar was poured into sealed metal moulds, which were pre-cured at 20±1 °C for 3 h. Subsequently, the pre-cured prism samples were carefully demoulded and transferred into an 18.5 L stainless-steel autoclave (*Model 4621, Parr Instruments*, USA). Hydrothermal curing was performed within the temperature range of 90–200

°C for 24 h. The selected temperatures were attained with a heating rate of 25 °C/h. After curing, the compressive strength of the samples was determined by using a compression and bending testing machine *MEGA 10-400-50 (FORM+TEST Seidner & Co. GmbH, Germany)* at a rate of 2.4 kN/s. The compressive strength values are presented by using the average of 3 samples. To analyze the phase composition of the resulting hydration products, the sample was crushed in an agate mortar by hand, rinsed in isopropanol, and oven-dried at 40 °C for 24 h.

2.2.9. Characterization methods

The *active CaO* was determined by following an experimental procedure. The weighed substance (1g) was poured into a conical flask (250 cm³) along with 7 glass beads (to ensure mixing) and filled with 150 ml of distilled water. The flask was gently heated by using a heating magnetic stirrer *F20500101 (VELP Scientifica Srl, Italy)* and stirred for 5 minutes, while ensuring that the substance would not reach the stage of boiling. After cooling the suspension, the inner walls of the flask were washed with a stream of distilled water. Afterwards, 2–3 drops of phenolphthalein solution were added to the suspension, and titration was carried out by using 1 N HCl until the pink colour disappeared, all the while constantly stirring. The titration was considered complete when the solution did not turn pink after 5 minutes of titration.

$$X = \frac{N \cdot V \cdot 28.4 \cdot 100}{G \cdot 100} \% \quad (\text{Eq. 2.1})$$

where: N – molar concentration of HCl equivalents; V – amount of HCl used for titration, cm³; 28.4 – CaO equivalent, g; G – sample mass, g; X – amount of active CaO, %.

The *loss on ignition (LOI)* was calculated by measuring the weight difference between the initial sample and the residual mass after heating and expressed as a percentage of the initial sample weight. The experiment was performed by using 1g of the sample, which was heated at 1000 °C for 30 min.

$$\text{LOI} = \frac{w_2 - w_3}{w_2 - w_1} \cdot 100\% \quad (\text{Eq. 2.2})$$

where: w₁ – weight of the crucible, w₂ – weight of the crucible plus sample, w₃ – weight of the crucible plus sample after the ignition.

The *particle size distribution (PSD)* was determined by using a laser granulometer *CILAS 1090 LD (Cilas, France)* within the 0.05–500 µm range. The dispersion phase involved compressed air (2500 mbar), the distribution of solid particles in the air stream was 12–15%, and the measurement duration was 15 s. Additionally, the specific surface area was calculated from the obtained measurement data.

The *density* of the samples was determined by using an automatic gas pycnometer *Ultrapyc 1200e (Quantachrome Instruments, USA)*. Helium gas was used

for analysis. The gas pycnometer was calibrated by using a large sphere with a volume of 4.5 cm³. The test substance was weighed with an accuracy of 0.1 µg by using an analytical scale. Then, it was transferred into a 10 cm³ sample cell and placed within a comparison cell situated inside the gas pycnometer. The density and volume of the sample were given as the arithmetic mean of three measurements. The deviation of the density measurement is equal to ±0.003%.

The *specific heat capacity* (C_p) was measured by applying the sapphire method [144]. The measurements were performed with a differential scanning calorimeter *Netzsch Polyma DSC 214* (*Netzsch*, Germany). The measurement parameters were as follows: temperature heating rate – 5 °C/min, temperature range – 10–50 °C, the crucible – aluminium (Al) crucible with a lid, the atmosphere in the furnace – nitrogen, the type E thermocouple. The data was evaluated with the *NETZSCH Proteus* software.

The *elemental compositions* of the materials were analyzed by employing the *X-ray fluorescence spectroscopy* (XRF) analytical technique. The analysis was performed with a Bruker X-ray *S8 Tiger WD* (*Bruker AXS GmbH*, Germany) spectrometer equipped with the Rh tube (60 keV), the measurement atmosphere – He. The analysis was carried out on samples after passing through a 63 µm sieve and then compressed (20 MPa for 45 sec) into 5×40 mm cylindrical tablets. The obtained data was analyzed with *SPECTRAplus QUANT EXPRESS* standardless software.

The *X-ray diffraction analysis* (XRD) was carried out to determine the phase composition of the materials. The measurements were performed at room temperature with the *D8 Advance* diffractometer (*Bruker AXS GmbH*, Germany) equipped with a CuK α X-ray tube operated at 40 kV and 45 mA. The diffraction patterns were recorded in the Bragg-Brentano geometry by using a fast-counting detector *Bruker LynxEye* based on the silicon strip technology. The measurement range was $2\theta = 3\text{--}70^\circ$ with steps of $0.020^\circ 2\theta$ with the time per step equaling to 0.2 s, corresponding to a total measurement duration of ~12 min per sample. The reaction degree of the compounds after hydration was determined by comparing the intensity of the peak changes with the unhydrated sample. Relative errors were estimated as ±3% based on three replicate samples.

The *quantitative content* of the crystalline phases was refined by the Rietveld method as implemented in the *TOPAS 4.2 software* (*Bruker AXS GmbH*, Germany). The quantitative phase analysis (QPA) was carried out on samples after grinding by hand to pass a 40 µm sieve, thus ensuring an isotropic distribution of the crystals in the sample. For the quantitative determination of the amorphous phase, 10% of the internal standard (ZnO) was added to the sample. Additionally, the sample holder was rotated during the data recording so that to improve the particle statistics and obtain high-quality QPA data. The analysis was carried out of 3 series samples, demonstrating up to 5% deviation. The crystal structures used in the refinements were adopted from the *PDF 2023* database.

The *average crystallite size* was calculated by using *DIFFRAC.TOPAS 4.2* software. The entire XRD pattern of the sample was analyzed by deconvoluting the

diffraction peaks with components of the Gaussian and Lorentzian equations. The average crystallite size was estimated following the Scherrer equation:

$$D_{\text{crystallite}} = \frac{K \cdot \lambda}{B \cdot \cos\theta} \quad (\text{Eq. 2.3})$$

where: K is the Scherrer constant (the value used in this study was 0.89), λ is the wavelength of $\text{CuK}\alpha$ radiation (1.5406 Å), θ is Bragg's diffraction angle, B is the *full width at half maximum* (FWHM) of the diffraction peak.

Thermogravimetric analysis (TGA: *thermogravimetry* – TG, *derivative thermogravimetry* – DTG, and *differential scanning calorimetry* – DSC) measurements of the obtained products were carried out by using:

- *LINSEIS STA PT 1000* (*Linseis Massgeraete GmbH*, Germany) thermal analyzer with the type S thermocouple. The sample (10±0.02 mg) was heated in the temperature range of 30–950 °C at a heating rate of 5 °C/min and 10 °C/min. The analysis was performed in the standard closed Pt – 10 wt.% Rh crucibles under nitrogen flow, and the measurement accuracy reached ± 3 °C. The obtained results were analyzed by using the *Linseis Platinum Evaluation* software.
- *Netzsch Polyma DSC 214* analyzer (*Netzsch*, Germany) with the type E thermocouple. The measurement parameters were as follows: the sample weight – 10±0.02 mg, the temperature heating rate – 5 °C/min, the temperature range – 15–400 °C, the crucible – aluminium (Al) crucible with a lid, the atmosphere in the furnace – nitrogen, the measurement accuracy – ±3 °C. The data was assessed with the *NETZSCH Proteus* software.
- *STA 449 3 Jupiter* (*Netzsch*, Germany) with the type E thermocouple. The measurement parameters were as follows: sample weight – 20 mg, temperature heating rate – 10 °C/min, temperature range – 25–900 °C, the crucible – corundum crucible (Ø 6,8 mm, 85 µl) with a lid, the atmosphere in the furnace – nitrogen (flow rate 20 ml/min), measurement accuracy – ±3 °C. The data was assessed with the *NETZSCH Proteus* software.

Weight loss is released from the formed hydrates during the heating of samples at 50–550°C. In the work, this weight loss will be referred to as bound water (H) and expressed as % of the dry sample weight at 550 °C (($W_{550} - W_{50}$): W_{550} = H, W – weight) [145]. Meanwhile, the quantification of calcium hydroxide (portlandite, CH) was performed by evaluating the mass loss at 400–500 °C (($W_{550} - W_{450}$): $W_{550} \cdot (74:18)$ = CH; $\text{Ca}(\text{OH})_2$ [74 g/mol] → $\text{CaO} + \text{H}_2\text{O}$ [18 g/mol]). The weight difference was determined by applying the stepwise method.

The *Fourier transform infrared spectroscopy* (FTIR) analysis was carried out by using the *Perkin Elmer FT-IR Spectrum X system* (*PerkinElmer*, USA). The samples were analyzed by using the KBr pressed pellet technique (~1 mg of the sample and ~200 mg of KBr), and the spectra were recorded in the range of 4000–400 cm^{-1} with a spectral resolution of 1 cm^{-1} .

The morphology of the samples was investigated by using a *scanning electron microscope* (SEM) (*Helios Nanolab 650* (FEI, Netherlands)) and energy-dispersive X-ray spectroscopy (EDS) (*Oxford Instruments*, United Kingdom), *Xmax* 20 mm² detector, *INCA 4.15* software). The powder samples were coated with a layer of Cr to ensure the surface electrical conductivity by using a *Q150T ES device* (*Quorum Technologies Ltd.*, United Kingdom). The micrographs were obtained in the secondary electron imaging mode at 3 kV accelerating voltage and 50 pA beam current under a high vacuum at working distances of 5.1 mm and 2.5 mm. EDS elemental maps were obtained at 15 kV accelerating voltage and 1.6 nA beam current.

The ²⁷Al Nuclear Magnetic Resonance (²⁷Al NMR) spectroscopy was carried out with a *Bruker Avance 500* spectrometer (*Bruker AXS GmbH*, Germany) with a magnetic field strength of 11.747 T (resonance frequency for ²⁷Al: 130.308 MHz). The measurements were performed by applying a single pulse MAS (*magic angle spinning*) technique. The samples were placed in a 4 mm zirconia rotor and spun at 12 kHz with a repetition time of 0.5 s, thus recording a total of 2000 scans. The ²⁷Al chemical shifts were referenced relative to Al(OH)₃. The obtained spectra patterns were assessed by using the *WINNMR* software.

Inductive plasma optical emission spectroscopy (ICP–OES) was used to determine the composition of the liquid phases. For this experiment, 50 g of the sample and the required amount of water (W/S=1.1) were placed in a plastic container and mixed with a spatula for 2 min. Afterwards, the container was sealed and stored at room temperature (23 °C) for 2 h. The pore solutions were gained by centrifugation (centrifuge *MIKRO 220*, *Hettich Lab*, Germany) for 5 min at 1100 rpm, and then by filtration (filter paper thickness 0.45 μm). Immediately after the extraction, the pH of the untreated solution was measured. For ICP–OES, the obtained pore solution was diluted by 1:10 HNO₃ (6.5%) to prevent the precipitation of solids. The total concentrations of the elements were determined by using the optical emission spectrometer *Optima 8000* (*PerkinElmer Instruments Co.*, USA). Argon was used as the ICP torch gas (7.0 L/min) and purge gas (1.0 L/min). The parameters of the recirculating cooling system (chiller): cooling capacity at 20 °C, 2850 watts, temperature stability ±0.5 °C, and the pump rate – 4 gal/min at 55 psi max. Meanwhile, the artificial *pore solution* (PS) was prepared, referring to the measured solution composition of YFA20, maintaining the same Na/K ratio and incorporating the Ca content within this ratio. For PS preparation, the required NaOH and KOH were weighed and diluted in 1 l of distilled water.

The *pH* and *conductivity* measurements were performed by mixing 1 g of the sample with water (W/S = 40) and storing it in sealed containers at room temperature (23 °C) for the required durations. At chosen points in time, the sample was filtered, and the obtained filtrate was used for measurements. The pH was recorded with a portable *PH/ORP/TEMP Meter PT-380* (*Boeco*, Germany), whereas the conductivity was established with an *EC meter HI2030* (*HANNA Instruments*, USA).

2.2.10. Thermodynamic calculations

Thermodynamic calculations were performed by employing the method of absolute entropies, as outlined in references [146–148]. By using this approach, the change in the standard free Gibbs energy $\Delta_r G_T^0$ for the reaction can be determined with the following equation:

$$\Delta_r G_T^0 = \Delta_r H_T^0 - T \Delta_r S_T^0 \quad (\text{Eq. 2.4})$$

where: $\Delta_r H_T^0$ – the reaction enthalpy, and $\Delta_r S_T^0$ – the reaction entropy at temperature T. $\Delta_r H_T^0$ and $\Delta_r S_T^0$ can be calculated by the following integrated equations:

$$\Delta_r H_T^0 = \Delta_r H_{298}^0 + \Delta a \cdot (T - 298) + \frac{\Delta b \cdot (T^2 - 298^2)}{2} + \frac{\Delta c \cdot (T^3 - 298^3)}{3} - \Delta c' \cdot \left(\frac{1}{T} - \frac{1}{298} \right) \quad (\text{Eq. 2.5})$$

$$\Delta_r S_T^0 = T \left[\Delta_r S_{298}^0 + \Delta a \cdot \ln \frac{T}{298} + \Delta b \cdot (T - 298) + \frac{\Delta c \cdot (T^2 - 298^2)}{2} - \frac{\Delta c'}{2} \cdot \left(\frac{1}{T^2} - \frac{1}{298^2} \right) \right] \quad (\text{Eq. 2.6})$$

where: $\Delta_r H_{298}^0$ – the standard change of enthalpy, J/mol; $\Delta_r S_{298}^0$ – the standard change of entropy, J/mol; Δa , Δb , Δc and $\Delta c'$ – constants describing the dependency of the heat capacity on temperature. The used standard thermodynamic values at 25 °C and 1 bar are listed in Table 2.3 [149,150]. Thermodynamic calculations were used to evaluate the different hydration states of the possibility of monosulfoaluminate (Ms14, Ms12, Ms10.5) formation. However, only the Gibbs free energy values for Ms14 are presented since they were the lowest compared to other hydration states.

Table 2.3. Standard thermodynamic properties at 25 °C (298 K) and 1 bar

Compound	$\Delta H_{298}^{0,f}$, kJ/mol	$S_{298}^{0,f}$, J/Kmol	$\Delta G_{298}^{0,f}$, kJ/mol	ΔC_p , J/K/mol
H ₂ O(g)	-242.4	187.2	-247.8	40.07
H ₂ O(aq)	-285.83	69.95	-237.18	75.3
CaO	-634.90	38.10	-603.29	42.02
Ca(OH) ₂	-9845.52	83.39	-896.88	87.49
Al ₂ O ₃	-1662.0	51.0	-1568.3	118.3
Al(OH) ₃ (amorphous)	-1280.93	70.08	-1143.21	93.07
Al(OH) ₃ (gibbsite)	-1288.7	70.01	-1151.0	91.69
AlO(OH)	-996.39	37.19	-918.4	54.24
CaSO ₄ ·2H ₂ O	-2022.94	193.9	-1797.38	186.2
CaSO ₄ ·0.5H ₂ O	-1575.27	134.3	-1436.34	124.1
CaSO ₄	-1434.40	107.4	-1322.13	101.23
C ₄ AŠH ₁₄	-9321.76	960.85	-8252.87	1028.53
C ₆ AŠ ₃ H ₃₂	-17535.00	1900.0	-15205.93	2174.36

2.2.11. Apparent kinetic parameter calculations

In order to evaluate the carbonation degree of the samples, the quotient between the percentage of the identified CaCO₃ (experimental) and the maximal theoretical CaCO₃ value was applied. For this, the Steinhour equation was used to determine the theoretical maximum CO₂ amount that can be sequestered by the sample (Eq. 2.7) [151]:

$$\text{CO}_2(\% \text{max}) = 0.785(\text{CaO} - 0.7\text{SO}_3) + 1.091\text{MgO} + 1.420\text{Na}_2\text{O} + 0.935\text{K}_2\text{O} \quad (\text{Eq. 2.7})$$

where: CaO, SO₃, MgO, Na₂O and K₂O represent the mass percentage relevant constituent oxides. Since the sample consists of only low amounts (at the ppm level) of MgO, Na₂O and K₂O, these oxides were not evaluated in the calculations. Based on the initial compounds used in the mixture, the sample consists of 34.89 wt.% of CaO and 12.26 wt.% of SO₃. Thus:

$$\text{CO}_2(\% \text{max}) = 0.785 \cdot (34.89 - 0.7 \cdot 12.26) = 20.65\% \quad (\text{Eq. 2.8})$$

Upon applying Eq. 2.7, the theoretical maximum CaCO₃ content of the sample is calculated to be 49.94%. The content of CaCO₃ in each sample was found according to the mass loss associated with CaCO₃ from TG (550–940 °C) and by using Eq. 2.9.

$$\text{CaCO}_3(\%) = \frac{\text{M}_{\text{CaCO}_3}}{\text{M}_{\text{CO}_2}} \times \text{m}_{\text{CaCO}_3} = \frac{100 \text{ g/mol}}{44 \text{ g/mol}} \times \text{m}_{\text{CaCO}_3} \quad (\text{Eq. 2.9})$$

where: M_{CaCO₃} is the mass loss of the sample related to the decomposition of calcium carbonate (wt.%), M_{CaCO₃} = 100 g/mol, the molar mass of calcium carbonate, and M_{CO₂} = 44 g/mol, the molar mass of carbon dioxide. To estimate the carbonation degree (α), the following equation was used:

$$\text{CaCO}_3(\alpha) = \frac{\text{M}_{\text{CaCO}_3 \text{ synthesis}} - \text{M}_{\text{CaCO}_3 \text{ carbonation}}}{\text{Maximum content of CaCO}_3} \times 100\% \quad (\text{Eq. 2.10})$$

where the numerator represents the calcium carbonate content after carbonization, while subtracting the formed calcium carbonate after the synthesis.

The apparent kinetic parameters were calculated to evaluate the influence of the water vapour pressure on the carbonation rate of the samples. Under an isothermal condition, the chemical reaction rate can be expressed as a function of time (on the grounds of the Reaction Rate Law):

$$w = \frac{dx}{dt} = kf(c)^n \quad (\text{Eq. 2.11})$$

where: k is the reaction rate constant, f(c)ⁿ is the concentration of the reactants or products influencing the reaction rate (w), which can be changed to a specific

reaction model. By considering the complexity of the carbonation mechanism, the following three apparent kinetic models were applied in this work:

- Order-based models are derived by using the general equation (Eq. 2.12). Based on the present reaction order (zero, first, or second), the equation is integrated, and the linear dependence is plotted [152].

$$\frac{d\alpha}{d\tau} = k(1 - \alpha)^n \quad (\text{Eq. 2.12.})$$

where: α is the conversion factor, and n is the reaction order. If $n = 0$, the reaction rate does not vary with the change in the reactant's concentration; if $n = 1$, the reaction rate depends linearly on the reactant's concentration. If $n = 2$, the reaction rate is proportional to the square of the reactant's concentration.

- The modified Jinder's kinetic model, which is mainly used to describe crystal formation by diffusion-controlled processes [153–155]. The mathematical expression is presented as Eq. 2.13.

$$(1 - (1 - \alpha)^{1/3})^{n_J} = k_J \tau \quad (\text{Eq. 2.13})$$

where: k_J is the apparent reaction rate constant, τ is the carbonation time, n_J is the apparent constant, classifying the governing reaction process in the system. The n_J constant is determined as the slope ($1/n_J$) in a plot of $\ln(1 - (1 - \alpha)^{1/3})$ vs $\ln(\tau)$. If $n \leq 1$, the reaction is controlled by nucleation processes (dissolution processes or immediate reactions on the grains' surfaces); if $n \geq 1$, the reaction is controlled by the phase boundary kinetics; if $n \geq 2$ ($n = 2$, known as Jander equation), the reaction is limited by diffusion throughout the growing layer.

- The *Avrami model* (sometimes named as the *Johnson-Mehl-Avrami-Kolmogorov model* (JMAK)) is commonly used to describe the formation of the reaction products [156–158]. The general form for the Avrami equation can be expressed as follows:

$$-\ln(1 - \alpha)^{n_A} = k_A \tau \quad (\text{Eq. 2.14})$$

where: k_A is the apparent reaction rate constant, τ is the carbonation time, n_A is the apparent constant classifying the dimension of the crystal growth and reaction kinetics. The n_A constant is calculated as the slope of the linear plot of $-\ln(-\ln(1 - \alpha))$ against $\ln \tau$. The original interpretation of the n_A value includes three cases where $1 \leq n \leq 2$ represents one-dimensional (linear) growth, $2 \leq n \leq 3$ is used for two-dimensional (plate-like) growth, and $3 \leq n \leq 4$ is employed for three-dimensional (polyhedral) growth [159].

2.2.12. Modeling of the calcium monosulfoaluminate 12-hydrate synthesis process

The simulations of the precursor synthesis process were carried out by using *Aspen Plus V12* and *Aspen HYSYS V12* (*Aspen Technology, Inc.*, USA) modeling programs. For the solid aggregate states simulations, the ‘Fluid Packages – Solid’ system of thermodynamic equations was employed. The estimations were performed according to the experimental data, by utilizing the particle size distribution of the materials and the synthesis conditions, such as the temperature, duration, and pressure.

The fluidized bed reactors were used to evaluate the thermal decomposition of $\text{Al}(\text{OH})_3$ and CaCO_3 . The model of the fluidized bed was considered the bottom zone (high solid concentration), where the fluid mechanism was estimated by applying the *Werther* and *Wein* mathematical model and the freeboard zone (low solid concentration), where the fluid mechanism was estimated by applying the *Kunii* and *Levenspiel* mathematical model. Identical fluidized bed reactor specifications were employed to evaluate both materials: bed mass – 120 kg; voidage at minimum fluidization – 0.5; correlation – Ergun; TDH model – George and Grace; elutriation model – Tasirin and Gerldart; dimension height – 5 meters; solids discharge location 0.95; cross-section – circular; constant diameter – 0.5; gas distributor type – perforated plates; number of orifices – 40; orifice discharge coefficient – 0.8; holdup and pressure convergence method – RootN1; solver – Newton; maximum temperature step – 90 °C. The air was compressed by using compressors where the specified model was ‘compressor’, the type – Isentropic using the ASME method, and the outlet specification – discharge pressure, efficiency – 72%. The streams were cooled by using coolers, where the flash specifications – the temperature and pressure – were selected. The cleaning of solid particles in the air stream was modeled by using cyclones. Identical cyclone specifications were employed to evaluate both materials: model – cyclone; mode – simulation; calculation method – Muschelknautz; type – Stairmand–HE; the diameter of the cylinder – 0.5 meters; the length of the cylinder – 0.75 meters; the length of the cone section – 1.25 meters; the width of the gas inlet – 0.1 meters. The initial material mixing was modeled by applying the convergence parameter of maximum iterations – 30, and an error tolerance of 0.0001. The mixer was specified with the crusher type – the ball mill, the distribution function – Gates Gaudin Schuhmann, the specific power – 45 kW/ton, D_{50} – 0.001 meter, and the mill diameter – 4 meters.

3. RESULTS AND DISCUSSION

3.1. Hydrothermal Synthesis of Calcium Monosulfoaluminate 12-hydrate

3.1.1. Characterization of the obtained samples

For the initial stage of this work, the effect of hydrothermal conditions (the temperature and duration) on the formation of calcium monosulfoaluminate 12-hydrate was investigated by using XRD analysis. After hydrothermally treating Sample S1 at 100 °C for 1 h, Ms12 ($\text{Ca}_2\text{Al}(\text{SO}_4)_{0.5}(\text{OH})_6(\text{H}_2\text{O})_3$, PDF No. 04-013-03303) is observed as the dominant crystalline phase in the synthesis products (Fig. 3.1). However, these conditions are insufficient for the initial compounds entirely to react, i.e., unreacted gypsum is still detected in the sample. Ettringite ($\text{Ca}_6\text{Al}_2(\text{SO}_4)_3(\text{OH})_{12}(\text{H}_2\text{O})_{26}$, PDF No. 04-013-3691), katoite ($\text{Ca}_3\text{Al}_2(\text{OH})_{12}$, PDF No. 00-024-0217), and portlandite also form under these synthesis conditions. Moreover, the identified calcium carbonate (CaCO_3 , PDF No. 01-080-2793) indicates that the sample has partially interacted with atmospheric carbon dioxide. By extending the duration of hydrothermal synthesis on Sample S1, it is observable that ettringite becomes metastable and recrystallizes progressively into Ms12. After 48 h, only small traces of ettringite and, conversely, an increase in Ms12 are detectable in the XRD patterns (Fig. 3.1). Additionally, an increase in the intensity of the diffraction peaks of katoite and portlandite is observed. Meanwhile, after hydrothermally treating Sample S2 at 100 °C for 1–48 h, only Ms12 and calcium carbonate are identified in the XRD patterns (Fig. 3.1). These results suggest that the mechanochemical activation of the initial mixture significantly influences the formation of the hydrothermal synthesis products. Also, the prolonged synthesis duration positively impacts the formation of Ms12, similar to Sample S1.

Further, hydrothermal synthesis was conducted at elevated temperatures (up to 130 °C) to enhance the reaction rate and to promote the formation of Ms12. Fig. 3.1 shows that an increase of the hydrothermal synthesis temperature to 110 °C has a positive effect on the formation of Ms12 and katoite in Sample S1. After 1 h of synthesis, higher intensities of Ms12 and katoite peaks are observed at 110 °C compared to 100 °C for the same duration. It should be noted that the synthesis conditions at 110 °C for 1 h are also insufficient for the initial compounds to react, i.e., gypsum and portlandite are identified in the XRD patterns. The prolongation of the synthesis duration to 8 h promotes the formation of Ms12, katoite, and ettringite, as confirmed by the higher intensity of the corresponding peaks in the XRD patterns. Additionally, the decreased intensity of the portlandite peaks is identified. The increase in the intensity of ettringite might be partially explained by the formation of katoite (C_3AH_6) in the samples, for which CaO and Al_2O_3 are consumed. Consequently, the reacting system is more saturated with SO_4^{2-} , driving the direction of chemical reactions towards ettringite crystallization. Meanwhile, as the synthesis duration is further increased to 48 h, the intensity of the presently discussed compounds gradually decreases, and gibbsite ($\text{Al}(\text{OH})_3$, PDF No. 04-013-6979) is identified in the XRD patterns.

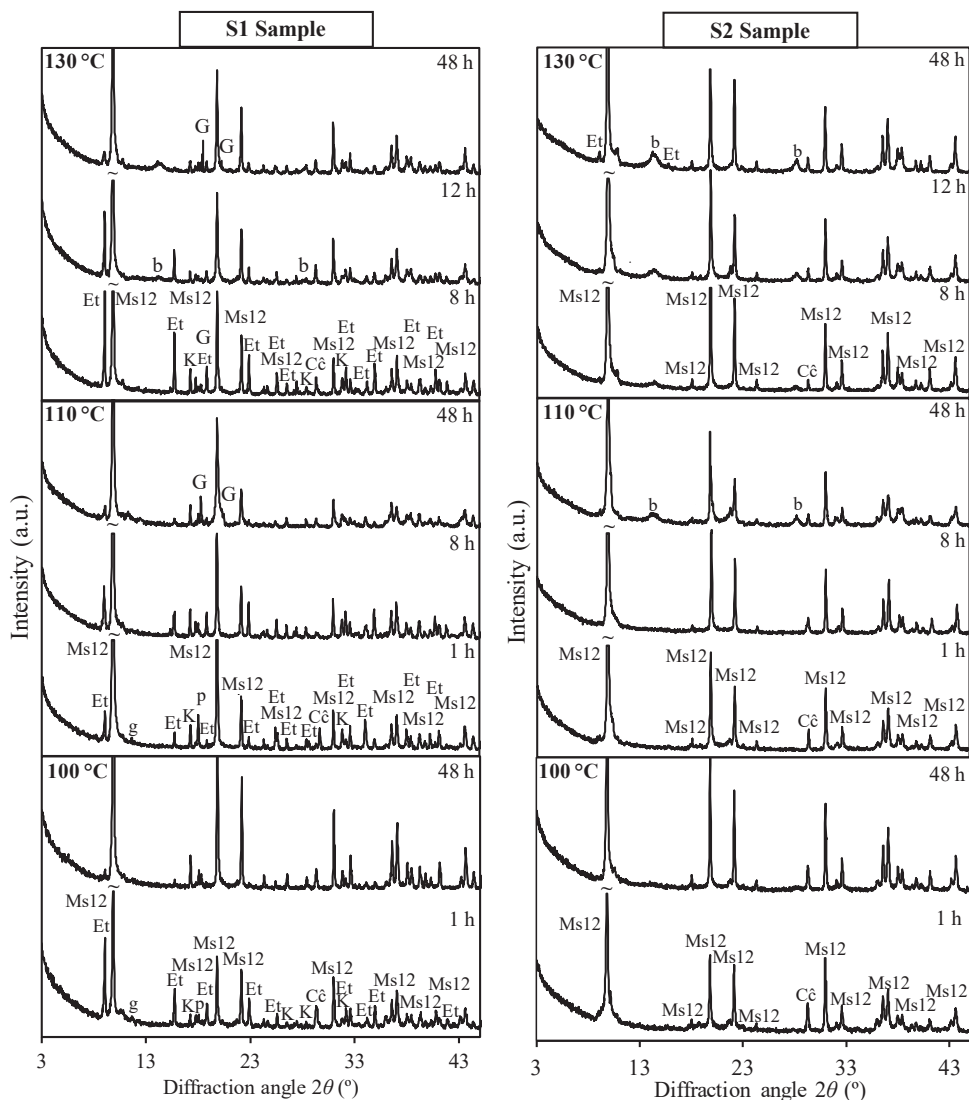


Fig. 3.1. XRD patterns of S1 and S2 samples products after hydrothermal synthesis. Indexes: Ms12 – monosulfoaluminate 12-hydrate, Et – ettringite, g – gypsum, K – katoite, Cc – calcium carbonate, b – boehmite, G – gibbsite, p – portlandite

The same formation tendency is observed in Sample S2 at 110 °C after 1–8 h of synthesis without the presence of any additional compounds, i.e., only Ms12 and calcite are identified in the XRD patterns (Fig. 3.1). It should be noted that a further extension of the synthesis duration to 12–48 h causes a gradual decrease in the characteristic diffraction peaks of Ms12. Additionally, after 48h of synthesis, the formation of low crystallinity boehmite ($\text{AlO}(\text{OH})$, PDF No. 00-001-1284) is observed in Sample S2. It is pertinent to recall that the used initial mixture ($\text{CaO}/\text{Al}_2\text{O}_3$

= 1.33; 3 moles of Al_2O_3) is non-stoichiometric to the composition of monosulfoaluminate ($\text{CaO}/\text{Al}_2\text{O}_3 = 4$; 1 mole of Al_2O_3). Therefore, the formation of boehmite can be attributed to the excess of alumina in the system, whose reactivity is enhanced by mechanochemical treatment and prolonged hydrothermal synthesis, leading to the direct formation of boehmite. The mechanism of phase transformations during the hydrothermal treatment of Al_2O_3 to boehmite was also observed by other authors [160,161].

Upon raising the hydrothermal synthesis temperature even higher (up to 130 °C), it is visible that the resulting products are consistent with those of previous syntheses (Fig. 3.1). Although the identified characteristic diffraction peaks of Ms12 in Sample S1 are slightly higher during the initial 8 h of synthesis at 130 °C compared to 110 °C; these conditions also favour the crystallization of ettringite and katoite. Meanwhile, a further extension of the synthesis duration causes a gradual decrease in the intensity of the peaks of the mentioned phases, with only traces of ettringite and katoite detectable in the XRD patterns after 48 h. Additionally, a higher temperature promotes the formation of aluminium hydroxides. Gibbsite and boehmite are identified in the XRD patterns after 8 and 12 h, respectively, and the peak intensities of both compounds increase with a prolonged duration of the synthesis. When examining the synthesis of Sample S2 at 130 °C, the formed dominant phase is Ms12 under all synthesis durations. It is notable that the diffraction peaks of Ms12 are slightly higher than at 110 °C for the same synthesis duration. However, small amounts of low crystallinity boehmite also form after 8 h, and the intensity of the peaks rises with the duration of the hydrothermal treatment. Additionally, ettringite is determined after 12–48 h of hydrothermal treatment. These results suggest that Ms12 becomes unstable and undergoes decomposition at higher temperatures, which seems to favour the equilibrium reaction towards the side of ettringite formation.

Considering the XRD data, it is seen that Samples S1 under all synthesis conditions consist of multi-phase systems. Meanwhile, based on the observations on Sample S2, it is observed that the mechanochemical treatment of the mixture promotes the formation of Ms12 and reduces the formation of the intermediate compounds. Referring to the data and aiming to reduce the energy consumption of the hydrothermal synthesis, Sample S2 synthesized at 110 °C was used for further investigations.

Figure 3.2 illustrates the TGA curves for Sample S2 after hydrothermal synthesis at 110 °C. The TGA analysis reveals that the sample synthesized for 8 h contains the largest quantity of the bound water (evaluated in the interval of 50–550 °C), thereby confirming the presence of the highest amount of the formed hydrates in this sample (Fig. 3.2 a) [145]. Further, it can be observed that all the synthesized Samples S2 exhibit a broad multi-peak thermal effect in the DTG curves within the temperature range of 30–145 °C, representing the evaporation of free water, the dehydration of amorphous compounds and Ms12 [107] (Fig. 3.2.b). The second effect at 177 °C is also related to the removal of interlayer water molecules from the Ms12 structure, where the measured mass loss after synthesis at 110 °C for 4 h is

~6.2%. Similar to the XRD results, thermal analysis also suggests that the amount of Ms12 increases (with a mass loss of ~6.7%) as the synthesis duration goes from 4 h to 8 h (Fig. 3.2.). Additionally, prolonging the synthesis duration to 24 h or 48 h adversely affects the formation of Ms12, i.e., the decrease in the mass loss by ~15% and ~18% at 145–200 °C is observed, respectively, compared to the sample synthesized for 8 h. Meanwhile, the thermal effect at ~288 °C reflects the water loss from the octahedral layers of Ms12, where the highest mass loss (~6.4%) is also identified in the sample hydrothermally treated for 8 h. Additionally, the thermal peak at ~420 °C and the increased mass loss observed within the temperature range of 410–600 °C in the sample after 48 h of the synthesis confirm the presence of boehmite (Fig. 3.2) [162,163]. It is worth noting that, despite the synthesis conditions, the formed amount of calcium carbonate is similar in all samples, i.e., the mass loss alters from ~2.8 to ~3.3% within the temperature range of 550–800 °C [33].

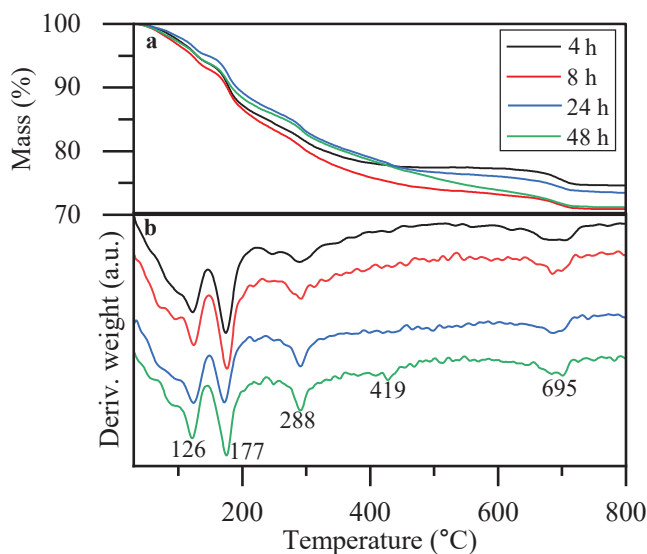


Fig. 3.2. TGA plots (a – TG; b – DTG) of Sample S2 after hydrothermal synthesis at 110 °C for varying durations

Figure 3.3 illustrates the FTIR spectrum of Samples S2 after hydrothermal synthesis at 110 °C for different durations. The bands observed can be attributed to the vibrations of the hydroxyl groups in the main layers, the water molecules between layers, intercalated anions, and the main layer lattice [105,165,166]. The spectral data demonstrates three distinct regions: the $>1550\text{ cm}^{-1}$ region, where the bands are attributed to water molecules, the $\sim 1200\text{--}1160\text{ cm}^{-1}$ region, where the bands correspond to sulphate bands, and the low-frequency region ($<1000\text{ cm}^{-1}$) [105]. Three distinct bands can be observed in the high-frequency region ($4000\text{--}2500\text{ cm}^{-1}$). The band at frequencies of $\sim 3637\text{ cm}^{-1}$ indicates OH-stretching in gibbsite [166]. Meanwhile, the bands at 3471 cm^{-1} and 3426 cm^{-1} show the stretching vibration of

hydroxyl groups (H–O–H) in the interlayer and the main layer of monosulfoaluminate [168]. The hydrogen bonds are responsible for the widening of these absorption bands. Additionally, the absorption band at $\sim 1624\text{ cm}^{-1}$ corresponds to the bending vibration of water molecules in the interlayer [105,165,166]. The presence of the carbonate phase in the analyzed samples is indicated by the distinctive spectral bands at 1456 cm^{-1} and 875 cm^{-1} . These bands arise from the asymmetric stretching mode (ν_3) vibrations and the out-of-plane bending mode (ν_2) of CO_3^{2-} groups, respectively. All the spectra of the samples demonstrate an intense absorption band at 1112 cm^{-1} and a small one at 1155 cm^{-1} , generated by ν_1 SO_4 vibrations [105,165,166]. Meanwhile, the adsorption band at 1080 cm^{-1} is visible only in the samples synthesized for 12–48 h, corresponding to the AlO–H bending vibrations, which confirms the presence of boehmite. In the region of low-frequency energy, characteristic absorptions of Al–O–H (bending at 783 cm^{-1} and 617 cm^{-1}) and AlO_6 vibrations (at 984 cm^{-1} , 588 cm^{-1} , and 522 cm^{-1}) are displayed [105,165,166]. The evaluation of the FTIR spectra confirmed the successful synthesis of Ms12 and the presence of intermediate phases, as indicated by the XRD and TGA data.

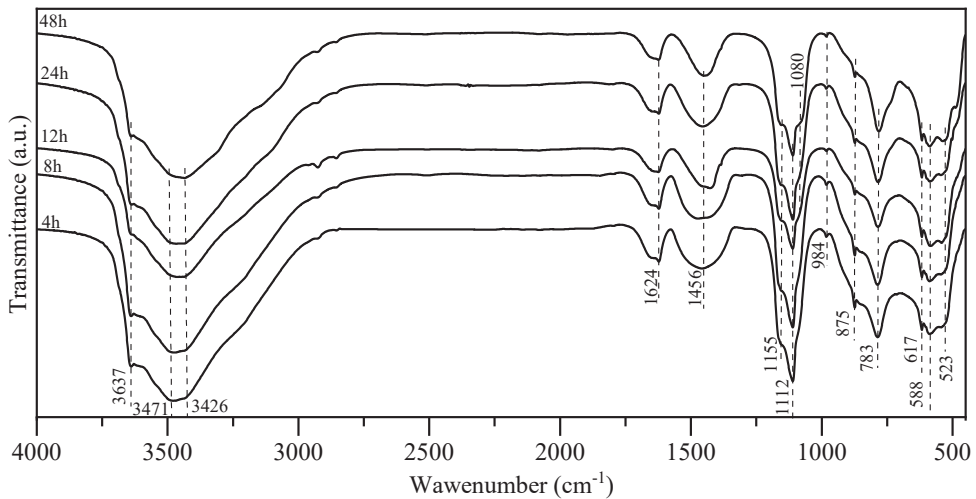


Fig. 3.3. FTIR spectrum of Sample S2 synthesized at $110\text{ }^\circ\text{C}$ for varying durations

Upon examining the synthesized samples, it is suggested that the optimal conditions for Ms12 formation at $110\text{ }^\circ\text{C}$ occur when the synthesis duration is 8 h. Therefore, for the microstructure investigation, Sample S1 was used to determine the morphology of the formed phases after hydrothermal synthesis. Figure 3.4 shows the SEM images and elemental maps of calcium, aluminium, and sulfur in the sample. In the images of Sample S2, heterogeneous systems with a diverse range of agglomerates are observed. The hexagonal plate-like shape particles of sizes ranging between $5\text{--}50\text{ }\mu\text{m}$ dominate in the sample, thereby indicating the presence of calcium monosulfoaluminate 12-hydrate [113]. This confirmation is validated through the elemental maps, revealing the presence of calcium, aluminium, and sulfur in these

particles. It is worth noting that many Ms12 particles do not exhibit orderly hexagonal shapes. The reason for this might be that the particle structure was damaged in the grinding and sieving process. Additionally, these particles are surrounded by small irregular-shaped agglomerates, corresponding to unreacted Al_2O_3 and, possibly, precipitated $\text{Al}(\text{OH})_3$ during the hydrothermal synthesis (the green colour in the maps) [139].

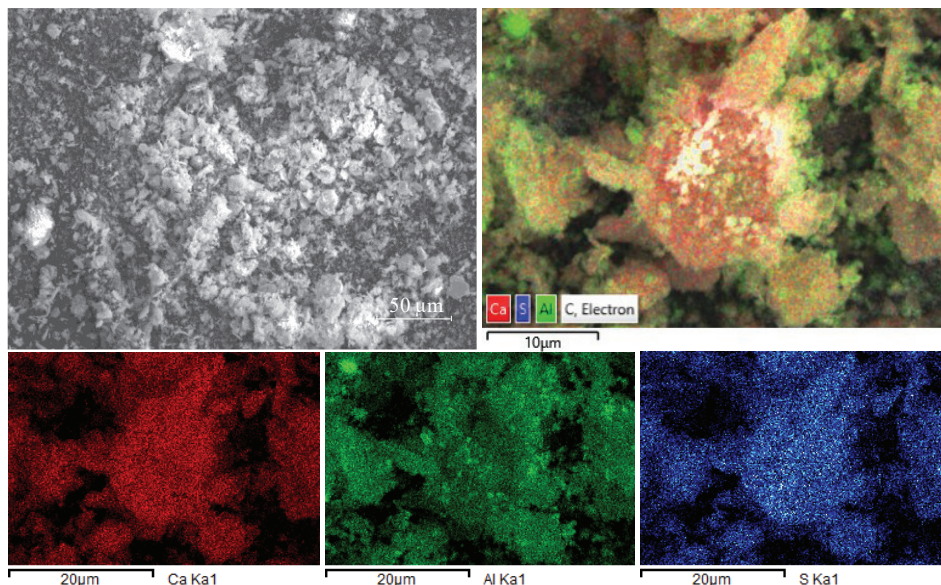


Fig. 3.4. SEM image and EDS elemental maps of Sample S2 after hydrothermal synthesis at 110 °C for 8 h

To estimate the amount of Ms2 formed in the samples, *quantitative phase analysis* (QPA) was performed. Given the unclear crystal structure patterns of the lower monosulfoaluminate hydration states (below Ms12), the crystal structure of kuzelite was employed as the initial model for Ms10.5 ($d = 0.820$ nm) refinement. To ensure reliable QPA data, adjustments were made to the space group and the initial lattice parameters, while taking into account the findings of prior studies [107]. The Rietveld analysis results indicated that Sample S2, following hydrothermal synthesis at 110 °C for 8 h, contains 54.8% Ms12, 0.7% Ms10.5, 1.9% calcite, and 42.6% of amorphous phase (Fig. 3.5.a).

The amorphous nature of the sample was investigated by using ^{27}Al NMR analysis. The data obtained for the sample is presented in Fig. 3.5.b. The analysis reveals two resonance ranges at higher (from 80 to 45 ppm) and lower (from 30 to –30 ppm) fields, corresponding to the resonances for 4-fold and 6-fold coordinated Al positions, respectively [165]. The predominant peak at ~ 9.4 ppm is a characteristic signal of AlO_6 in calcium monosulfoaluminate 12-hydrate. Meanwhile, a broad shoulder at ~ 67 ppm indicates the presence of unreacted Al_2O_3 , with the resonance of the 6-fold coordinated aluminium part concealed beneath the Ms12 resonance.

According to the XRD and ^{27}Al NMR results, the primarily amorphous content consists of unreacted Al_2O_3 . Additionally, the deconvolution reveals a small peak at 0–2 ppm, suggesting the presence of a small amount of amorphous $\text{Al}(\text{OH})_3$ in the sample.

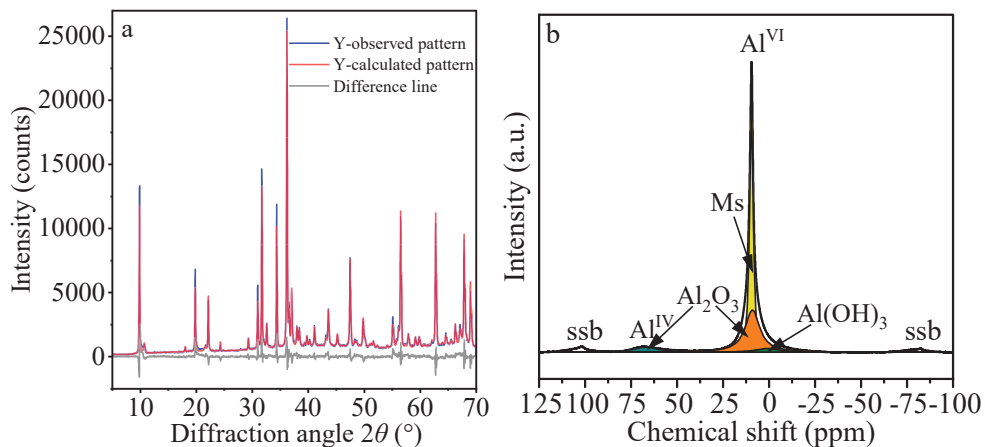


Fig. 3.5. Quantitative phase analysis refinement plot (a) and ^{27}Al NMR spectrum (b) of Sample S2 after hydrothermal synthesis at 110 °C for 8 h

Upon examining all Samples S2, it was also observed that, when subjected to hydrothermal conditions of 130 °C for 8 h, the samples exhibit higher characteristic diffraction peaks of Ms12 than at 110 °C for 8 h (Fig. 3.1). Therefore, additional characterization of Sample S2 synthesized at 130 °C for 8 h was performed to better understand the temperature impact on the formation of Ms12.

The DTG curve of Sample S2 hydrothermally treated at 130 °C for 8 h exhibited the same three initial thermal effects as observed in Sample S2 treated at 110 °C (Fig. 3.6 and Fig. 3.2). It was determined that a higher synthesis temperature promotes the formation of a higher amount of Ms12, as confirmed by the greater mass loss (~7.7%) observed at the main dehydration peak at 169 °C. Moreover, the TGA results correspond well with the XRD data, where the slight peak at ~419 °C reflects the presence of boehmite in the sample. Meanwhile, the last peak at ~670 °C corresponds to the decarbonization of calcium carbonate.

The examination of the amorphous nature of Sample S2, hydrothermally treated at 130 °C for 8 h, by ^{27}Al NMR analysis confirmed the same two resonance ranges as observed at 110 °C (Fig. 3.7.a and Fig. 3.5.b). The characteristic signals reflected the presence of Ms12 (at ~9.4 ppm), aluminium oxide (at ~67 ppm and ~8.8 ppm), and aluminium hydroxide (at 0–2 ppm) [165]. It is noteworthy that the signal corresponding to the boehmite structure (expected at ~9 ppm) was not detected, possibly due to the low quantity of boehmite and overlapping with other signals [167].

The FTIR spectroscopy of Sample S2 after synthesis at 130 °C for 8 h also displays mainly the characteristic bands of calcium monosulfoaluminate 12-hydrate (Fig. 3.7.b). The only impurities identified correspond to the carbonate C–O bond ν_3

vibration bands and boehmite AlO–H bending vibrations. The summarized and attributed infrared spectrum bands are presented in Table 3.1.

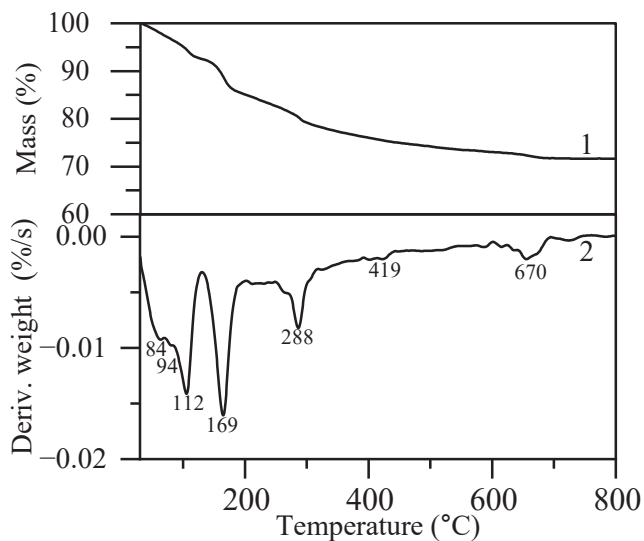


Fig. 3.6. TGA curves (1 – TG, 2 – DTG) of Sample S2 after hydrothermal synthesis at 130 °C for 8 h

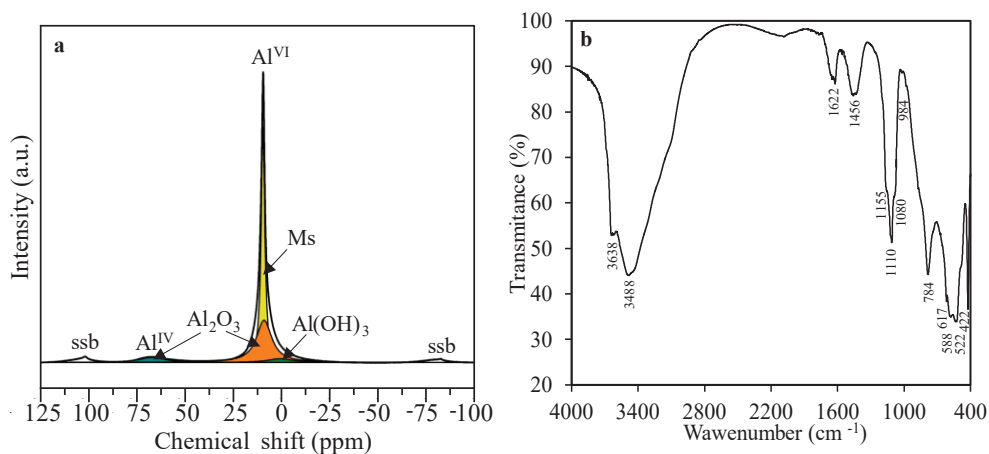


Fig. 3.7. ^{27}Al NMR spectrum (a) and FTIR spectrum (b) of Sample S2 after hydrothermal synthesis at 130 °C for 8 h

Table 3.1. Assignments of the FTIR spectrum absorption bands of the formed synthesis products at 130 °C for 8 h [105,166]

ν (cm ⁻¹)	Assignment
3638	O–H stretching
3488	O–H stretching
1622	H–O–H bending
1155	SO ₄ vibrations
1456	C–O stretching
1110	S–O stretching
1080	AlO–OH bending
984	AlO ₆ vibrations
784	Al–O–H bending
617	Al–O–H bending
588	AlO ₆ vibrations
522	AlO ₆ vibrations
422	SO ₄ ²⁻ bending

Finally, the SEM analysis verified that, after hydrothermal synthesis at 130 °C for 8 h, Sample S2 prevails with hexagonal plate-like shaped particles corresponding to the morphology of Ms12 (Fig. 3.8). The characterization of Sample S2 synthesized at 130 °C for 8 hours revealed that the prolonged treatment duration not only promotes the formation of boehmite, but also facilitates the formation of Ms12.

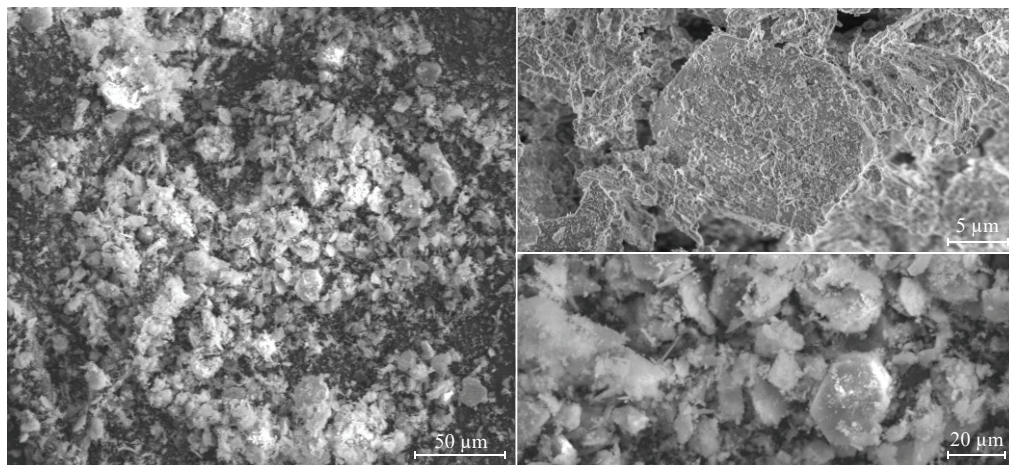


Fig. 3.8. SEM micrographs of Sample S2 after hydrothermal synthesis at 130 °C for 8 h

A summary of the phase composition which developed under the hydrothermal conditions of both Samples S1 and S2 is presented in Figure 3.9. As it is evident from the experimental results, multiple distinct compounds can be formed in the CaO–

$\text{Al}_2\text{O}_3\text{-SO}_4\text{-H}_2\text{O}$ system under hydrothermal conditions. It was determined that not only the production measures (the synthesis conditions) are essential for stabilizing Ms12, but also the preparation of the initial mixture. The methods employed in this work do not allow for the direct production of high-purity Ms12 from calcium oxide, aluminium oxide, and gypsum. In the effort to stimulate the formation of Ms12, the initial mixture must undergo mechanochemical treatment. This treatment alters the phases and the physical characteristics of the initial mixture, leading to more complete reactions inducing the formation of Ms12. In order to better understand the possible pathways through which Ms12 is formed in the $\text{CaO-Al}_2\text{O}_3\text{-SO}_4\text{-H}_2\text{O}$ system in the water medium, further, the reaction feasibility was determined by the thermodynamic calculations.

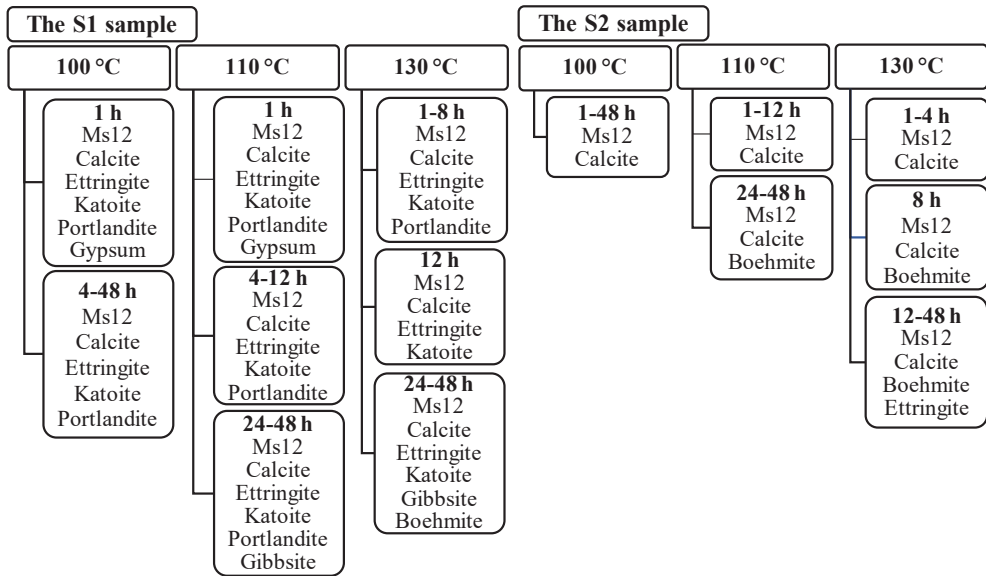


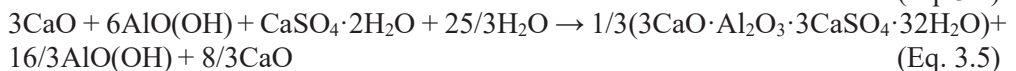
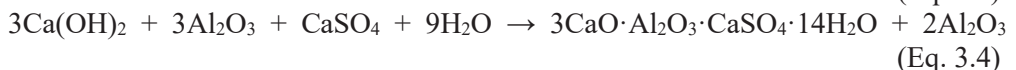
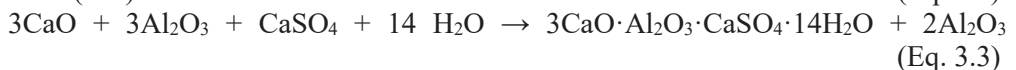
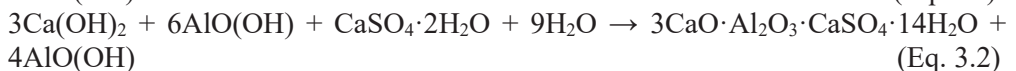
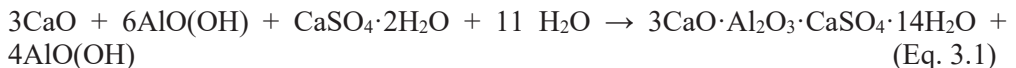
Fig. 3.9. Sequences of crystalline product formation in the $\text{CaO-Al}_2\text{O}_3\text{-SO}_4\text{-H}_2\text{O}$ system under hydrothermal conditions

3.1.2 Thermodynamic calculations

The feasibility of a chemical reaction (i.e., if it can occur spontaneously under specific conditions) can be described by applying thermodynamic calculations. Referring to the synthesis conditions of Ms12 at 110 °C, it is worth highlighting that the initial mixture remains in a water medium (<100 °C) for approximately 1 h 50 min. This preheating duration may be sufficient for chemical reactions to occur in the initial mixture. For this reason, the obtained thermodynamic data is divided into temperature intervals, <100 °C and >100 °C, where the conversion of water phases takes place ($\text{H}_2\text{O}_{(\text{aq})} \rightarrow \text{H}_2\text{O}_{(\text{v})}$) during the reactions. Additionally, it is essential to note that calcium oxide is a highly reactive material in water already at room temperature [168,169]. Meanwhile, gypsum dehydration (to hemihydrate \rightarrow anhydrite) in a water

solution can occur depending on the temperature [169]. Therefore, the formation probability of Ms14 and ettringite was evaluated by using thermodynamic calculations from the feasible initial compounds in hydrated and non-hydrated forms. The possible formation reactions are presented in Appendix 1 (Eqs. 1–55). Meanwhile, all the formation reactions are illustrated in Appendix 1 Figs. 1–5 as $\Delta G_T^0=f(T)$ plots.

From the analysis of the thermodynamic data acquired (as shown in Appendix 1 Fig. 1 and Fig. 3), it can be observed that for, a number of calculated reaction equations, the Gibbs free energy values for the formation of ettringite are more negative than those for Ms14 within the temperature range of 0–100 °C. However, it is of importance to emphasize that the evaluated equations for Ms14 formation also demonstrate negative Gibbs free values. This also suggests the possibility for the formation of both Ms14 and ettringite during the preheating period of the autoclave. Furthermore, results suggest that, with rising temperatures, the likelihood of these compounds forming in liquid water diminishes in most reactions. When evaluating the formation possibility from the initial compounds and their feasible hydrates (Eqs. 3.1–3.8), the highest possibility is demonstrated by Equation 3.1 (ΔG_T from –135.2 kJ to –54.5 kJ) for Ms14 formation, followed by reactions Eqs. 3.2, 3.3, and 3.4 (Fig. 3.10). Meanwhile, for ettringite formation at <100 °C temperature, Equation 3.8 (ΔG_T from –97.4 kJ to –49.9 kJ) reveals the greatest feasibility, along with Equations 3.5, 3.6, and 3.7. In both cases (formation of monosulfoaluminate or ettringite), the initial raw materials must undergo hydration, i.e., the system requires the presence of Ca(OH)_2 or AlO(OH) . It is worth noting that almost all Gibbs free energy curves exhibit a bending when approaching 100 °C. This is most likely due to phase transition, where the water reaches its boiling point (liquid → gas) and causes a sudden change in the conditions, thereby influencing the thermodynamic data. Additionally, the behaviour of the Gibbs free energy curves as they approach or surpass the point of 100 °C can also be influenced by other factors, including equilibrium position shifts, activation energy, kinetics, pressure, concentration effects, etc. [170]. Therefore, the calculated thermodynamic data is valid and evaluated only up to 90 °C (the red-dotted line in Fig. 3.10).



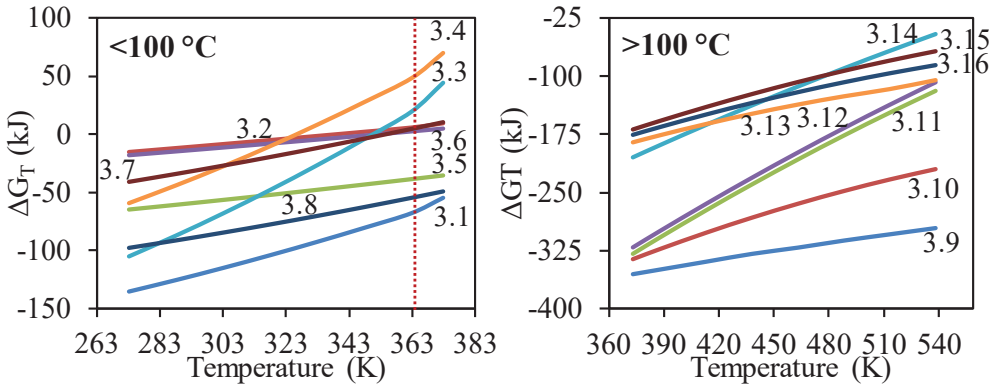
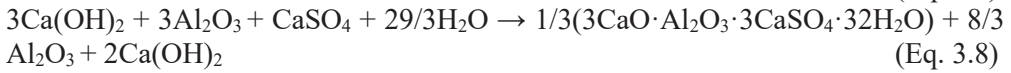
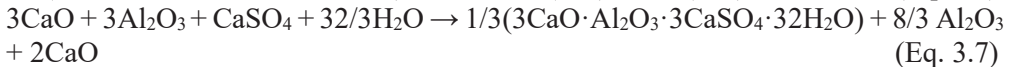
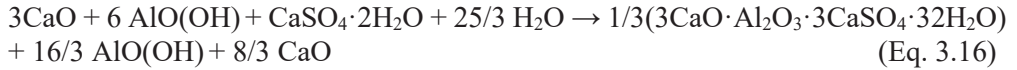
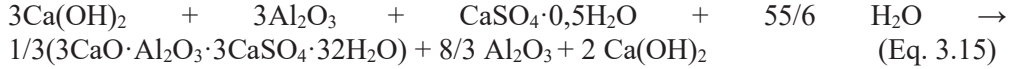
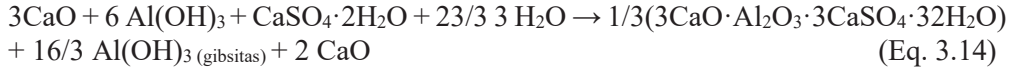
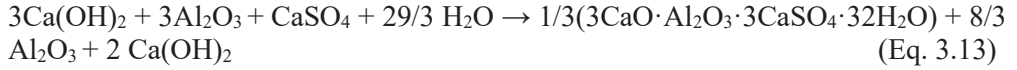
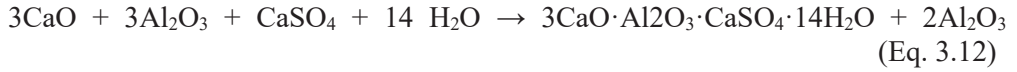
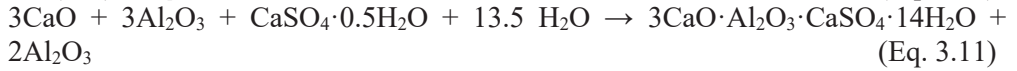
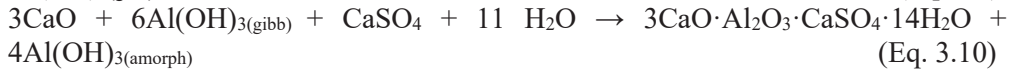
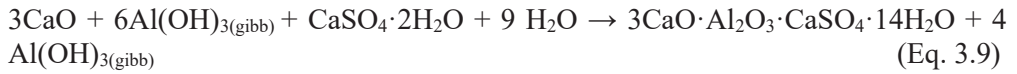


Fig. 3.10. Temperature dependence of Gibbs free energy based on Equations 3.1–3.16

Looking at thermodynamic data above 100°C , noticeable changes in the formation feasibility of monosulfoaluminate and ettringite are identified (Appendix 1 Fig. 2 and Fig. 4). The probability of monosulfoaluminate formation increases with a higher temperature of hydrothermal synthesis, where the calculated ΔG_T of the reactions is more negative compared to ettringite reactions. Equations 3.9, 3.10, 3.11, and 3.12 indicate that monosulfoaluminate has the lowest Gibbs free reaction energy, where, at 110°C , it is equal to -353.1 kJ , -327.5 kJ , -315.7 kJ , and -306.3 kJ , respectively (Fig. 3.10). These results also demonstrate the possibility that, under hydrothermal conditions, Ms12 is likely to form directly from the initial materials. Meanwhile, Eqs. 3.9.–3.16. propose that the highest probability for ettringite formation requires aluminium hydroxides. It is of importance to understand that other chemical reactions also show negative ΔG_T values and confirm their feasibility to occur spontaneously under given conditions. Therefore, based on thermodynamic calculations, monosulfoaluminate and ettringite can form simultaneously in a combination of reactions, and further investigation is still needed to understand their formation better (e.g., kinetic evaluation). Nevertheless, these thermodynamic calculations are in good agreement with the experimental data, where monosulfoaluminate is identified as the dominant phase under hydrothermal conditions ($>100^\circ\text{C}$). Additionally, the data confirms the possibility for the formation of $\text{Al}(\text{OH})_3$ and $\text{AlO}(\text{OH})$, whose presence was observed in the samples with a prolonged duration of the synthesis or an increased temperature.



3.2. Technological Recommendations for the Hydrothermal Synthesis of Calcium Monosulfoaluminate 12-hydrate

Summarizing the experimental work on Ms12 synthesis, two distinct processes can be distinguished: 1) the initial mixture preparation, and 2) the hydrothermal synthesis. These two processes are not commonly used in the production of cementitious hydrates. Therefore, these production stages were designed/ modeled by calculating the complete material and energy balance.

To estimate the preliminary energy requirements for the precursor production, the *Aspen Plus V12* and *Aspen HYSYS V12* (*Aspen Technology, Inc.*, USA) modeling software was used. The initial stream of materials was selected by referring to the stoichiometry of ye'elinite. In the first modeling stage, the *Aspen Plus* program was used to evaluate the energy requirements for the initial mixture preparation. For this, the thermal decomposition of aluminium hydroxide and calcium carbonate, the cleaning of solid particles in the air stream, the cooling of the products, the initial mixture mixing and milling were modeled. The particle size of the starting materials used in the calculations varied from 0.1 to 10 mm, as stated by the suppliers. The initial mixture preparation scheme, modeled by *Aspen Plus*, is presented in Figure 3.11. All the presented results are described, allowing the production of one cycle of the precursor.

The heating agent (ambient air; 2800 kg/h, 25 °C, 1 atm) is preheated to 100 °C (required power – 68.98 kW/cycle), and then supplied to the compressor (C–A), where it is compressed to 5 atm. During this process, the air heats up to 394.36 °C, where the used energy is equal to 235.98 kW/cycle. The compressed air (AIRIN–A) is further delivered to the *fluidized bed reactor* (FBA), where $\text{Al}(\text{OH})_3$ is thermally treated to produce Al_2O_3 . It can be seen that the selected fluidized bed reactor specifications and streams are well-balanced due to the high Al_2O_3 content (the mass

fraction of 0.99) in the product. Table 3.2 displays the parameters for the simulated thermal decomposition streams of $\text{Al}(\text{OH})_3$.

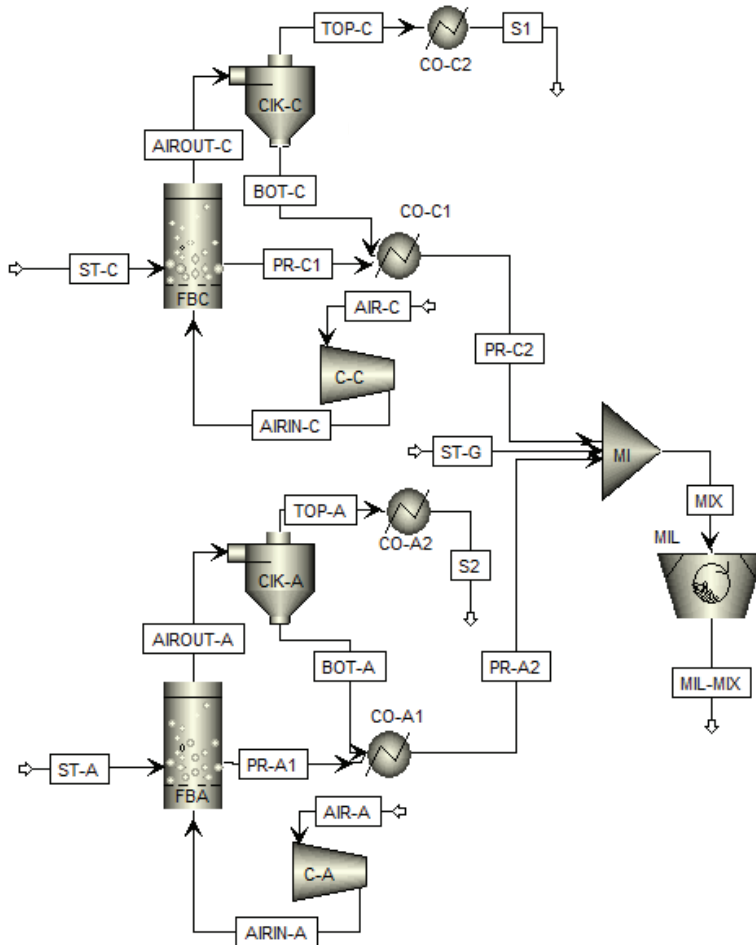


Fig. 3.11. The preparation scheme of the initial mixture, modeled by *Aspen Plus*. Here: FBA, FBC – fluidized bed reactor; C–A, C–C – compressor; AIR–A, AIR–C – ambient air; AIR–IN–A, AIR–IN–C – compressed air; AIROUT–A, AIROUT–C – outgoing air stream; CIK–A, CIK–C – cyclone; TOP–A, TOP–C – cleaned air stream; BOT–A, BOT–C – separated solid particles; ST–A ($\text{Al}(\text{OH})_3$), ST–C (CaCO_3), ST–G ($\text{CaSO}_4 \cdot 2\text{H}_2\text{O}$) – initial material stream; PR–A1, PR–C1 – product; PR–A2, PR–C2 – cooled product; CO–A1, CO–A1, CO–C1, CO–C2 – cooler; S1, S2 – cooled air stream; MI – mixer; MIX – initial mixture stream (resulting mixture of CaO , Al_2O_3 and gypsum); MIL – mill; MIL–MIX – milled initial mixture stream

The obtained product is further supplied to the cooler (CO–A1), where it is cooled to 50 °C. The outgoing air stream (AIROUT–A) from the fluidized bed reactor contains a small amount of solid particles (0.035 kg/h). Therefore, this flow is additionally directed to the air cleaning system, i.e., the cyclone (CIK–A). In the cyclone, the solid particles are separated (efficiency 100%) from the air stream and directed to the cooler (CO–A1) (Table 3.3). In the real-life production processes, heat exchanger systems can effectively recycle the energy from exhaust hot air (80–70% of the total) to either dry materials, or preheat the incoming ambient air. This approach enhances the energy efficiency of the process. Therefore, it was estimated how much power can be released by cooling the exhaust hot air stream by supplying it to the cooler (CO–A2). The modeling demonstrated that cooling the exhaust hot air stream (2886.59 kg/h, 283.23 °C) to 50 °C discharges 195.22 kW/cycle of energy.

Table 3.2. Simulated stream parameters of the thermal decomposition of Al(OH)₃

Stream	AIR–A	AIRIN–A	AIROUT–A	ST–A	PR–A1
Mass Flows (kg/h)	2800	2800	2886.62	250	163.38
Temperature (°C)	100	394.36	283.23	25	283.23
Pressure (atm)	1	5	4.76	1	4.76
Flow rates of compounds in streams (kg/h)					
Al(OH) ₃	0	0	1.10E–05	250	0.059
Al ₂ O ₃	0	0	0.0305	0	163.30
AIR	2800	2800	2800	0	0
WATER	0	0	86.59	0	0

Table 3.3. Simulated stream parameters in the cyclone from the thermal decomposition of Al(OH)₃

Stream	AIROUT–A	TOP–A	BOT–A
Mass Flows (kg/h)	2886.62	2886.59	0.0305
Temperature (°C)	283.23	283.23	283.23
Pressure (atm)	4.76	4.76	4.76
Flow rates of compounds in streams (kg/h)			
Al(OH) ₃	1.10E–05	0	1.10E–05
Al ₂ O ₃	0.0305	0	0.0305
AIR	2800	2800	0
WATER	86.59	86.59	0.00

The same process scheme was applied to the thermal decomposition of CaCO₃ as for Al(OH)₃ (Fig. 3.11). The preheated air (3300 kg/h, 200 °C; AIR–C) is supplied

to the compressor (C–C), where preheating necessitates the amount of power of 137.3 kW/cycle. Within the compressor (C–C), air undergoes compression up to 14 atm, causing it to heat up to 867.43 °C. This process requires an energy input of 668.92 kW/cycle. The heated air is further fed to the *fluidized bed reactor* (FBC), where the incoming CaCO₃ stream (ST–C) is thermally treated. The simulated stream parameters of the thermal decomposition of CaCO₃ are presented in Table 3.4. The obtained product (CaO mass fraction of 0.99) is further supplied to the cooler (CO–C1), where it is cooled down to 50 °C. Meanwhile, the outgoing air stream (AIROUT–C) from the fluidized bed reactor containing a small amount of solid particles is delivered to the cyclone (CIK–C). Here, the solids are separated and fed to the cooler (CO–C1), while the hot air stream (3394.08 kg/h, 727.48 °C) is discharged to the cooler (CO–C2) (Table 3.5). By cooling the hot air to 50 °C, 679.96 kW/cycle of energy is released.

Table 3.4. Simulated stream parameters of the thermal decomposition of CaCO₃

Stream	AIR–C	AIRIN–C	AIROUT–C	ST–C	PR–C1
Mass Flows (kg/h)	3300	3300	3394.11	215	120.89
Temperature (°C)	200	867.43	727.46	25.0	727.48
Pressure (atm)	1	14	13.78	1	13.78
Flow rates of compounds in streams (kg/h)					
AIR	3300	3300	3300	0	0
CaO	0	0	0.0265	0	119.85
CO ₂	0	0	94.08	0	0.00
CaCO ₃	0	0	0.00023	215	1.04

Table 3.5. Simulated stream parameters in the air cleaning system from the thermal decomposition of CaCO₃

Stream	AIROUT–C	TOP–C	BOT–C
Mass Flows (kg/h)	3394.11	3394.08	0.027
Temperature (°C)	727.46	727.48	727.48
Pressure (atm)	13.78	13.78	13.78
Flow rates of compounds in streams (kg/h)			
AIR	3300	3300	0
CaO	0.026	0	0.026
CO ₂	94.08	0	0
CaCO ₃	0.00023	94.08	0.00023

After cooling, the products (PR–A2, PR–C2), together with gypsum (ST–G) (42 kg/h, 25 °C, 1 atm), are supplied to the mixer (MI) (Fig. 3.11). The homogenized

initial mixture stream (MIX; 326 kg/h, 46.03 °C, 1 atm) is further delivered to the mill (MIL). Here, the solid particles of the initial mixture undergo milling, requiring 14.38 kW/cycle of energy in the simulated process. The solid particle size distribution in the streams is given in Table 3.6. The modeling indicates that the particle diameter of the milled initial mixture, which is larger than 80% of the outlet mass, is below 0.8 mm. In summarizing the modeling of the initial mixture preparation, it is calculated that this process demands 519.93 kW per cycle (326 kg/h), when already factoring in the reuse of 70% of the hot air energy from the exhaust. Further, the prepared initial mixture is fed to the autoclave.

Table 3.6. Solid particle size distribution in the streams

Stream	PR-A2	PR-C2	ST-G	MIX	MIL-MIX
PSD (mm)	Relative amount of particles (%)				
0-1	0.129	0.082	0.164	0.116	1
1-2	0.074	0.060	0.075	0.069	0
2-3	0.096	0.085	0.091	0.091	0
3-4	0.114	0.110	0.105	0.111	0
4-5	0.124	0.128	0.113	0.124	0
5-6	0.124	0.136	0.113	0.127	0
6-7	0.114	0.130	0.107	0.119	0
7-8	0.096	0.114	0.094	0.103	0
8-9	0.074	0.090	0.078	0.081	0
9-10	0.053	0.065	0.060	0.058	0

To simulate the processing conditions during hydrothermal synthesis of the precursor – calcium monosulfoaluminate, the *Aspen HYSYS* modeling program was employed. The simulation parameters were selected according to the following experimental conditions: $\text{CaO}/\text{Al}_2\text{O}_3 = 1.33$, $W/S = 10$, temperature – 110 °C, duration – 8 h. The initial material quantities utilized in this modeling are consistent with those obtained in the previous modeling conducted in *Aspen Plus*, i.e., $\text{CaO} = 120$ kg, $\text{Al}_2\text{O}_3 = 164$ kg, $\text{CaSO}_4 \cdot 2\text{H}_2\text{O} = 42$ kg, and $\text{H}_2\text{O} = 3260$ kg. The volume of the modeled autoclave was 10000 l. Reaction interactions were not evaluated in this modeling. The simulations were performed by using two models, i.e., a static model and a dynamic model. The process scheme of the precursor synthesis, modeled by *Aspen HYSYS*, is illustrated in Figure 3.12.

Initially, the static model was utilized to assess the power needed to elevate the autoclave temperature from 25 °C to 110 °C under ideal conditions, where no thermal losses were considered. The modeling reveals that the energy required to accomplish this process amounts to 339.6 kW/cycle. Additionally, the dynamic model was utilized to assess how the thermal loss varies with the geometric dimensions of the autoclave during the temperature rise and isothermal dwell period (8 h). For this, the

influence of the insulating layer's thickness (1–10 cm) on the thermal loss during the temperature rise was calculated when the selected metal layer thickness of the autoclave was 5 cm. The properties of the autoclave metal and the insulating layer are presented in Table 3.7.

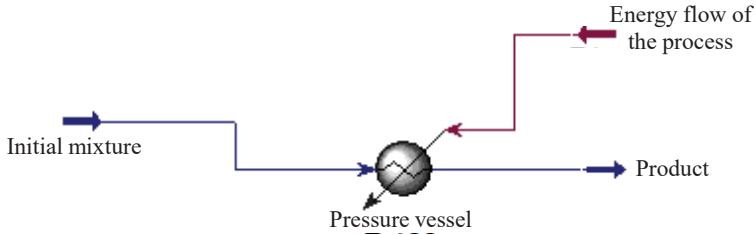


Fig. 3.12. The process scheme of precursor synthesis, modeled by *Aspen HYSYS*

Table 3.7. Properties of the materials composing the autoclave

Properties	Metal layer	Insulating layer
C_p , (kJ/kg·C)	0.473	0.82
Density (kg/m ³)	7801	520
Conductivity (W/m·K)	45	0,15

As expected, the energy losses and the temperature of the autoclave's outer surface directly depend on the thickness of the insulating layer (Fig. 3.13). During the temperature rise, the energy losses reach 23.8 kW/cycle, and the temperature of the autoclave's outer surface is ~53 °C without the insulating layer. When utilizing an insulating layer with a thickness of up to 7 cm, it has the most significant effect in minimizing both the energy losses (by ~81%) and the temperature of the autoclave's outer surface, which are reduced to 4.4 kW/cycle, and ~30 °C, respectively. The impact is not that significant with a further increase in the thickness of the insulating layer. For instance, with a thickness of 10 cm, the calculated energy losses are 3.3 kW/cycle, and the temperature of the autoclave's outer surface remains at ~28 °C.

A similar trend is evident when calculating both the energy losses and the temperature of the autoclave's outer surface during the isothermal temperature dwell period (Fig. 3.13). Without employing an insulating layer, it is estimated that the energy losses escalate to 380.92 kW/cycle, while the temperature of the autoclave's outer surface rises to ~81 °C. Meanwhile, when applying a 7 cm thickness of the insulating layer, it leads to a reduction of the energy losses to 71.1 kW/cycle, and the temperature of the autoclave's outer surface decreases to ~36 °C. To summarize the modeling of hydrothermal treatment, it is calculated that this process demands 415.1 kW/cycle, including the energy losses during the temperature rise and dwell period, when an insulating layer of 7 cm thickness is used.

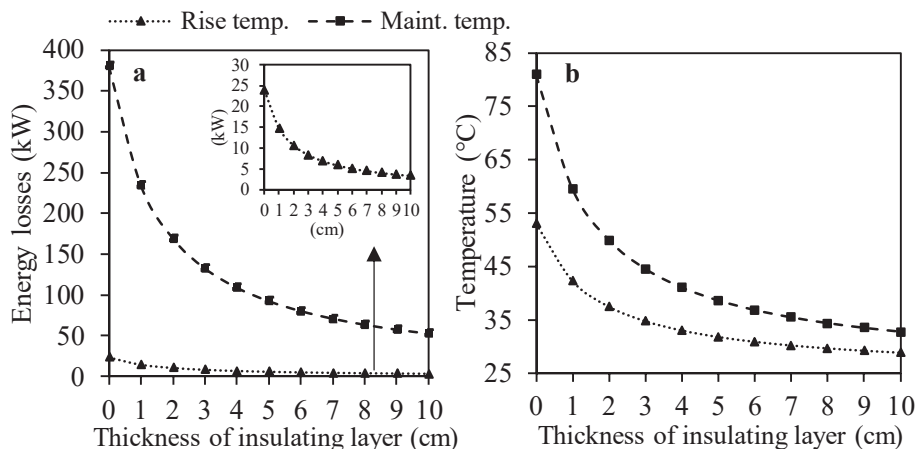


Fig. 3.13. Dependence of energy losses (a) and the autoclave's surface temperature (b) on the thickness of the insulating layer during temperature rise (2 h) and the dwell period (8 h)

After hydrothermal treatment, the resulting homogeneous suspension is supplied to the drum centrifuge, where the excess water is separated from the solid material (precursor). The modeling did not include this aspect of production. Nevertheless, industrial centrifuge suppliers, such as *Broadbent Industrial Process Division*, *Alfa Laval*, and others specify the total amount of energy required as 18–24 kW/cycle, when referring to the stream performance used in the modeling. After centrifugation, the produced precursor contains 12% moisture. Consequently, this stream is subsequently directed to the dryer so that to remove the remaining moisture. The modeling was performed by using the *Aspen Plus* software to assess the energy requirement for the final precursor drying. The modeled process scheme of the precursor drying is presented in Figure 3.14.

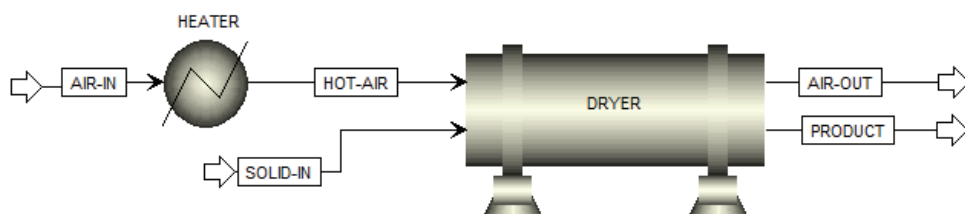


Fig. 3.14. The process scheme of the precursor drying, modeled by *Aspen Plus*

For the drying process, ambient air (1200 kg/h, 25 °C) is supplied to the heater, where it is heated to 120 °C. The calculated energy requirement for this process is 31.8 kW/cycle. The heated air and the precursor with 12% moisture (SOLID-IN; 370 kg/h, 25 °C) are fed to the 4 m dryer when the solid has a residence time of 3 h and a specific mass transfer coefficient of 0.005 m/sec. Table 3.8 presents the parameters of the simulated stream in the precursor drying system. In the course of drying, a total

evaporation rate of 39.32 kg/h is achieved, and the moisture in the precursor decreases to 1.56%.

Table 3.8. Simulated stream parameters in the precursor drying system

Stream	AIR-IN	HOT-AIR	AIR-OUT	SOLID-IN	PRODUCT
Mass Flows (kg/h)	1200	1200	1239.31	370	330.68
Temperature (°C)	25	120	37.01	25	36.71
Pressure (atm)	1	1	1	1	1
Flow rates of compounds in streams (kg/h)					
WATER	0.15	0.15	39.46	44.4	5.08
AIR	1199.85	1199.85	1199.85	0	0
PRECURSOR	0	0	0	325.6	325.6

Upon consolidating the obtained data, it becomes evident that the most energy-intensive stage of Ms12 production is the thermal treatment of the initial materials. The conducted calculations indicate that it is beneficial to utilize the energy acquired during the cooling of process streams to elevate the temperature of the other cycle streams, thereby offsetting a portion of the production energy.

3.3. Influence of Water Vapour Pressure on the Stability of Calcium Monosulfoaluminate 12-hydrate in the Presence of Environment CO₂

As discussed in the literature review, calcium monosulfoaluminate hydrates are cementitious phases whose stability influences the durability of concrete structures. A review of the stability of calcium monosulfoaluminate hydrates under CO₂ conditions revealed that most studies were conducted on mortar samples, with only a few focusing on pure calcium monosulfoaluminate hydrates. Additionally, the effect of the relative humidity on the stability of Ms is still insufficiently reported. Therefore, the impact of the water vapour pressure (p/p_0) on calcium monosulfoaluminate 12-hydrate composition alterations in the presence of environment CO₂ was further investigated.

3.3.1. Characterization of the phase transitions

According to the literature [171], higher synthesis temperatures promote the formation of well-ordered crystal structures. Meanwhile, phases synthesized at lower temperatures may exhibit a significant number of structural defects. To obtain reliable structural (fundamental) data and avoid accidental changes in the structure, Ms12 synthesized from Sample S2 at 130 °C for 8 h was selected for the experiment. The obtained results described below are also presented in the publication¹.

The changes in the mass of the samples during the experiment at different water vapour pressures are presented in Fig. 3.15. It was determined that the mass of the

¹ RUBINAITE, Dovile, et al. Influence of water vapour pressure on the carbonation process of calcium monosulfoaluminate 12-hydrate. *Journal of Thermal Analysis and Calorimetry*, 2024, 1-12.

samples slightly decreases (~1%) under 0.355 water vapour pressure. At 0.565 p/p_0 , the sample mass remains relatively stable throughout the entire duration of the experiment. Meanwhile, samples stored at 0.756–1 p/p_0 demonstrate an increase in mass, from ~11% to ~48%, respectively. It should be emphasized that, in this case, the mass change of the samples might be induced by two factors: 1) carbonation (change in sequestered CO₂), and 2) environmental moisture (change in chemically bound or physically adsorbed water).

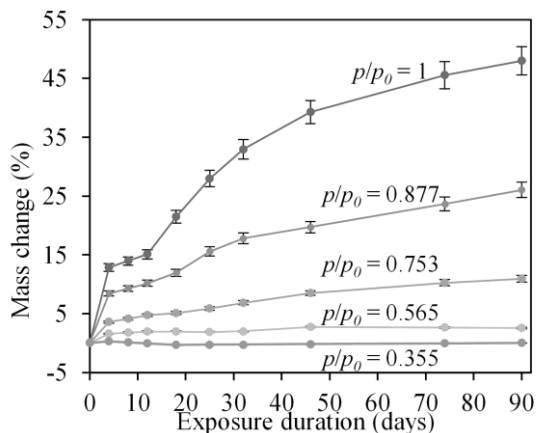


Fig. 3.15. Mass change of Sample S2 synthesized at 130 °C for 8 h, depending on the duration at different p/p_0 values (the error bars represent standard deviation)

In order to further assess the water vapour pressure effect on the carbonation of the synthetic Ms12, XRD and TGA were used to characterize the phase assemblage evolution in the samples. In the further description, the term ‘reference sample’ refers to the sample after the synthesis. Also, compared to the reference sample, the characteristic peaks of boehmite do not show any changes after 90 days at any given experimental p/p_0 conditions. Therefore, boehmite is no longer discussed in the description of the further experimental results. Additionally, it should be noted that the experimental CO₂ level is slightly higher (668±4 ppm) (due to poorer conditioning in the room) than the global/natural level (~417 ppm) registered. Thus, the observed carbonation reactions might be marginally accelerated compared to the outside conditions.

The XRD patterns of the reference samples exposed to different water vapour conditions are shown in Fig. 3.16. It can be seen that the samples exposed at the lowest water vapour pressure (0.355) demonstrate the lowest carbonation, and only minor changes in the phase assemblage are identified. Ms12 is still seen as the main crystalline phase in the sample throughout the duration of the experiment. The change is observed with the peak at $d = 0.820$ nm, which shifts to the $d = 0.823$ nm position, thus suggesting the presence of hemicarboaluminate (Hc) (Ca₄Al₂O₆(CO₃)_{0.5}(OH)·11.5H₂O, PDF No. 00–041–0221) in the sample. In addition, the difference is seen in the characteristic peak intensities of the presently mentioned

compounds. The intensity of the Ms12 peaks slowly decreases, and this material becomes less crystalline (as broader peaks are observed) with an increasing exposure duration. Moreover, the Ms12 peaks shift slightly towards higher angles, thus suggesting that, at 0.355 water vapour pressure, Ms12 becomes thermodynamically metastable and slowly disintegrates. The opposite trend is observed with Hc, whose peak intensity slightly increases after 4 days and remains unchanged throughout the remaining experiment duration. This suggests that Hc forms within the synthesis or drying process, while, at a low p/p_0 , Hc crystallinity or the crystal order likely increases, thus causing the above-mentioned peak rise. A minor increase in the intensity of the calcium carbonate (calcite) peaks is also observed in the XRD patterns.

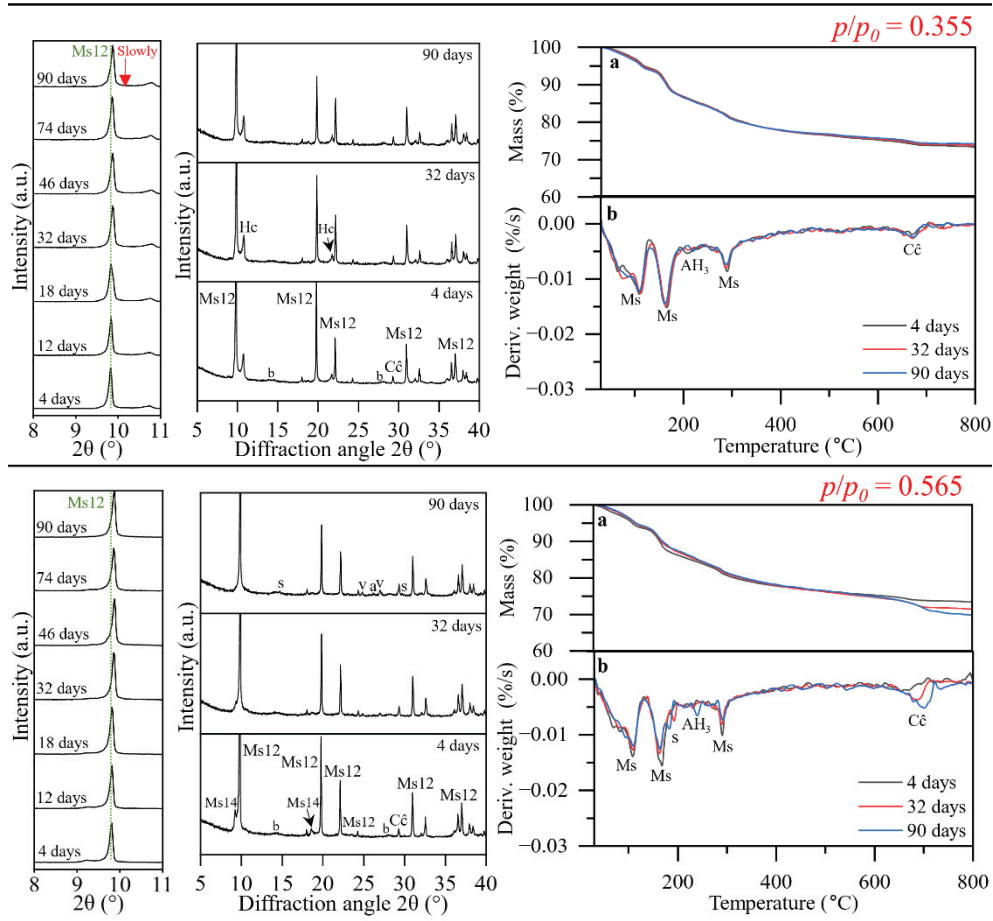


Fig. 3.16. XRD patterns (left) and TGA plots (right) (a – TG, b – DTG) of Sample S2 hydrothermally treated at 130 °C for 8 h exposed at different p/p_0 and durations. Indexes: Ms – monosulfoaluminate (the number shows the water content), Hc – hemicarboaluminate, Et – ettringite, b – boehmite, G – gibbsite, Cc – calcium carbonate, s – bassanite, a – aragonite, v – vaterite, g – gypsum

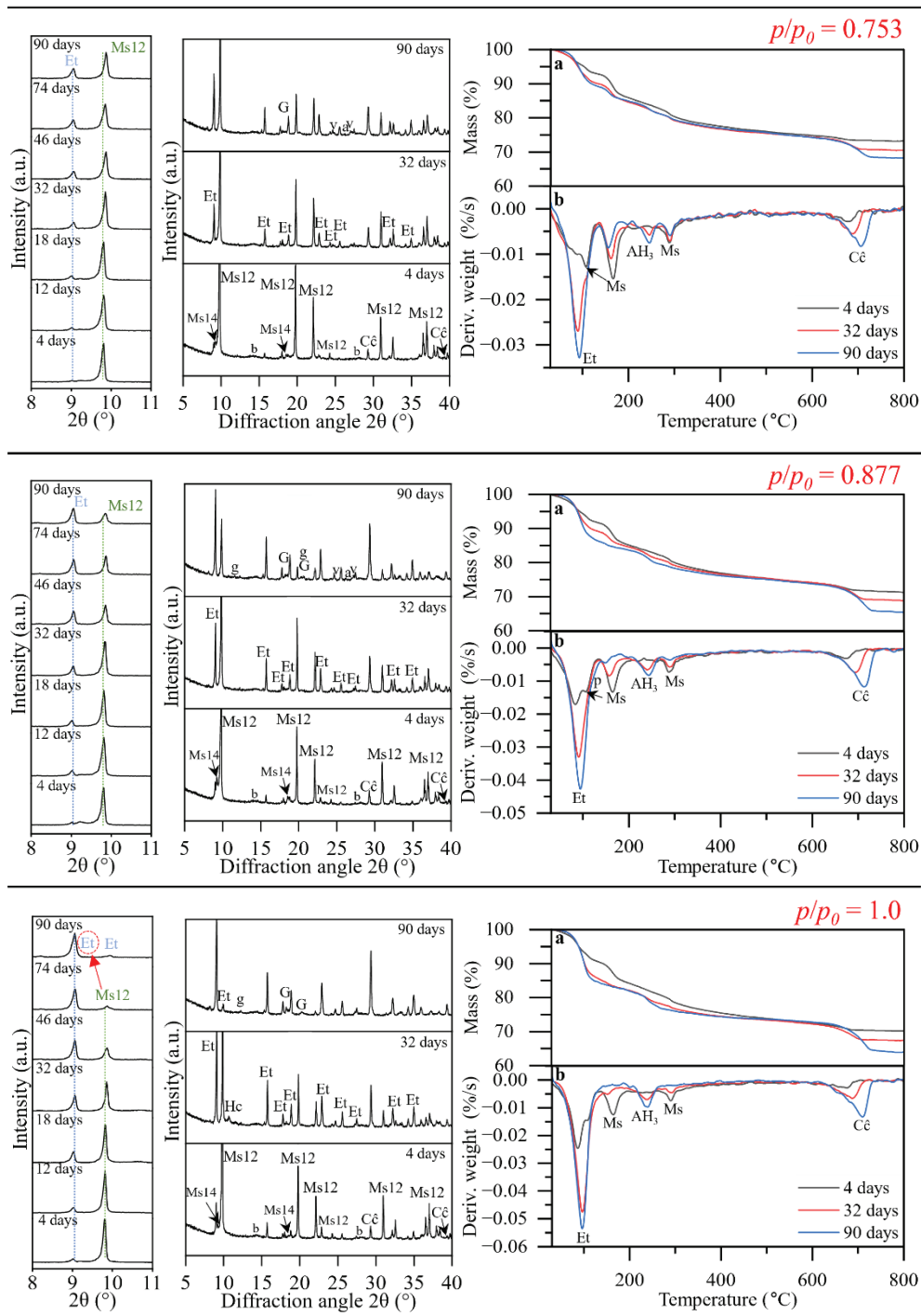


Fig. 3.16. (Continuation)

The thermogravimetric analysis demonstrated similar results, where no significant alterations were identified (Fig. 3.16). The main derivative peaks at 30–550 °C show a slight decrease, the same as the total mass with an increasing duration of the experiment (~2% reduction after 90 days), thus reflecting the partial dehydration of the sample. Additionally, observations within a temperature range of 550–800 °C demonstrate a slight increase (~0.2%) in the calcium carbonate content after 90 days compared with the reference sample. It should be noted that the observed carbonation is very slow; thus, the identified quantities of the carbonation products are low.

Under higher water pressure conditions (0.565), the samples demonstrated accelerated carbonation with similar Ms12 decomposition trends like under 0.355 conditions (Fig. 3.16). After exposing the samples to 0.565 p/p_0 conditions for 4 days, Ms12 was identified as the dominant phase, which it remained throughout the duration of the experiment. However, it is also observed that the decomposition rate increases, i.e., the intensity of the peaks corresponding to Ms12 decreases faster (~10%) compared to the sample stored at 0.355 p/p_0 . Meanwhile, the peak at $d = 0.820$ nm becomes unstable in the 0.565–0.877 p/p_0 range and is no longer detected in the XRD patterns (the presence of this peak under the presently mentioned conditions is not discussed in the further discussion of the results). Ms14 is determined as the intermediate phase at the given 0.565 p/p_0 value, and it is observed from 4 to 32 days. Additionally, traces of two more crystalline polymorphs of calcium carbonate (vaterite (PDF No. 04-017-8634) and aragonite (PDF No. 04-013-9616)) are detected after 4 days, whose intensity of the peaks slowly increases with the exposure duration. Also, the characteristic peaks of bassanite (calcium sulphate hemihydrate) are detected from 74 days onwards, which keep slowly increasing within the exposure time. The TGA data revealed complementary results (Fig. 3.16). The DTG curves show a slight reduction in the main peaks of monosulfoaluminate (30–400 °C) within the experimental duration, thus indicating the partial decomposition of Ms12. Meanwhile, the new peak at ~182 °C reflects the presence of hemihydrate, as also confirmed by the XRD patterns [172]. It is of importance to emphasize that the formation of hemihydrate is determined with a shorter duration of storage (after 18 days) by means of TGA than XRD analysis, which suggests that the earliest bassanite emerges as the amorphous state. The presence of the derivative peak at 240 °C shows the newly formed amorphous aluminium hydroxide, whose mass loss reaches ~2% after 90 days. Finally, the higher carbonation of the sample was also determined by TGA. It is worth highlighting that aragonite and vaterite recrystallize into calcite without any weight change at ~450 °C in the course of heating [145]. The total CO₂ binding capacity of the sample is recorded at 550–800 °C, which alters from ~2.6% to ~6.2% after 4 and 90 days, respectively. These results demonstrate that the increase in the water vapour pressure (0.565) promotes the interaction between monosulfoaluminate and ambient CO₂, yielding Ms12 decomposition into calcium carbonate, bassanite, and aluminium hydroxide.

For the samples exposed at 0.753 p/p_0 , the XRD patterns demonstrate a slightly different mineral assemblage evolution compared with the observations at 0.355–0.565 p/p_0 conditions (Fig. 3.16). It was determined that Ms12 becomes metastable and actively begins to recrystallize into ettringite, where the intensity of Ms12 peaks decreases by ~56% after 90 days compared with the reference sample. The intermediate phase Ms14 is also detected in the XRD pattern, but with a shorter duration of presence (up to 25 days). In contrast to the previously discussed conditions, the crystallization of gibbsite is identified after 46 days. Additionally, the rise in calcium carbonates is observed in the sample: the dominant calcium carbonate polymorph (calcite) intensity of peaks increases by ~2.5 times after 90 days compared with the reference sample. Meanwhile, the formation of vaterite and aragonite is detected after 12 days and 90 days, respectively. As expected, the TGA analysis confirms the XRD results. The first peak at ~93 °C corresponds to the water loss from the ettringite structure [173]. In addition, it was established that, in this region (30–150 °C), the content of bound water increases up to ~11.7% after 90 days. Meanwhile, the peak of Ms12 (at 150–200 °C) diminishes and moves to lower temperatures as less and less Ms12 is identified. The increment of the water loss at 240 °C (the total loss is ~2.6% after 90 days) also confirms the formation of aluminium hydroxide (gibbsite). Finally, the increase of the bound CO₂ content to ~7.2% after 90 days affirms that a rise in the p/p_0 conditions (0.753) also leads to a higher carbonation degree. It should be stressed that, for samples exposed at the water vapour pressure of 0.753 (or higher), neither TGA nor XRD analysis demonstrates the formation of bassanite. It might be the case that, under these conditions, the content of free water (released from carbonation, or present in vapour) is too high for bassanite to form, and the chemical reaction equilibrium shifts towards gypsum formation. However, the gypsum resulting from Ms12 carbonization could have been consumed in the formation of ettringite, and it was not detected by instrumental analysis.

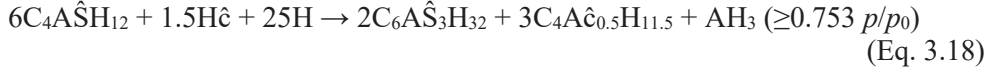
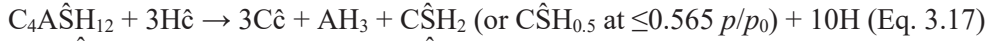
Similarly to samples exposed to the water vapour pressure of 0.753, both the conversion into ettringite and carbonation of Ms12 are observed at 0.877 p/p_0 (Fig. 3.16). It can be seen that the intensity of the Ms12 peaks decreases by ~81% after 90 days compared with the reference sample, thereby indicating that higher moisture conditions accelerate the disintegration rate. Meanwhile, the identified significant increase in the intensity of the calcite peaks (~4 times after 90 days) confirms that a higher p/p_0 environment also promotes carbonization. The detected minor crystalline phases cover gibbsite after 46 days, aragonite after 74 days, vaterite after 90 days, and the new carbonation product – gypsum – after 74 days. From the TGA curves, it can be observed that the peak displayed at 30–150 °C is even more intense at 0.877 p/p_0 in comparison to the previously discussed conditions. This confirms that a higher amount of ettringite developed throughout the experiment, i.e., that the mass loss reaches ~14.5% after 90 days. In addition, a slight broadening at ~120 °C can be ascribed to the water loss from the formed gypsum, which corresponds well with the XRD results [145,172]. The gradual decrease of the DTG peaks at 150–200 °C and 260–300 °C within the exposure duration reflects the reduction of the Ms12 content

in the sample. Under these experimental conditions, a higher amount of freshly formed aluminium hydroxide is also determined, with a mass loss of ~3.5% after 90 days. The data also clearly demonstrates that raising the p/p_0 value to 0.877 promotes the CO₂ uptake from the environment, which results in the sequestered CO₂ increase in the sample to 9.3% after 90 days.

The experiment demonstrates that, at saturated water vapour conditions (1.0 p/p_0), 90 days is sufficient for Ms12 to decompose entirely (Fig. 3.16). Meanwhile, ettringite is identified as the dominant crystalline phase in the sample. In comparison to 0.877 p/p_0 conditions, the sample exhibited a slightly higher intensity of the peaks of gibbsite and calcite. Additionally, other polymorphs of calcium carbonate were not observed in the XRD patterns throughout the experiment. This agrees with other experimental works claiming that the optimal conditions to form vaterite and aragonite are at moderate relative humidity environments [174]. Moreover, the XRD data revealed the appearance of intermediate phases: Ms14 (between 4–8 days), and Hc (between 12–46 days). The XRD results are adequately consistent with these sourced from the TGA data. It was determined that the thermal effect of ettringite shifts to a higher temperature (101 °C) and is more potent than at 0.877 p/p_0 , i.e., the mass loss reaches ~16.6% after 90 days. This confirms that a higher water vapour pressure promotes rearrangements of the atoms of Ms12, thus generating the recrystallization into ettringite. At the same time, the thermal effects at 169 °C and 288 °C corresponding to water removal from Ms12 gradually diminish and disappear entirely after 90 days. The water weight loss at 240 °C, reflecting the dehydration of AH₃, also shows an increase (in total, of ~3.8%). Meanwhile, the weight loss registered at the calcium carbonate decomposition region is the highest (~9.7% after 90 days) compared to the previously investigated samples.

The presented results demonstrate that the water vapour pressure is the controlling factor of the Ms12 carbonation rate, and it determines the pathways by which Ms12 decompose, i.e., the formation of the carbonation products. These results correspond well with the previous studies [124]. The present study confirms that the final carbonation products of Ms12 are calcium carbonate, aluminium hydroxide, and gypsum under higher-saturated water vapour conditions (above 0.565), or hemihydrate under lower-saturated ones (Eq. 3.17). Regardless of the p/p_0 conditions, calcite is the dominating polymorph of calcium carbonate in the samples. Meanwhile, aragonite and vaterite are formed within the 0.355–0.877 p/p_0 range, where a lower p/p_0 environment promotes the formation of vaterite, whereas a higher p/p_0 environment promotes the formation of aragonite. At a sufficient moisture level ($\geq 0.753 p/p_0$), Ms12 also recrystallizes to ettringite, where the conversion is favoured with the higher p/p_0 values (Eqs. 3.18–3.19). Additionally, hemicarboaluminate and Ms14 are identified as intermediate products of the reaction in this work. Hemicarboaluminate forms only at 1.0 p/p_0 , presumably due to Ms12 partially interacting with C \hat{c} formed during the carbonation. Ms14 is observed within the 0.565–1.0 p/p_0 range, where the duration of its presence decreases with the increasing

p/p_0 conditions. This suggests that the carbonation behaviour of Ms12 and the formation of the intermediate products strongly rely on the reaction kinetics.



3.3.2. Carbonation mechanism

The apparent kinetic parameter calculations were applied to verify the experimental data and the theoretical hypothesis. Firstly, the carbonation efficiency of the samples under different p/p_0 conditions was evaluated by calculating the carbonation degree (α) of CaO in the samples. As it is seen in the above presented results, 0.355 p/p_0 conditions lead to only a small carbonation degree of the sample. Therefore, the apparent kinetic parameter calculations were not considered for this sample. Meanwhile, the higher p/p_0 value promotes the dissolution of gaseous CO₂ and the interaction with Ca²⁺ from the sample. Thus, the carbonation degree growth from ~25.17% at 0.565 p/p_0 to ~46.60% at 1.0 p/p_0 after 90 days is observed (Fig. 3.17). However, there are authors [175,176] who pointed out that, when exceeding the optimal moisture conditions (50–80%, or 0.5–0.8 p/p_0), carbonation no longer increases because of the water saturation in pores and/or lack of cement particles for the carbonation reactions. In this work, a powder sample was used, which represented a less compacted structure (of a high porosity) than concrete samples with high internal filling. Therefore, it is considered that, in this case, the mass transfer of CO₂ and water vapour disobeys the conventional diffusion-controlled phenomenon. The influence of the microstructure and the pore size on the carbonation rate was also observed in other studies [177,178].

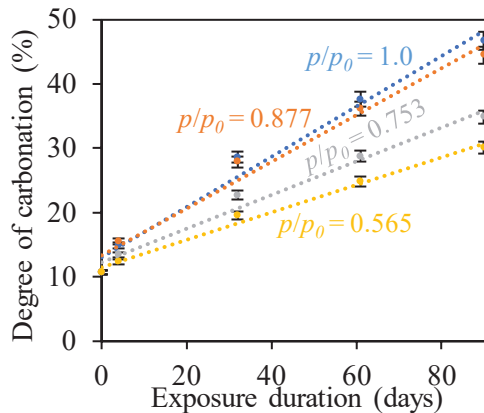


Fig. 3.17. Relationship of the carbonation degree of CaO in the samples and the exposure duration at different p/p_0 values. The dashed line – the linear trendline (the error bars represent standard deviation)

In order to assess the powder sample carbonation process mechanism, kinetic analysis was performed by applying the model-fitting approach. Order-based models (see Eq. 2.12) are the simplest, as they express the reaction rate as the concentration changes over time [152]. As it is seen in Figure 3.17 and Table 3.9, the coefficient of determination R^2 demonstrates a good linear correlation between the carbonation degree and time. Based on this, it could be suggested that the carbonation reactions of the samples seem to follow the apparent pseudo-zero-order kinetics model. This model indicates that the reaction rate apparently is independent of the reactant concentration, and the apparent reaction rate (k) is governed by external factors, i.e., in this case, p/p_0 conditions. It should be noted that this assumption is valid until the reactants are depleted, or other reactions become more prominent.

Table 3.9. Apparent kinetic reaction constants of carbonated CaO during the carbonation of samples at different p/p_0 conditions calculated by with different kinetic models

Water vapour pressure	0.565	0.753	0.877	1.0
Zero-order model				
k	0.0954	0.1197	0.1654	0.1779
n	0	0	0	0
R²	0.992	0.971	0.960	0.961
Jander model				
k	0.00566	0.00942	0.0166	0.0147
n_J	0.599	0.535	0.497	0.524
R²	0.918	0.931	0.945	0.918
Avrami model				
k	0.00741	0.0136	0.0253	0.0189
n_A	0.818	0.729	0.682	0.768
R²	0.995	0.995	0.996	0.999

The carbonation reaction mechanism was classified by using the Jander model. It is observed that the model fits relatively well, with the coefficient of determination R^2 ranging from 0.918 to 0.945 (Fig. 3.18.a and Table 3.9.). The apparent reaction rate (k_J) increases within a higher p/p_0 environment up to 0.877 p/p_0 , where a slight decrease (11.5 %) is observed at a given 1.0 p/p_0 . Meanwhile, the value of n_J attains a maximum at 0.565 p/p_0 and gradually declines until conditions of 0.877 p/p_0 are reached. The exception is observed again under the 1.0 p/p_0 conditions, where the n_A value slightly increases. The deviation in both k_J and n_J values indicates changes in the carbonation mechanism of the sample under 1.0 p/p_0 conditions. Based on the XRD and TGA results, the reason for this observation might be that, under the lower p/p_0 experimental conditions, only monosulfoaluminate (or/and a little ettringite) undergo(es) carbonation. Meanwhile, when monosulfoaluminate is depleted, or a little of it is left in the system (at 1.0 p/p_0), the carbonation reactions of ettringite become more prominent, leading to changes in the carbonation mechanism. Nevertheless, the

samples exposed to experimental water vapour conditions demonstrate the n_j values of less than 1. This suggests that dissolution and nucleation processes control the kinetics of sample carbonation.

In order to preliminarily describe the nature of the nucleation and crystal growth process of CaCO_3 , the Avrami model equation was applied. It has to be taken into consideration that this model assumes nuclei grow without area restrictions, which means that growth is not hindered by impingement [157]. Compared with the previous kinetic models, the Avrami equation demonstrates the best reliability ($R^2 = 0.99$) (Fig. 3.18.b and Table 3.9). The calculated apparent reaction rate (k_A) and the apparent constant (n_A) values by the Avrami equation exhibit a similar trend as when applying the Jander model, where the same assumption can be used to explain the deviation. Additionally, the decreasing value of n_A in the range of 0.565–877 p/p_0 confirms that an increasing amount of environmental moisture accelerates the completion of the nucleation stage. Meanwhile, the obtained n_A value under all conditions is less than 1, which indicates that CaCO_3 crystal formation is controlled by one-dimensional growth. The low values of n_A (<1) were also observed by other authors, explaining that the nucleation occurring in the system is an instantaneous and transient process [156].

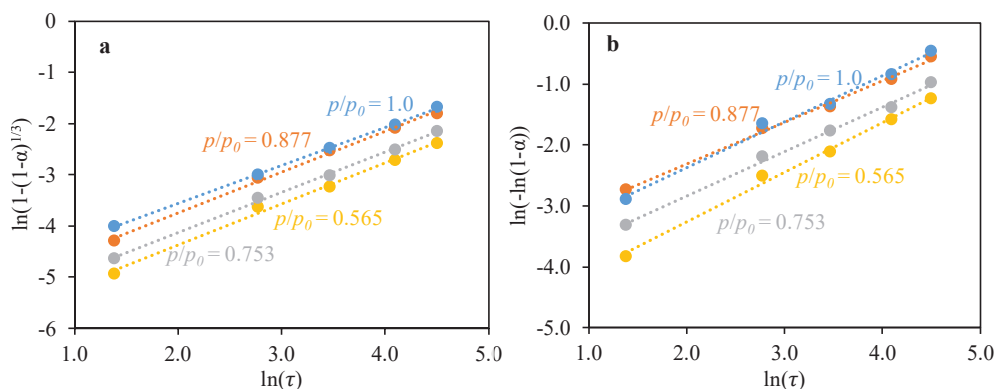


Fig. 3.18. Plots of the Jander model (a) and the Avrami model (b) applied for the carbonated CaO during the carbonation of samples under different p/p_0 conditions

It is of importance to note that only the carbonation degree of CaO in the samples was used in this study to determine the nature of the carbonation kinetics of the samples. Thus, the calculated apparent kinetics and the mechanisms of the reactions only preliminarily describe the carbonation processes in the samples. First of all, it has to be comprehended that carbonation reactions take place in a multiphase and polydisperse system. Secondly, carbonization itself is a very complex multi-step process, i.e., it covers aspects like gas dissolution, pore saturation, nucleation, etc. Thirdly, the environment of the reactants changes throughout the course of the carbonation reactions. Lastly, the crystal parameters, such as the crystal structure, size, the grain boundaries, their shape, etc., highly influence the reaction kinetics.

3.4. Investigation of the Thermal Transition Mechanism from Calcium Monosulfoaluminate 12-hydrate to Ye'elimite

The thermal stability of calcium monosulfoaluminate hydrates has already been examined by several authors [116–118]. Nevertheless, unresolved questions persist regarding the decomposition of monosulfoaluminate, precisely, the beginning and end temperatures of the different hydration states of calcium monosulfoaluminate hydrates and the stability of the transitional phase. *In-situ* X-ray analysis is a powerful tool which enables real-time observations of phase transitions and helps reveal the reaction mechanisms. Additionally, this method also allows for the detection of intermediate phases in reactions or high-temperature phases which recrystallize to low-temperature phases during cooling. Therefore, firstly, the phase changes associated with the thermal decomposition of the hydrothermally synthesized precursor (Sample S2 at 110 °C for 8 h) were investigated by using *in-situ* XRD analysis. Furthermore, there is a scarcity of literature addressing the formation of ye'elimite through the hydrothermal-calcination method. Therefore, the effect of the sintering conditions (i.e., the temperature and duration) on the formation of ye'elimite was evaluated by *ex-situ* XRD analysis.

3.4.1. Investigation by in-situ X-ray diffraction method at 25–1250 °C

The *in-situ* X-ray diffraction method and simultaneous thermal analysis were employed to determine phase transitions in the course of the heating of the precursor. The *in-situ* XRD experiments were performed within the temperature range of 25–1250 °C, with a heating rate of 50 °C/min; the data was recorded after equilibration of 2 min at the desired temperature. It is worth noting that the XRD patterns were registered at the process temperature. Therefore, the thermally-induced shifts are visible for the positions of the peaks in the XRD patterns.

Two main temperature intervals can be distinguished based on the obtained results (Fig. 3.19). The first one (the phase decomposition interval) is seen within the temperature range of 25–800 °C, which is associated with dehydration and decarbonization. Immediately after incrementing the temperature, the intensity of the peaks corresponding to Ms12 (with the main peak at $d = 0.893$ nm) begins to decrease, thus reflecting Ms12 dehydration. Meanwhile, Ms12 completely dehydrates at ~90 °C. At the same time, the formation of additional Ms10.5 ($d = 0.814$ nm) at ~50 °C is observed, which is generated by the dehydration of Ms12. The increase in the intensity of Ms10.5 peaks is seen up to ~80 °C. Meanwhile, a further temperature increase adversely affects the stability of Ms10.5, causing a gradual decrease in the intensity of peaks that are no longer visible at 220 °C. Similarly, the formation of a lower hydration state is observed at 90 °C, corresponding to Ms9 ($d = 0.796$ nm). The highest intensities of its peaks are seen at ~140 °C, while its peaks remain visible even up to ~370 °C. These results indicate that the dehydration of Ms10.5 presumably begins at ~80 °C, causing the formation of Ms9. In the same way, the dehydration of Ms9 presumably begins at around ~140 °C, yielding the appearance of the lower hydration states of monosulfoaluminate. As a result, a broad low-intensity diffraction peak at d

– 0.617 nm is observed at 170–330 °C. Unfortunately, based on the *PDF-4* database, the detected peak could not be determined. Nevertheless, this peak might indicate the transitional Ms6-x phase (where x refers to water molecules; the value of x may attain values from 0 to 6); most likely, it is Ms6, which may be of an amorphous/low crystallinity nature. However, a high amount of the formed compound and/or elevated ambient temperatures might have contributed to the peak detection. Additionally, the temperature (~200 °C) at which the peak’s intensity begins to decrease might show the beginning of the water elimination out of Ms main (octahedral) layers.

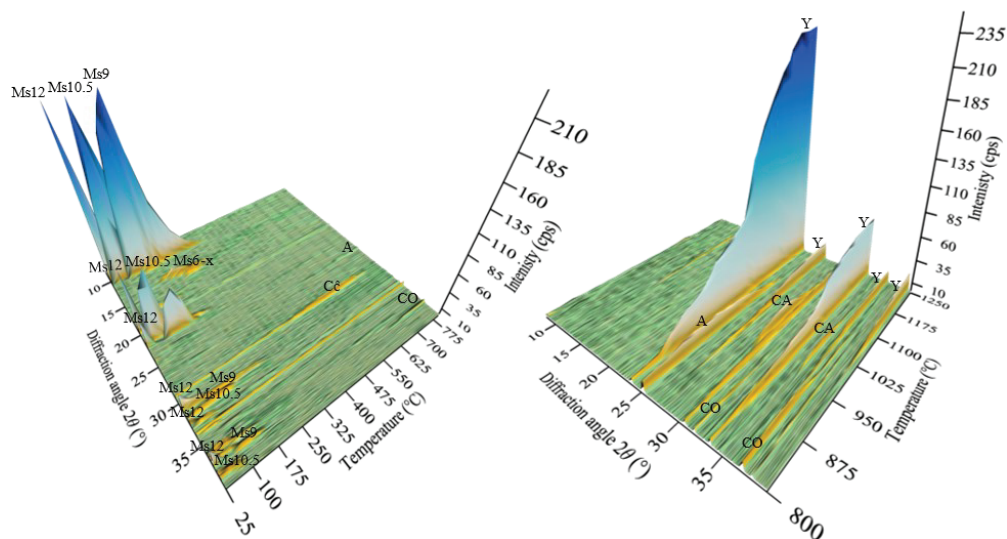


Fig. 3.19. *In-situ* XRD patterns of the precursor with the calcination temperature varying within 25–1250 °C range. Indexes: Ms – calcium monosulfoaluminate (the number shows the water content), Cê – calcium carbonate, CO – calcium oxide, A – anhydrite, CA – calcium aluminate, Y – ye’elimitite

It is of importance to emphasize that the Ms10.5 and Ms9 crystal structures are still not characterized (there is no relevant data in the *PDF-4* database), and only the main peak positions of these monosulfoaluminate states were presented in the previous studies [107,112]. Therefore, in this work, the unclear Ms positions were assigned based on the thermal stability of the main phase peak. For instance, the main Ms10.5 peak is detected at 50 °C, and it remains visible up to 220 °C. According to this tendency, the appearing peaks which maintained their presence within this temperature interval were assigned to this hydrate state. The identified thermal stability of the monosulfoaluminate states and the assigned peak positions are summarized in Table 3.10.

Table 3.10. Thermal stability of different hydration states of calcium monosulfoaluminate

Phase	Stable in the temperature interval	Interplanar distance (this work), nm
C ₄ A \hat{S} H ₁₂	25 °C < T < 90 °C	0.893; 0.490; 0.447; 0.399; 0.365; 0.288; 0.278; 0.274; 0.245; 0.241; 0.236; 0.233
C ₄ A \hat{S} H _{10.5}	50 °C < T < 220 °C	0.816; 0.481; 0.471; 0.408; 0.375; 0.357; 0.287; 0.279; 0.271; 0.243; 0.234
C ₄ A \hat{S} H ₉	90 °C < T < 370 °C	0.798; 0.492; 0.433; 0.398; 0.286; 0.280; 0.257; 0.248; 0.240
C ₄ A \hat{S} H _{6-x}	170 °C < T < 330 °C	0.616

Further investigation demonstrated that no phase changes are observed between ~380 °C and ~700 °C (Fig. 19). Meanwhile, at the end of the phase decomposition interval (at ~720 °C), the decarbonation of calcium carbonate is seen, which lasts up to ~800 °C. Accordingly, the peaks of calcium oxide arise ($d = 0.278$ nm) (CaCO₃ → CaO + CO₂), whose maximum intensities are seen at 940 °C. At the same time, above ~700 °C, the peaks of anhydrite (CaSO₄) ($d = 0.349$ nm) are detected, thus indicating the beginning of the crystalline phase formation interval (700–1250 °C). These observations demonstrate that the first and the second temperature intervals slightly overlap. Additionally, the appearance of anhydrite may mainly be attributed to the decomposition of calcium monosulfoaluminate hydrates, as shown in Equation 3.20.



As the heating temperature rises to ~860 °C, the diffraction peaks attributed to ye'elimite (Ca₄Al₆O₁₂SO₄, PDF No. 00-033-0256) ($d = 0.375$ nm) begin to appear, which gradually increase with the increasing heating temperature (up to 1250 °C). Simultaneously, peaks corresponding to the calcium aluminate phase (CA; CaAl₂O₄, PDF No. 04-014-8445) ($d = 0.297$ nm) begin to appear at ~940 °C (Eq. 3.21). However, with the temperature rise up to ~1100 °C, the diffraction maximums of C \hat{S} , CA and C strongly attenuate, while those of ye'elimite are generated. This indicates that the above-mentioned phases are consumed for the formation of ye'elimite through the solid-state reactions (Eqs. 3.22, 3.23), and an increase in temperature promotes the interaction of the phases. It was observed that the critical temperature values for CaSO₄ and CA are 1160 °C and 1200 °C, respectively. When exceeding these temperatures, the previously mentioned phases are no longer recorded in the XRD patterns. In the highest thermal treatment temperature (1250 °C), ye'elimite is observed as the dominating crystalline phase. Additionally, small intensity peaks attributed to C also remain visible, thereby showing incomplete solid-state reactions.

In order to obtain more information about calcium monosulfoaluminate 12-hydrate decomposition, simultaneous thermal analysis was performed. It is worth

noting that, for this investigation, a slower heating rate of 5 min/°C was applied in order to better distinguish the thermal transitions. The thermal phase transitions which occurred during the sample heating are presented in Fig. 3.20.

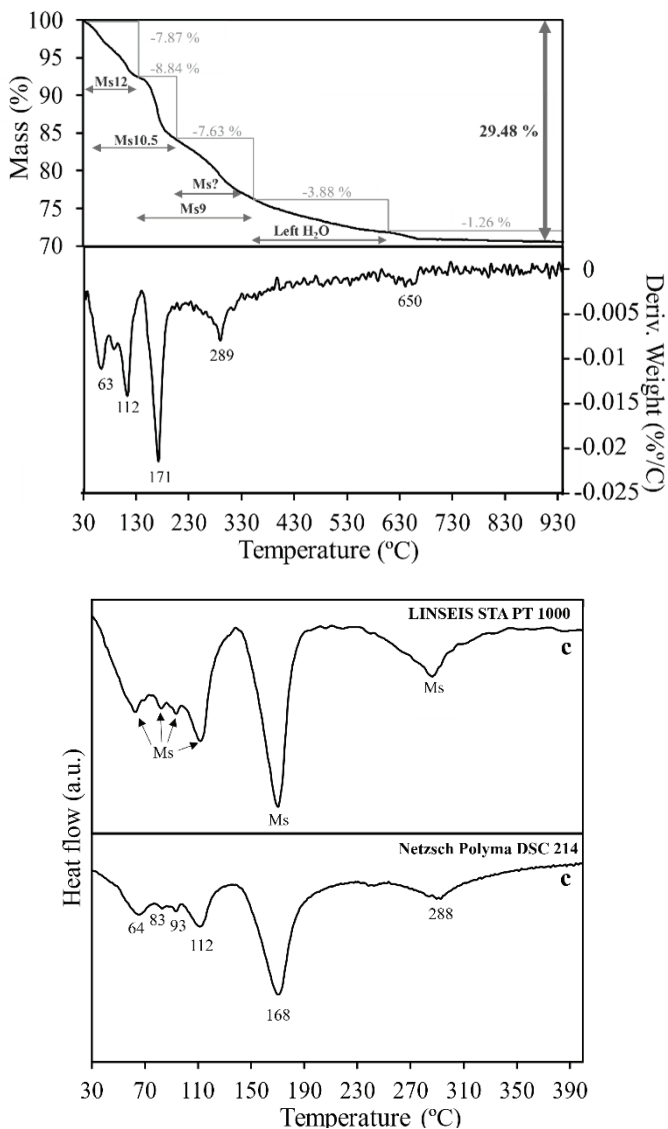


Fig. 3.20. TG (a), DTG (b) and DSC (c) curves of the precursor

According to the obtained TG/DTG/DSC results, the thermal decomposition of the sample can be divided into 5 mass loss regions. The first region of the DSC curve reflects 4 endothermic peaks (at ~64 °C, ~82 °C, ~95 °C, and ~112 °C), representing several chemical reactions which gradually took place. In comparison, only 3

incidents of effects are seen in the DTG curve. By striving to ensure that the observed fourth peak in the curve is not an equipment noise, DSC measurements were carried out with another device (*Netzsch Polyma DSC 214*). Both devices confirmed the presence of a peak at $\sim 95\text{ }^{\circ}\text{C}$ in the DSC curves, which might reflect the crystal structure changes of calcium monosulfoaluminate hydrate since it is not observed in the DTG case. However, further research is needed to confirm it. Nevertheless, these effects can be assigned to the removal of adsorption water, the dehydration of the amorphous compound structure, and the release of the unbonded and loosely bonded water molecules in the interlayer of the calcium monosulfoaluminate hydrate structure. This observation corresponds well with the results of XRD *in-situ* analysis, which demonstrated the overlapping dehydration mechanism of different hydrate states of calcium monosulfoaluminate ($\text{Ms}_{12}\rightarrow\text{Ms}_{10.5}\rightarrow\text{Ms}_9$) within this temperature interval.

The second temperature region is denoted by the highest mass loss ($140\text{--}220\text{ }^{\circ}\text{C}$), and the effect at $168\text{ }^{\circ}\text{C}$ corresponds to the continuation of the dehydration of the interlayer water (mainly, the transition of $\text{Ms}_{10.5}\rightarrow\text{Ms}_9$). Based on the XRD insights, it might be argued that the dehydration of the main layers begins at the end of this temperature range. Meanwhile, the dehydration behaviour between $220\text{ }^{\circ}\text{C}$ and $370\text{ }^{\circ}\text{C}$ reflects not only the water loss from the main layers but also the remaining water loss out of the interlayers, i.e., dehydration of Ms_9 and lower states. In the fourth region ($370\text{--}600\text{ }^{\circ}\text{C}$), neither DSC nor DTG reflects any thermal transition. However, a gradual mass loss increase in the TG curve indicates the dehydration of the remaining crystal water out of the Ms main layers. In the final region, the thermal shoulder ($\sim 650\text{ }^{\circ}\text{C}$) corresponds to the decomposition of calcium carbonate.

The data of the current study complements the missing gaps in the thermal deterioration reaction sequences of calcium monosulfoaluminate hydrates and the conversion into ye'elimite. The ranges of the intermediate phases developing in the thermal heating process at $25\text{--}1250\text{ }^{\circ}\text{C}$ are summarized and presented in Fig. 3.21. As it is evident from the experimental data presented above, the dehydration of calcium monosulfoaluminate 12-hydrate occurs in a wide temperature range. The complexity of its structure (the presence of different amounts of water in the interlayers) causes the dehydration of four different hydration states of Ms ($25\text{--}370\text{ }^{\circ}\text{C}$), which was observed by the *in-situ* X-ray diffraction. Additionally, the dehydration processes of different hydrate states of calcium monosulfoaluminate do not take place sequentially (stepwise); instead, they were found to overlap. Accordingly, these results were also confirmed by simultaneous thermal analysis: 1) the loss of mass is controlled by the removal of water from the interlayer structure, and it occurs in several steps, while 2) the observed water loss in TG has poorly defined steps, which indicates the overlaps. Furthermore, this dehydration process distorted and disintegrated the crystalline structure of calcium monosulfoaluminate hydrates, thus inducing the amorphization of the dehydration products. Therefore, this limits the application of X-ray diffraction in distinguishing the beginning and end temperatures of the dehydration of the main layers of Ms.

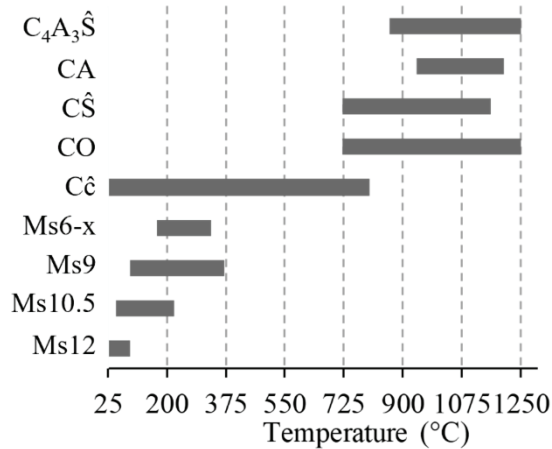


Fig. 3.21. Ranges of crystalline phases developing in the heating process of the precursor detected by *in-situ* X-ray diffraction. Indexes: Ms – calcium monosulfoaluminate hydrate (the number shows the water content), Cc – calcium carbonate, CO – calcium oxide, A – anhydrite, CA – calcium aluminate, Y – ye'elimite

It should also be considered that the obtained results show the influence of the drying conditions on the cement hydration products (Ms) at elevated temperatures. For instance, 50 °C can condition partial dehydration and shrinkage of Ms (Ms12→Ms10.5; a decrease ~9% in volume) [107]. In the long term, this can be a reason for concrete structures to deteriorate, and their durability would be adversely affected. Additionally, the temperature is essential for applying the drying techniques for the sample preparation before characterizing the hydrated cement paste. An incorrectly chosen drying temperature can lead to the formation of different hydration states of calcium monosulfoaluminate. Therefore, temperature and humidity must always be considered for adequate and comparable results. Finally, it is of importance to underline that the identified stability ranges for different phases can be influenced and slightly altered by numerous changeable factors. Namely, the grain size, the degree of the raw meal homogenization, the presence of impurities, the choice of the experimental methods, etc. can affect the obtained results. Therefore, it should be considered that the presented decomposition of monosulfoaluminate results might slightly differ under the conditions of real-life cementitious systems.

3.4.2. Investigation by *ex-situ* X-ray diffraction method at 750–1250 °C

The application of solid-state synthesis requires the main attention being devoted to the kinetic parameters, such as the calcination temperature and duration since these have the most decisive influence on the C₄A₃S formation. Considering the XRD *in-situ* results that ye'elimite is identified only from 860 °C, the sintering of the precursor (an *ex-situ* method) was performed at 750–1250 °C, with the steps of 50 °C, and a heating rate of 10 °C/min. The dependence of the *loss on ignition* (LOI) on the

calcination temperature maintained for 1 h when using powder samples is presented in Fig. 3.22. It can be seen that LOI increases steadily up to 950 °C (~28.3%) and remains relatively constant up to 1250 °C. Meanwhile, higher calcination temperatures stimulate additional slow solid-phase reactions, resulting in a slight increase in LOI within the error limits.

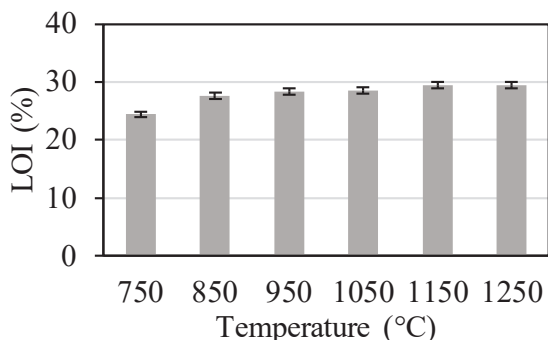


Fig. 3.22. Dependence of LOI on the calcination temperature maintained for 1 h

As expected, the qualitative phase analysis results of the calcined precursor samples demonstrate similar trends as those observed when using *in-situ* X-ray diffraction analysis (Fig. 3.23). It is observed that the characteristic peaks of ye'elimitite appear at 850 °C and increase throughout the sintering temperature range. The most significant increase in ye'elimitite occurs in the temperature range of 950–1100 °C, which is initiated by solid-state reactions involving interaction between $C\hat{S}$, C, CA, and $C_{12}A_7$ ($Ca_{12}Al_{14}O_{33}$, PDF No. 04-015-0818). Above 1100 °C, aluminate phases (CA, $C_{12}A_7$) are fully consumed and are no longer detected in the XRD patterns. Meanwhile, the traces of anhydrite and calcium oxide remain visible in the XRD pattern at the calcination temperature of 1250 °C.

It is worth noting that crystalline Al_2O_3 is not identified in the samples throughout the entire sintering temperature range. It is possible that most of the amorphous aluminium oxide directly contributes to the formation of $C_4A_3\hat{S}$, CA, and $C_{12}A_7$, and, at higher temperatures, the remaining aluminium oxide residues are below the detection level of the equipment, or they overlap with the ye'elimitite peaks. In contrast to *in-situ* XRD analysis, the samples demonstrate the formation of an additional aluminate phase ($C_{12}A_7$) at 850–1050 °C, which might be attributed to the use of larger sample sizes. Generally, a larger amount of the reactant (in terms of volume) leads to a slower heat diffusion and requires more time for the reactants to reach the required formation energy, thereby causing the formation of intermediate phases. The possible formation of mayenite can be described by Equations 3.24 and 3.25.



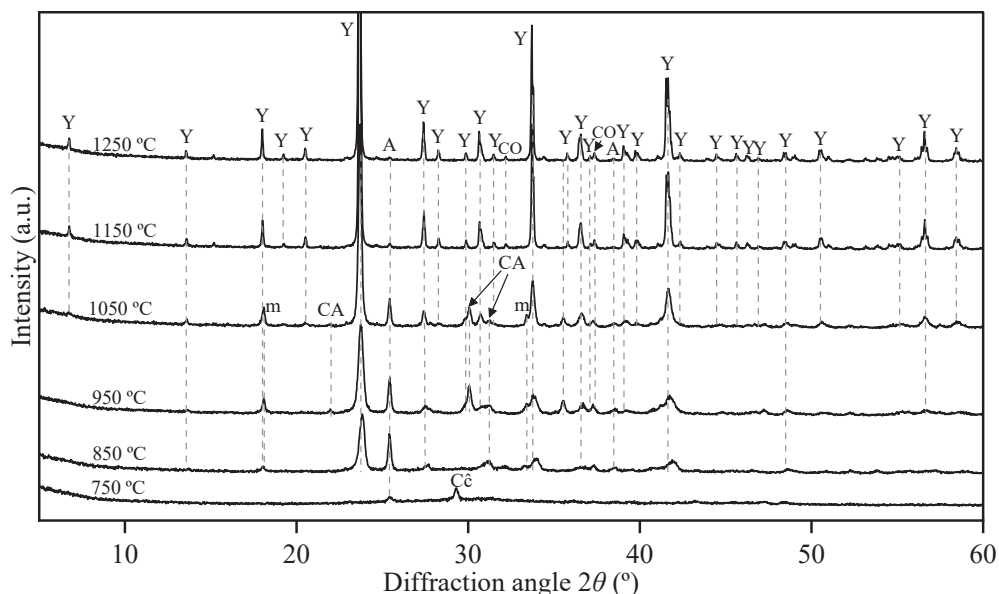


Fig. 3.23. XRD patterns of precursor sintered at different temperatures for 1 h. Indexes: Y – ye'elimeite, m – mayenite, A – anhydrite, CA – calcium aluminate, co – calcium oxide

In order to evaluate the purity of the synthesized ye'elimeite in the samples, a quantitative phase (Rietveld) analysis was performed. The purity of the synthesized ye'elimeite samples from the precursor samples calcinated from 950 °C to 1250 °C for 1 h and *R_w* values, which demonstrate the quality of the analysis fitting, are presented in Table 3.11.

Table 3.11. Quantitative phase analysis of the precursor samples calcinated from 950 °C to 1250 °C for 1 h

Synthesis temperature, °C	Crystalline phases, wt %						<i>R_w</i>
	C ₄ A ₃ S̄	CA	C̄S	C ₁₂ A ₇	CaO	Amorp.	
950	48.48	19.81	11.56	6.15	0.78	13.22	10.27
1000	56.91	19.24	10.01	1.42	0.52	11.9	10.92
1050	75.02	10.28	7.32	0.89	0.46	6.03	10.77
1100	95.73	–	1.69	–	0.63	1.95	11.35
1150	97.73	–	0.17	–	0.31	1.8	12.08
1200	98.76	–	0.13	–	0.89	0.22	11.67
1250	97.56	–	0.12	–	0.42	1.9	12.19

The results indicate that the highest purity of synthetic ye'elimeite is attained through sintering precursor samples within the temperature range of 1100–1250 °C. This temperature range yields approximately 95–98% ye'elimeite content in the resulting samples. Additionally, a slight decrease in the ye'elimeite content at 1250 °C suggests that ye'elimeite underwent a partial decomposition at this temperature. It is

worth specifying that ye'elimite was only determined in the orthorhombic crystalline structure.

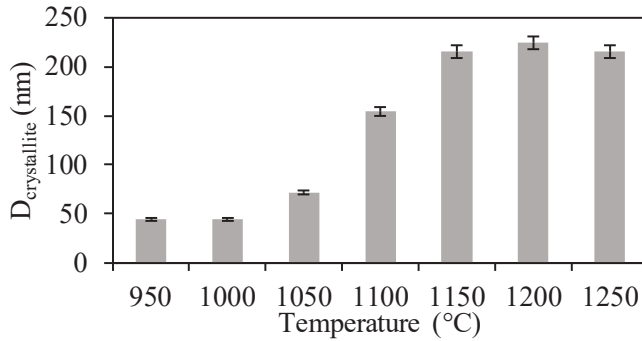


Fig. 3.24. Effect of the calcination temperature (dwell for 1 h) on the crystallite size of the synthesized ye'elimite (the error bars represent standard deviation)

The temperature effect on the crystallite size of synthetic ye'elimite was estimated by applying the Scherrer equation (Eq. 2.3). As it can be observed in Fig. 3.24, the crystallite size of synthetic ye'elimite increases with the sintering temperature. At 1150 °C, 1200 °C and 1250 °C temperatures, at which the highest amount of pure ye'elimite is obtained, the average crystallite sizes are 216.5 nm, 224.75 nm, and 214.5 nm, respectively. The obtained results demonstrate that elevated temperatures (up to 1200 °C) promote the formation of a well-ordered ye'elimite crystal structure.

Referring to a lower energy consumption for the production and quantitative phase analysis results, the high-purity ye'elimite (~98%) can be synthesized at 1150 °C. Therefore, the influence of the sintering duration on the formation of ye'elimite was investigated at this temperature. Figure 3.25.a depicts the XRD patterns of the precursor samples sintered for various dwell durations (0–180 min), when the heating rate was 10 °C/min. Only by raising the sintering temperature to 1150 °C (while maintaining at an elevated temperature for 0 min), ye'elimite as the main crystalline phase, along with calcium oxide and anhydrite, are identified in the sample. It is worth highlighting that traces of CA might be present in the samples with the sintering durations of 0–15 min. By increasing the dwell durations from 0 to 60 min, the intensity of the diffraction peaks of C and CŜ remains relatively stable, and, with further prolonged durations (>60 min), the intensity begins to attenuate slowly. However, even after calcination under the specified conditions of 1150 °C for 180 min, it is still observed that C and CŜ did not fully react, as evidenced by the presence of these compounds in the XRD patterns. Meanwhile, when extending the calcination duration (from 60 min to 180 min), we achieve an increase in the intensity of the ye'elimite peaks within the error limits.

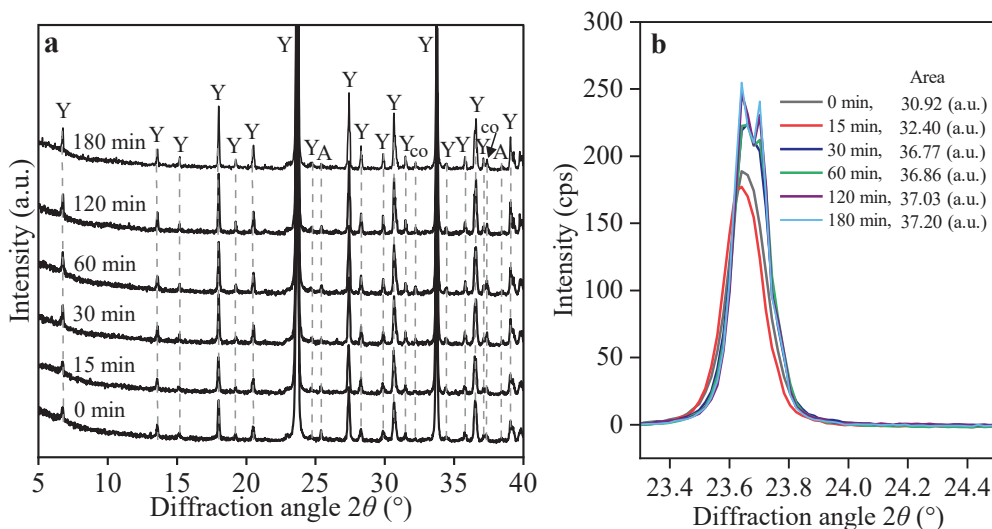


Fig. 3.25. XRD patterns of the precursor calcinated for varying durations at 1150 °C (a), and the change in the main diffraction peak of ye'elinite ($d = 0.375$ nm) depending on the duration of calcination (b). Indexes: Y – ye'elinite, A – anhydrite, co – calcium oxide

In order to better evaluate the calcination duration effect on the formation of ye'elinite, the change in the main diffraction peak ($d = 0.375$ nm) was investigated. As it is seen in Figure 3.25.b, three apparent changes in the intensity of the peaks and areas can be identified, i.e., within 0–15 min, 30–60 min, and 120–180 min. The most significant change in the peak area is observed when prolonging the dwell from 0 to 30 min, i.e., an increase of ~16% is achieved. This alteration is likely primarily associated with the solid-state reactions leading to the formation of ye'elinite. Meanwhile, with a further duration growth from 60 min to 180 min, the main diffraction peak area of ye'elinite increases by less than 1%. It is worth emphasizing that the main diffraction peak ($d = 0.375$ nm) of ye'elinite is characterized by a doublet, which becomes distinct with prolonged sintering durations (120–180 min). These alterations suggest that longer sintering durations affect the arrangement of atoms or molecules in the crystal structure of ye'elinite, leading to a greater orderliness in the crystal lattice. The findings affirm that the most effective dwell duration for sintering falls within the range of 30 to 60 min. During this timeframe, the intensity of the diffraction peaks of ye'elinite reaches the optimal heights. Conversely, extending the duration beyond this optimal range demonstrates a minimal impact and proves to be energetically inefficient.

To summarize, the noted occurrence of solid-state reactions at elevated temperatures aligns closely with the findings of El Khessaimi et al. [52], revealing similar mechanisms of ye'elinite formation. The process initiates with the observation of ye'elinite formation from an amorphous phase. Further, it is driven by a solid-state reaction involving intermediate phases. In contrast, when applying the two-stage

approach, the onset of ye'elimite formation is observed at a lower temperature (800 °C) than with the application of the conventional ye'elimite synthesis method (1000 °C).

Referring to the obtained results, the precursor calcinated at 1150 °C for 1 h (specific surface area – 439.5 m²/kg, density – 2634 kg/m³, d₅₀ – 12.7 μm) was selected for further examination; it was named synthetic ye'elimite

3.5. Reactivity and Early Hydration Mechanism of Synthetic Ye'elimite

As discussed in the Literature Review chapter, the strength and durability properties of calcium sulfoaluminate concrete rely on the hydration behaviour of ye'elimite. Therefore, it is crucial to evaluate the hydration properties of synthesized ye'elimite by using the hydrothermal-calcination method. Thus, this chapter discusses the hydration properties of synthetic ye'elimite, its hydration kinetics, and the development of hydration products.

For this experiment, isothermal conduction calorimetry was employed to measure the heat evolution during the hydration of synthetic ye'elimite. Hydration was conducted at 25 °C for 72 h with a water-to-solid ratio of 1.1. XRD and TGA measurements were used to identify the formed hydration products, while SEM analysis was employed to observe changes in the morphology of the samples. Additionally, the pH values and the conductivity of the prepared suspensions (W/S of 40) were measured to monitor the ion transport during the hydration of synthetic ye'elimite. It is worth noting that the use of a higher W/S ratio enhances the solubility of compounds and accelerates the hydration kinetics. Nevertheless, the obtained results exhibit a similar trend in hydration, thereby providing valuable qualitative information about the dissolution of the anhydrous phases and the precipitation of hydrates [80,179].

Referring to the isothermal calorimetry results, the hydration of synthetic ye'elimite can be defined in five stages (Fig. 3.26):

Stage I (the initial period (up to 30 min)). Immediately upon contact of ye'elimite with water, a rapid increase in the heat flow is monitored, whose maximum (0.01535 W/g) is reached within the first ~4 min of the hydration (Fig. 3.26). Further, the decline in the heat flow curve is seen, which lasts up to ~30 min. Meanwhile, the accelerated increase in the cumulative heat (13.4 J/g) is observed within the first 30 min of hydration, followed by consistent growth thereafter. The increase in conductivity and pH correlates with the dissolution of ye'elimite, showing local maxima after approximately 4 min (Fig. 3.27). With further hydration, stable values are observed, thus indicating the slowdown in the hydration kinetics of ye'elimite. It is worth noting that the observed reductions are related to the formation of the hydration products. The rapidly dissolved ions interact and initiate the precipitate within the saturation level, thereby lowering the concentration in the solution. XRD results indicate the formation of ettringite (low-intensity peaks) during this stage, where the intensity of the ye'elimite peaks is reduced by ~7%. (Fig. 3.28.a and Table 3.12). Meanwhile, the data sourced from TGA supplements the findings with the

presence of amorphous aluminium hydroxide in the sample, which is indicated by the broadening of the DTG curve at 100–200 °C (Fig. 3.28.b) [180,181]. The obtained SEM images confirm the partial dissolution of ye'elimitite. As shown in Figure 3.29, a portion of ye'elimitite particles is dissolved, i.e., only empty layers or remains are identified. Meanwhile, the remaining ones are surrounded by needle-shaped particles of varying sizes, thus indicating the presence of ettringite. These observations also correspond well with the results obtained by other authors [75].

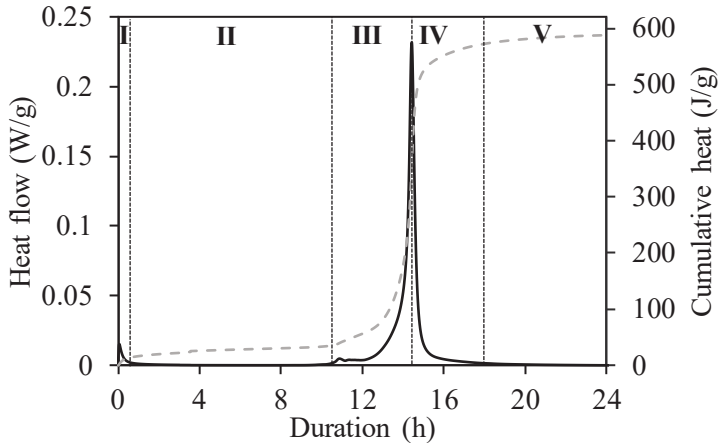


Fig. 3.26. Calorimetric curves measured during isothermal hydration (W/S=1.1) of synthetic ye'elimitite (Roman numerals represent the hydration stages)

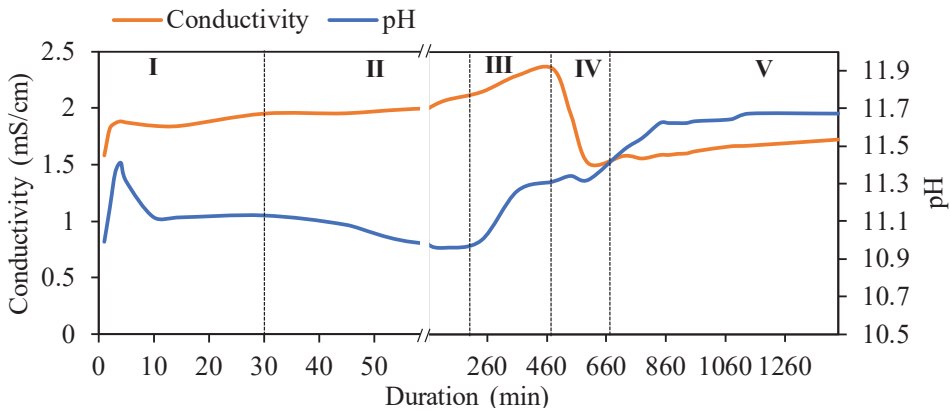


Fig. 3.27. Results of conductivity and pH measurements (W/S=40) of the hydration solution

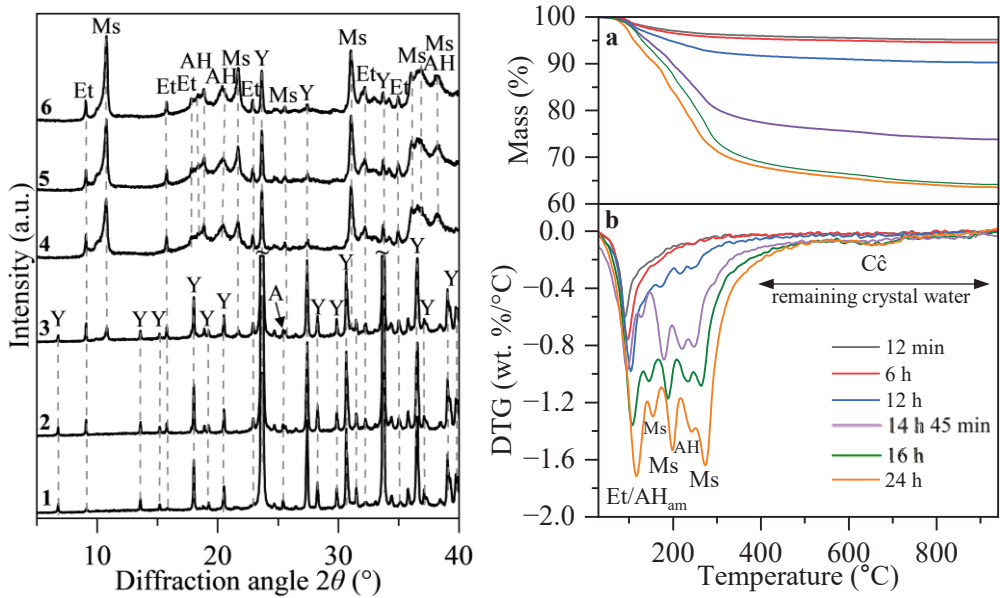


Fig. 3.28. XRD patterns (left) and TGA plots (right) (a – TG, b – DTG) of ye'elimite hydration (W/S=1.1) at different durations (1 – 12 min, 2 – 6 h, 3 – 12 h, 4 – 14 h 45 min, 5 – 16 h, 6 – 24 h). Indexes: Y – ye'elimite, A – anhydrite
Ms – calcium monosulfoaluminate hydrate, Et – ettringite, AH – aluminium hydroxide

Table 3.12. Changes in the intensities of the main diffraction peaks during the hydration (W/S 1.1) of synthetic ye'elimite

Compound \ Duration	Intensity of the peak (cps)						
	0 min	12 min	6 h	12 h	14 h 45 min	16 h	24 h
Ye'elimite (0.375 nm)	8625	8020	7890	6490	2795	320	142
Ettringite (0.975 nm)	–	75	105	226	282	303	371
Monosulfoaluminate (0.823 nm)	–	–	–	73	739	1078	1236

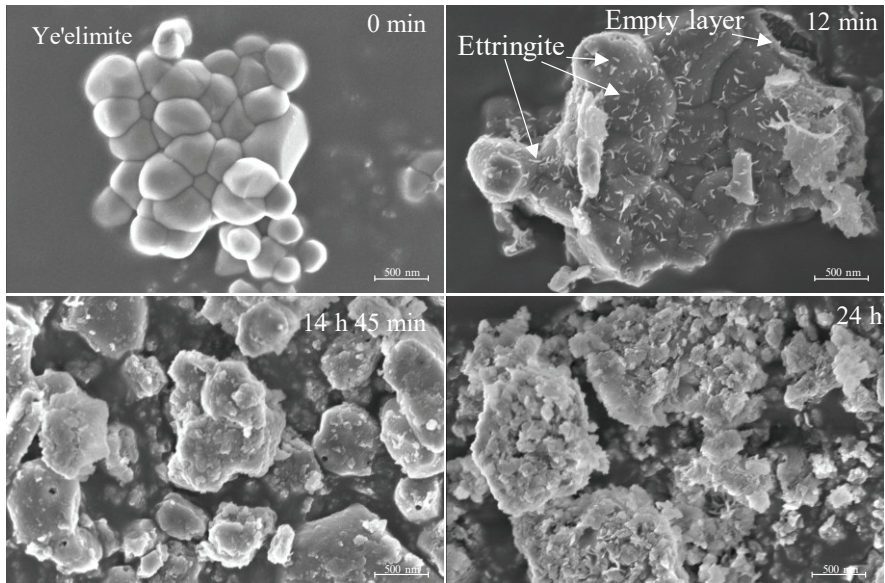


Fig. 3.29. SEM images during the hydration (W/S=1.1) of synthetic ye'elimite at different durations

Stage II (induction period) (30 min – 10 h 40 min). During this stage, no recorded instances of hydration reactions contribute to the curve of the heat flow (Fig. 3.26). Nevertheless, the curve of the cumulative heat continues to increase slowly. The values at 30 min and 10 h 40 min of hydration are equal to 16 J/g and 37 J/g, respectively. Further, the fact that the conductivity curve demonstrates a slight incline also indicates the slow dissolution of ye'elimite (Fig. 3.27). Meanwhile, the slope of the pH curve suggests that the precipitation of hydrates is ongoing. These observations are consistent with the XRD and TGA results. It was determined that, after 6 h of hydration, the characteristic peaks of ye'elimite decline by an additional $\sim 1.5\%$ (Fig. 3.28 and Table 3.12). Consequently, due to the dissolution, precipitation and nucleation growth processes, the increase in the peaks of ettringite is identified. The DTG curves also show a slight increase in the main peak of ettringite (98 °C) within the hydration duration, thus confirming that a higher amount of ettringite is forming. To date, the appearance of the induction period during the hydration of cementitious materials raised considerable discussions in the scientific community. The latest literature emphasizes two primary hypotheses: the protective membrane theory, and the dissolution theory [69]. Based on the first theory, the cement particles are covered with a formed hydrated layer, which is the limiting factor for water to diffuse and interact with the particles. According to the second theory, the dissolution of cementitious phases is controlled by the undersaturation state in the solution, i.e., as the system moves towards equilibrium (the saturation state).

Stage III (acceleration period) (10 h 40 min – 14 h 45 min). During this stage, the beginning of the second exothermic reaction is observed, until reaching its peak

heat flow (0.4544 W/g) after 14 h 45 min of hydration (Fig. 3.26). It is worth mentioning that a small exothermic peak is observed at 11 h 40 min (0.0026 W/g), after which, the heat flow remains relatively stable (i.e., a low increase is observed) and, after 12 h 54 min, the main acceleration (a rapid heat release) begins. Furthermore, it is determined that this period is marked by a rapid increase in conductivity and pH, thereby suggesting an increment of ions in the solution due to the dissolution of ye'elimite (Fig. 3.27). Meanwhile, the XRD data indicates that the observed increase of the heat flow after 11 h 40 min is attributed to the depletion of sulphate (resulting from the dissolution of anhydrite), which, in turn, accelerates the partial hydration of ye'elimite (Fig. 3.28.a) [76]. This is confirmed by the decline in the intensity of the anhydrite peaks observed after 12 h of hydration. Accordingly, the increase in the intensity of the ettringite peaks (~48%), as well as the formation of monosulfoaluminate, is identified in the samples. The TGA data complies well with the XRD results. The further slowdown might be explained by the low quantity of anhydrite (0.17%) in the sample, which is insufficient to accelerate the overall hydration of ye'elimite. Therefore, the beginning of the dissolution of the majority of ye'elimite is observed at 12 h 54 min. At this point, pH could be the primary factor driving the acceleration of ye'elimite dissolution, which is controlled by the nucleation and growth of the resultant hydration products [179]. At the peak of this stage (14 h 45 min), the majority of ye'elimite has already been consumed (~48% of all the peak intensity of ye'elimite), resulting in extensive formation of monosulfoaluminate, additional ettringite as well as microcrystalline aluminium hydroxide (Fig. 3.28.a and Table. 3.5). The DTG curves also demonstrate a notable increase in the main peaks of ettringite (98 °C), thus indicating an increase of the amount of ettringite. Meanwhile, the peaks at ~145 °C, ~190 °C and ~275 °C reflect the presence of Ms, whereas the peak at 240 °C confirms the presence of AH₃ (Fig. 3.28.b). Moreover, the substantial rise in the mass loss (with a total of ~24%) within the 50–550 °C temperature signifies an increased accumulation of the formed hydrates. The SEM images also demonstrate that all anhydrous particles are covered by layers of formed hydrates (Fig. 3.29). The formation of the identified hydration products can be explained by the following equations:



Stage IV (deceleration period) (14 h 45 min – 16 h). This period is related to the end of the second exothermic reaction, which lasts up to ~16 h (Fig. 3.26). The ongoing rise in the cumulative heat is still evident. Meanwhile, the sudden drop in conductivity and pH during this stage indicates a deceleration in ye'elimite dissolution and the progressive formation of the hydration products (Fig. 3.27). This was confirmed by XRD and TGA analysis. As seen in Figure 3.28, after 16 h of hydration, the intensity peaks of ye'elimite continue to reduce, while those of ettringite and monosulfoaluminate are increasing. The TGA analysis also indicates the growth in the formed hydration products, i.e., the total mass loss is equal to ~32% at 50–550 °C.

To summarize, the hydration rate slows down gradually as the amount of still-unreacted ye'elimite declines, whereas the rate of the hydration process becomes diffusion-controlled [68].

Stage V (the final period) (>16 h). During this stage, no change in the heat flow curve was determined (Fig. 3.26). Furthermore, the cumulative heat stabilized at ~580 J/g after 24 h of hydration. It is worth noting that, with a longer duration of hydration, a slow increase is monitored in the cumulative heat, i.e., after 72 h, the determined value is ~585 J/g. These findings are consistent with the data reported in the literature on ye'elimite synthesized via the conventional methods [182]. At the onset of this period, conductivity and pH experience an increase before stabilizing later on, which is a phenomenon that can be attributed to the formation of hydrates (Fig. 3.27). The XRD data demonstrates that the intensity of the ye'elimite peaks is reduced by ~98% after 24 h of hydration (Fig. 3.28 and Table 3.12). Meanwhile, according to the TGA results, when extending the duration of hydration from 16 h to 24 h, this change results in a slight increase of ~2.1% in the quantity of the formed hydrates, mainly in Ms and microcrystalline aluminium hydroxide. Finally, the SEM images confirm that ye'elimite has converted to hydrates, which have accumulated in an extensive range of agglomerate sizes (Fig. 3.29). According to the literature, the reduced heat release observed in Stage V corresponds to a restricted transport process through the densifying microstructure. In other words, the formation of hydrates is constrained by the volume of the pre-existing hydrates, filling only small voids [68,69].

To sum up, the results indicate that synthetic ye'elimite produced by the hydrothermal-calcination method exhibits a high hydraulic activity and forms identical hydration products as those formed during the hydration of ye'elimite produced by the conventional solid-state method.

3.6. Fly Ash Effect on the Hydration and Properties of Synthetic Ye'elimite

In the recent years, there has been a growing interest in blending different types of cement together with supplementary cementitious materials. These cements can form binary or ternary systems, which contribute substantially to reducing the clinker factor, thereby saving energy as well as conserving the natural resources. One of the more promising approaches is the utilization of various sources of fly ash because it provides a sustainable and widely available alternative to the traditional raw materials. Numerous studies have investigated the CSA–fly ash system, thus revealing promising findings regarding the substitution of CSA with fly ash, with potential replacements of up to 15% without compromising the relevant mechanical properties [183]. However, the literature still lacks information about the impact of fly ash on the early hydration of ye'elimite. Therefore, further work was dedicated to studying the hydration and properties of ye'elimite blended with fly ash (FA).

3.6.1. Kinetics of the initial hydration

For this investigation, ye'elimite was replaced with 5%, 10%, 20%, and 40% siliceous fly ash (F class); these samples were accordingly named YFA5, YFA10,

YFA20, and YFA40, whereas synthetic ye'elimite without fly ash shall be referred to as Y. The isothermal calorimetry results (W/S=1.1) for the samples prepared with different blends of ye'elimite and fly ash are presented in Figure 3.30. The results have been adjusted to account for the amount of synthetic ye'elimite present in each sample, i.e., 100%.

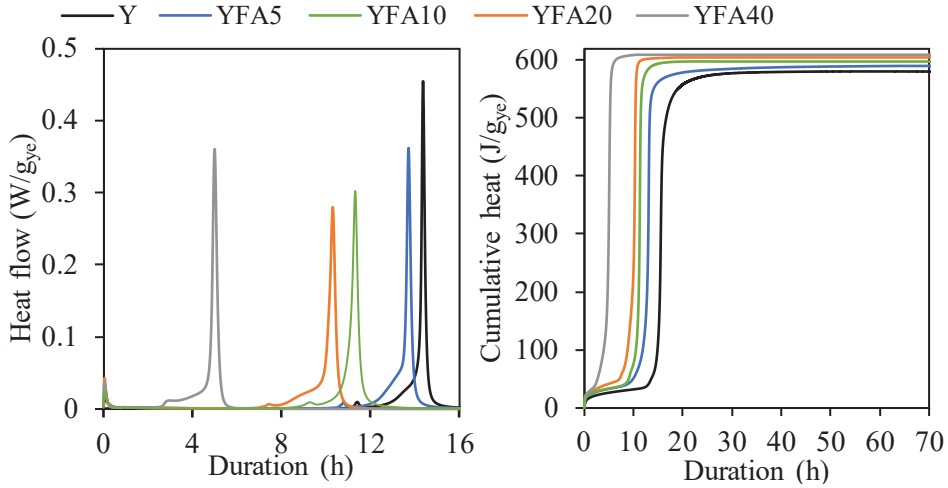


Fig. 3.30. Calorimetric curves obtained during isothermal hydration (W/S=1.1) of various ye'elimite–fly ash blends

The data demonstrates that the addition of fly ash accelerates the hydration of synthetic ye'elimite. As a result, the shortest induction period, which lasted only for ~2 h, is observed in the sample with the highest fly ash content (40%). Furthermore, samples with 5–20% fly ash exhibited a higher heat flow and a wider duration prior to the main acceleration peak than the sample of pure ye'elimite, thus indicating a higher reaction in ye'elimite hydration. Consequently, this results in a reduced amount of ye'elimite available for the main hydration reaction, thus lowering the heat flow maxima of the second exothermic reaction, i.e., YFA5 – 0.3542 W/g (13 h 42 min), YFA10 – 0.2916 W/g (11 h 15 min) and YFA20 – 0.2802 W/g (10 h 18 min). Meanwhile, this period for YFA40 is shorter, which means that, possibly, faster dissolution of ye'elimite is manifested during the main reaction, demonstrating an increase in the reaction heat (0.4278 W/g; 4 h 54 min). Furthermore, it has been identified that the inclusion of fly ash leads to an increase in the total heat released by the samples, thus suggesting a higher reactivity of ye'elimite. Specifically, the monitored values are as follows: YFA5 – 590 J/g, YFA10 – 597 J/g, YFA20 – 604 J/g, and YFA40 – 609 J/g. The higher effective water/binder (ye'elimite) ratio can explain the observed increment in the cumulative heat. The experiments maintained a water/solid ratio of 1.1. However, the water/binder ratio increases with the addition of fly ash by diluting the binder. For instance, recalculating the water/binder ratio for YFA20 has a value of 1.375. This phenomenon regarding CSA cement was

extensively investigated by Martin et al. [184]. The authors demonstrated that, when maintaining the same W/B ratio for CSA–FA samples, a similar cumulative heat to the plain binder without fly ash was displayed. These findings confirmed that the available water for the cement particles is the controlling factor for the hydration reactions. Meanwhile, in order to understand the accelerated hydration of ye'elimite in the presence of fly ash, supplementary experiments were performed.

It is well-known that fly ash demonstrates no or minimal reaction during the 7 initial days of cement hydration [184,185]. Nevertheless, fly ash particles serve as supplementary surfaces providing additional nucleation sites (this is the so-called filler effect). This phenomenon accelerates the nucleation and formation of cement hydrates. One of the non-hydraulic fillers – limestone powder (LS) – is widely used to investigate the filler effect on the hydration of cementitious materials [186,187]. Therefore, a sample with 20% LS replacement was chosen to determine the impact of the filler effect on the hydration of ye'elimite; this sample was named *YLS20*. In order to compare the filler effects, the fineness of limestone powders must be similar to or exceed that of fly ash. As expected, the calorimetry results (W/S = 1.1) confirmed that the addition of limestone accelerates the hydration of ye'elimite (Fig. 3.31). The maximum of the second exothermic reaction is reached after ~14 h 8 min. However, the observed acceleration is significantly lower compared to that induced by fly ash (Fig. 3.30 and Fig. 3.31). Nevertheless, the cumulative heat is the same as for *YFA20* (604 J/g). These results confirm that: 1) another factor (*not* the filler effect) is the main stimulant of hydration acceleration, and 2) a higher water/binder ratio increases the reactivity of ye'elimite. It is worth noting that LS exhibits a lower distribution of the particle size. Therefore, the filler effect of fly ash on the acceleration of hydration might be even lower than the value detected in *YLS20*.

Looking at the composition of liquid phases during the initial hours of cement hydration, alkalis such as Na^+ , K^+ and Ca^{2+} enter the system [188]. The studies highlight that the presence of low-to-moderate quantities of alkalis enhances the dissolution of ye'elimite and the formation of hydrates [82,166]. Therefore, the pore solution chemistry was performed on the ye'elimite and *YFA20* samples after 2 h of hydration (W/S=1.1). The obtained ICP–OES data of the pore solution composition is presented in Table 3.6. It can be seen that the *YFA20* sample has a slightly higher pH value than ye'elimite. This can be attributed to the ongoing release of alkali ions from fly ash, i.e., a higher Na^+ , K^+ and Ca^{2+} content is identified in *YFA20* than in the ye'elimite sample. In order to confirm whether the increase in the alkalis is the main factor accelerating the hydration of ye'elimite, an artificial *pore solution* (PS) was prepared, referring to the measured pore solution composition of *YFA20*. For that, the Na/K ratio was maintained, while incorporating the Ca content within this ratio. The prepared total alkali content in the artificial PS was slightly lower due to measuring errors (Table 3.13). It is worth noting that the higher pH observed in the artificial PS may be attributed to the accessibility of alkali anions within the solution. The *YFA20* sample has an increased variety of ions originating from fly ash, which likely enhances the buffering capacity, thereby potentially resulting in a lower pH value.

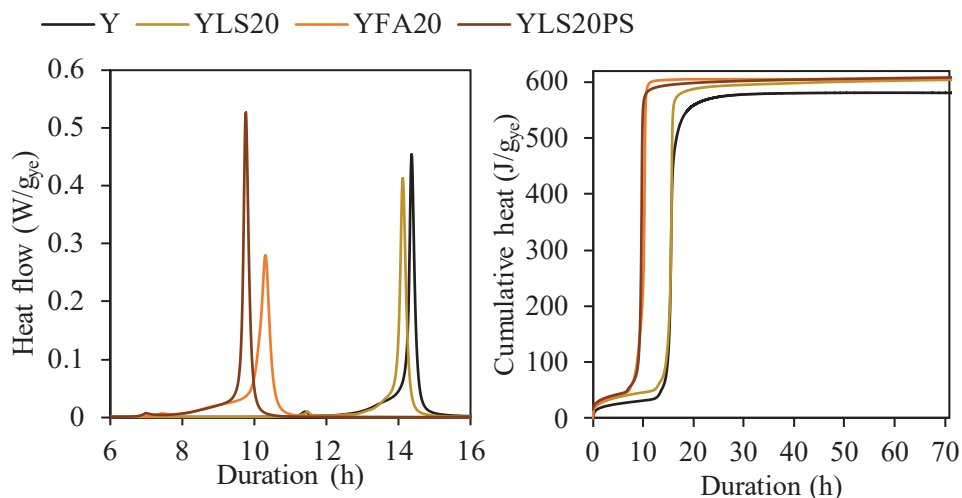


Fig. 3.31. Calorimetric curves measured during isothermal hydration of blends containing ye'elimite-fly ash and ye'elimite-limestone when using different solutions

Table 3.13. Compositions of extracted and prepared pore solutions by ICP–OES

Name of the pore solution	Measured ions (mmol/l)							
	Na	K	Ca	Mg	Al	S	pH	Na/K
Ye'elimite	8.03	2.20	16.10	0.01	42.34	0.05	11.10	3.64
YFA20	9.58	2.55	18.04	0.01	42.59	0.05	11.18	3.76
Artificial PS	29.80	7.90	–	–	–	–	11.67	3.77

Calorimetric measurements were conducted by using *YLS20* (including the filler effect), whereas water was substituted with the prepared PS, referred to as the *YLS20PS* sample. It has been determined that the use of the artificial pore solution significantly increases the hydration rate of ye'elimite, i.e., the maximum of the second exothermic reaction was reached after 9 h 45 min (Fig. 3.31). The determined faster hydration rate and the higher heat flow maxima of the second exothermic reaction can be attributed to the higher pH value in the solution. To summarize, the conducted investigations have demonstrated that the substitution of ye'elimite with fly ash accelerates hydration. This acceleration can be attributed primarily to two factors: 1) the filler effect, and 2) the alkalinity content (its influence is the higher of the two).

3.5.2. Characterization of hydration products

In order to assess the impact of fly ash on hydrate formation, ye'elimite-fly ash blended samples hydrated for 72 h were investigated. The hydration degree of ye'elimite after hydration was determined by comparing the intensity of the peak changes with the unhydrated sample. In the presence of some content of fly ash, a greater degree of ye'elimite reaction is determined within the initial hours of hydration, i.e., before the second exothermic reaction (Fig. 3.20 and Fig. 3.32).

Additionally, as the fly ash substitution percentage increases, a slight rise in the degree of ye'elinite reaction is observed, i.e., the degree of the ye'elinite reaction increases from 98.3% in the pure synthetic ye'elinite sample to 99.2% in the sample with 40% fly ash replacement. These findings confirm that a higher effective water/binder ratio promotes the hydration of ye'elinite [184].

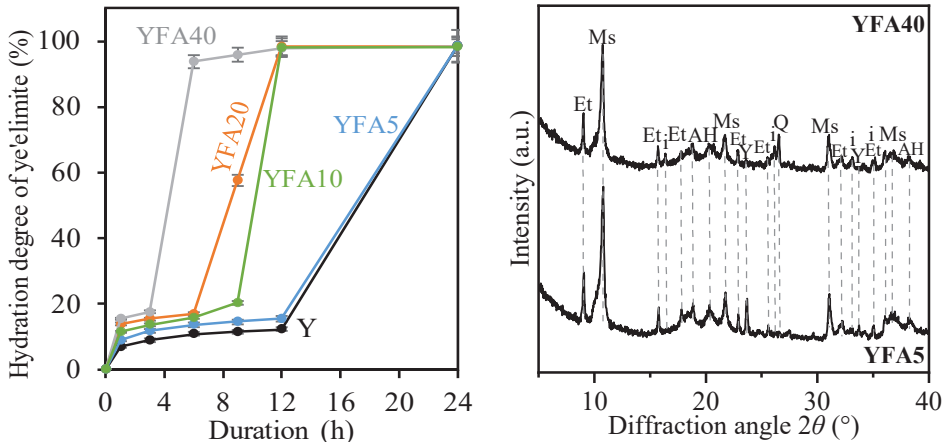


Fig. 3.32. Degree of ye'elinite reaction (left) and XRD patterns (right) of different ye'elinite-fly ash blends after 72 h of hydration. Indexes: Y – ye'elinite, Ms – monosulfoaluminate, Et – ettringite, AH – aluminium hydroxide, i – mullite, Q – quartz

XRD analysis reveals that the phase composition of the formed hydrates during the hydration of ye'elinite-fly ash blends remains unchanged (Fig. 3.32). As in the pure synthetic ye'elinite sample, ettringite, monosulfoaluminate (the dominant phase) and aluminium hydroxides were identified in the XRD patterns of all the blends. The difference between the samples is observed in the characteristic peak intensities of the formed hydrates. The intensities gradually decrease when increasing the fly ash replacement amount (Table 3.7). These phenomena can be attributed to the dilution effect on the binding material. To hypothetically exclude the dilution effect, the theoretical intensity of the formed hydrate peaks was calculated, by assessing the potential reduction in the intensity from a pure hydrated synthetic ye'elinite sample to the percentage of the fly ash replacement in each sample. When comparing the theoretical and measured peak intensities of the hydration products, it can be seen that the decrease in the measured peaks is not directly proportional to the replacement level (Table 3.14). The observed intensities of ettringite are higher, while those of monosulfoaluminate are lower than those theoretically anticipated. This might indicate that the addition of fly ash in synthetic ye'elinite samples limits the formation and/or promotes the decomposition of monosulfoaluminate, resulting in additional formation of ettringite and/or its stabilization during the hydration. It is acknowledged that, in the $C_4A\hat{S}H_{12}$ structure, some SO_4^{2-} groups can be replaced by other anions

(Cl⁻, NO₃⁻, CO₃²⁻, etc.) during the hydration/ageing process [86,105]. Accordingly, this supplements the pore system with SO₄²⁻, which could either stabilize ettringite or, when being of sufficient quantity, promote the conversion of monosulfoaluminate to ettringite. Additionally, compared to the theoretical calculations, the samples featuring a replacement of up to 20% fly ash demonstrate a slightly elevated intensity of the aluminium hydroxide peaks (Table 3.14). These results might suggest a couple of hypotheses. First, the total reaction degree of ye'elimite increases with the substitution level (probably due to a higher effective water/binder ratio), resulting in a higher formation of aluminium hydroxides. Second, the resulting amorphous aluminium hydroxide interacts with fly ash (alkalis), which stimulates the transformation of amorphous aluminium hydroxide towards microcrystalline aluminium hydroxide [189]. Meanwhile, the above-described intensity trends are less visible in the samples with 40% fly ash replacement, which might suggest that the dilution effect is too high to be compensated by the filler effect and/or an increased effective water/binder ratio. Additionally, no observable changes in the intensity of phase peaks corresponding to fly ash compounds, such as quartz and mullite, after 72 h of hydration in the samples were identified.

Table 3.14. Changes in the main diffraction peaks after 72 h of hydration in various ye'elimite-fly ash blends

Sample Compound	Measured intensity of the peaks (cps)				
	Y	YFA5	YFA10	YFA20	YFA40
Ye'elimite (0.375 nm)	79	72	65	54	39
Ettringite (0.975 nm)	461	455	439	413	379
Monosulfoaluminate (0.823 nm)	1775	1557	1461	1400	1047
Aluminium hydroxide (0.436 nm)	208	202	213	179	113
	Theoretical intensity of the peaks (cps)				
Ye'elimite (0.375 nm)	79	75	71	63	47
Ettringite (0.975 nm)	461	437	414	368	276
Monosulfoaluminate (0.823 nm)	1775	1686	1597	1420	1065
Aluminium hydroxide (0.436 nm)	208	197	187	166	125

Similar to the XRD results, the TGA data reveals a decrease in the formed hydrates as the fly ash content increases in the samples, accompanied by a reduction in both the mass loss and the bound water (H) content in the samples (Fig. 3.33). The same thermal effects were identified in ye'elimite-fly ash blends as in the pure synthetic ye'elimite samples after 72 h of hydration corresponding to ettringite (at ~97 °C), monosulfoaluminate (at ~178 °C and ~260 °C), aluminium hydroxides (at ~220 °C and ~290 °C), and calcium carbonate (~675 °C). As mentioned above, the

decomposition temperatures of the different hydration products significantly overlap. Normalization of the formed separate compounds to the synthetic ye'elimite content (100%) could result in significant errors, potentially leading to overestimations. Therefore, in order to exclude the dilution effect, only the bound water content (at 50–550 °C) was normalized as a percentage relative to the synthetic ye'elimite content (100%). This normalization confirms a slight increase in the amount of bound water (i.e., the amount of the formed hydrates) per synthetic ye'elimite content as the fly ash content increases in the samples (Fig. 3.33). These results are consistent with the observed increase in the total heat released by the samples with an increasing fly ash content, thus suggesting a growth in the reaction degree of ye'elimite (Fig. 3.30).

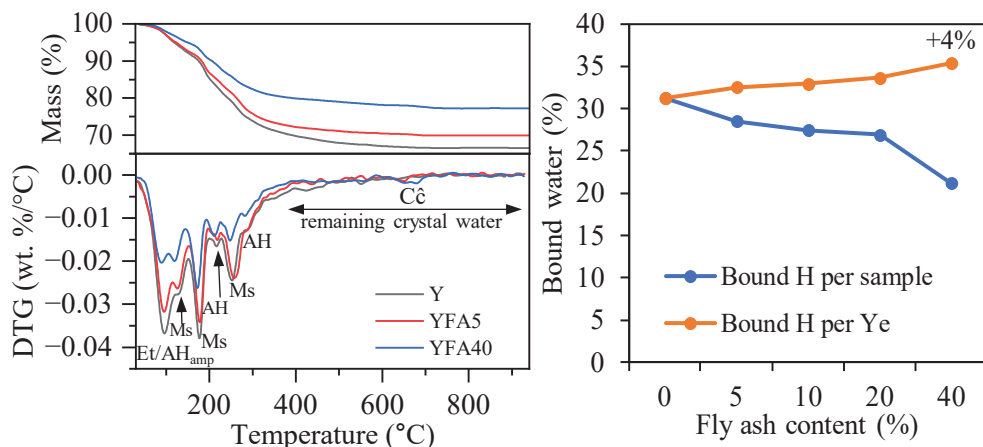


Fig. 3.33. TGA plots (left) and the amount of bound water (right) of different ye'elimite-fly ash blends after 72 h of hydration

To summarize the findings in this section, it can be concluded that the addition of fly ash not only accelerates the hydration of ye'elimite, but also potentially influences the formation of monosulfoaluminate and ettringite. Meanwhile, the observed increase in the reaction degree of ye'elimite with fly ash substitution levels can be attributed to a higher effective water/binder ratio. It is of importance to emphasize that the intensity of the peaks depends not only on the concentration of the formed hydrates, but also on the crystallinity, the crystal order, the crystal size, microstrains, the incorporation of other ions in the structure, etc. Therefore, further investigations are still needed to confirm the above presented hypotheses.

3.7. Effect of Synthetic Ye'elimite on the Hardening Process of Ordinary Portland – Fly Ash Blended Cement

As part of the sustainability movement, there is a notable focus on preparing different cement blends, where part of the cement would be replaced with supplementary cementitious materials such as fly ash [190,191]. Utilizing such materials, which do not require an additional clinkering process, substantially decreases CO₂ emissions per ton of cementitious materials, and even improves the

performance of concrete. Moreover, this approach offers a means to effectively utilize the by-products generated from industrial manufacturing processes. Furthermore, cement blends may demonstrate enhanced long-term strengths and durability compared to pure OPC mixtures. However, the concrete prepared from cement blends sometimes encounters issues related to retardation or a delayed setting time and low early-age strengths [192,193]. The placement of concrete in formwork depends on the setting time of the concrete. Therefore, the delayed setting time of cement blends with SCMs might be the limiting factor depending on the application field.

As highlighted in the literature review and as evident from the results of the hydration investigation, ye'elimite sets and initially hardens within the first 24 h of hydration. Therefore, further investigation was conducted to examine the influence of a synthetic ye'elimite additive on the hardening processes of OPC–FA blends as a potential additive to regulate the setting time of mortars.

3.7.1. Setting time and compressive strength

Standard tests were conducted to assess the impact of a synthetic ye'elimite additive on the properties of OPC–FA cement blends. These included the cement paste standard consistency and setting time tests, as well as a compressive strength test on the prepared mortars. The samples included: Portland cement only, Portland cement with fly ash (without an additive), and Portland cement with fly ash and a synthetic ye'elimite additive.

First, the samples of Portland cement and Portland cement blended with fly ash were studied. It was determined that the replacement of OPC with 20% fly ash requires a higher water-to-solid ratio in order to obtain the standard paste consistency, i.e., $W/S = 0.290$ for OPC, and 0.306 for *80P20FA* samples. Furthermore, OPC–FA samples demonstrated a delay in both the initial (by 107 min) and the final setting (by 40 min) times compared to the pure OPC samples (Fig. 3.34.a). Meanwhile, the compressive strength test results indicate that the blending of fly ash with OPC ash has a positive effect on the strength development of mortars (Fig. 3.34.b). After 2 days of curing, *80P20FA* samples demonstrated ~29% higher compressive strength values than the OPC samples, whereas the OPC samples slightly surpassed the compressive strength of *80P20FA* samples after 7 days of curing. Meanwhile, after 28 days of curing, the compressive strength of the *80P20FA* mortars exceeded that of OPC by ~16%.

It is crucial to emphasize that the substitution of OPC with fly ash increases the available surface area and provides additional precipitation sites (the filler effect) for the hydration products of OPC. This substitution also increases the effective water-to-OPC ratio. Moreover, depending on its composition, fly ash can engage in the pozzolanic reaction. Here, portlandite generated from the hydration of OPC reacts with the available SiO_2 and Al_2O_3 present in fly ash. These adjustments accelerate the hydration reaction and foster a greater hydrate growth, ultimately resulting in an increased compressive strength [190,194].

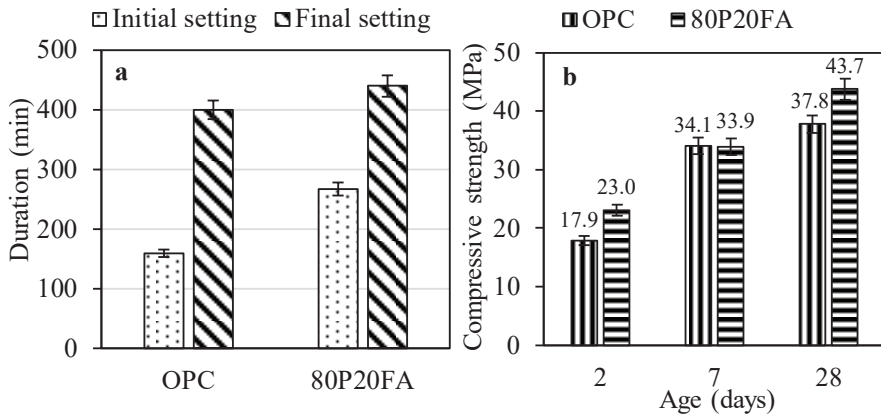


Fig. 3.34. The setting time of paste (a) and the compressive strength of mortars (b) prepared by using OPC–FA blends

Further results revealed that the preparation of ternary blended cement (OPC–FA–Y) necessitates a higher water-to-solid ratio in order to achieve the standard consistency of the pastes with increasing quantities of synthetic ye'elimite in the blends (Fig. 3.35). In terms of the setting time, the inclusion of synthetic ye'elimite into the blends reduces both the initial and the final setting time. Addition of 0.5% of synthetic ye'elimite decreases the initial and final setting time in the *80P19.5FA0.5Y* sample by 107 min and 40 min, respectively, and in the *79.5P20FA0.5Y* sample by 93 min and 151 min, respectively, compared to the *80P20FA* sample. It is worth noting that both samples demonstrated shorter final setting times, and the *80P19.5FA0.5Y* sample also had a shorter initial setting time than the pure OPC sample.

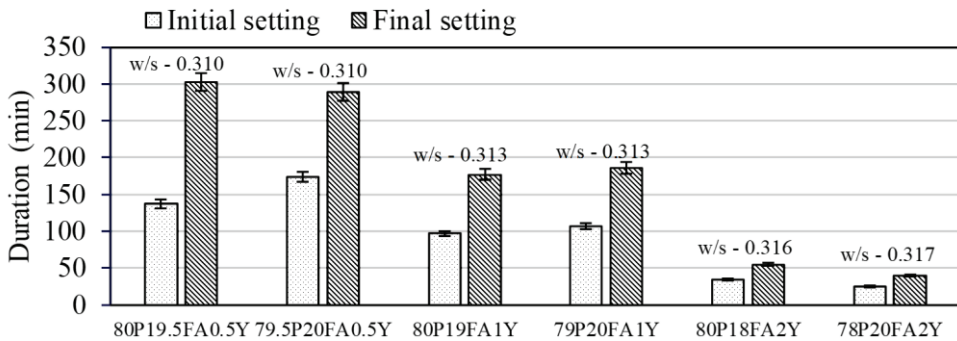


Fig. 3.35. Setting times of the prepared OPC–FA–Y paste samples

With a higher addition of synthetic ye'elimite, the reduction in the setting time becomes even more pronounced. In the *80P19FA1Y* sample, the initial and the final setting time is reduced accordingly by 170 min and 263 min, whereas, in the *79P20FA1Y* sample, by 160 min and 254 min compared to the *80P20FA* sample. Meanwhile, by increasing the quantity of synthetic ye'elimite to 2% in the blends, the initial setting is observed in the *80P18FA2Y* sample after 35 min, and, in the

78P20FA2Y sample, after 25 min. According to the LTS EN 197-1 Standard, the setting time of the cement paste must be not less than 60 min in order to ensure its optimal operational properties. Therefore, the amount (2%) of a synthetic ye'elimitite additive is unsuitable for preparing cement mortars.

As shown in Figure 3.36, incorporation of a synthetic ye'elimitite additive in ternary blended cement reduces the strength development of mortars during the first 7 days of curing compared to the OPC sample. An exception is observed with the 79.5P20FA0.5Y sample after 2 days of curing. Nevertheless, after 28 days of curing, the samples of ternary blended cement with 0.5% of a synthetic ye'elimitite additive exhibits higher compressive strength values than OPC, i.e., 80P19.5FA0.5Y by ~3.3%, and 79.5P20FA0.5Y by 6.2%. Meanwhile, ternary blended cement with 1% synthetic ye'elimitite additive demonstrates compressive strength values similar to OPC after 28 days of curing. Further, an investigation into the hydration products was conducted to understand the obtained compressive strength development of the samples.

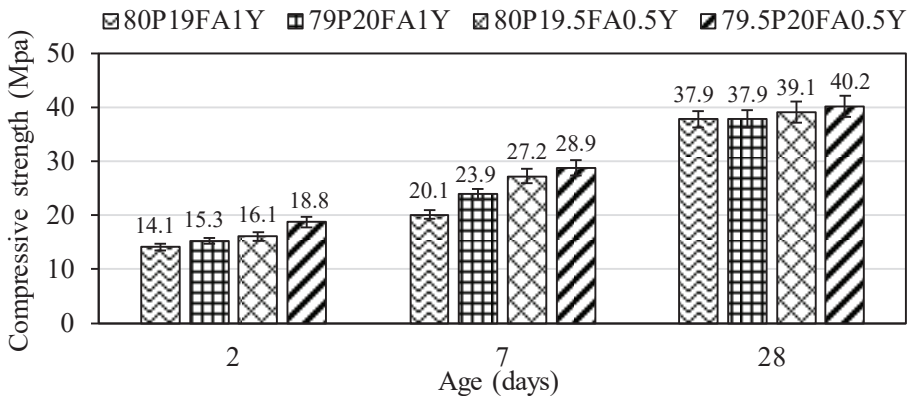


Fig. 3.36. Compressive strength of the prepared OPC–FA–Y mortar samples

3.7.2. Characterization of hydration products

The formed hydrates were determined by XRD and TGA analysis to evaluate the influence of the synthetic ye'elimitite additive on the formation of the hydration products in ternary blended cement (OPC–FA–Y).

The XRD results revealed that the replacement of OPC with fly ash and synthetic ye'elimitite does not change the phase composition of the hydration products after 2 days of hydration. In all the investigated samples, ettringite, portlandite and calcium carbonate were identified (Fig. 3.37.a). Moreover, it was determined that the incorporation of synthetic ye'elimitite in the samples enhances the formation of ettringite. As the synthetic ye'elimitite content increases in the samples, a slight elevation in the intensity of the diffraction peaks corresponding to ettringite was observed in the XRD patterns. It is worth noting that ye'elimitite and gypsum are no longer detected in the XRD patterns of all samples after 2 days of hydration.

Additionally, a significant decrease in the intensity of the peaks of the OPC phases (alite, belite, brownmillerite, tricalcium aluminate) was identified. The formation of the hydrates can be explained by the following reactions [195]:

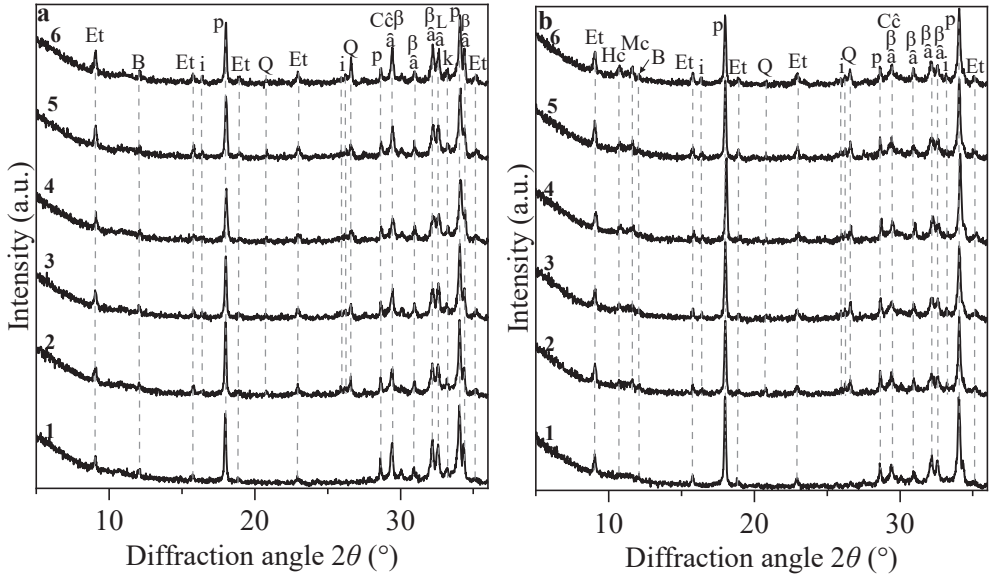
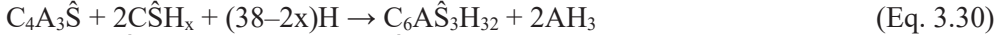


Fig. 3.37. XRD patterns of different OPC–FA–Y samples after 2 days (a) and 28 days (b) of curing (1 – OPC, 2 – 80P20FA, 3 – 80P19.5FA0.5Y, 4 – 79.5P20FA0.5Y, 5 – 80P19FA1Y, 6 – 79P20FA1Y). Indexes: p – portlandite, Et – ettringite, Hc – hemicarboaluminate, Mc – monocarboaluminate, â – alite, β – belite, B – brownmillerite, i – mullite, Q – quartz, Cĉ – calcium carbonate, k – tricalcium aluminate

It was determined that, when prolonging the hydration duration, it promotes further dissolution of the unhydrated phases (Fig. 3.37.b). After 28 days of hydration, tricalcium aluminate is no longer detected in the XRD patterns of all samples, while only traces of brownmillerite remain visible. Further, C_3S and C_2S dissolution induces the formation of portlandite, i.e., an increase in the intensity of the portlandite peaks is identified. A slight increase is also observed in the intensity of the ettringite peaks. Additionally, in all samples, the formation of hemicarboaluminate is observed after 28 days of hydration. Meanwhile, the replacement of OPC with fly ash and (or without) synthetic ye'elimite induces the formation of monocarboaluminate ($Ca_4Al_2O_6CO_3 \cdot 11H_2O$, PDF No. 00-014-0083). Additionally, the intensity of the

peaks for both hemicarboaluminate and monocarboaluminate increases with the rise in the synthetic ye'elimite content in the ternary blended cement. It is noteworthy that a minor reduction in the intensity of mullite peaks is observed in all samples after 28 days of hydration. Meanwhile, the intensity of the quartz peaks remains constant throughout the entire duration of hydration.

It was recognized that, in the absence of calcium carbonate during cement hydration, ettringite reacts with the remaining tricalcium aluminate, which results in the formation of monosulfoaluminate (Eq. 3.31). However, the presence of calcium carbonate destabilizes monosulfoaluminate, consequently promoting the formation of mono- and hemicarboaluminate hydrates instead (Eqs. 3.32–3.33) [194,196]. This can explain the presence of mono- and hemicarboaluminate hydrates observed in all the mortar samples after 28 days of hydration. Meanwhile, amorphous/microcrystalline AH_3 forms during the hydration of ye'elimite. According to the literature [195], with the prolonged hydration durations in OPC–CSA cement blends, the formed AH_3 can react with portlandite and calcium carbonate, leading to the formation of mono- and hemicarboaluminate hydrates (Eqs. 3.34–3.35). Theoretically, an increase of the amount of a synthetic ye'elimite additive in ternary blended cement should enhance the formation of AH_3 . Therefore, it might explain the observed increase in the intensity of $C_4A\hat{C}_{0.5}H_{11.5}$ and $C_4A\hat{C}H_{11}$ peaks due to AH_3 interaction with CH and $C\hat{C}$.



Alite is the paramount constituent of Portland cement, exerting substantial control over its setting and hardening characteristics [188]. Therefore, the reaction degree of alite in all the samples was further assessed by estimating the alteration in the intensity of the main peak ($d - 0.278$) at varying durations of hydration. Relative errors were estimated below $\pm 3\%$; they were calculated from three replicate samples.

It can be observed that the OPC–FA samples demonstrate higher reaction degrees of C_3S compared to the OPC samples throughout the entire duration of hydration (Fig. 3.38). This observation coincides well with the results achieved by other authors [154,194], which can be attributed to the increased effective water-to-OPC ratio ($0.5 \rightarrow 0.625$), and/or the filler effect. Meanwhile, the opposite tendency is identified with the prepared samples of the OPC–FA–Y cement blends. The results suggest that the addition of synthetic ye'elimite delays or slows down the hydration of C_3S in the ternary blended cement system, which is particularly notable during the initial week of hydration. This phenomenon becomes even more pronounced with an increase in the content of synthetic ye'elimite in the samples. These results can explain the slower strength development observed during the 7 initial days of curing (Fig. 3.36). Furthermore, a lower hydration degree of C_3S is also observed after 28 days of

hydration in the samples containing synthetic ye'elimitite. Specifically, with 0.5% replacement, the reduction is noted to be within the range of 0.9–1.3%, while, with 1% replacement, it falls by 3.7–4.2% compared to the OPC samples.

□ OPC ■ 80P20FA ▨ 80P19.5FA0.5Y ▩ 79.5P20FA0.5Y ▧ 80P19FA1Y ▦ 79P20FA1Y

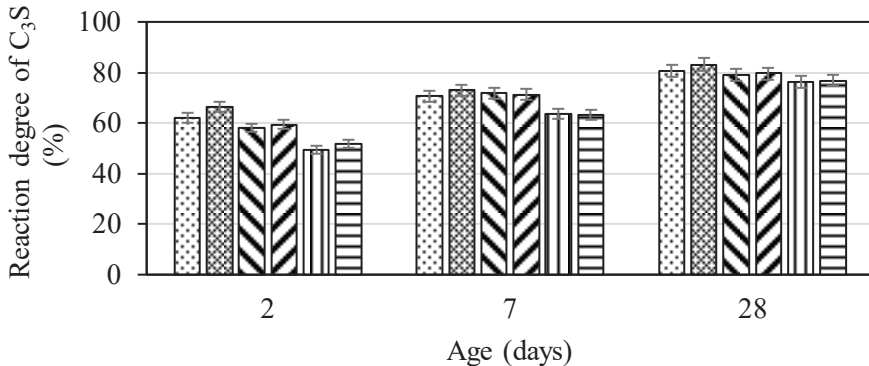


Fig. 3.38. Reaction degree of alite during the curing of different OPC–FA–Y samples

Several authors have also observed the delayed hydration of alite in CSA/OPC blended cements [197–199]. They determined that the dissolution of CSA phases (i.e., ye'elimitite) primarily occurs during the initial 7 days of hydration, followed by the initiation of the dissolution of the main OPC phases (i.e., alite). The slow and/or limited hydration of silicate (C_3S and C_2S) might be partially explained by the large amount of water consumed during the formation of ettringite (32 moles). However, the mechanism behind the delayed hydration of alite in CSA/OPC blends still remains unclear to date.

For the further investigation, thermogravimetric analysis was utilized with the objective to identify the formed hydrates during the curing of the samples. The DTG curves of all the experimental samples after 28 days of hydration are presented in Fig. 3.39. The thermogravimetric data of all the samples reveals three distinct thermal regions. The first area at a temperature interval of 50–230 °C reflects dehydration of C–S–H, ettringite, AFm phases (mono-/hemicarboaluminates), hydrogarnets, and calcium aluminate hydrates [145]. The second effect at ~440 °C identifies the decomposition of portlandite, and, at 550–750 °C, the decarbonization of calcium carbonate, Hc and Mc. It can be observed that the curves of all the samples exhibit considerably similar profiles. The primary distinction is evident in the shoulders observed at around ~98 °C and ~145 °C, corresponding to the ettringite and AFm phases, respectively. In the samples containing synthetic ye'elimitite, the derivative peaks of ettringite appear to be notably more intense if compared to those of the pure OPC or OPC–FA samples. Additionally, the shoulder observed at around ~145 °C is stronger in the OPC–FA sample compared to OPC alone. This trend is further enhanced by the presence of synthetic ye'elimitite in the samples. These results align closely with the XRD data, wherein the higher intensity of the peaks associated with

ettringite, mono- and hemicarboaluminates has been observed in the OPC–FA–Y samples. Furthermore, in the OPC–FA and OPC–FA–Y samples, the shoulder observed within the temperature range of 180–230 °C exhibits a gentler slope compared to the OPC sample. This suggests a shift of the shoulder towards higher temperatures, likely attributed to the increased formation of amorphous and/or semi-crystalline aluminium-containing hydrates in the samples [145,200].

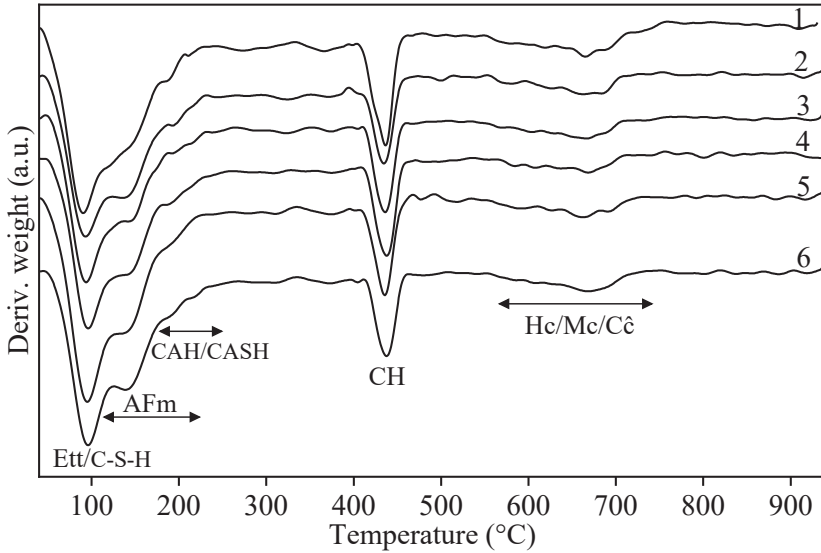


Fig. 3.39. DTG curves of the prepared OPC–FA–Y samples after 28 days of curing. Samples: 1 – OPC, 2 – *80P20FA*, 3 – *80P19.5FA0.5Y*, 4 – *79.5P20FA0.5Y*, 5 – *80P19FA1Y*, 6 – *79P20FA1Y*

The effect of the fly ash and synthetic ye'elinite replacement on the amount of water in hydrates (50–400 °C), and the amount of portlandite was also determined by TGA analysis. The presented results were normalized as a percentage relative to the binder content (100%) in order to exclude the dilution effect, i.e., they are dependent on the sample to OPC or OPC plus the synthetic ye'elinite content.

The results demonstrate that, by replacing 20% of OPC with fly ash, we increase the amount of hydrate water, while also increasing the CH content during the first week of curing in the samples (Fig. 3.40). As the curing duration is prolonged to 28 days, the amount of hydrate water increases, whereas the CH content decreases. This confirms that CH is consumed for the pozzolanic reactions which produce hydration products in the *80P20FA* sample. According to the literature [145,201], CH interacting with fly ash (mainly, Al_2O_3 and SiO_2) can produce C–S–H and C–A–S–H, hydrated calcium aluminates (C_4AH_{13} , C_2AH_8), and hydrated calcium aluminosilicates of the hydrogelenite (C_2ASH_8) and hydrogarnet (C_3AS_3 – C_3AH_6) types. Meanwhile, samples containing both fly ash and synthetic ye'elinite additives exhibited a difference in the evolution of the hydrate water and CH contents. It is evident that the amount of hydrate water and the formed CH content is lower in

samples after 2 days of curing with synthetic ye'elimite compared to the OPC or *80P20FA* samples. This reduction is more pronounced with an increased synthetic ye'elimite content in the samples. These results are in good agreement with the observed lower hydration degree of C_3S by XRD analysis in the OPC–FA–Y samples after 2 days of hydration (Fig. 3.38).

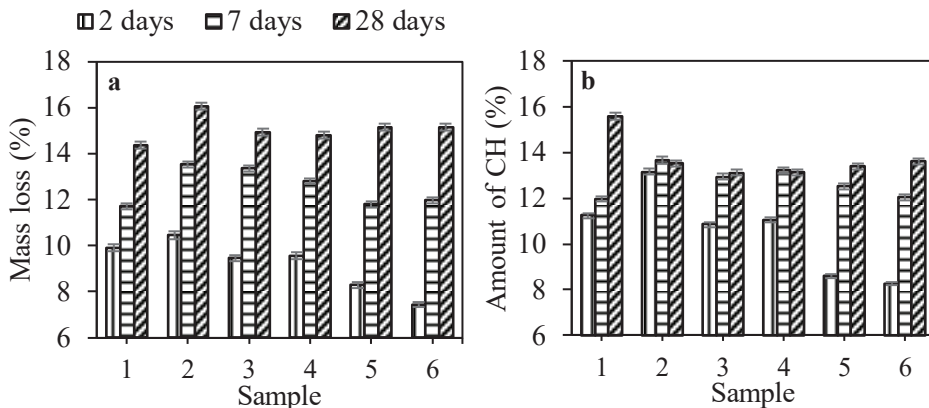


Fig. 3.40. Mass loss of samples within the temperature range of 50–400 °C (a) and the formed amount of portlandite (b) at various curing ages relative to the binder content. Samples: 1 – OPC, 2 – *80P20FA*, 3 – *80P19.5FA0.5Y*, 4 – *79.5P20FA0.5Y*, 5 – *80P19FA1Y*, 6 – *79P20FA1Y* (error bars represent the standard deviation)

Interestingly, after 7 days of curing, the OPC–FA–Y samples show a higher amount of hydrate water and formed CH content compared to the OPC sample, but this value is still lower than that of the *80P20FA* sample (Fig. 3.40). From 7 to 28 days of curing, as in the *80P20FA* samples, the CH content diminishes in the samples containing synthetic ye'elimite, as it is utilized for the formation of hydrates. Consequently, this leads to a higher amount of hydrate water compared to the OPC sample, but the amount is still lower than that of the *80P20FA* sample. It is worth noting that samples with 1% synthetic ye'elimite demonstrate a slightly higher amount of hydrate water (0.21–0.36%) and CH content (0.27–0.5%) than those with 0.5% additive. The higher formation of the ettringite content (or other hydrates) might explain the observed difference in the water content of the hydrates. Meanwhile, the delayed hydration of C_3S and the subsequent formation of CH may also decelerate the pozzolanic reactions, potentially leading to the identification of a higher CH content in the sample.

In summary, the experimental results demonstrate that the inclusion of the synthetic ye'elimite additive (0.5–1%) notably reduces both the initial and the final setting times when preparing ternary blended cement (OPC–FA–Y). However, synthetic ye'elimite also influences OPC hydration and the development of compressive strength. The XRD and TGA results suggest that the addition of synthetic ye'elimite delays or slows down the hydration of calcium silicates, especially during the first week of curing. Consequently, the OPC–FA–Y samples exhibit a lower

compressive strength than the OPC samples. The observed phenomena could be attributed to a variety of factors. One potential factor might be the additional and rapid formation of ettringite or/and the AFm phases, which may restrict the available space for the precipitation of the C–S–H phases [202]. This limitation could restrict the rapid precipitation of C–S–H and CH, consequently slowing down the dissolution of C_3S . It is noteworthy that the OPC–FA–Y samples exhibit a higher amount of hydrate water and the formed CH content after 7 days of hydration than the OPC sample, but they also display a lower compressive strength. This might be attributed to the delayed formation of the hydration products within the hardened stone [68,69]. This phenomenon could induce micro-stress and strain in the structure of the mortar samples (i.e., a volume change), ultimately leading to a reduced compressive strength. It is of importance to emphasize that these are *only* theoretical assumptions that must be further investigated experimentally. Nevertheless, the preparation of OPC–FA–Y blended cement with 0.5–1% synthetic ye'elimite additive does not compromise the compressive strength of mortars after 28 days of hydration compared to pure OPC mortars.

3.8. Ye'elimite Formation during High-Temperature Sintering of Belite-Ye'elimite-Ferrite Clinker and the Properties of the Obtained Cement

As discussed in the literature section, manufacturing pure ye'elimite or CSA cement with a high ye'elimite content entails higher costs compared to OPC, primarily due to the expense of the raw materials, such as bauxite. Meanwhile, belite-ye'elimite-ferrite (BYF) cement requires less aluminium and allows for the use of industrial wastes or by-products in its production, thereby reducing the use of natural resources and the cost of cement production [24]. One such readily available waste in Lithuania is the granite cutting waste. Unfortunately, scientific studies demonstrate that this waste suffers from low reactivity under hydrothermal conditions and is thus unsuitable for the two-stage synthesis of cement [203,204]. Nevertheless, granite cutting waste contains a significant amount of silicon oxide and aluminium oxide, which are essential components for producing the BYF clinker. Additionally, this waste contains ~7.5% alkali, which might act as a fluxing element and lower the sintering temperature. Therefore, the final stage of the research focused on the pilot synthesis of the BYF cement by using a solid-state reaction method incorporating industrial waste as the raw material. Therefore, the final phase of the research focused on conducting a trial synthesis of the BYF cement by adopting the solid-state reaction method. This strategy involved evaluating the formation of ye'elimite during high-temperature sintering and the assessment of the resulting properties of the cement.

First, the impact of the sintering temperature on the development of the BYF clinker phases was examined, with the temperatures ranging from 1000 °C to 1250 °C. The initial mixture was prepared from industrial waste (~18%) (granite cutting waste and silica-gel waste from AlF_3 production) and natural raw materials (~82%), thereby targeting the clinker composition of 60% belite, 20% ye'elimite, and 20% ferrite. It was determined that, following solid sintering at temperatures of 1000–

1050 °C, the samples exhibited the formation of belite, mayenite, brownmillerite, and ye'elimite (Fig. 3.41). However, this temperature interval is insufficient for the initial material to react fully, i.e., the characteristic diffraction peaks of quartz are still observed in the XRD patterns.

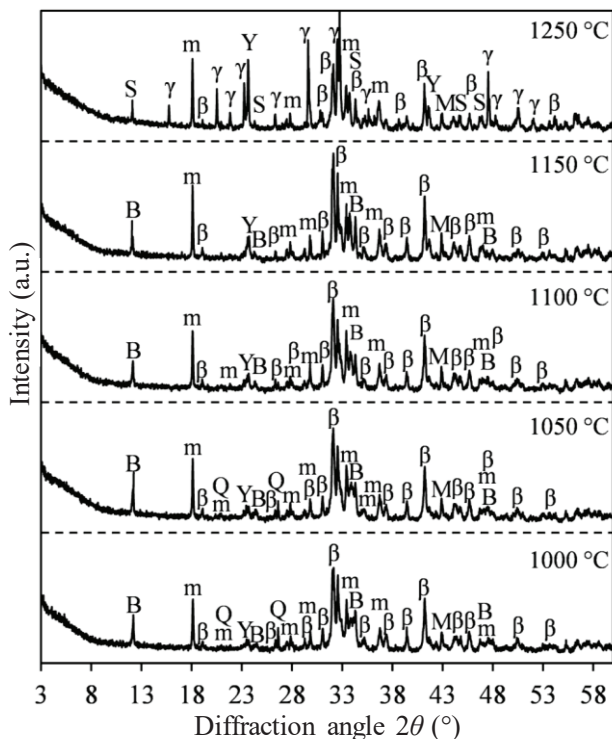


Fig. 3.41. XRD patterns of BYF clinker sintered at different temperatures for 1 h. Indexes: Q – quartz, S – srebrodolskite; m – mayenite, β – belite (β - C_2S), γ – dicalcium silicate (γ - C_2S), M – magnesium oxide, Y – ye'elimite, B – brownmillerite

Further temperature increments induce the solid-state reactions, leading to the complete reaction of quartz at 1100 °C (Fig. 3.41). Moreover, the temperature promotes the formation of the aforementioned crystalline phases. It is noteworthy that, due to the interaction between MgO and brownmillerite, srebrodolskite ($Ca_2Mg_{0.1}FeAl_{0.9}O_5$, PDF No. 04-014-9001), a cognate phase of brownmillerite (a ferrite phase) is observed in the XRD patterns at 1250 °C. It is crucial to note that a temperature increment exerts the most significant influence on the formation of ye'elimite, with the highest intensity of its diffraction peaks being observed at 1200–1250 °C. Nevertheless, despite the rapid cooling of the clinkers (reaching room temperature within 5 min), it was observed that β - C_2S which was formed at these temperatures is unstable, which leads to the recrystallisation into γ - C_2S in the samples. Other authors have also observed the formation of γ - C_2S during extended

holding times at high temperatures during the BYF clinker calcination process [188]. It is of importance to note that the formation of γ -C₂S in the clinker is undesirable because of its low hydration activity [205]. Additionally, it is noteworthy that the concentration of F⁻ ions in the initial batch is below 0.04%. Consequently, no compounds containing fluorine were identified in the XRD analysis, likely due to equipment limitations or because of the overlap of the intensive diffraction peaks from other cement phases.

Based on the obtained results, the temperature chosen to produce the BYF clinker was 1150°C, and the dwell duration was extended to 2 h. This adjustment aimed to ensure the uniform sintering of the initial mixture due to the increased quantity of the initial batch (20 g → 500 g). The quantitative phase analysis results indicate that the produced BYF clinker contains 53.5% belite, 17.4% mayenite, 15.3% srebrodolskite, 5.2% ye'elimite, 4.8% gehlenite (Ca₂Al₂SiO₇, PDF No. 00-009-0216), 3.2% magnesium oxide, and 0.6% other phases (Fig. 3.42).

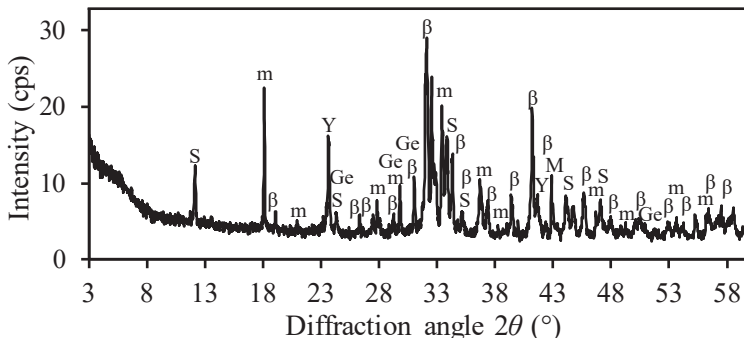


Fig. 3.42. XRD pattern of BYF clinker sample sintered at 1150 °C for 2 h. Indexes: β – belite (β -C₂S), m – mayenite, M – magnesium oxide, Y – ye'elimite, S – srebrodolskite, Ge – gehlenite

As previously discussed in the literature review, the addition of gypsum is crucial for regulating the rate of hydration (the setting time) of cement. Therefore, the amount of the gypsum additive which is necessary to achieve the optimal hydration of the synthesized belite cement was determined by conducting a calorimetric study (Fig. 3.43). It was established that samples with 5% and 7.5% of a gypsum additive exhibit two exothermic peaks. The initial exothermic reaction in both investigated samples lasted ~1 h with similar values of the heat flow maximum (0.046–0.048 W/g) being observed. This effect can be attributed to the wetting of binder grains, their superficial dissolution, and the initial hydration processes, mainly related to the interaction between C₁₂A₇, C₄A₃Ŝ, and gypsum. In most cases, this leads to the precipitation of hydrates, such as ettringite and aluminium hydroxide [39,137].

The next stage of hydration is the induction period, which, in the sample with 5% gypsum, lasts for ~1 h, while, in a sample with a higher amount of gypsum (7.5%), it extends to ~1.5 h. This stage is associated with the release of the inhibited heat and the initiation of hydration nuclei, leading to the growth of the layer of hydrates on the

surface of the cement phases [68]. When the induction period has been completed, the second exothermic reaction follows. It was observed that the peaks of the heat flow maximum of both samples are similar (~ 0.04 W/g), occurring after ~ 2 h (with 5%) and ~ 3 h (with 7.5%) of hydration.

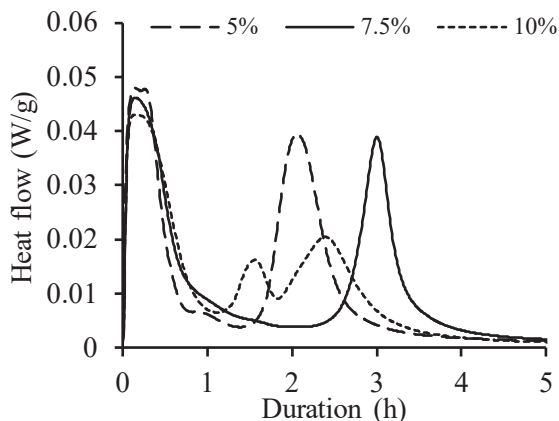


Fig. 3.43. Heat flow curves of BYF cement samples with different gypsum additive

Interestingly, a further increase of the gypsum additive to 10% has a detrimental effect on the BYF cement hydration, i.e., the main hydration reactions proceed immediately after the first exothermal peak (Fig. 3.43). Moreover, this reaction occurs in stages, as reflected by two exothermic reactions which occur between ~ 1 h and ~ 4 h of hydration. It is likely that the gypsum excess does not slow down, but, instead, accelerates the hydration of the cement phases, thus causing the false set effect. As a result, a premature setting of cement paste might be observed. As indicated in the literature [68,206], such an occurrence is undesirable in cement chemistry because some primary hydration reactions occur in the already-hardened stone. Consequently, this may lead to a decrease in the strength of the cement stone. It is worth noting that, despite the addition of gypsum, the monitored values of cumulative heat remain close, ranging from 255 J/g to 258 J/g. Based on the results of the calorimetry study, the BYF cement with a 7.5% gypsum additive was selected for further investigations.

It is known that the compressive strength of concrete is a critical factor which determines the potential applications of cement. Therefore, in the next step, the compressive strength and hydration behaviour of mortars (with a 1:3 ratio of cement:sand) were performed by using the prepared BYF cement. The investigation was conducted in a water environment at 20 °C, during which, samples were cured for up to 90 days. The test results indicate that the prepared mortars demonstrate a slow compressive strength development (Table 3.15), with values increasing from 4.25 MPa after 3 days to 10.35 MPa after 90 days of curing in the water environment. It is worth indicating that the observed slight decrement of the compressive strength (by 0.2 MPa) after 14 days of curing has also been reported in other studies [124,184]. However, the reason behind this phenomenon is debated, but it may be attributed to

It is worth observing that, due to the diverse phase composition of the synthesized BYF clinker, other compounds could also form during the hydration of mortar samples, including hydrogarnet (C_3AFSH_4), monosulfoaluminate, portlandite (CH), aluminium hydroxide (AH_3), calcite ($CaCO_3$), and so forth. However, they cannot be clearly distinguished in the XRD patterns, likely due to their low crystallinity and/or small quantities.

Table 3.16. Changes in the main diffraction peaks of compounds during the curing of BYF mortar samples.

Compound	Duration	Intensity of peaks (cps)					
		3 days	7 days	14 days	28 days	56 days	90 days
Belite (0.279 nm)		579	563	557	548	334	319
Ettringite (0.973 nm)		382	379	397	404	443	436
Stratlingite (1.250)		320	421	452	472	348	389
Ferro-actinolite (0.837)		322	353	349	450	377	375
Magnesium oxide (0.211)		312	307	316	245	202	197
Katoite (0.505)		214	237	253	257	196	231
Calcite (0.303)		207	209	213	213	223	253

The XRD results were also confirmed by the STA data (Fig. 3.45.a). It was determined that the mortar samples cured for 3 days display 4 endothermic effects in the DSC curve. The first effect at $\sim 105^\circ C$ can be assigned to the removal of adsorption water and the decomposition of ettringite and compounds of an amorphous structure [25,137]. The second endothermic effect (at $159^\circ C$) can be related to the dehydration of the AFm phases, such as monosulfoaluminate, hemi- and monocarboaluminates.

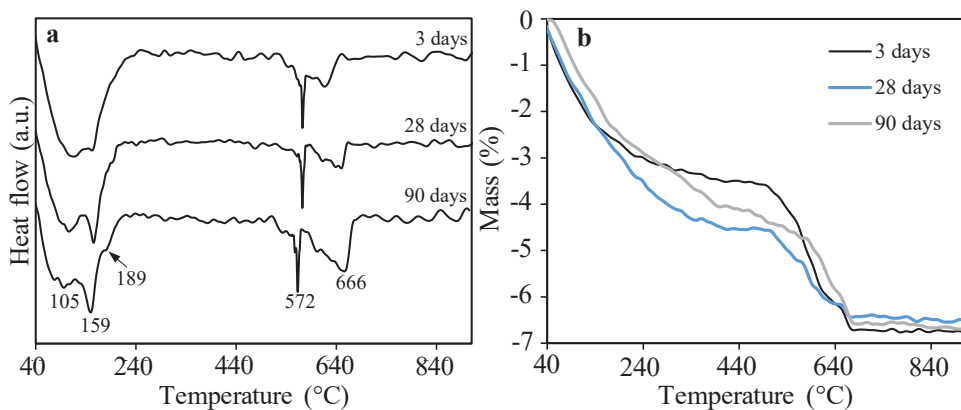


Fig. 3.45. STA curves (a – DSC, b – TG) of mortar samples after different durations of curing

It is worth noting that the decomposition of such phases as hydrated calcium aluminates (CAH_{10} , C_2AH_8) and hydrated calcium aluminosilicates of the

hydrogehlenite (C_2ASH_8) and hydrogarnet ($C_3AS_3-C_3AH_6$) types typically occurs at 180–230 °C [201]. Meanwhile, the main dehydration of C–S–H is identified within the temperature interval of 50–230 °C, whereas katoite dehydrates at 320–400 °C [208,209]. Referring to the TG results, it is observed that the mass loss of the hydration products at temperatures up to 240 °C amounts to ~2.9% (Fig. 3.45.b). Further, at higher temperatures (510–740 °C), two endothermic effects are observed which reflect reversible transformations of quartz $\alpha \leftrightarrow \beta$ phase (at ~572 °C) and the decomposition of calcium carbonate (~666 °C) [210].

It was observed that, from 3 days to 28 days of curing, belite continues to exhibit slow hydration, as evidenced by the fact that the intensity of the main belite diffraction peak decreases by only ~5% (Fig. 3.44 and Table 3.16). Furthermore, an increase in the intensity of the peaks of the hydration products is also observed. The most significant differences are noted in stratlingite and ferro-actinolite, with their diffraction peaks increasing approximately by 1.5 and 1.4 times, respectively. This increment is likely attributed to the interaction between C_2S and AH_3 (resulting from the hydration of ye'elimite), which leads to the formation of calcium aluminosilicate hydrates [166]. These results were also confirmed by STA, demonstrating the mass loss increase in the temperature interval of 30–550 °C (Fig. 3.45.b). Moreover, a slight shoulder at around 192 °C is identified, likely resulting from increased quantities of semi-crystalline C–S–H, hydrated calcium aluminates, and other hydration products in the mortar samples.

The investigation reveals that an increase in the strength of mortar samples observed during further curing (up to 90 days) is primarily attributed to the hydration of belite, evidenced by the decrease in the intensity of the main peak by ~45% (Table 3.16). Moreover, it is estimated that the intensities of the diffraction peaks of ettringite and calcite increased by ~7% and ~16%, respectively, while those of the other major hydration products decreased by 10–18%. The reduction in the hydration products is also monitored by the STA results (Fig. 3.45). After 90 days of curing, the mass loss of the samples in the temperature range of 30–240 °C slightly decreases, up to ~2.8%. The reduction in the mass loss may be partly attributed to the partial recrystallization of the C–S–H gel into more ordered structures with a lower water content, which necessitates higher temperatures for decomposition (note a shoulder at 189 °C). It is probable that the C–S–H gel undergoes recrystallization to compounds with a lower Ca/Si ratio, as the dehydration temperature of the C–S–H gel tends to increase with a decreasing Ca/Si ratio [211].

Compared to Ordinary Portland cement, the drawback of the synthesized BYF cement is its comparatively slower rate of the development of mortar strength. The performed experiments demonstrated that this weak strength development appears due to the slow hydration of the main compound – belite. Meanwhile, the initial hydration of the presently discussed cementitious phases (mayenite, srebrodolskite, ye'elimite, gehlenite) in the BYF cement contributes only marginally to the mortar strength. It is known that the optimization of the curing conditions, such as the temperature and the required humidity, can accelerate the hydration process of the

cement phases, which can also contribute to the increase in the strength development [212]. For this reason, the curing assessment of the prepared BYF cement mortars was conducted in a saturated water vapour environment at temperatures ranging from 90 to 200 °C, with a treatment duration of 24 h.

As expected, the temperature of hydrothermal curing significantly influences the mechanical properties of the BYF cement mortars (Table 3.17). It is determined that the hydrothermal curing of the BYF mortars at 90–125 °C adversely affects their strength development, by reducing it from 3.92 MPa to 1.22 MPa. Nevertheless, a significant increase in the compressive strength of the BYF cement mortars is observed when the samples are cured at ≥ 150 °C. The highest compressive strength values of the BYF mortars are achieved by curing samples at 200 °C for 24 h, which is twice as high as the values obtained in samples cured in a water environment after 90 days. It is worth noting that the obtained compressive strength values of the produced BYF mortars cured at 200 °C for 24 h conform to the values defined by the standards for masonry products (EN 771-2).

Table 3.17. Strength development of BYF cement mortar samples cured in hydrothermal environment at different temperatures with an isothermal time of 24 h

Temperature	90 °C	100 °C	125 °C	150 °C	175 °C	200 °C
Compressive strength (MPa)	3.92	2.68	1.22	15.25	18.32	20.07
Flexural strength (MPa)	1.9	0.9	0	2.50	3.30	3.70

The data collected from the experiments conducted on BYF cement highlights several important aspects requiring discussion. Firstly, it has been established that a temperature of 1150 °C is sufficient for the formation of the majority of the BYF phases. Meanwhile, a notable increase in the intensity of the ye'elimite peaks is observed above this temperature. As a result, after sintering the BYF clinker at 1150 °C for 2 h, the identified composition of the belite and ferrite phases closely matches the expected content, i.e., 53.5% and 15.3%, respectively. However, the estimated content of ye'elimite significantly differs, being ~4 times less than expected. Instead, calcium aluminate (17.4% mayenite) is identified in the BYF clinker. The literature also discusses this phenomenon [52], confirming that the observed calcium aluminates are intermediate phases during the synthesis of ye'elimite, resulting from an insufficient thermal energy for solid-state reactions. Secondly, the formed cementitious phases (mayenite and gehlenite) fail to compensate for the initial strength of the mortar samples, resulting in low compression strength values during the curing in the water environment. While the hydrothermal curing results suggest potential applications for the prepared BYF cement, the determined properties will constrain its broader production and application. Thirdly, and perhaps most importantly, these results highlight the potential of the hydrothermal-calcination method for producing the BYF cement. As discussed in the previous sections, the utilization of the hydrothermal-calcination method facilitates a decrease in the sintering temperature required for the formation of ye'elimite. Inclusion of

hydrothermal treatment while following the same calcination conditions is highly likely to promote the formation of ye'elinite in the BYF clinker, especially when utilizing wastes or by-products that are highly reactive under hydrothermal conditions. Additionally, depending on the phase composition, this approach could potentially reduce the overall sintering temperature required for synthesizing the BYF clinker, potentially by 100–150 °C. Nevertheless, these findings confirm that the waste materials and the natural resources available in Lithuania can effectively contribute to the production of the BYF cement. Meanwhile, when cured hydrothermally, the resulting mortar samples meet the compressive strength values outlined for masonry products.

4. CONCLUSIONS

1. It has been determined that the optimal hydrothermal synthesis conditions for the formation of calcium monosulfoaluminate 12-hydrate (Ms12, precursor) are: 110 °C for 8 h. The prior mechanochemical treatment (three 10 min on-off cycles at 900 rpm) of the initial mixture promotes the crystallization of MS12 and prevents the formation of ettringite, katoite, and portlandite. The obtained experimental results are supported by thermodynamic calculations.
2. The carbonation behaviour of Ms12 is governed by the water vapour pressure. This compound is most resistant against carbonation at 0.355 p/p_0 . The final carbonation products after 90 days under all conditions include calcium carbonate, aluminium hydroxide and calcium sulphate hydrate (if ≤ 0.565 , p/p_0 – hemihydrate; if ≥ 0.565 , p/p_0 – gypsum). At sufficient moisture levels (0.753–1.0 p/p_0), it is observed that Ms12 also converts to ettringite. The apparent kinetic calculations show that the carbonation reaction rate directly depends on the content of external moisture. Meanwhile, the adopted Jander and Avrami models suggest that the dissolution and nucleation processes control the formation of one-dimensional CaCO_3 crystal growth.
3. The thermal stability assessment has confirmed that the temperature interval for the dehydration of monosulfoaluminate is 25–370 °C, where four different hydration states of monosulfoaluminate are identified (Ms12→Ms10.5→Ms9→Ms6-x). The data proposes that the removal of water molecules from the main (octahedral) layers begins at ~200 °C. At 720–1250 °C, the solid-state reactions between C_2S , CA, C_{12}A_7 , and CaO are observed, generating the formation of ye'elimite. The optimal sintering conditions for producing high-purity (~97%) ye'elimite are 1150 °C for 1 h.
4. It has been established that ye'elimite produced by adopting the two-stage synthesis method displays the five typical stages of cement hydration. The induction period lasts 10 h 10 min, the second exothermic reaction maximum occurs after 14 h 45 min, and the cumulative heat value after 72 h of hydration is ~585 J/g. The ye'elimite hydration results in the formation of monosulfoaluminate, ettringite, and amorphous/microcrystalline aluminium hydroxides.
5. It has been observed that partial substitution of synthetic ye'elimite with fly ash accelerates its hydration, which is attributed to an increased alkalinity content in the system (whose influence is the strongest), additional nucleation sites (the filler effect), and a higher water-to-binder ratio. The inclusion of fly ash possibly restricts the formation and/or promotes the decomposition of monosulfoaluminate, feasibly leading to the additional formation and/or stabilization of ettringite during hydration.
6. It has been determined that the incorporation of 0.5–1% synthetic ye'elimite in Ordinary Portland-fly ash blended cement effectively decreases both the initial

and the final setting times without compromising the compressive strength of mortars after 28 days of curing compared to the pure OPC mortar.

7. It has been determined that the produced belite-ye'elinite-ferrite mortars demonstrate a slow development of strength (~10 MPa after 90 days) when cured in a water environment, attributed to the slow hydration of the main cementitious phase – belite. Meanwhile, the curing mortar samples under hydrothermal conditions improve the compressive strength; the samples reach their highest strength of ~20 MPa at 200 °C sustained for 24 h.

5. SANTRAUKA

5.1. Įvadas

Šiuo metu dėl nuoseklios urbanizacijos ir industrializacijos metinis suvartojamo betono kiekis padidėjo iki stulbinam 30 milijardų tonų. Dėl tokios didžiulės statybinių medžiagų paklausos cemento pramonė yra atsakinga už ~8 % pasaulio antropogeninių šiltnamio efektą sukeliančių dujų emisijų. Atsižvelgiant į klimato krizę ir tarptautinius susitarimus, tokius kaip Paryžiaus susitarimas ir Europos žaliasis kursas, cemento pramonė turi įvykdyti reikšmingus pokyčius, kuriais būtų sumažinamas gamybos metu išskiriamas CO₂ pėdsakas. Per pastaruosius dešimtmečius buvo įdiegta daugybė sprendimų, kaip sumažinti neigiamą cemento gamybos poveikį aplinkai. Vis dėlto nors papildomų cementinių medžiagų, alternatyvaus kuro naudojimas ir naujų gamybos technologijų bei procesų diegimas yra žingsniai teisinga kryptimi, šie metodai tik iš dalies sprendžia minėtą problemą. Dėl šios priežasties statybinių medžiagų pramonė ir mokslo bendruomenė susiduria su dideliais iššūkiais kurdamos naujas alternatyvias rišamąsias medžiagas, kurios gali sumažinti poveikį aplinkai, išlaikydamos panašias eksploatacines savybes ir gamybos sąnaudas, kaip ir įprastinis cementas.

Cementai, į kurių sudėtį įeina jelimitas, yra patraukli mažai anglies dioksido išskiriančių rišamųjų medžiagų kategorija. Šios cemento rūšys patrauklios tuo, kad joms pagaminti reikalingas mažesnis CaO/SiO₂ santykis ir kalcinuoti reikalinga temperatūra yra žemesnė ~200 °C, lyginant su įprastiniu portlandcemenčiu. Dėl to gamybos metu išmetamas CO₂ pėdsakas sumažėja iki 25–35 %. Jelimitas yra kalcio sulfoaluminatas (4CaO·3Al₂O₃·SO₃), atliekantis lemiamą vaidmenį reguliuojant pradines betono hidratacijos charakteristikas ir galutines mechanines savybes. Dėl šių priežasčių vis daugiau mokslininkų savo dėmesį skiria šio junginio sintezei ir savybių tyrimams. Šiuo metu didelio grynumo jelimito sintezei taikomi du metodai: 1) kietojo kūno reakcijos metodas, kurį taikant pradinių medžiagų mišinys iš kalcio karbonato, aliuminio oksido ir gipso sukepinamas 1250–1350 °C temperatūroje. Svarbu tai, kad pagal šį metodą didelio grynumo jelimito milteliai sintetunami keliais malimo, mišinio presavimo ir sukepinimo ciklais. Be to, jelimito ir anhidrito nestabilumas aukštoje temperatūroje (>1300 °C) apsunkina sintezės procesą; 2) zolių-gelių metodas (cheminis būdas) apima gelio paruošimą, kaip pradines žaliavas naudojant neorganines metalų druskas (Ca(NO₃)₂·4H₂O, Al(NO₃)₂·9H₂O ir Al₂(SO₄)₃·16H₂O) su polimerų pirtakais, kuris paskui sukepinamas 1250 °C temperatūroje. Šio metodo trūkumas – jis užima daug laiko, jam taikyti reikalingos brangios medžiagos ir įranga. Kitas pažangus dviejų stadijų metodas, taikomas didelio grynumo cemento fazėms (pvz., β-C₂S, C₃A, C₁₂A₇ ir kt.) gaminti, apima cemento hidratų hidroterminę sintezę ir gautų pirtakų kalcinavimą. Šis metodas patrauklus tuo, kad leidžia sumažinti galutinę kalcinavimo temperatūrą, o susidarantys junginiai yra didelio grynumo ir reaktyvumo. Be to, šios sintezės metu galima lengvai kontroliuoti susidarantių junginių pagrindinius fizikinius parametrus, tokius kaip savitasis paviršiaus plotas, dalelių dydis, kristališkumas ir kt.

Visgi mokslinėje literatūroje trūksta duomenų apie šio dviejų stadijų metodo taikymą didelio grynumo jelimito gamybai. Kalbant apie šį sintezės metodą, norimos tikslinio produkto savybės tiesiogiai priklauso nuo įvairių veiksnių, įskaitant žaliavų paruošimą, hidroterminės sintezės sąlygas (temperatūrą ir trukmę), pirmtakų stabilumą, sukepinimo aukštoje temperatūroje sąlygas (temperatūras ir trukmę) ir kitus susijusius parametrus. Tikėtina, kad šis sintezės metodas leistų susintetinti didelio grynumo jelimito miltelius sumažinant kalcinavimo temperatūrą ir suteiktų daugiau įžvalgų apie jelimito susidarymo mechanizmą. Be to, gautas produktas galėtų būti veiksmingas priedas cemento mišiniuose, gerinantis jų rišamąsias savybes, o pasiūlyta technologija galėtų būti taikoma cementų, turinčių jelimito, gamybai.

Darbo tikslas

Ištirti jelimito susidarymą dviejų stadijų metodu, kuris apima atitinkamos sudėties pirmtako hidroterminę sintezę ir jo kalcinavimą, nustatyti gaunamų junginių susidarymo seką ir hidratacijos savybes, taip pat pasiūlyti galimas gauto produkto naudojimo sritis.

Darbo uždaviniai

1. Nustatyti pradinio mišinio mechanocheminio aktyvinimo bei hidroterminės sintezės parametrų įtaką kalcio monosulfoaluminato 12-hidrato susidarymo procesams.
2. Ištirti vandens garų slėgio įtaką kalcio monosulfoaluminato 12-hidrato sudėties pokyčiams, esant aplinkos CO₂.
3. Nustatyti terminio apdorojimo sąlygų įtaką kalcio monosulfoaluminato 12-hidrato stabilumui ir jelimito susidarymo mechanizmui.
4. Išnagrinėti sintetinio jelimito ankstyvosios hidratacijos ypatumus ir įvertinti silicinių lakiųjų pelenų (V klasė) įtaką jo hidratacijai.
5. Įvertinti į pelenų portlandcementį įmaišyto ir belitiniame-jelimitiniame-feritiniame cemento susidariusio jelimito įtaką jų kietėjimo procesui, hidratacijai, susidarančių produktų mineralinei sudėčiai ir stiprumui.

Disertacijos ginamieji teiginiai

1. Mechanocheminis pradinio mišinio aktyvinimas skatina tikslinio hidroterminės sintezės produkto – kalcio monosulfoaluminato 12-hidrato – susidarymą.
2. Dalinis vandens garų slėgis reguliuoja kalcio monosulfoaluminato 12-hidrato karbonizacijos greitį ir skatina tarpinių bei galutinių produktų susidarymą.

Mokslinio darbo naujumas

1. Įrodyta, kad mechanocheminis aktyvinimas (trys 10 min įjungimo ir išjungimo ciklai esant 900 aps./min) ir dviejų stadijų metodas (hidroterminė sintezė 110 °C 8 h ir kalcinavimas 1150 °C 1 h) leidžia sumažinti sukepinimo temperatūrą 150 °C ir pagaminti didelio grynumo (~97 %) jelimitą.
2. Nustatyta, kad lakiųjų pelenų priedas greitina jelimito ankstyvąją hidrataciją dėl padidėjusio šarmingumo sistemoje (turi stipriausią įtaką), papildomų branduolių

susidarymo vietų (užpildo efektas) ir padidėjusio vandens bei rišamosios medžiagos santykio.

Praktinė vertė

1. Jelimito priedas (0,5–1 %) gali būti naudojamas kaip pelenų portlandcemenčio rišimosi greitiklis, nes $\sim 1,7$ karto sutrumpina jo tešlos rišimosi pradžios ir pabaigos trukmes.
2. Belitinio-jelimitinio-feritinio cemento skiedinių hidroterminis apdorojimas teigiamai veikia stiprumo raidą, o kietinant skiedinio bandinius 200 °C 24 val. nustatytos gniuždymo stiprio vertės atitinka mūro gaminių (EN 771-2) standarte nustatytas vertes.

Darbo aprobavimas ir publikavimas

Disertacijos darbo tema paskelbtos penkios mokslinės publikacijos recenzuojamuose mokslo leidiniuose *Web of Science* duomenų bazėje, indeksuotuose leidiniuose su citavimo rodikliu JCR SCIE. Iš darbo rezultatų parengta ir Lietuvos patentų biurui įteikta viena paraiška (Nr. LT2024 002), rezultatai pristatyti šešiose tarptautinėse mokslinėse konferencijose.

Autoriaus ir bendraautorių mokslinis indėlis

D. Rubinaitė sudarė tyrimų planą, ištyrė dviejų stadijų sintezę, kalcio monosulfoaluminato 12-hidrato stabilumą, sintetinio jelimito hidratacijos savybes ir trijų komponentų mišinio cemento kietėjimo savybes, atliko šiame darbe aprašytus teorinius skaičiavimus. Prof. dr. Raimundas Šiaučiūnas konsultavo Kauno technologijos universitete atliktų tyrimų eigos ir rankraščių rengimo klausimais. Dėl eksperimentų ir teorinių skaičiavimų konsultavo doc. dr. Tadas Dambrauskas. Eksperimento eigos ir rankraščių rengimo klausimais konsultavo prof. dr. Kęstutis Baltakys. Doc. dr. Anatolijus Eisinas konsultavo kinetinių skaičiavimų ir technologinės schemos klausimais. Prof. dr. Alisa Machner ir dr. Anne Heisig konsultavo Miuncheno technikos universitete dėl atliekamų eksperimentų eigos. Dr. Harald Hilbig konsultavosi dėl ^{27}Al branduolinio magnetinio rezonanso spektroskopinės analizės rezultatų.

Darbo apimtis

Disertaciją sudaro įvadas, literatūros duomenų analizė, eksperimentinė dalis, tyrimų rezultatai ir jų aprašymas, išvados, 212 literatūros šaltinių sąrašas ir mokslinių publikacijų sąrašas. Pagrindinė medžiaga išdėstyta 182 puslapių, įskaitant 25 lenteles, 59 paveikslus ir 1 priedą.

5.2. Medžiagos ir metodai

5.2.1. Naudotos medžiagos

Kalcio karbonatas (CaCO_3 , $\geq 99,0$ %, „Eksparas“, Lietuva). CaCO_3 buvo kalcinuotas 950 °C temperatūroje 1 h (kaitmenys – 42,98 %; laisvas CaO ~98,1 %).

Aluminio hidroksidas ($\text{Al}(\text{OH})_3$, $\geq 99,0$ %, „Honeywell“, Vokietija). $\text{Al}(\text{OH})_3$ buvo išdegtas 475 °C temperatūroje 4 h (kaitmenys – 34,28 %).

Gipsas ($\text{CaSO}_4 \cdot 2\text{H}_2\text{O}$, $\geq 99,0$ %, „Lach–Ner“, Lenkija).

Akmens anglių siliciniai **lakieji pelenai** (V klasė) (SAFAMENT, Vokietija). Nustatyta tokia mineraloginė sudėtis: 24,9 % mulito ($\text{Al}(\text{Al}_{0,8}\text{Si}_{1,08}\text{O}_{4,85})$, PDF Nr. 01-089-2645), 8,9 % kvarco (SiO_2 , PDF Nr. 00-005-0490), 0,9 % hematito (Fe_2O_3 , PDF Nr. 01-076-9683), 0,7 % magnetitos (Fe_3O_4 , PDF Nr. 00-065-0731), 0,2 % kalcio oksido (CaO , PDF Nr. 01-077-2010), 0,1 % anatazės (TiO_2), 0,2 % magnio oksido (MgO , PDF Nr. 00-045-0946) ir 64,1 % amorfinės fazės.

Klintermilčiai (LS) („Max Bögl Stiftung und Co. KG“, Wiesenhofen, Vokietija). Nustatytos fazės kalcio karbonatas (~97,1 %) (CaCO_3) ir kalcio oksidas (CaO).

Portlandcementis (OPC) (CEM I 42.5N, AB „Akmenės cementas“, Lietuva). Nustatyti mineralai OPC: alitas (Ca_3SiO_5 , PDF Nr. 04-018-9702), larnitas (Ca_2SiO_4 , PDF Nr. 00-033-0302), braunmilleritas ($\text{Ca}_2\text{FeAlO}_5$, PDF Nr. 01-072-7995), trikalcio aluminatas ($\text{Ca}_3\text{Al}_2\text{O}_6$, PDF No. 00-006-0495), gipsas ($\text{CaSO}_4 \cdot 2\text{H}_2\text{O}$, PDF Nr. 04-010-9409) ir magnio oksidas (MgO).

Standartinis smėlis CEN atitinka standartą EN 196-1 („Normensand“, Vokietija).

Klinteris (~92,8 % CaCO_3 , AB „Naujasis kalcitas“, Lietuva).

Silikagelis, aluminio fluorido gamybos atlieka (UAB „Lifosa“, Kėdainiai, Lietuva). Nustatyta sudėtis: aluminio hidroksidas ($\text{Al}(\text{OH})_3$, PDF No. 04-011-1369), aluminio fluorido trihidratas ($\text{AlF}_3 \cdot 3\text{H}_2\text{O}$, PDF No. 00-035-0627), aluminio hidroksido fluorido hidratas ($\text{AlF}_{1,5}(\text{OH})_{1,5}(\text{H}_2\text{O})_{0,375}$, PDF No. 01-074-0940) ir amorfinis silicio dioksidas.

Granitmilčiai, granito gamybos atlieka (UAB „Granitas“, Lietuva). Granitmilčiuose nustatyti junginiai: kvarcas, mikroklinas (KAlSi_3O_8 , PDF No. 04-008-1783), albitas ($(\text{Na,Ca})\text{Al}(\text{Si,Al})_3\text{O}_8$, PDF No. 00-041-1480), annitas-1M ($\text{KFe}_2(\text{Si,Al})_4\text{O}_{10}(\text{OH})_2$, PDF No. 00-042-1413), anortitas ($\text{CaAl}_2\text{Si}_2\text{O}_8$, PDF No. 00-041-1486), aktinolitas ($\text{Na}_{0,08}\text{Ca}_{1,76}\text{Mn}_{0,16}\text{Mg}_{1,88}\text{Fe}_{2,72}\text{Fe}_{0,32}\text{Al}_{0,32}\text{Si}_{7,68}\text{O}_{22}(\text{OH})_2$, PDF No. 00-073-2339) ir labradoritas ($\text{Ca}_{0,64}\text{Na}_{0,35}(\text{Al}_{1,63}\text{Si}_{2,37}\text{O}_8)$, PDF No. 00-083-1371).

Pushidratis gipsas ($\text{CaSO}_4 \cdot 0,5\text{H}_2\text{O}$, „Knauf“, Vokietija).

Geležies (III) oksidas (Fe_2O_3 ≥ 97 %, „Honeywell Riedel de Haën“, Vokietija).

Kitos naudotos medžiagos: natrio hidroksidas (NaOH $\geq 99,0$ %) (Honeywell Riedel-de-Haën™, Vokietija), kalio hidroksidas (KOH $\geq 86,0$ %) (Carl Roth, Vokietija), izopropilo alkoholis (2-propanolis $\geq 99,0$ %) (RECHEM, Slovakija), azoto rūgštis (HNO_3 65 %) (RECHEM, Slovakija).

5.2.2. Taikyti metodai

Pradinių mišinių paruošimas

Pradinė dviejų bandinių, pavadintų S1 ir S2, mišinių sudėtis buvo paruošta naudojant CaO, Al₂O₃ ir CaSO₄·2H₂O remiantis jelimito stechiometrija (Ca₄(Al₂O₃)₃SO₄; CaO/Al₂O₃ = 1,33):

- Ruošiant pradinį S1 bandinio mišinį, pasverti reikiami komponentų kiekiai supilti į plastikinį indą su trimis porcelianiniais malimo kūnais (siekiant užtikrinti homogenizavimo kokybę), sandariai uždaryti ir homogenizuoti 45 min (34 aps./min) naudojant TURBULA TYPE T2F („Willy A Bachofen AG“, Šveicarija) homogenizatorių. Gauta mišinio tankis – 2513 kg/m³, $d_{50} = 4,79 \mu\text{m}$.
- Ruošiant pradinį S2 bandinio mišinį, pasverti reikiami komponentų kiekiai supilti į planetarinį vibracinių diskų malūną „Pulverisette 9“ (FRITSCH, Vokietija) ir malti (mechanochemiškai apdoroti) trimis 10 min įjungimo ir išjungimo ciklais 900 aps./min greičiu. Gauta mišinio tankis – 3290 kg/m³, $d_{50} = 1,57 \mu\text{m}$.

Hidroterminė sintezė

Hidroterminė sintezė buvo vykdyta 1 l nerūdijančiojo plieno autoklave („Parr instruments“, JAV). Bandinių hidroterminiam apdorojimui buvo naudojami 25 ml PTFE indeliai, kuriuose pagaminti pradinių bandinių milteliai (2 g) buvo sumaišyti su distiliuotu vandeniu (vandens ir kietosios medžiagos santykis, V/K, 10), įdėti į autoklavą („Parr Instruments“, Vokietija) ir 1–48 h apdoroti izotermine išlaikymo temperatūroje 100–130 °C. Išlaikymo trukmė pasiekta per 2 h. Hidrotermiškai apdorotų bandinių suspensijos buvo nudekantuotos, perplautos izopropanoliu (~5 min), nufiltruotos ir išdžiovintos 50±0,2 °C temperatūroje 24 h, esant 35 % santykiniam drėgnumui. Didesniam prekursoriaus kiekiui pagaminti suspensija buvo paruošta iš 60 g pradinio mišinio ir 600 ml distiliuoto vandens 1 l autoklave („Parr instruments“ 4621, JAV) ir hidrotermiškai apdorojama 110 °C temperatūroje 8 h. Po hidroterminės sintezės gauta suspensija buvo dekantuojama, nuplaunama ir džiovinama identiškomis sąlygomis, kaip nurodyta anksčiau.

Dalinio vandens garų slėgio įtakos stabilumui tyrimas

Bandiniai buvo tiriami esant aplinkos CO₂ koncentracijai (668±4 ppm), kuri stebėta naudojant „IAQ–Calc“ patalpų oro kokybės matuoklį, (7545, „TSI IAQ–Calc™“, JAV), skirtingoje santykinio vandens garų slėgio (p/p_0) aplinkoje (0,355, 0,565, 0,753, 0,877 ir 1,0). Atitinkamas p/p_0 buvo palaikomas penkiuose atskiruose eksikatoriuose, naudojant įvairias sieros rūgšties tirpalo koncentracijas. Porcelianinės lėkštutės su bandiniu (~1 g) buvo laikomos eksikatoriuose virš skirtingos p/p_0 aplinkos, neleidžiant lėkštutei liestis su rūgšties tirpalu. Eksperimentai buvo atlikti 20±0,5 °C temperatūroje 90 dienų. Bandiniai buvo išimami iš eksikatorių kas savaitę ar dvi ir stebimi mėginių masės pokyčiai per visą eksperimentą.

Terminio stabilumo tyrimas

Pirmiausia buvo ištirtas hidrotermiškai susintetinto prekursoriaus terminis stabilumas, taikant RSDA *in situ* metodą naudojant MTC–HIGHTEMP kamerą („Bruker AXS“, Vokietija). Eksperimentai buvo atlikti 25–1250 °C temperatūroje, kėlimo greitis 50 °C/min. Difraktogramos buvo užregistruotos po 2 min subalansavimo norimoje temperatūroje $2\theta = 8\text{--}38^\circ$ intervale su $\sim 0,02^\circ$ 2θ žingsniu, esant 0,2 s skaičiavimo trukmei per žingsnį.

Antra, jelimito susidarymas kietfazio sukepinimo metu buvo ištirtas naudojant sintetinį prekursorių, taikant kalcinavimo metodą (*ex situ* metodas). Po hidroterminės sintezės ir džiovinimo (24 h 50 °C) mėginiai buvo siojami per 315 μm sietą, kad būtų užtikrintas dalelių pasiskirstymas. Kalcinavimas buvo atliktas aukštatemperatūroje krosnyje (Nabertherm HTC 03/16, Nabertherm, Vokietija), naudojant 4 g bandinio. Reikiama temperatūra (700–1250 °C) buvo pasiekta 10 °C/min temperatūros kėlimo greičiu. Norint pagaminti didesnę sintetinio jelimito kiekį, keraminėje lėkštelėje buvo paskirstytas tolygus prekursoriaus miltelių sluoksnis (~ 60 g, ~ 4 mm storio) ir kalcinuotas reikiamoje temperatūroje.

Ankstyvosios hidratacijos tyrimas

Sintetinių jelimito miltelių ankstyvoji hidratacija buvo ištirta naudojant TAM AIR III mikrokolorimetą („TA Instruments“, JAV). Tyrimai atlikti pagal dvi metodikas: 1) ampulės maišymo eksperimentas; 2) uždaro ampulės eksperimentas. Pagal pirmąją stiklinės ampulės (20 ml) buvo užpildytos 1,80 g sauso bandinio, o švirkštai – vandeniu, atitinkančiu V/K santykį 1,1. Po terminės pusiausvyros į ampulės suleidžiamas vanduo ir kalorimetro viduje maišomas su sausa medžiaga ~ 20 s (1–2 kartus per sekundę). Pagal antrąjį metodą pirmiausia bandinio tešla buvo sumaišyta plastikiniame indelyje, išlaikant tą patį V/K santykį. Pirmąsias 15 s tešla buvo maišoma mentele, paskui 1 min 45 s elektriniu maišytuvu (1700 aps./min). Paruošta tešla ($\sim 3,8$ g) buvo supilta į stiklines ampules ir dedama į kalorimetą. Visi matavimai atlikti 25 °C temperatūroje 72 h. Verta paminėti, kad sintetinio jelimito ir lakiųjų pelenų izoterminės kalorimetrijos duomenys buvo normalizuoti iki 100 % pradinio sintetinio jelimito kiekio kiekviename bandinyje.

Norint ištirti susidariusio hidrato mineraloginę sudėtį, paruošti mėginiai buvo sumaišyti su vandeniu (V/K = 1,1), sudėti į sandarius indus ir kietinti reikiamą laiką 25 °C temperatūroje. Bandinių hidratacija sustabdyta tokia technika: paimtas bandinys rankomis susmulkintas agato grūstuvėje, perplautas izopropanoliu ir džiovinamas 24 h 40 °C temperatūroje. Vėliau mėginiai buvo siojami per 80 μm akučių sietą ir naudojami instrumentinei analizei.

Trijų komponentų cemento mišinių tyrimų metodai

Dalies OPC pakeitimo įvairiais silicinių lakiųjų pelenų ir sintetinio jelimito santykiais įtaka buvo tiriama ruošiant skirtingas trikomponenčių cemento mišinių kompozicijas. Norint paruošti skirtingus mišinius, reikiamos komponentų dalys buvo

pasvertos ir homogenizuojamos 45 min 34 aps./min, naudojant homogenizatorių TURBULA TYPE T2F („Willy A Bachofen AG“, Šveicarija).

Paruoštos cemento mišinio tešlos normali konsistencija ir rišimosi trukmė nustatyta pagal standartą LST EN 196-3 (E), naudojant automatinį Viko prietaisą EO44N („MATEST“, Italija).

Paruošto skiedinio mechaninės savybės nustatytos pagal LST EN 196-1 ir LST EN 197-1 standartus. Skiedinio kubeliai (30×30×30 mm) buvo paruošti, kai vandens ir cemento santykį (V/C) buvo 0,50, cemento mišinio ir standartinio smėlio santykis – 1/3. Paruošti bandiniai kietinti vandenyje (20±1 °C) 2, 7 ir 28 dienas. Gniuždymo stipris buvo nustatytas naudojant gniuždymo ir lenkimo bandymo mašiną MEGA 10-400-50 („FORM+TEST Seidner & Co. GmbH“, Vokietija) 2,4 kN/s gniuždymo greičiu.

Belitinio-jelimitinio-feritinio cemento sintezė ir tyrimų metodai

Atsižvelgiant į cementinių fazių hidraulinį reaktyvumą, pasirinkta belitinio-jelimitinio-feritinio (BYF) klinkerio mineraloginė sudėtis: 60 % $2\text{CaO}\cdot\text{SiO}_2$, 20 % $4\text{CaO}\cdot3\text{Al}_2\text{O}_3\cdot\text{SO}_3$ ir 20 % $4\text{CaO}\cdot3\text{Al}_2\text{O}_3\cdot\text{Fe}_2\text{O}_3$. Remiantis nustatyta žaliavų oksidų sudėtimi ir tiksline BYF klinkerio mineralogine sudėtimi, buvo sukurta lygčių sistema ir apskaičiuota pradinio mišinio sudėtis (žr. 5.1 lent.).

5.1 lentelė. Pradinio mišinio sudėtis BYF klinkeriui paruošti

Žaliavų sudėtis, %	
Klintis	66,67
Pushidratas gipsas	3,17
Granitmilčiai	14,35
Geležies (III) oksidas	2,50
Aliuminio hidroksidas	9,47
Silikagelis	3,81

Norint paruošti BYF klinkerį, pasverti reikiami komponentų kiekiai homogenizuoti (1 h 120 aps./min greičiu) ir mišinys maltas (4 h 60 aps./min greičiu). Paskui mišinys sudrėkintas (V/K = 0,1) ir gauta masė supresuota hidrauline presavimo mašina 10 MPa jėga, kai jėgos kėlimo greitis – 0,5 MPa/s, maksimali apkrova išlaikyta 20 s. Paruoštos tabletės buvo išdegtos penkiais etapais aukštatemperatūroje krosnyje „Nabertherm HTC 03/16“ („Nabertherm GmbH“, Vokietija): 1) temperatūra kelta iki 900 °C temperatūros 5 °C/ min kėlimo greičiu; 2) išlaikyta 30 min šioje temperatūroje; 3) temperatūra pakelta nuo 900 °C iki reikiamos temperatūros (kito nuo 1000 iki 1250 °C) 2 °C/min kėlimo greičiu; 4) šioje temperatūroje išlaikyta 1 h; 5) galiausiai tabletės buvo išimamos karštos (~1000 °C) ir vienu metu smulkinamos ir greitai aušinamos.

Paruošto skiedinio mechaninės savybės nustatytos pagal modifikuotą standartinę LST EN 196-1 ir LST EN 197-1 metodiką. Standartinės prizmės (40×40×160 mm) buvo paruoštos naudojant V/C 0,67, cemento mišinio / standartinio smėlio santykis – 1/3. Paruošti skiedinio bandiniai kietinti pagal dvi metodikas: 1)

suformuotos prizmės 24 h kietinamos 20 ± 1 °C, paskui perkeliama į vandenį ir išlaikomos 3, 7, 14, 28, 56 ir 90 paras 20 ± 1 °C temperatūroje; 2) suformuotos prizmės 3 h kietinamos 20 ± 1 °C, paskui kietinamos 90–200 °C temperatūroje 24 h, kai temperatūros kėlimo greitis – 25 °C/h. Gniuždymo stipris nustatytas pirmiau minėta metodika.

Aktyvaus CaO nustatymas

Analitinėmis svarstyklėmis pasverta medžiaga (1 g) buvo sumaišyta su 150 ml distiliuoto vandens kūginėje kolboje (250 cm^3) ir įdėti 7 stikliniai rutuliai. Kolba švelniai kaitinama 5 min (neleidžiant užvirti), atvėsinama ir vidinės kolbutės sienelės plaunamos distiliuotu vandeniu. Į kolbą įlašinami 2–3 lašai fenolftaleino tirpalo ir titruojama 1 N HCl, kol išnyks rausva spalva, nuolat maišant. Titravimas buvo laikomas baigtu, kai tirpalas išlieka bespalvis 5 minutes.

Aktyvaus CaO keikis apskaičiuojamas taip:

$$X = \frac{N \cdot V \cdot 28.4 \cdot 100}{G \cdot 100} \% \quad (5.1)$$

čia x – CaO aktyvumas, %; V – titruoti sunaudoto HCl kiekis, cm^3 ; n – HCl koncentracija (1 mol/dm^3); m – tyrimui paimto kalcio oksido masė, g.

Dalelių dydžio pasiskirstymo tyrimas

Naudotų medžiagų dalelių dydžio pasiskirstymas buvo nustatytas lazeriniu granulometru CILAS 1090 LD (Cilas, Prancūzija) 0,05–500 μm diapazone. Dispersijos fazė – suslėgtasis oras (2500 mbar), kietųjų dalelių pasiskirstymas oro sraute 12–15 %, matavimo trukmė – 15 s. Papildomai pagal gautus matavimo duomenis buvo apskaičiuotas savitasis paviršiaus plotas.

Tankio nustatymo tyrimas

Mėginių tankis nustatytas naudojant automatinį dujų piknometrą „Ultrapyc 1200e“ („Quantachrome instruments“, JAV). Analizei naudotos helio dujos. Mėginio tankis pateiktas kaip trijų matavimų aritmetinis vidurkis. Tankio matavimo nuokrypis $\pm 0,003$ %.

Savitiosios šiluminės talpos tyrimas

Savitoji šiluminė talpa (C_p) buvo išmatuota safyro metodu. Matavimai atlikti diferencinės skenuojamosios kalorimetrijos kalorimetru „Netzsch Polyma DSC 214“ („Netzsch“, Vokietija). Matavimų parametrai: temperatūros kėlimo greitis – 5 °C/min, temperatūros diapazonas – 10–50 °C, tiglio – aliuminio (Al) su dangčiu, atmosfera krosnyje – azotas, E tipo termopora. Duomenys buvo įvertinti naudojant „NETZSCH Proteus“ programinę įrangą.

Rentgeno spinduliuotės fluorescencinė analizė (RSFA)

Medžiagų elementinė kompozicija buvo nustatyta naudojant rentgeno spinduliuotės fluorescencinį spektrometrą „Bruker X-ray S8 Tiger WD“ („Bruker AXS GmbH“, Vokietija) su Rh vamzdeliu (60 keV), matavimo atmosfera – He. Mėginių analizė buvo atlikta per 63 µm sietą ir supresuota (20 MPa 45 s) į 5×40 mm cilindrinės tabletes. Gauti duomenys buvo analizuojami „SPECTRAPlus QUANT EXPRESS“ programine įranga.

Rentgeno spinduliuotės difrakcijos analizė (RSDA)

Rentgeno spindulių difrakcijos analizė buvo atlikta medžiagų mineraloginei sudėčiai nustatyti. Matavimai buvo atlikti kambario temperatūroje „D8 Advance“ difraktometru („Bruker AXS GmbH“, Vokietija), turinčiu CuK α rentgeno vamzdelį, veikiantį 40 kV ir 45 mA. Junginių reakcijos laipsnis po hidratacijos buvo nustatytas lyginant smailių pokyčių intensyvumą su nehidratuotu mėginio smailės intensyvumu.

Kiekybinė junginių analizė

Kiekybinis junginių (Rietveldo) analizė buvo atlikta Rietveldo metodu, įdiegtu DIFFRAC.TOPAS 4.2 programinėje įrangoje („Bruker AXS GmbH“, Vokietija). Naudotas vidinis etalonas – 10 % ZnO. Užrašant duomenis mėginio laikiklis buvo sukamas, siekiant pagerinti dalelių statistiką ir gauti aukštos kokybės RSDA duomenis. Kristalų struktūros nustatytos naudojant „PDF 2023“ duomenų bazę.

Kristalų dydžio nustatymas

Vidutinis kristalų dydis apskaičiuotas naudojant DIFFRAC.TOPAS 4.2 programinę įrangą. Visos bandinių RSDA kreivės buvo išanalizuotos išskaidant difrakcijos smailes su Gauso ir Lorencio lygčių komponentais. Šiame tyrime naudota Šererio konstanta buvo 0,89.

Termogravimetrinė analizė (TGA)

Junginių termogravimetrinės analizės matavimai buvo atlikti naudojant:

- LINSEIS STA PT 1000 analizatorius („Linseis Massgeraete GmbH, Selb“, Vokietija) su S tipo termopora. Matavimo parametrai: bandinio svoris – 10±0,02 mg, temperatūros kėlimo greitis – 5 °C/min ir 10 °C/min, intervalas – 30–950 °C, dujos – azotas, tiglio – Pt su dangteliu.
- „Netzsch Polyma DSC 214“ analizatorius („Netzsch“, Vokietija) su E tipo termopora. Matavimo parametrai: bandinio masė – 10±0,02 mg, temperatūros kaitinimo greitis – 5 °C/min, temperatūros diapazonas – 15–400 °C, tiglio – aliuminio (Al) tiglio su dangčiu, atmosfera krosnyje – azotas.
- „STA 449 3 Jupiter“ analizatorius („Netzsch“, Vokietija) su E tipo termopora. Matavimo parametrai: bandinio svoris – ~20 mg, temperatūros kėlimo greitis – 10 °C/min, intervalas – 25–900 °C, tiglio – korundinis (Ø 6,8 mm, 85 µL) su dangteliu, atmosfera krosnis – azotas (tėkmės greitis 20 ml/min).

Furjė transformacijos infraraudonųjų spindulių spektroskopija (FTIR)

FTIR analizė buvo atlikta „Perkin Elmer FT–IR Spectrum X“ spektrometru („PerkinElmer“, JAV). Mėginiai buvo analizuojami KBr presuotų tablečių metodu (~1 mg mėginio ir ~200 mg KBr), o spektrai buvo užfiksuoti 4000–400 cm^{-1} diapazone su 1 cm^{-1} spektrine skiriamąja geba.

Skenuojamoji elektroninė mikroskopija ir energija dispersinė rentgeno spektroskopija (SEM–EDS)

Mėginių morfologija iširta naudojant skenuojantįjį elektroninį mikroskopą (SEM) („Helios Nanolab 650“ („FEI“, Olandija) ir energijos dispersinę rentgeno spektroskopiją (EDS) („Oxford Instruments“ (Jungtinė Karalystė), Xmax 20 mm^2 detektorius, „INCA 4.15“ programinė įranga). Greitinimo įtampas – 3 kV ir 50 pA pluošto srovė su vakuumu, esant 5,1 mm ir 2, 5 mm darbiniais atstumams. EDS elementų žemėlapiai gauti naudojant 15 kV greitinimo įtampą ir 1,6 nA pluošto srovę.

²⁷Al Branduolinio magnetinio rezonanso spektrometrija (BMR)

²⁷Al BMR spektroskopija buvo atlikta naudojant „Bruker Avance 500“ spektrometrą („Bruker“, Vokietija), kurio magnetinio lauko stiprumas buvo 11,747 T (²⁷Al rezonanso dažnis – 130,308 MHz). Matavimai atlikti taikant vieno impulso MAS (stebuklingo kampo sukimosi) techniką. Mėginiai buvo įdėti į 4 mm cirkonio oksido rotorių ir sukami 12 kHz dažniu, pasikartojant 0,5 s, iš viso įrašant 2000 nuskaitymų.

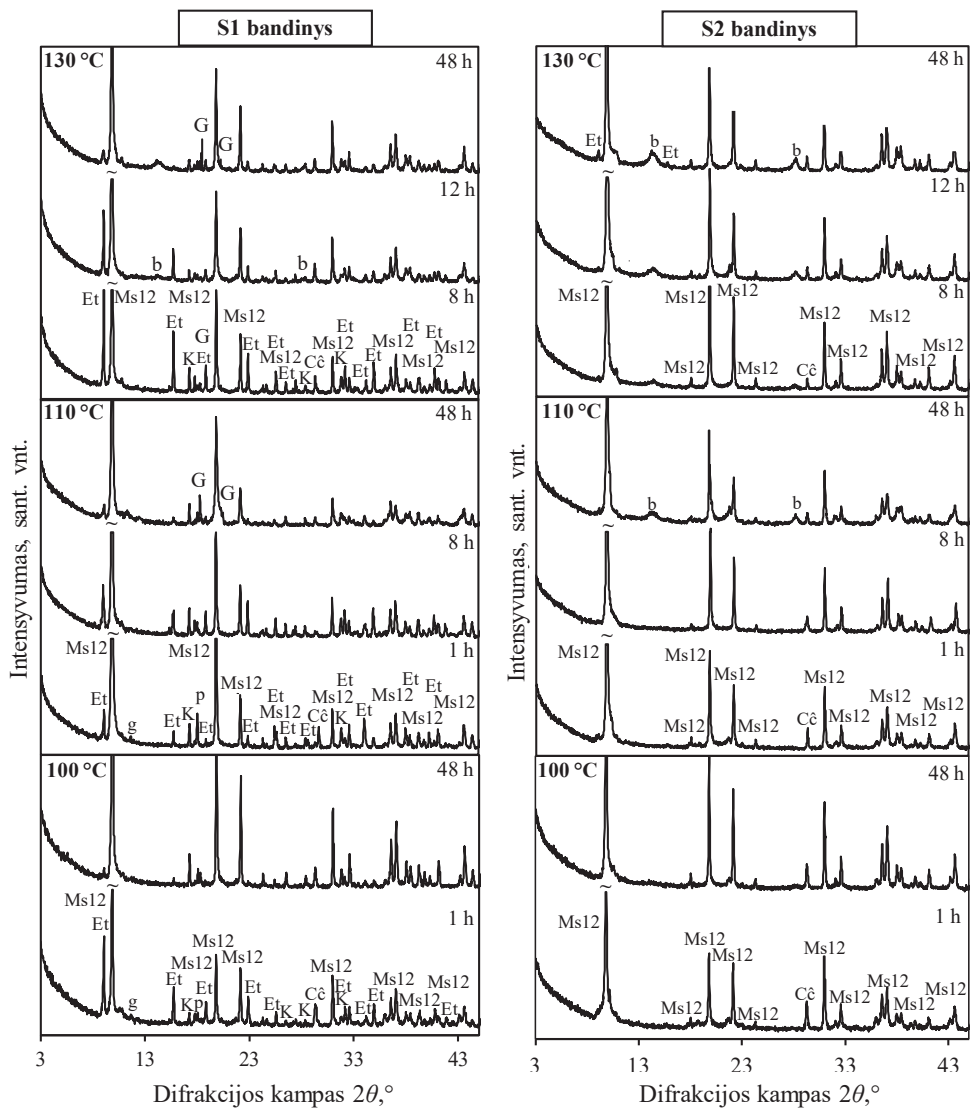
Indukcinė plazminė optinės emisijos spektroskopija (ICP–OES)

Skystųjų fazių sudėčiai nustatyti buvo naudojama indukcinė plazminė optinės emisijos spektroskopija (ICP-OES). Bendros elementų koncentracijos buvo nustatytos naudojant spektrometrą „Optima 8000“ („PerkinElmer Instruments Co.“, JAV). Argonas buvo naudojamas kaip ICP degiklio dujos (7,0 l/min) ir prapūtimo dujos (1,0 l/min). Recirkuliacinės aušinimo sistemos (aušintuvo) parametrai: aušinimo galia, esant 20 °C, 2850 vatų, temperatūros stabilumas – ±0,5 °C ir siurblio greitis – 4 gal/min.

5.3. Rezultatai ir aptarimas

5.3.1. Kalcio monosulfoaluminato 12-hidrato hidroterminė sintezė

Pirmiausia, naudojant RSDA analizę, buvo tiriama hidroterminių sąlygų (temperatūros ir trukmės) įtaka kalcio monosulfoaluminato 12-hidrato (Ms12) susidarymui. Gauti rezultatai pateikti 5.1 pav.



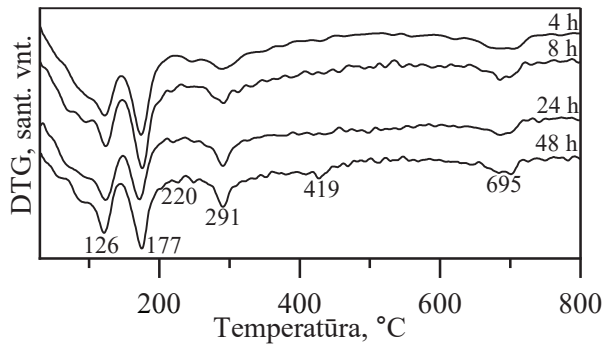
5.1 pav. S1 ir S2 bandinių hidroterminės sintezės produktų RSDA kreivės: Ms12 – kalcio monosulfoaluminato 12-hidratas; Et – etringitas; g – gipsas; K – katoitas; Cc – kalcio karbonatas; b – bemitas; G – gibzitas; p – portlanditas

Nustatyta, kad hidrotermiškai apdorojant S1 bandinį 100–130 °C aplinkoje nepriklausomai nuo izoterminio išlaikymo trukmės, Ms12 ($\text{Ca}_2(\text{SO}_4)_{0.5}(\text{OH})_6(\text{H}_2\text{O})_3$, PDF Nr. 04-013-03303) yra dominuojantis kristalinis junginys sintezės produktuose. Kartu su Ms12 taip pat pastebėtas etringito ($\text{Ca}_6\text{Al}_2(\text{SO}_4)_3(\text{OH})_{12}(\text{H}_2\text{O})_{26}$, PDF Nr. 04-013-3691), katoito ($\text{Ca}_3\text{Al}_2(\text{OH})_{12}$, PDF Nr. 00-024-0217), portlandito ($\text{Ca}(\text{OH})_2$, PDF Nr. 00-044-1481) ir kalcio karbonato (CaCO_3 , PDF Nr. 01-080-2793) susidarymas S1 bandinyje. Ištirta, kad sintezės temperatūros didinimas skatina Ms12 susidarymą, o išlaikymo trukmės ilginimas (12–48 h) skatina šio junginio skilimą. Visgi aukštesnėje sintezės temperatūroje taip pat identifiкуotas etringito ir katoito susidarymas, o ilgesnė išlaikymo trukmė skatina šių junginių skilimą, bet inicijuoja aliuminio hidroksidų, tokių kaip gibsitą ($\text{Al}(\text{OH})_3$, PDF Nr. 04-013-6979) ir mažo kristališkumo bemitą ($\text{AlO}(\text{OH})$, PDF Nr. 00-001-1284), susidarymą.

Išanalizavus hidrotermiškai apdoroto 100–130 °C temperatūroje S2 bandinio RSDA kreives, galima teigti, kad pradinio mišinio mechanocheminis apdorėjimas skatina Ms12 susidarymą ir apriboja kitų junginių formavimąsi (žr. 5.1 pav.). Priešingai nei hidrotermiškai apdorojant S1 bandinį, po sintezės identifiкуojami difrakciniai maksimumai būdingi tik Ms12 ir kalcio karbonatui S2 bandinyje. Nustatyta, kad aukštesnė sintezės temperatūra (110–130 °C) ir izoterminio išlaikymo trukmės ilginimas iki 8 h visomis sintezės sąlygomis taip pat skatina Ms12 smailių intensyvumo augimą. Pažymėtina, kad tolesnis sintezės trukmės ilginimas (12–48 h) sukelia Ms12 skilimą ir nustatomas laipsniškas šiam junginiui būdingų difrakcijos maksimumų mažėjimas. Be to, ilgesnė sintezės trukmė skatina kitų junginių susidarymą (bemito ir etringito).

Remiantis RSDA duomenimis nustatyta, kad, hidrotermiškai apdorojant S1 bandinį visomis sintezės sąlygomis, produktuose susidaro daugiakomponentės sistemos. Atsižvelgiant į šiuos duomenimis ir siekiant, kad hidroterminės sintezės energinės sąnaudos būtų mažesnės, tolesniems tyrimams buvo naudojamas tik S2 bandinys, hidrotermiškai apdorotas 110 °C temperatūroje.

Atlikus S2 bandinių termogravimetrinę analizę (TGA) po hidroterminės analizės 110 °C, galima pastebėti, kad visų bandinių DTG kreivės yra panašaus profilio (žr. 5.2 pav.). Visuose bandiniuose būdingas platus kelių smailių šiluminis efektas 30–145 °C temperatūros diapazone, atspindintis laisvojo vandens (absorbuoto) išgarinimą, amorfinių junginių ir monosulfoaluminato dehidrataciją. Kiti terminiai efektai, esantys ~177 °C ir ~291 °C temperatūrose, taip pat atitinka tolesnę vandens dehidrataciją iš tarp sluoksnių ir pagrindinių (oktaedrų) sluoksnių, esančių monosulfoaluminato struktūroje. Aukštesnėje temperatūroje (~695 °C) vykstantis terminis efektas priskiriamas kalcio karbonato skilimui. Verta paminėti, kad smailė ties ~419 °C nustatyta tik bandiniui, sintetintam 48 h, kuris atitinka bemito dehidrataciją. Gauti TGA duomenys sutampa su RSDA analizės rezultatais.



5.2 pav. Hidroterminės sintezės produktų masės išvestinės kreivės (DTG), kai S2 bandinys apdorojamas 110 °C temperatūroje skirtingomis izoterminio išlaikymo trukmėmis

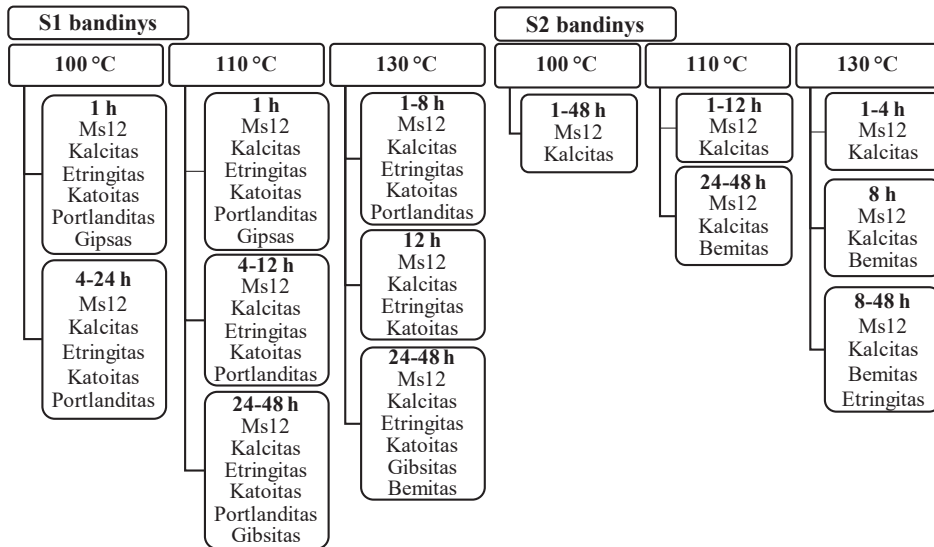
Toliau TGA analizės metodu gauti masės nuostoliai patvirtino, kad S2 bandinyje po 8 h hidroterminio apdorojimo susidaro didžiausias surišto vandens kiekis (vertinamas 50–550 °C intervalas), tai rodo, kad šiame bandinyje yra didžiausias susidariusių hidratų kiekis (žr. 5.2. lent.). Be to, didžiausi masės nuostoliai 145–200 °C intervale, susiję su vandens pašalinimu tik iš Ms12 struktūros, taip pat nustatyti S2 bandinyje, kai sintezės išlaikymo trukmė – 8 h.

5.2 lentelė. Hidroterminės sintezės produktų masės nuostoliai, kai S2 bandinys apdorojamas 110 °C temperatūroje skirtingomis izoterminio išlaikymo trukmėmis.

Temperatūros intervalas, °C	Sintezės trukmė, h			
	4	8	24	48
	Masės nuostoliai, %			
30–145	6,1	7,1	6,1	5,1
145–200	6,2	6,7	5,7	5,5
200–300	5,7	6,6	5,7	6,1
300–400	3,3	4,2	4,1	4,1
400–450	0,6	0,7	0,9	1,6
450–550	0,8	1,1	1,2	2,3
550–940	3,2	3,1	2,8	3,7
50–550	22,1	25,9	23,4	25
30–940	25,5	29,4	26,4	29

Apibendrinant gautus rezultatus, galima teigti, kad hidrotermiškai apdorojant CaO–Al₂O₃–SO₄–H₂O mišinio sistemą, galimas daugelio fazių susidarymas (žr. 5.3 pav.). Siekiant skatinti Ms12 susidarymą, pradinis mišinys turi būti mechaniškai ir chemiškai aktyvuojamas, t. y. sintezės sąlygų (temperatūros ir trukmės) optimizavimas nėra pakankamas susintetinti Ms12 be papildomų junginių. Ištyrus

susintetintus bandinius, siūloma, kad optimalios sintezės sąlygos susidaryti kalcio monosulfoaluminato 12-hidratui yra 110 °C temperatūroje, kai išlaikymo trukmė – 8 h. Rietveldo analizės duomenimis, ši bandinį sudaro 54,8 % Ms12, 0,7 % Ms10,5, 1,9 % CaCO₃ ir 42,6 % amorfinės fazės.



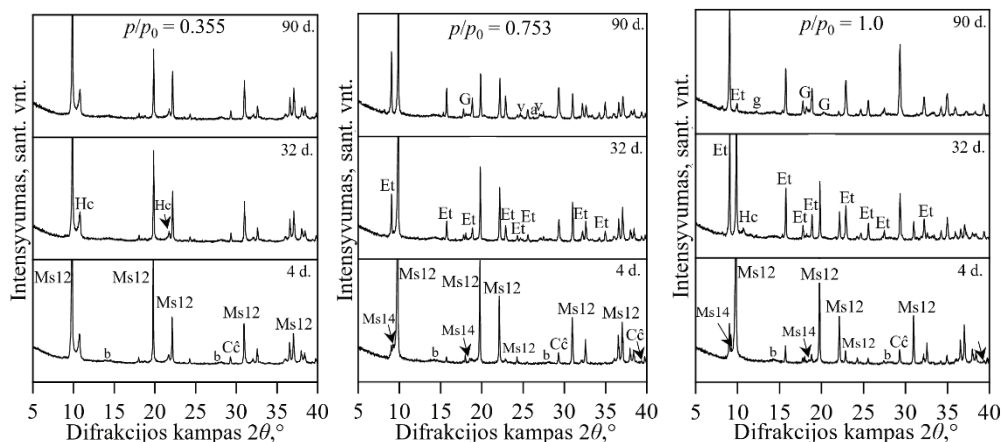
5.3 pav. Kristalinių produktų susidarymo sekos hidroterminėmis sąlygomis CaO–Al₂O₃–SO₄–H₂O sistemoje

5.3.2. Dalinio vandens garų slėgio įtaka kalcio monosulfoaluminato 12-hidrato stabilumui esant aplinkos CO₂

Žinoma, kad aukštesnėje temperatūroje susintetintų junginių kristalinė gardelė yra tvarkingesnė, o tai turi lemiamą įtaką didesniai junginių stabilumui. Atsivėlgiant į tai, ištirti dalinio vandens garų slėgio (p/p_0) įtaką kalcio monosulfoaluminato 12-hidrato karbonizacijos elgsenai buvo pasirinktas S2 bandinys, sintetintas 130 °C 8 h.

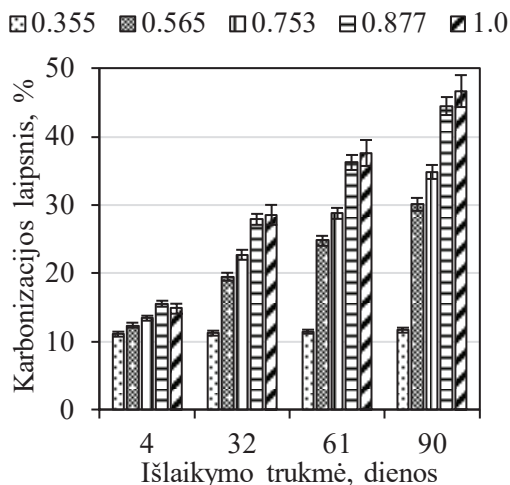
Gauti rezultatai parodė, kad dalinis vandens garų slėgis yra Ms12 karbonizacijos greitį kontroliuojantis veiksnys ir lemia Ms12 skilimo kelius, t. y. karbonizacijos produktų susidarymą. Rezultatai patvirtino, kad galutiniai Ms12 karbonizacijos produktai yra kalcio karbonatas (CaCO₃), aluminio hidroksidas (Al(OH)₃) ir gipsas (CaSO₄·2H₂O, PDF Nr. 04010–409), esant aukštesnėmis sočiųjų vandens garų sąlygomis ($p/p_0 > 0,565$), arba hemihidratas (CaSO₄·0,5H₂O, PDF Nr. 00–033–0310) žemesnėmis sąlygomis (žr. 5.4 pav.). Nepriklausomai nuo p/p_0 sąlygų, kalcitas yra identifikuojamas kaip dominuojantis kalcio karbonato polimorfai bandiniuose. Aragonitas (PDF Nr. 040139616) ir vateritas (PDF Nr. 040178634) susidaro 0,355–0,877 p/p_0 intervale, kur žemesnė aplinka skatina vaterito susidarymą, o aukštesnė – aragonito. Esant pakankamai drėgmei ($\geq 0,753 p/p_0$), Ms12 persikristalizuoja į

etringitą, kurio virsmą sustiprina aukštesnio p/p_0 aplinka. Ištirta, kad hemikarboaluminatas ($\text{Ca}_4\text{Al}_2\text{O}_6(\text{CO}_3)_{0,5}(\text{OH})\cdot 11,5\text{H}_2\text{O}$, PDF Nr. 000410221) ir Ms14 ($\text{Ca}_4\text{Al}_2\text{O}_6(\text{SO}_4)\cdot 14\text{H}_2\text{O}$, PDF Nr. 00042-0062) yra tarpiniai karbonizacijos reakcijos produktai. Hemikarbonatas susidaro tik esant 1,0 p/p_0 , kurį galima paaiškinti daline Ms12 sąveika su karbonizacijos metu susidariusiu CaCO_3 . Ms14 matomas esant 0,565–1,0 p/p_0 diapazonui, kurio stabilumas mažėja aukštesnėje p/p_0 aplinkoje.



5.4 pav. S2 bandinio, hidrotermiškai apdoroto 130 °C 8 h, RSDA kreivės, esant skirtingai p/p_0 aplinkai skirtingomis išlaikymo trukmėmis: Ms – kalcio monosulfoaluminato hidratas (skaičius rodo vandens kiekį); Hc – hemikarbonatas; Et – etringitas; b – bemitas; G – gipsitas; Cc – kalcio karbonatas; s – basanitas; a – aragonitas; v – vateritas; g – gipsas

Galiausiai bandinių karbonizacijos efektyvumas skirtingomis p/p_0 sąlygomis buvo įvertintas apskaičiuojant karbonizacijos laipsnį (α) (nuo esamo CaO kiekio bandinyje), parodant esamo CaCO_3 kiekio santykį su teoriniu maksimaliu CaCO_3 , kuris gali susidaryti bandiniuose. Kaip matyti iš 5.5 pav. pateiktų rezultatų, 0,355 p/p_0 aplinka lemia tik nedidelę bandinio karbonizaciją. Kita vertus, didėjanti p/p_0 aplinka skatina dujinio CO_2 tirpimą ir sąveiką su Ca^{2+} jonais, esančiais bandinio paviršiuje. Dėl to karbonizacijos laipsnis auga nuo ~26 % esant 0,565 p/p_0 iki ~47 % esant 1,0 p/p_0 po 90 dienų išlaikymo (žr. 5.5 pav.). Daugelis autorių atkreipė dėmesį, kad viršijant optimalias drėgmės sąlygas (50–80 % arba 0,5–0,8 p/p_0), karbonizacija lėtėja dėl porų prisotinimo vandeniu ir (arba) karbonizacijai reikalingų cemento dalelių trūkumo reakcijoms. Šiame darbe buvo naudojamas miltelinis mėginys, kuris pasižymi mažiau sutankinta struktūra (didelis poringumas) nei betono mėginiai su dideliu vidiniu užpildu. Dėl to manoma, kad šiuo atveju CO_2 ir vandens garų judėjimas nepaklūsta įprastiniam difuzijos kontroliuojamam reiškiniui. Apibendrinant galima teigti, kad Ms12 karbonizacijos elgesys ir reakcijų kinetika tiesiogiai priklauso nuo dalinio vandens garų slėgio.

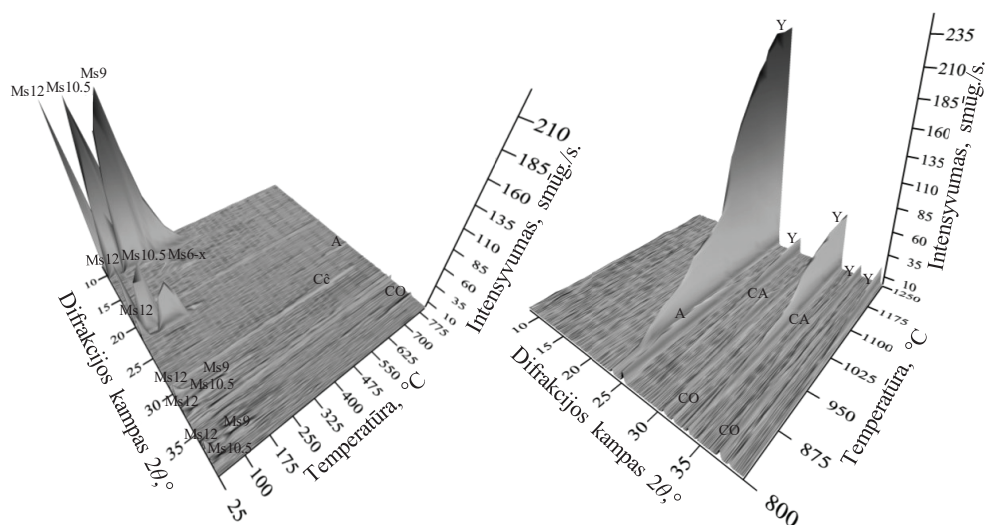


5.5 pav. Bandinių karbonizacijos laipsnio priklausomybė nuo išlaikymo trukmės esant skirtingam p/p_0 (paklaidų juostos rodo standartinę nuokrypį)

5.3.2. Terminio skilimo iš kalcio monosulfoaliuminato 12-hidrato į jelimitą mechanizmo tyrimas

Kalcio monosulfoaliuminato 12-hidrato terminis stabilumas ir jelimito susidarymo mechanizmas buvo ištirtas taikant *in situ* ir *ex situ* analizės metodus. Tolesniems tyrimams buvo naudojamas S2 bandinys, hidrotermiškai apdorotas 110 °C temperatūroje 8 h, kuris pavadintas prekursoriumi.

Nustatyta, kad kalcio monosulfoaliuminato 12-hidrato skilimas vyksta plačiame temperatūros diapazone (25–370 °C). Dėl šio junginio struktūros sudėtingumo (gebėjimo kaupti skirtingą vandens kiekį tarp sluoksniuose) terminio apdorojimo metu nustatyta keturių kalcio monosulfoaliuminatų su skirtingu struktūrinio vandens kiekiu dehidratacija, kuri buvo pastebėta atlikus *in situ* RSDA analizę (žr. 5.6 pav.). Ištirta, kad Ms12 fazė išlieka stabili nuo 25 iki 90 °C, Ms10,5 buvimą nuo 50 iki 220 °C, Ms9 nuo 90 iki 370 °C ir Ms6–x nuo 170 iki 330 °C. Aukštesnėje temperatūroje (700–1250 °C) susidaro kristalinės fazės ir identifikuojamas jelimitas ($C_4A_3\hat{S}$; $Ca_4Al_6O_{12}SO_4$, PDF Nr. 00-033-0256), kalcio oksidas (CaO, PDF Nr. 00-037-1497), anhidritas ($CaSO_4$, PDF Nr. 00-037-1496) ir kalcio aliuminatai (CA [$CaAl_2O_4$, PDF Nr. 04-014-8445] ir $C_{12}A_7$ [$Ca_{12}Al_{14}O_{33}$, PDF Nr. 04-015-0818]). Ištirta, kad jelimito formavimosi temperatūros pradžia yra 800 °C. Tolesnis temperatūros didinimas skatina kietojo kūno reakcijas, kurių metu kalcio oksidas, anhidritas ir kalcio aliuminatai sąveikauja ir lemia tolesnį jelimito difracinių smailių augimą (žr. 5.6 pav.). Viršijus 950 °C terminio apdorojimo temperatūrą, jelimitas identifikuojamas kaip dominuojanti kristalinė fazė.



5.6 pav. Kalcio monosulfoaluminato 12-hidrato *in situ* RSDA analizės kreivės atlikus terminį apdorojimą 25–1250 °C temperatūros intervale: Ms – monosulfoaluminatas (skaičius rodo vandens kiekį); Cc – kalcio karbonatas; CO – kalcio oksidas; A – anhidritas; CA – kalcio aluminatas; Y – jelimitas

Remiantis Rietveldo analizės rezultatais apskaičiuota, kad didžiausias sintetinio jelimito grynumas pasiekiamas sukepinant prekursoriaus bandinį 1100–1250 °C temperatūros intervale, kai išlaikymo trukmė 1 h (žr. 5.3 lent.). Verta paminėti, kad susidariusio sintetinio jelimito kristalinė struktūra yra tik ortorombinė. Taikant Šererio lygtis apskaičiuota, kad didžiausias sintetinio jelimito vidutinis kristalitų dydis gaunamas 1150 °C, 1200 °C ir 1250 °C temperatūrose, kuris atitinkamai yra 216,5 nm, 224,75 nm ir 214,5 nm. Atsižvelgiant į gautus rezultatus, siūloma prekursorių degti 1 h 1150 °C temperatūroje, optimaliai sintetinio jelimito (grynumas ~97 %) gamybai.

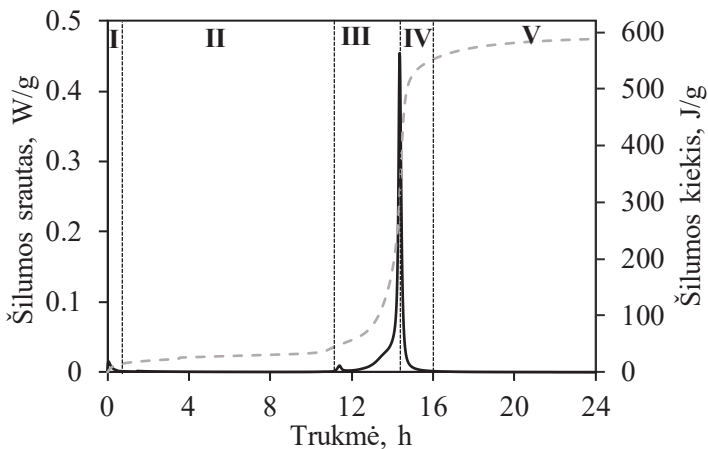
5.3 lentelė. Kiekybinės RSDA analizės rezultatai, atlikus prekursoriaus terminį apdorojimą 950–1250 °C temperatūroje, kai išlaikymo trukmė – 1 h

Temperatūra, °C	Kristalinė fazė, %					
	C ₄ A ₃ Š	CA	CŠ	C ₁₂ A ₇	CaO	Amorf.
950	48,48	19,81	11,56	6,15	0,78	13,22
1000	56,91	19,24	10,01	1,42	0,52	11,9
1050	75,02	10,28	7,32	0,89	0,46	6,03
1100	95,73	–	1,69	–	0,63	1,95
1150	97,73	–	0,17	–	0,31	1,8
1200	98,76	–	0,13	–	0,89	0,22
1250	97,56	–	0,12	–	0,42	1,9

5.3.3. Sintetinio jelimito ankstyvosios hidratacijos tyrimas

Siekiant įvertinti sintetinio jelimito aktyvumą ir nustatyti hidratacijos mechanizmą, ankstyvosios hidratacijos eksperimentai buvo atlikti 25 °C temperatūroje 72 h, kai pasirinktas vandens ir kietųjų dalelių santykis (V/K) – 1,1. Remiantis izoterminės kalorimetrijos rezultatais (žr. 5.7 pav.), sintetinio jelimito hidrataciją galima apibrėžti penkiomis stadijomis / periodais:

I stadija (pradinis laikotarpis (iki 30 min)). Iš karto po sintetinio jelimito kontakto su vandeniu šilumos srautas greitai padidėja, jo maksimumas (0,01535 W/g) pasiekiamas per pirmąsias ~4 min. Toliau šilumos srauto kreivė mažėja, o per šį laikotarpį išsiskiriančios šilumos kiekis yra lygus ~13,4 J/g. Remiantis RSDA ir TGA rezultatais, šiame etape susidaro etringitas ir amorfinis aliuminio hidroksidas (žr. 5.8 pav.).

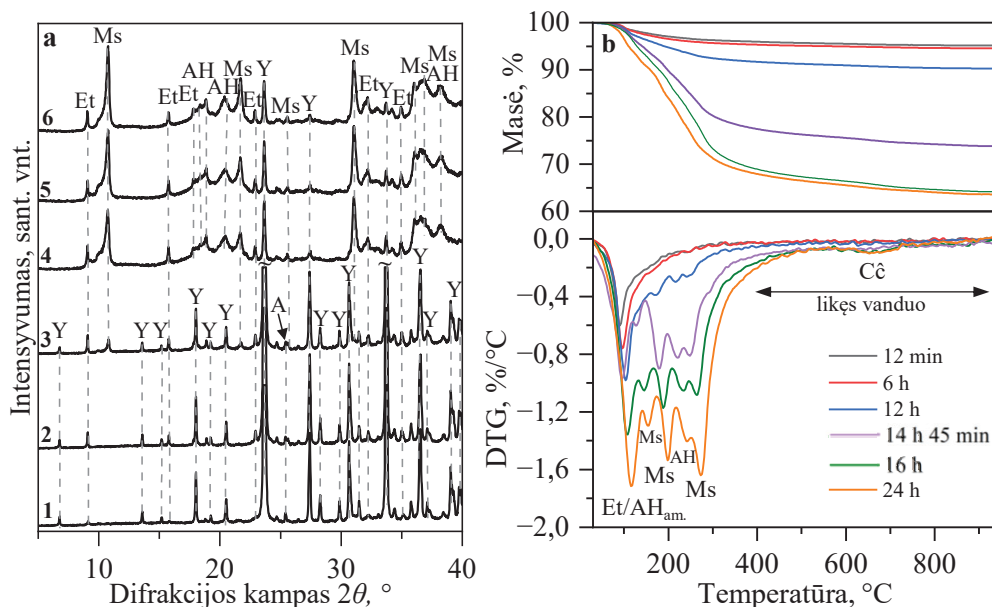


5.7 pav. Kalorimetrinės kreivės, išmatuotos sintetinio jelimito izoterminės hidratacijos metu

II stadija (indukcinis laikotarpis) (30 min – 10 h 40 min). Per šį laikotarpį šilumos srauto kreivės didėjimas nebuvo užfiksuotas (žr. 5.7 pav.). Visgi išsiskyrusios šilumos kreivė ir toliau lėtai didėja, jos vertė išauga iki ~37 J/g periodo pabaigoje. Nustatyta, kad šiuo laikotarpiu jelimitas lėtai tirpsta (būdingų smailių intensyvumas mažėja), tai skatina etringito ir amorfinio aliuminio hidroksido susidarymą (žr. 5.8 pav.).

III stadija (pagreitėjimo laikotarpis) (10 h 40 min – 14 h 45 min). Šiuo periodu stebima antrosios egzoterminės reakcijos pradžia, kurios šilumos srauto maksimumas (0,4544 W/g) pasiekiamas po 14 h 45 min hidratacijos (žr. 5.7 pav.). Paminėtina, kad nustatytas mažas egzoterminis pikas, pastebėtas 11 val. 40 min, priskiriamas anhidrito ištirpimui sistemoje, kur susidarę sulfatų jonai sąveikauja su jelimitu ir pagreitina dalies minėto junginio hidrataciją. Šio periodo metu nustatytas didžiausias jelimito smailių sumažėjimas (~48 %) ir identifikuojamas intensyvus monosulfoaluminato,

papildomo etringito bei mikrokrystalinio aliuminio hidroksido susidarymas (žr. 5.8 pav.).



5.8 pav. Sintetinio jelimito hidratacijos produktų RSDA kreivės (a) ir TGA kreivės (b) skirtingomis hidratacijos trukmėmis (1 – 12 min, 2 – 6 h, 3 – 12 h, 4 – 14 h 45 min, 5 – 16 h, 6 – 24 h): Y – jelimitas; Ms – monosulfoaliuminatas; Et – etringitas; AH – aliuminio hidroksidas; A – anhidritas

IV stadija (lėtėjimo laikotarpis) (14 h 45 min – 16 h). Šis laikotarpis yra susijęs su antrosios egzoterminės reakcijos pabaiga, kai didėja išsiskiriančios šilumos kiekis (žr. 5.7 pav.). Šioje stadijoje vis dar matomas jelimito difrakcinių smailių intensyvumo mažėjimas, o etringito ir monosulfoaliuminato – didėjimas (žr. 5.8 pav., a). TGA analizės duomenys taip pat patvirtino susidariusių hidratacijos produktų kiekio augimą, t. y. bendras masės praradimas 50–550 °C temperatūros intervale išauga iki ~32 % (žr. 5.8 pav., b).

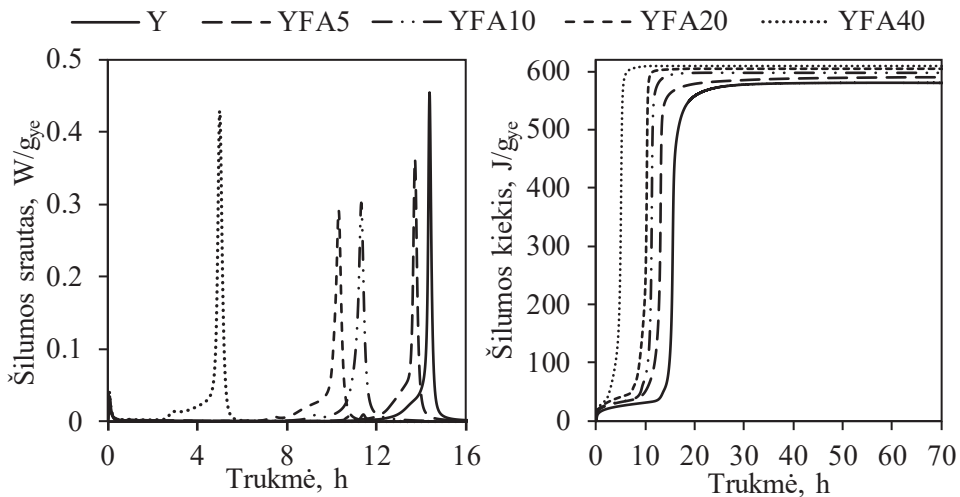
V stadija (lėtasis laikotarpis) (>16 h). Šiuo periodu šilumos srauto kreivėje pokytis nenustatomas, po 24 h išsiskyrusios šilumos kiekis stabilizavosi esant ~580 J/g (5.7 pav.). Remiantis RSDA duomenimis apskaičiuota, kad jelimito difrakcinių maksimumų intensyvumas sumažėja ~98 % po 24 h hidratacijos. Pailginus hidratacijos trukmę nuo 16 iki 24 h, matomas hidratacijos produktų (monosulfoaliuminato ir mikrokrystalinio aliuminio hidroksido) padaugėjimas, t. y. masės nuostoliai papildomai išauga ~2,1 % (žr. 5.8 pav.).

Apibendrinant gautus rezultatus galima teigti, kad sintetinis jelimitas, pagamintas hidroterminio kalcinavimo metodu, pasižymi dideliu hidrauliniu

aktyvumu, o susidarantys hidratacijos produktai yra identiški kaip ir hidratuojant jelimitą pagamintą įprastiniu kietojo kūno metodu.

5.3.4. Lakiųjų pelenų įtaka sintetinio jelimito ankstyvajai hidratacijai

Šiam tyrimui sintetinis jelimitas buvo pakeistas 5 %, 10 %, 20 % ir 40 % lakiisiais pelenais ir bandiniai atitinkamai buvo pavadinti YFA5, YFA10, YFA20 ir YFA40, o sintetinis jelimitas be lakiųjų pelenų – Y. Izoterminės kalorimetrijos eksperimentai atlikti anksčiau minėtomis sąlygomis. Nustatyta, kad pridėti lakieji pelenai greitina sintetinio jelimito hidrataciją, t. y. antrosios egzoterminės reakcijos šilumos srauto maksimumas YFA5 bandinyje pasiekiamas po 13 h 42 min, YFA10 – 11 h 15 min, YFA20 – 10 h 18 min ir YFA40 – 4 h 54 min (žr. 5.9 pav.). Be to, iširta, kad didinant lakiųjų pelenų kiekį bandiniuose išskiriamos šilumos kiekis taip pat laipsniškai didėja. Papildomi eksperimentai buvo atlikti siekiant suprasti nustatytą jelimito hidratacijos pagreitinimą.

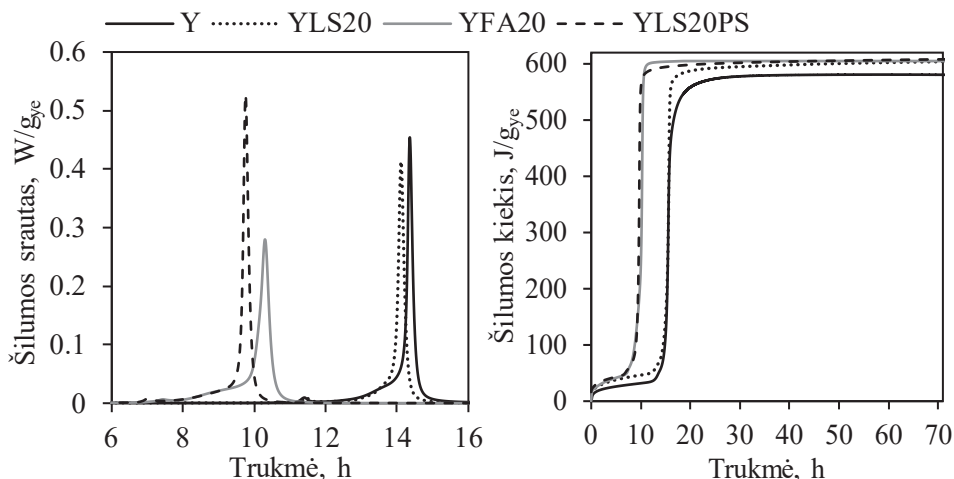


5.9 pav. Kalorimetrinės kreivės, išmatuotos įvairių jelimito ir lakiųjų pelenų mišinių izoterminės hidratacijos metu

Lakieji pelenai per pirmąsias 7 cemento hidratacijos dienas nereaguoja arba reaguoja minimaliai, tačiau lakiųjų pelenų dalelės yra tartum papildomas paviršius, suteikiantis hidratacijos produktams papildomus kristalizacijos centrus (vadinamasis užpildo efektas). Be to, nedidelis ar vidutinis šarmų kiekis (Na^+ , K^+ ir Ca^{2+}) sistemoje greitina jelimito tirpimą ir hidratų susidarymą. Siekiant įvertinti užpildo efekto poveikį jelimito hidratacijai, jelimitas buvo pakeistas 20 % klintmilčių (LS) ir bandinys pavadintas YLS20, o šarmų įtakai įvertinti (patenka į sistemą iš lakiųjų pelenų) buvo paruoštas porų tirpalas (PS) pagal išmatuotą YFA20 bandinio porų tirpalą po 2 h hidratacijos, atsižvelgiant į Na^+ , K^+ ir Ca^{2+} jonų kiekį ir pH. Paruoštas porų tirpalas buvo naudojamas vietoje vandens ir sumaišytas su YLS20, kuris

pavadintas YLS20PS bandiniu. Kalorimetriniai eksperimentai atlikti tomis pačiomis sąlygomis.

Rezultatai patvirtino, kad pridėti klintmilčiai minimaliai pagreitina jelimito hidrataciją (YLS20 bandinys), t. y. antrosios egzoterminės reakcijos maksimumas pasiekiamas po 14 h 8 min, o išsiskyręs šilumos kiekis yra toks pat kaip ir YFA20 bandiniui (604 J/g) (žr. 5.10 pav.). Tikėtina, kad šis pagreitėjimas gali būti siejamas su padidėjusiu vandens ir rišamosios medžiagos santykiu (1,1→1,375) ir užpildo efektu. Kita vertus, ištyrus YLS20PS bandinį, nustatytas žymus jelimito hidratacijos pagreitėjimas, t. y. antrosios egzoterminės reakcijos maksimumas pasiektas po 9 h 45 min. Šie eksperimentai patvirtina, kad šarmų kiekio padidėjimas sistemoje turi didžiausią įtaką jelimito hidratacijos pagreitėjimui pakeitus jį lakiaisiais pelenais.



5.10 pav. Kalorimetrinės kreivės, išmatuotos jelimito ir lakiųjų pelenų bei jelimito ir klinties miltelių mišinių izoterminės hidratacijos metu

RSDA analizė atskleidžia, kad hidratuojant jelimito ir lakiųjų pelenų mišinius, susidariusių hidratų mineraloginė sudėtis išlieka nepakitusi (žr. 5.4 lent.). Nustatytas skirtumas tarp susidariusių hidratacijos produktų difrakcijos smailių intensyvumo, kuris palaipsniui mažėja didėjant lakiųjų pelenų pakaitimo kiekiui bandiniuose. Šis reiškinys siejamas su rišamosios medžiagos praskiedimo poveikiu. Norint hipotetiškai pašalinti praskiedimo efektą, buvo apskaičiuotas teorinis susidariusių hidratų smailių intensyvumas. Tam buvo įvertintas galimas hidratų intensyvumo sumažėjimas nuo gryno hidratuoto sintetinio jelimito bandinio pagal lakiųjų pelenų pakeitimo procentinę dalį kiekviename bandinyje. Palyginus teorinius ir nustatytus hidratacijos produktų smailių intensyvumus, matoma, kad nustatytų smailių mažėjimas nėra tiesiogiai proporcingas pakeitimo lygiui (žr. 5.4 lent.). Nustatytas etringito intensyvumas yra didesnis, o kalcio monosulfoaluminato hidrato – mažesnis, nei teoriškai tikėtasi. Tai gali reikšti, kad sintetinio jelimito pakeitimas lakiaisiais pelenais riboja monosulfoaluminato susidarymą ir (arba) skatina jo skilimą, dėl to papildomai susidaro etringitas ir (arba) jis stabilizuojamas hidratacijos metu. Svarbu pabrėžti, kad

identifikuojamas smailių intensyvumas priklauso ne tik nuo susidarančių hidratacijos produktų kiekio, bet ir nuo kristališkumo, kristalų tvarkingumo, kristalų dydžio, mikrotempių, kitų jonų įterpimo į kristalo struktūrą ir kt. Dėl to, norint patvirtinti pateiktą hipotezę, reikalingi papildomi tyrimai.

5.4 lentelė. Pagrindinių difrakcijos smailių pokyčiai po 72 h hidratacijos įvairiuose jelimitinių ir lakiųjų pelenų mišiniuose

Junginys	Bandinys	Nustatytas smailių intensyvumas, smūg./s				
		Y	YFA5	YFA10	YFA20	YFA40
Jelimitas (0,375 nm)		79	72	65	54	39
Etringitas (0,975 nm)		461	455	439	413	379
Monosulfoaluminatas (0,823 nm)		1775	1557	1461	1400	1047
Aluminio hidroksidas (0,436 nm)		208	202	213	179	113
		Teorinis smailių intensyvumas, smūg./s				
Jelimitas (0,375 nm)		79	75	71	63	47
Etringitas (0,975 nm)		461	437	414	368	276
Monosulfoaluminatas (0,823 nm)		1775	1686	1597	1420	1065
Aluminio hidroksidas(0,436 nm)		208	197	187	166	125

5.3.5. Jelimito priedo įtaka pelenų portlandcemenčio kietėjimo savybėms

Norint nustatyti sintetinio jelimito priedo įtaką pelenų portlandcemenčio rišimosi ir kietėjimo savybėms, buvo atlikti normalios cemento tešlos konsistencijos, rišimosi pradžios ir pabaigos trukmės bei cemento skiedinio gniuždymo stiprio tyrimai. Šiems eksperimentams buvo naudojami šie bandiniai: tik portlandcementis (OPC, P), portlandcementis su lakiaisiais pelenais (FA) (be priedo) ir portlandcementis su lakiaisiais pelenais ir sintetiniu jelimito priedu (Y).

Nustatyta, kad pelenų portlandcemenčio tešlai pasiekti normalią konsistenciją reikalingas didesnis vandens ir paruoštos rišamosios medžiagos santykis nei grynam portlandcemenčio bandiniui, o rišimosi pradžios ir pabaigos trukmės atitinkamai pailgėja 107 min ir 40 min (žr. 5.5 lent.). Ištirta, kad naudojant cemento mišinius su sintetinio jelimito priedu, reikalingas dar didesnis vandens ir paruoštos rišamosios medžiagos santykis, norint gauti normalią cemento tešlos konsistenciją. Kalbant apie rišimosi trukmę, sintetinio jelimito priedo įtraukimas į cemento mišinius efektyviai sutrumpina tešlos rišimosi pradžios ir pabaigos trukmes (žr. 5.5 lent.). Vis dėlto, padidinus sintetinio jelimito kiekį iki 2 % mišiniuose, cemento tešlos rišimosi pradžia 80P18FA2Y bandinyje nustatyta po 35 min, o 78P20FA2Y bandinyje – po 25 min. Remiantis LST EN 197-1 standartu, cemento rišimosi trukmė turi būti ne trumpesnė nei 60 min, siekiant užtikrinti optimalias cemento tešlos eksploatacines savybes, todėl naudotas sintetinio jelimito priedo kiekis (2 %) yra netinkamas cemento skiediniams ruošti.

Gniuždymo stiprio rezultatai patvirtino, kad lakiųjų pelenų maišymas su OPC teigiamai veikia skiedinių stiprumo vystymąsi, t. y. po 28 kietinimo parų 80P20FA bandinio gniuždymo stiprio vertės yra ~16 % didesnės, lyginant su OPC bandinio vertėmis (žr. 5.6 lent.). Kita vertus, pirmąją savaitę pelenų portlandcemenčio skiedinių su jelimito priedu gniuždymo stipris auga lėčiau, bet po 28 kietinimo parų gniuždymo stiprio nustatytos vertės su 0,5 % priedo yra didesnės, o su 1 % priedo – artimos OPC bandinio vertėms.

5.5 lentelė. Paruoštų cemento tešlų rišimosi pradžios ir pabaigos trukmės

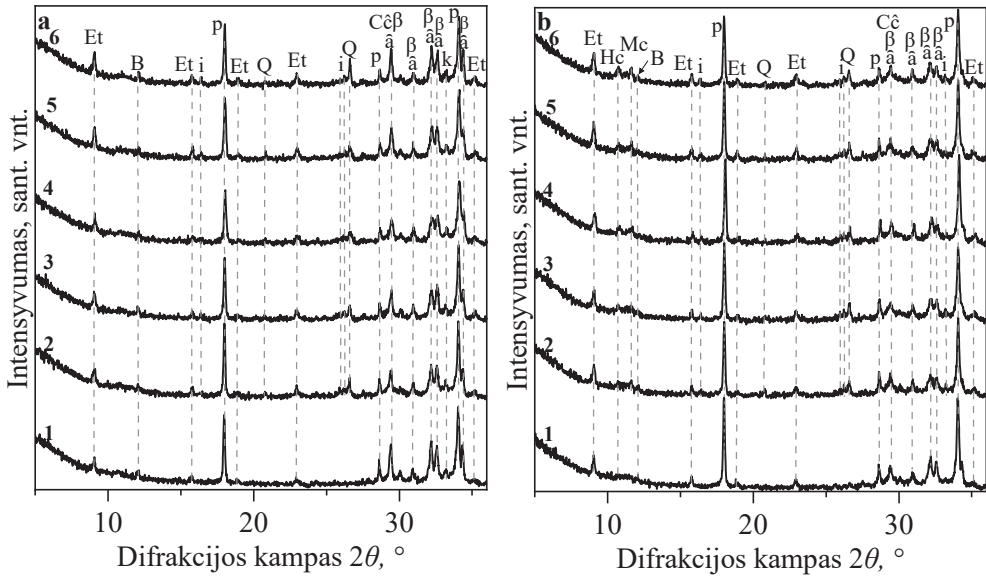
Bandinys	Mišinio kompozicija, %			Rišimosi trukmė, min		V/K
	OPC	FA	Jelimitas	Pradžia	Pabaiga	
OPC	100	–	–	160	400	0,290
80OPC20FA	80	20	–	267	440	0,306
80P19.5FA0.5Y	80	19,5	0,5	137	302	0,310
79.5P20FA0.5Y	79,5	20	0,5	174	289	0,310
80P19FA1Y	80	19	1	97	177	0,313
79P20FA1Y	79	20	1	107	186	0,313
80P18FA2Y	80	18	2	35	55	0,316
78P20FA2Y	78	20	2	25	40	0,317

5.6 lentelė. Paruoštų skiedinio bandinių gniuždymo stiprio priklausomybė nuo hidratacijos trukmės

Bandinys	Mišinio kompozicija, %			Gniuždymo stipris, MPa		
	OPC	FA	Jelimitas	Po 2 parų	Po 7 parų	Po 28 parų
OPC	100	–	–	17,9	34,1	37,8
80OPC20FA	80	20	–	23,0	33,9	43,7
80P19.5FA0.5Y	80	19,5	0,5	16,1	27,2	39,1
79.5P20FA0.5Y	79,5	20	0,5	18,8	28,9	40,2
80P19FA1Y	80	19	1	14,1	20,1	37,9
79P20FA1Y	79	20	1	15,3	23,9	37,9

RSDA rezultatai patvirtino, kad OPC pakeitimas lakiaisiais pelenais ir (arba be) sintetiniu jelimito priedu nedaro įtakos susidarančių hidratacijos produktų mineraloginei sudėčiai po dviejų hidratacijos parų. Visuose bandiniuose identifikuojamas etringitas, portlanditas ir kalcio karbonatas (žr. 5.11 pav., a). Be to, iširta, kad sintetinio jelimito priedo įtraukimas į cemento mišinius skatina etringito susidarymą, t. y. bandiniuose su jelimito priedu nustatytos intensyvesnės smailės, būdingos etringitui, lyginant su OPC ir 80P20FA bandiniais. Verta paminėti, kad jelimitas ir gipsas nebeaptinkami visų bandinių RSDA kreivėse ir OPC fazių (alito,

braunmillerito, trikalčio aluminato) smailių intensyvumas labai sumažėja po dviejų hidratacijos parų. Pailginus hidratacijos trukmę iki 28 dienų, vyksta tolesnė cemento fazių hidratacija, kuri skatina portlandito ir etringito susidarymą (žr. 5.11 pav., b). Be to, visuose bandiniuose po 28 hidratacijos parų identifikuojamas hemikarboaliuminatas. Kita vertus, pakeitus OPC lakiisiais pelenais ir (arba be) sintetiniu jelimito priedu, susidaro monokarboaliuminatas ($\text{Ca}_4\text{Al}_2\text{O}_6\text{CO}_3 \cdot 11\text{H}_2\text{O}$, PDF Nr. 00-014-0083). Paminėtina, kad didžiausias hemikarboaliuminato ir monokarboaliuminato smailių intensyvumas nustatytas bandiniuose, paruoštuose su didžiausiu jelimito priedo kiekiu.

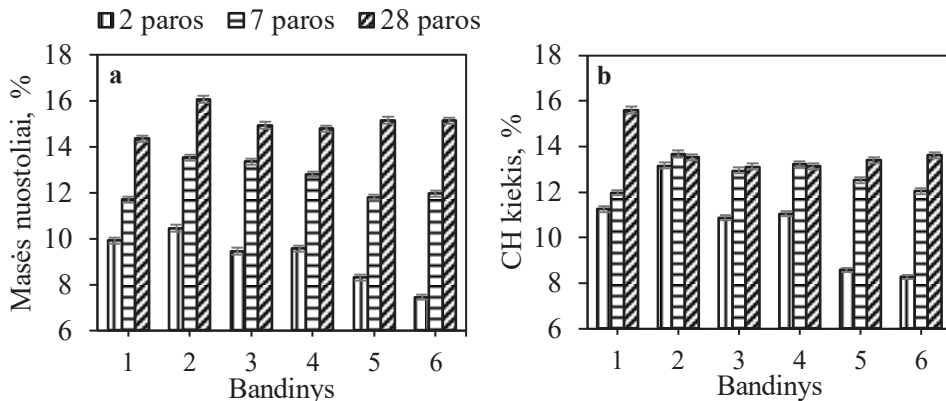


5.11 pav. Bandinių RSDA kreivės po 2 (a) ir 28 (b) hidratacijos parų (1 – OPC, 2 – 80P20FA, 3 – 80P19.5FA0.5Y, 4 – 79.5P20FA0.5Y, 5 – 80P19FA1Y, 6 – 79P20FA1Y): p – portlanditas; Et – etringitas; Hc – hemikarboaliuminatas; Mc – monokarboaliuminatas; â – alitas; ð – belitas; B – braunmilleritas; i – mulitas; Q – kvarcas; Cc – kalcio karbonatas; k – trikalčio aluminatas

Siekiant nustatyti lakiųjų pelenų ir sintetinio priedo įtaką susidariusiam hidratacijos produktų vandens ($50\text{--}400\text{ }^\circ\text{C}$) ir portlandito kiekiui (CH) ($400\text{--}480\text{ }^\circ\text{C}$), buvo naudota VTA analizė. Gauti rezultatai buvo normalizuoti pagal rišamosios medžiagos kiekį (100 %), kad būtų pašalintas praskiedimo efektas, t. y. priklausomai nuo mėginio iki OPC arba OPC ir sintetinio jelimito priedo kiekio.

Rezultatai rodo, kad, pakeičiant OPC 20 % lakiisiais pelenais, per pirmąją hidratacijos savaitę bandiniuose susidaro didesnis hidratacijos produktų vandens ir CH kiekis, lyginant su OPC bandiniu (žr. 5.12 pav.). Kita vertus, pailginus hidratacijos trukmę iki 28 dienų, hidratacijos produktų vandens kiekis toliau didėja, bet CH kiekis mažėja. Tai patvirtina, kad hidratacijos metu portlanditas sunaudojamas

pucolaninėse reakcijose, kurios 80P20FA bandinyje lemia didesnę hidratacijos produktų susidarymą ir skiedinio gniuždymo stiprio padidėjimą.



5.12 pav. Bandinių masės nuostoliai 50–400 °C temperatūroje (a) ir susidaręs portlandito kiekis (b) įvairiu kietėjimo laikotarpiu, normalizuoti pagal rišamosios medžiagos kiekį: 1 – OPC; 2 – 80P20FA; 3 – 80P19.5FA0.5Y; 4 – 79.5P20FA0.5Y; 5 – 80P19FA1Y; 6 – 79P20FA1Y

Ištirta, kad bandiniuose su sintetinio jelimito priedu hidratacijos produktų vandens ir CH kiekio raida skiriasi nuo OPC ir 80O20FA bandinių. Nustatyta, kad susidaręs hidratacijos produktų vandens ir CH kiekis yra mažesnis bandiniuose po dviejų hidratacijos parų su sintetiniu jelimito priedu, lyginant su OPC ir 80P20FA bandiniais (žr. 5.12 pav.). Šie rezultatai rodo, kad jelimito priedas atideda arba lėtina kalcio silikatų hidrataciją (alito ir galimai belito), o tai lemia mažesnes stiprio gniuždant vertes per pirmąją hidratacijos savaitę. Įdomu tai, kad po 7 hidratacijos parų OPC–FA–Y bandiniuose susidaro didesnis hidratacijos produktų vandens ir CH kiekis lyginant su OPC bandiniu, nors ir OPC–FA–Y bandinių gniuždymo stiprio vertės mažesnės. Nuo 7 iki 28 hidratacijos parų, kaip ir 80P20FA bandiniuose, nustatytas mažesnis CH kiekis OPC–FA–Y bandiniuose, o hidratacijos produktų vandens kiekis didesnis nei OPC bandinyje.

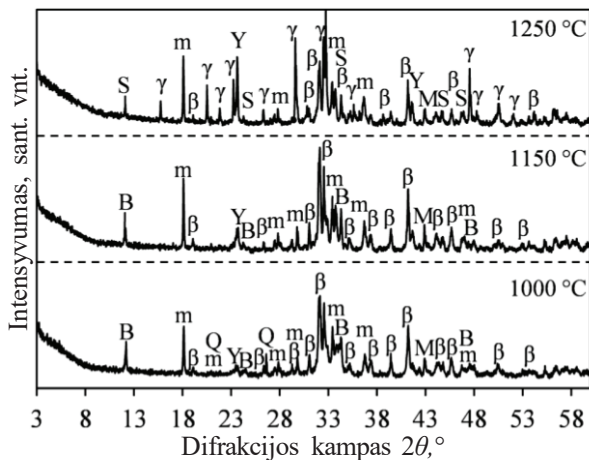
Apibendrinant gautus rezultatus, galima teigti, kad jelimito priedas gali būti naudojamas kaip pelenų portlandcemenčio tešlos rišamosi trukmės reguliatorius, kuris nepablogina galutinių gaminių mechaninių savybių.

5.3.6. Jelimito susidarymas belitinio-jelimitinio-feritinio cemento sintezės metu ir paruošto cemento mechaninių savybių tyrimas

Baigiamajame tyrimų etape buvo atlikta bandomoji belitinio-jelimitinio-feritinio (BJF) cemento sintezė kalcinavimo metodu, siekiant įvertinti jelimito susidarymą sistemoje ir gauto skiedinio mechanines savybės. Šiam tikslui pradinis mišinys buvo paruoštas iš Lietuvoje aptinkamų pramoninių atliekų (~ 18 %) (granitmilčių ir silikagelio) ir natūralių žaliavų (~ 82 %), kai pasirinkta tokia tikslinė klinkerio sudėtis: 60 % belito, 20 % jelimito ir 20 % ferito. Degimo temperatūros įtaka

BJF klinkerio fazių susidarymui ištirta 1000–1250 °C temperatūros intervale, kai išlaikymo trukmė 1 h.

Nustatyta, kad bandiniuose, išdegtuose 1000–1050 °C temperatūroje, susidaro belitas, majenitas, braunmileritas, jelimitas (žr. 5.13 pav.). Visgi šio temperatūros intervalo nepakanka iki galo sureaguoti pradiniai žaliavai – kvarcui. Tolesnis temperatūros didėjimas skatina kietojo kūno reakcijas, dėl kurių 1100 °C temperatūroje iki galo sureaguoja kvarcas ir auga minėtų cemento fazių difrakciniai maksimumai. Pažymėtina, kad temperatūros didinimas turi reikšmingiausią įtaką jelimito susidarymui, kur didžiausi šio junginio difrakcinių smailių intensyvumai nustatyti 1200–1250 °C temperatūroje. Visgi šiame temperatūros intervale pagrindinis sintezės produktas – β -C₂S – aušinimo metu tampa metastabilus ir persikristalizuoja į giminingą junginį γ -C₂S, kuris nepasizymi hidrataciniu aktyvumu.



5.13 pav. BCF klinkerio, dego įvairiose temperatūrose 1 h, RSDA kreivės: Q – kvarcas; S – srebrodolskitas; m – majenitas; β – belitas (β -C₂S); γ – dikalcio silikatas (γ -C₂S); M – magnio oksidas; Y – jelimitas; B – braunmileritas

Remiantis gautais rezultatais, BCF klinkerio gamybai pasirinkta 1150 °C temperatūra. Rietveldo analizės metodu apskaičiuota, kad susintetintą BCF klinkerį sudaro 53,5 % belito, 17,4 % majenito, 15,3 % srebrodolskito (Ca₂Mg_{0,1}FeAl_{0,9}O₅, PDF Nr. 04-014-9001) (giminingas junginys feritui), 5,2 % jelimito, 4,8 % gelenito (Ca₂Al₂SiO₇, PDF Nr. 00-009-0216), 3,2 % magnio oksido ir 0,6 % kitų fazių. Pagamintas BCF klinkeris sumaišytas su gipsu (7,5 %), siekiant užtikrinti optimalią cemento junginių hidrataciją, ir paruoštas cementas naudotas mechaninių savybių tyrimams.

Skiedinių gniuždymo stiprio tyrimai atlikti kietinant standartines prizmes vandens aplinkoje iki 90 parų. Rezultatai parodė, kad paruoštų skiedinių gniuždymo stipris auga lėtai (žr. 5.7 lent.), kurių vertės po trijų parų padidėja nuo 4,25 MPa iki 10,35 MPa po 90 kietėjimo parų vandens aplinkoje.

izoterminio išlaikymo trukmė – 24 h. Nustatyta, kad skiedinio bandinių hidroterminis apdorojimas 90–125 °C temperatūroje neigiamai veikia gniuždymo stiprio vertes, kurios atitinkamai sumažėja nuo 3,92 MPa iki 1,22 MPa (žr. 5.8 lent.). Nepaisant to, žymus gniuždymo stipris labai didėja, kai bandiniai apdorojami ≥ 150 °C temperatūroje. Didžiausios skiedinio bandinių gniuždymo stiprio vertės pasiekiamos kietinant bandinius 24 h 200 °C temperatūroje, kurios atitinka mūro gaminių (EN 771-2) standarte nurodytas vertes.

5.8 lentelė. Hidroterminėje aplinkoje kietintų BJB cementų skiedinio gniuždymo ir lenkimo stiprio vertės, kai izoterminio išlaikymo trukmė – 24 h

Temperatūra	90 °C	100 °C	125 °C	150 °C	175 °C	200 °C
Gniuždymo stipris, MPa	3,92	2,68	1,22	15,25	18,32	20,07
Lenkimo stipris, MPa	1,9	0,9	0	2,50	3,30	3,70

Galima daryti išvadą, kad BJB klinkerio sintezė 1150 °C temperatūroje nėra pakankama jelimitui susidaryti. Vietoje šio junginio susidariusios cemento fazės (majenitas ir gelenitas) nekompensuoja pradinio skiedinio stiprumo, todėl kietinant bandinius vandens aplinkoje gaunamos gniuždymo stiprio vertės yra mažos. Kaip aptarta ankstesniuose skyriuose, dviejų stadijų sintezės metodas leidžia susintetinti didelio grynumo jelimitą tomis pačiomis degimo sąlygomis (1150 °C). Tai rodo šio metodo potencialą, kuris, labai tikėtina, leis susintetinti BJB klinkerį su tiksliniu jelimito kiekiu, o gal ir sumažins kalcinavimo temperatūrą priklausomai nuo cemento fazių sudėties.

5.4. Išvados

1. Nustatyta, kad optimalios hidroterminės sintezės sąlygos kalcio monosulfoaluminato 12-hidratui (Ms12, prekursorius) susidaryti yra 110 °C 8 h. Pradinio mišinio mechaninis cheminis apdorojimas (trys 10 min įjungimo ir išjungimo ciklai esant 900 aps./min) skatina Ms12 kristalizaciją ir neleidžia susidaryti etringitui, katoitui ir portlanditui. Gauti eksperimentiniai rezultatai patvirtinti termodinaminiais skaičiavimais.
2. Dalinis vandens garų slėgis (p/p_0) kontroliuoja Ms12 karbonizacijos elgseną. Nustatyta, kad šis junginys atspariausias karbonizacijai esant 0,355 p/p_0 . Galutiniai susidarantys karbonizacijos produktai po 90 dienų visomis sąlygomis yra kalcio karbonatas, aliuminio hidroksidas ir kalcio sulfato hidratas (jei $\leq 0,565 p/p_0$ – pushidratis gipsas; jei $\geq 0,565 p/p_0$ – gipsas). Esant pakankamai drėgmei (0,753–1,0 p/p_0), pastebima, kad Ms12 taip pat persikristalizuoja į etringitą. Tariamieji kinetiniai skaičiavimai patvirtino, kad karbonizacijos reakcijos greitis tiesiogiai priklauso nuo išorinės drėgmės kiekio. Pritaikyti Janderio ir Avrami modeliai parodė, kad tirpimo ir branduolių susidarymo procesai kontroliuoja vienmačio CaCO₃ kristalų augimo susidarymą.
3. Terminis stabilumo tyrimas patvirtino, kad Ms12 skylimas vyksta 25–370 °C temperatūros intervale, kur nustatyta keturių kalcio monosulfoaluminatų su skirtingu struktūrinio vandens kiekiu dehidratacija (Ms12→Ms10,5→Ms9→Ms6-x). Rezultatai rodo, kad vandens molekulių pašalinimas iš pagrindinių (oktaedrinių) sluoksnių prasideda ~200 °C temperatūroje. 720–1250 °C temperatūroje vyksta kietojo kūno reakcijos tarp C^Š, CA, C₁₂A₇ ir CaO, kurios skatina jelimito susidarymą. Nustatytos optimalios sukepinimo sąlygos didelio grynumo (~97 %) jelimito sintezei yra 1150 °C 1 h.
4. Ištirta, kad susintetintas jelimitas dviejų stadijų sintezės metodu pasižymi penkiais tipiniais cemento hidratacijos periodais. Indukcinis periodas trunka 10 h 10 min, antrasis egzoterminės reakcijos maksimumas pasiekiamas po 14 h 45 min, o išsiskyręs šilumos kiekis po 72 h yra ~585 J/g. Kaip hidratacijos produktai susidaro monosulfoaluminatas, etringitas ir amorfiniai / mikrokristaliniai aliuminio hidroksidai.
5. Nustatyta, kad, pakeičiant jelimitą silicininiais lakiaisiais pelenais, pagreitėja jo ankstyvoji hidratacija, kuri siejama su padidėjusiu šarmų kiekiu sistemoje (stipriausia įtaka), papildomomis branduolių susidarymo vietomis (užpildo efektas) ir didesniu vandens ir rišamosios medžiagos santykiu. Lakiųjų pelenų įtraukimas galimai riboja monosulfoaluminato susidarymą ir (arba) skatina jo skilimą, todėl hidratacijos metu galimai susidaro ir (arba) stabilizuojasi etringitas.
6. Nustatyta, kad ruošiant tešlą iš pelenų portlandcemenčio su 0,5–1 % jelimito priedu, efektyviai sumažinamos tiek pradžios, tiek pabaigos rišimosi trukmės,

nepaveikiant skiedinio gniuždymo stiprio po 28 kietėjimo parų, lyginant su grynų OPC skiedinio bandiniu.

7. Nustatyta, kad paruošto belitinio-jelimitinio-feritinio cemento skiedinio stiprumas didėja lėtai (~10 MPa po 90 dienų), kietinant bandinius vandens aplinkoje, kuri siejama su lėta pagrindinės cemento fazės, belito, hidratacija. Kita vertus, skiedinio bandinių kietinimas hidroterminėmis sąlygomis pagerina gniuždymo stiprio vertes; bandiniai pasiekia didžiausią ~20 MPa stiprumą kietinami 200 °C temperatūroje 24 h.

REFERENCES

- [1] MIKHAYLOV, A., et al. Global climate change and greenhouse effect. *Entrepreneurship and Sustainability Issues*, 2020, 7.4: 2897. Available from: [https://doi.org/10.9770/jesi.2020.7.4\(21\)](https://doi.org/10.9770/jesi.2020.7.4(21)).
- [2] BELLARD, C., et al. Impacts of climate change on the future of biodiversity. *Ecology letters*, 2012, 15.4: 365–377. Available from: <https://doi.org/10.1111/j.1461-0248.2011.01736.x>.
- [3] TONG, S., EBI, K. Preventing and mitigating health risks of climate change. *Environmental research*, 2019, 174: 9–13. Available from: <https://doi.org/10.1016/j.envres.2019.04.012>.
- [4] HOROWITZ, C. A. Paris agreement. *International Legal Materials*, 2016, 55.4: 740–755. Available from: <https://doi.org/10.1017/S0020782900004253>
- [5] FETTING, C. The European Green Deal. ESDN report, 2020, 53. Available from: https://www.esdn.eu/fileadmin/ESDN_Reports/ESDN_Report_2_2020.pdf
- [6] YORK, I. N.; EUROPE, I. Concrete needs to lose its colossal carbon footprint. *Nature*, 2021, 597.7878: 593–594. Available from: <https://www.nature.com/articles/d41586-021-02612-5>
- [7] World Green Building Council. Bringing embodied carbon upfront. Report. Available from: <https://worldgbc.org/article/bringing-embodied-carbon-upfront/>
- [8] The European Cement Association. REACHING CLIMATE NEUTRALITY ALONG THE CEMENT AND CONCRETE VALUE CHAIN BY 2050. Report. Available from: <https://cembureau.eu>
- [9] Materials Economics Journal. Industrial transformation 2050: Pathways to net-zero emissions from EU heavy industry. *University of Cambridge Institute for Sustainability Leadership (CISL): Cambridge, UK*, 2019. Available from: <https://materialeconomics.com>
- [10] CHAUDHURY, R., et al. Low-CO₂ emission strategies to achieve net zero target in cement sector. *Journal of Cleaner Production*, 2023, 137466. Available from: <https://doi.org/10.1016/j.jclepro.2023.137466>.
- [11] WESSELSKY, A., JENSEN, O. M. Synthesis of pure Portland cement phases. *Cement and Concrete Research*, 2009, 39.11: 973–980. Available from: <https://doi.org/10.1016/j.cemconres.2009.07.013>.
- [12] STANDARD, E. Cement–Part 1: Composition, specifications and conformity criteria for common cements. 2000. Available from: http://168.101.26.37/notific_otros_miembros/mwi40_t.pdf.
- [13] AN, J., et al. Estimated material metabolism and life cycle greenhouse gas emission of major plastics in China: A commercial sector-scale perspective. *Resources, Conservation and Recycling*, 2022, 180: 106161. Available from: <https://doi.org/10.1016/j.resconrec.2022.106161>.

- [14] CAVALIERE, P., SILVELLO, A. CO₂ Emission Reduction in Blast Furnaces. *Ironmaking and Steelmaking Processes: Greenhouse Emissions, Control, and Reduction*, 2016, 151–171. Available from: <https://doi.org/10.1007/978-3-319-39529-6>.
- [15] CHEN, S., et al. A systematic review of the life cycle environmental performance of cotton textile products. *Science of The Total Environment*, 2023, 163659. Available from: <https://doi.org/10.1016/j.scitotenv.2023.163659>.
- [16] SCRIVENER, K. L., JOHN, V. M., GARTNER, E. M. Eco-efficient cements: Potential economically viable solutions for a low-CO₂ cement-based materials industry. *Cement and concrete Research*, 2018, 114: 2–26. Available from: <https://doi.org/10.1016/j.cemconres.2018.03.015>.
- [17] SOUSA, V., BOGAS, J. A. Comparison of energy consumption and carbon emissions from clinker and recycled cement production. *Journal of cleaner production*, 2021, 306: 127277. Available from: <https://doi.org/10.1016/j.jclepro.2021.127277>.
- [18] MADLOOL, N. A., et al. A critical review on energy use and savings in the cement industries. *Renewable and sustainable energy reviews*, 2011, 15.4: 2042–2060. Available from: <https://doi.org/10.1016/j.rser.2011.01.005>.
- [19] IMBABI, M. S., CARRIGAN, C., MCKENNA, S. Trends and developments in green cement and concrete technology. *International Journal of Sustainable Built Environment*, 2012, 1.2: 194–216. Available from: <https://doi.org/10.1016/j.ijbsbe.2013.05.001>.
- [20] NAQI, A., JANG, J. G. Recent progress in green cement technology utilizing low-carbon emission fuels and raw materials: A review. *Sustainability*, 2019, 11.2: 537. Available from: <https://doi.org/10.3390/su11020537>.
- [21] KLEIN, Alexander. Studies of calcium sulphoaluminate admixtures for expansive cements. In: *Proceedings of ASTM*. 1958. p. 968–1008.
- [22] ZHANG, L., SU, Muzhen., WANG, Y. Development of the use of sulfo- and ferroaluminate cements in China. *Advances in cement research*, 1999, 11.1: 15–21. Available from: <https://doi.org/10.1680/adcr.1999.11.1.15>.
- [23] PIMRAKSA, K., CHINDAPRASIRT, P. Sulfoaluminate cement-based concrete. In: *Eco-Efficient Repair and Rehabilitation of Concrete Infrastructures*. Woodhead Publishing, 2018. p. 355–385. Available from: <https://doi.org/10.1016/B978-0-08-102181-1.00014-9>.
- [24] GARTNER, E., SUI, T. Alternative cement clinkers. *Cement and Concrete Research*, 2018, 114: 27–39. Available from: <https://doi.org/10.1016/j.cemconres.2017.02.002>.
- [25] CHEN, I. A., JUENGER, M. CG. Synthesis and hydration of calcium sulfoaluminate-belite cements with varied phase compositions. *Journal of Materials Science*, 2011, 46: 2568–2577. Available from: <https://doi.org/10.1007/s10853-010-5109-9>.

- [26] ARANDA, M. A. G., DE LA TORRE, A. G. Sulfoaluminate cement. In: *Eco-efficient concrete*. Woodhead Publishing, 2013. p. 488–522. Available from: <https://doi.org/10.1533/9780857098993.4.488>.
- [27] TELESCA, A., et al. A hydration study of various calcium sulfoaluminate cements. *Cement and Concrete Composites*, 2014, 53: 224–232. <https://doi.org/10.1016/j.cemconcomp.2014.07.002>.
- [28] WOLF, J. J., et al. Mechanisms of early ettringite formation in ternary CSA–OPC–anhydrite systems. *Advances in Cement Research*, 2019, 31.4: 195–204. Available from: <https://doi.org/10.1680/jadcr.18.00115>.
- [29] WOLF, J. J., et al. Application of thermodynamic modeling to predict the stable hydrate phase assemblages in ternary CSA–OPC–anhydrite systems and quantitative verification by QXRD. *Cement and Concrete Research*, 2020, 128: 105956. Available from: <https://doi.org/10.1016/j.cemconres.2019.105956>.
- [30] VAPNIK, Y., et al. Stone–tool workshops of the Hatrurim Basin, Israel: mineralogy, geochemistry, and rock mechanics of lithic industrial materials. In: *Case Studies–Coal Fires*. Elsevier Inc., 2014. p. 282–316. Available from: <https://doi.org/10.1016/B978-0-444-59509-6.00010-7>.
- [31] CUESTA, A., et al. Structure, atomistic simulations, and phase transition of stoichiometric yeelimite. *Chemistry of Materials*, 2013, 25.9: 1680–1687. Available from: <https://doi.org/10.1021/cm400129z>.
- [32] KRSTANOVIĆ, I., RADAKOVIĆ, A., KARANOVIĆ, L. X–Ray Powder Data for Ca₄Al₆O₁₂SO₄. *Powder Diffraction*, 1992, 7.1: 47–48. Available from: <https://doi.org/10.1017/S0885715600016092>.
- [33] CALOS, N. J., et al. Structure of calcium aluminate sulfate Ca₄Al₆O₁₆S. *Journal of Solid State Chemistry*, 1995, 119.1: 1–7. Available from: [https://doi.org/10.1016/0022-4596\(95\)80002-7](https://doi.org/10.1016/0022-4596(95)80002-7).
- [34] SAALFELD, H., DEPMEIER, W. Silicon–free compounds with sodalite structure. *Krist. Tech*, 1972, 7: 229–233. Available from: <https://doi.org/10.1515/9783112653302-025>.
- [35] KUROKAWA, D., et al. Phase transformation of Ca₄[Al₆O₁₂]SO₄ and its disordered crystal structure at 1073 K. *Journal of Solid State Chemistry*, 2014, 215: 265–270. Available from: <https://doi.org/10.1016/j.jssc.2014.03.040>.
- [36] NDZILA, J. S., et al. The effect of Fe³⁺ ion substitution on the crystal structure of ye’elimite. *Ceram. Silik*, 2020, 64: 18–28. <https://doi.org/10.13168/cs.2019.0044>.
- [37] CUESTA, A., et al. Pseudocubic crystal structure and phase transition in doped ye’elimite. *Crystal growth & design*, 2014, 14.10: 5158–5163. Available from: <https://doi.org/10.1021/cg501290q>.
- [38] BULLERJAHN, F., SCHMITT, D., HAHA, M. B. Effect of raw mix design and of clinkering process on the formation and mineralogical composition of (ternesite) belite calcium sulfoaluminate ferrite clinker. *Cement and*

- Concrete Research*, 2014, 59: 87–95. Available from: <https://doi.org/10.1016/j.cemconres.2014.02.004>.
- [39] BULLERJAHN, F., ZAJAC, M., BEN HAHA, M. CSA raw mix design: effect on clinker formation and reactivity. *Materials and Structures*, 2015, 48.12: 3895–3911. <https://doi.org/10.1617/s11527-014-0451-z>.
- [40] HALSTEAD, P. E., MOORE, A. E. The composition and crystallography of an anhydrous calcium aluminosulphate occurring in expanding cement. *Journal of Applied Chemistry*, 1962, 12.9: 413–417. Available from: <https://doi.org/10.1002/jctb.5010120906>.
- [41] SAALFELD, H., DEPMEIER, W. Silicon-free compounds with sodalite structure. *Krist. Tech*, 1972, 7: 229–233. Available from: <https://doi.org/10.1515/9783112653302-025>.
- [42] HANIC, F., et al. Crystal chemistry and thermodynamics of the sulphate compounds $\text{Ca}_4[\text{Al}_6\text{O}_{12}](\text{SO}_4)$ and $\text{Ca}_5(\text{SiO}_4)_2(\text{SO}_4)$. *British ceramic. Transactions and journal*, 1986, 85.2: 52–57.
- [43] KRSTANOVIĆ, I., RADAKOVIĆ, A., KARANOVIĆ, L. X-Ray Powder Data for $\text{Ca}_4\text{Al}_6\text{O}_{12}\text{SO}_4$. *Powder Diffraction*, 1992, 7.1: 47–48. Available from: <https://doi.org/10.1017/S0885715600016092>.
- [44] PEIXING, Z., et al. The crystal structure of $\text{C}_4\text{A}_3\text{S}$. *Proceedings of 9th ICC*, 1992, 31: 201-208.
- [45] ALI, M. M., GOPAL, S., HANDOO, S. K. Studies on the formation kinetics of calcium sulphoaluminate. *Cement and concrete research*, 1994, 24.4: 715–720. Available from: [https://doi.org/10.1016/0008-8846\(94\)90196-1](https://doi.org/10.1016/0008-8846(94)90196-1).
- [46] ANDAC, O., GLASSER, F. P. Polymorphism of calcium sulphoaluminate ($\text{Ca}_4\text{Al}_6\text{O}_{16}\cdot\text{SO}_3$) and its solid solutions. *Advances in Cement Research*, 1994, 6.22: 57–60. Available from: <https://doi.org/10.1680/adcr.1994.6.22.57>.
- [47] IKEDA, K., KISHIMOTO, K., SHIMA, H. Structure refinement of calcium sulfoaluminate, $\text{C}_4\text{A}_3\text{S}$ with emphasis to oxygen deficiency. *Cement and concrete research*, 1996, 26.5: 743–748. Available from: [https://doi.org/10.1016/S0008-8846\(96\)85011-3](https://doi.org/10.1016/S0008-8846(96)85011-3).
- [48] SONG, J. T., YOUNG, J. F. Direct synthesis and hydration of calcium aluminosulfate ($\text{Ca}_4\text{Al}_6\text{O}_{16}\text{S}$). *Journal of the American Ceramic Society*, 2002, 85.3: 535–539. Available from: <https://doi.org/10.1111/j.1151-2916.2002.tb00129.x>.
- [49] WINNEFELD, F., BARLAG, S. Calorimetric and thermogravimetric study on the influence of calcium sulfate on the hydration of ye'elimite. *Journal of thermal analysis and calorimetry*, 2010, 101.3: 949–957. Available from: <https://doi.org/10.1007/s10973-009-0582-6>.
- [50] CUESTA, A., et al. Pseudocubic crystal structure and phase transition in doped ye'elimite. *Crystal growth & design*, 2014, 14.10: 5158–5163. Available from: <https://doi.org/10.1021/cg501290q>.

- [51] MOKRÁ, J., et al. Long-term observation of yeelimite clinker hydration in environment of saturated water vapour. *Procedia Engineering*, 2016, 151: 94–99. Available from: <https://doi.org/10.1016/j.proeng.2016.07.385>.
- [52] EL KHESSAIMI, Y., et al. Solid-state synthesis of pure ye'elimite. *Journal of the European Ceramic Society*, 2018, 38.9: 3401–3411. Available from: <https://doi.org/10.1016/j.jeurceramsoc.2018.03.018>.
- [53] EL KHESSAIMI, Y., EL HAFIANE, Y., SMITH, A. Ye'elimite synthesis by chemical routes. *Journal of the European Ceramic Society*, 2019, 39.4: 1683–1695. Available from: <https://doi.org/10.1016/j.jeurceramsoc.2018.10.025>.
- [54] WU, Shuang, et al. Synthesis, structure, and hydration of stoichiometric ye'elimite and iron-bearing ye'elimite. *Journal of Sustainable Cement-Based Materials*, 2024, 13.1: 164–177. Available from: <https://doi.org/10.1080/21650373.2023.2258500>.
- [55] TOUZO, B., SCRIVENER, K. L., GLASSER, F. P. Phase compositions and equilibria in the CaO–Al₂O₃–Fe₂O₃–SO₃ system, for assemblages containing ye'elimite and ferrite Ca₂ (Al, Fe) O₅. *Cement and concrete research*, 2013, 54: 77–86. Available from: <https://doi.org/10.1016/j.cemconres.2013.08.005>.
- [56] EL KHESSAIMI, Y., EL HAFIANE, Y., SMITH, A. Examination of ye'elimite formation mechanisms. *Journal of the European Ceramic Society*, 2019, 39.15: 5086–5095. Available from: <https://doi.org/10.1016/j.jeurceramsoc.2019.07.042>.
- [57] LI, X., et al. Kinetics of calcium sulfoaluminate formation from tricalcium aluminate, calcium sulfate and calcium oxide. *Cement and concrete research*, 2014, 55: 79–87. Available from: <https://doi.org/10.1016/j.cemconres.2013.10.006>.
- [58] IFTEKHAR, S., et al. Phase formation of CaAl₂O₄ from CaCO₃–Al₂O₃ powder mixtures. *Journal of the European Ceramic Society*, 2008, 28.4: 747–756. Available from: <https://doi.org/10.1016/j.jeurceramsoc.2007.08.012>.
- [59] DE BILBAO, E., et al. Time-resolved high-temperature X-ray diffraction for studying the kinetics of corrosion of high-alumina refractory by molten oxides. *Corrosion Science*, 2018, 139: 346–354. Available from: <https://doi.org/10.1016/j.corsci.2018.05.003>.
- [60] VISWANATH, B., RAVISHANKAR, N. Interfacial reactions in hydroxyapatite/alumina nanocomposites. *Scripta Materialia*, 2006, 55.10: 863–866. Available from: <https://doi.org/10.1016/j.scriptamat.2006.07.049>.
- [61] BOKOV, D., et al. Nanomaterial by sol-gel method: synthesis and application. *Advances in Materials Science and Engineering*, 2021, 2021: 1–21. Available from: <https://doi.org/10.1155/2021/5102014>.
- [62] ZARZUELA, R., et al. Producing CSH gel by reaction between silica oligomers and portlandite: A promising approach to repair cementitious materials. *Cement and Concrete Research*, 2020, 130: 106008. Available from: <https://doi.org/10.1016/j.cemconres.2020.106008>.

- [63] LEIVO, J., et al. Sol–gel synthesis of a nanoparticulate aluminosilicate precursor for homogeneous mullite ceramics. *Journal of materials research*, 2006, 21.5: 1279–1285. Available from: <https://doi.org/10.1557/jmr.2006.0152>.
- [64] NAIR, P. A. K., et al. A review on applications of sol–gel science in cement. *Construction and building materials*, 2021, 291: 123065. Available from: <https://doi.org/10.1016/j.conbuildmat.2021.123065>.
- [65] HE, Z., et al. Synthesis of C3S by sol–gel technique and its features. *Journal of Wuhan University of Technology–Mater. Sci. Ed.*, 2010, 25.1: 138–141. Available from: <https://doi.org/10.1007/s11595–010–1138–0>.
- [66] THOMAS, J. J., GHAZIZADEH, S., MASOERO, E. Kinetic mechanisms and activation energies for hydration of standard and highly reactive forms of β -dicalcium silicate (C2S). *Cement and Concrete Research*, 2017, 100: 322–328. Available from: <https://doi.org/10.1016/j.cemconres.2017.06.001>.
- [67] SELYUNINA, L., et al. Sol–gel synthesis of fluorescent materials based on tricalcium aluminate. In: *Journal of Physics: Conference Series*. IOP Publishing, 2019. p. 012031. Available from: <https://doi.org/10.1088/1742–6596/1145/1/012031>.
- [68] BULLARD, J. W., et al. Mechanisms of cement hydration. *Cement and concrete research*, 2011, 41.12: 1208–1223. Available from: <https://doi.org/10.1016/j.cemconres.2010.09.011>.
- [69] SCRIVENER, K., et al. Advances in understanding cement hydration mechanisms. *Cement and Concrete Research*, 2019, 124: 105823. Available from: <https://doi.org/10.1016/j.cemconres.2019.105823>.
- [70] WINNEFELD, F., et al. Using gypsum to control hydration kinetics of CSA cements. *Construction and Building Materials*, 2017, 155: 154–163. Available from: <https://doi.org/10.1016/j.conbuildmat.2017.07.217>.
- [71] CHEN, I. A., HARGIS, C. W., JUENGER, M. CG. Understanding expansion in calcium sulfoaluminate–belite cements. *Cement and Concrete Research*, 2012, 42.1: 51–60. Available from: <https://doi.org/10.1016/j.cemconres.2011.07.010>.
- [72] ALLEVI, S., et al. Hydration of calcium sulphoaluminate clinker with additions of different calcium sulphate sources. *Materials and Structures*, 2016, 49: 453–466. Available from: <https://doi.org/10.1617/s11527–014–0510–5>.
- [73] GARCÍA–MATÉ, M., et al. Effect of calcium sulfate source on the hydration of calcium sulfoaluminate eco–cement. *Cement and Concrete Composites*, 2015, 55: 53–61. Available from: <https://doi.org/10.1016/j.cemconcomp.2014.08.003>.
- [74] HARGIS, C. W., et al. Further insights into calcium sulfoaluminate cement expansion. *Advances in Cement Research*, 2019, 31.4: 160–177. Available from: <https://doi.org/10.1680/jadcr.18.00124>.

- [75] CUESTA, A., et al. Hydration mechanisms of two polymorphs of synthetic ye'elimite. *Cement and concrete research*, 2014, 63: 127–136. Available from: <https://doi.org/10.1016/j.cemconres.2014.05.010>.
- [76] JANSEN, D., et al. Studies on the early hydration of two modifications of ye'elimite with gypsum. *Cement and Concrete Research*, 2017, 91: 106–116. Available from: <https://doi.org/10.1016/j.cemconres.2016.11.009>.
- [77] IDRISSE, M., et al. Hydration behavior of iron doped calcium sulfoaluminate phase at room temperature. In: *MATEC Web of Conferences*. EDP Sciences, 2012. p. 01005. Available from: <https://doi.org/10.1051/C>.
- [78] CHEN, D., FENG, X., LONG, S. The influence of ferric oxide on the properties of $3\text{CaO} \cdot 3\text{Al}_2\text{O}_3 \cdot \text{SrSO}_4$. *Thermochimica acta*, 1993, 215: 143–155. Available from: [https://doi.org/10.1016/0040-6031\(93\)80088-R](https://doi.org/10.1016/0040-6031(93)80088-R).
- [79] BULLERJAHN, F., HAHA, M. B., SCRIVENER, K. L. Iron solid solutions of ye'elimite—Effect on reactivity. In: *The 14th International Congress on the Chemistry of Cement*. 2015. Available from: <https://www.researchgate.net/publication/282910382>.
- [80] BULLERJAHN, F., et al. Factors influencing the hydration kinetics of ye'elimite; effect of mayenite. *Cement and Concrete Research*, 2019, 116: 113–119. Available from: <https://doi.org/10.1016/j.cemconres.2018.10.026>.
- [81] HARGIS, C. W., TELESCA, A., MONTEIRO, P. JM. Calcium sulfoaluminate (Ye'elimite) hydration in the presence of gypsum, calcite, and vaterite. *Cement and Concrete Research*, 2014, 65: 15–20. Available from: <https://doi.org/10.1016/j.cemconres.2014.07.004>.
- [82] PADILLA-ENCINAS, P., et al. Effect of alkalinity on early-age hydration in calcium sulfoaluminate clinker. *Cement and Concrete Research*, 2022, 155: 106781. Available from: <https://doi.org/10.1016/j.cemconres.2022.106781>.
- [83] PADILLA-ENCINAS, P., et al. Calcium sulfoaluminate clinker hydration at different alkali concentrations. *Cement and Concrete Research*, 2020, 138: 106251. Available from: <https://doi.org/10.1016/j.cemconres.2020.106251>.
- [84] TAMBARA JR, L. U. D., et al. Effect of alkalis content on calcium sulfoaluminate (CSA) cement hydration. *Cement and concrete research*, 2020, 128: 105953. Available from: <https://doi.org/10.1016/j.cemconres.2019.105953>.
- [85] EL KHESSAIMI, Y., EL HAFIANE, Y., SMITH, A. Effect of fineness and citric acid addition on the hydration of ye'elimite. *Construction and Building Materials*, 2020, 258: 119686. Available from: <https://doi.org/10.1016/j.conbuildmat.2020.119686>.
- [86] PADILLA-ENCINAS, P., et al. Monitoring early hydration of calcium sulfoaluminate clinker. *Construction and Building Materials*, 2021, 295: 123578. Available from: <https://doi.org/10.1016/j.conbuildmat.2021.123578>.
- [87] DORN, T., BLASK, O., STEPHAN, D. Acceleration of cement hydration—A review of the working mechanisms, effects on setting time, and compressive strength development of accelerating admixtures. *Construction and building*

- materials*, 2022, 323: 126554. Available from: <https://doi.org/10.1016/j.conbuildmat.2022.126554>.
- [88] GOUGAR, M. L. D., SCHEETZ, B. E., ROY, D. M. Ettringite and C–S–H Portland cement phases for waste ion immobilization: A review. *Waste management*, 1996, 16.4: 295–303. Available from: [https://doi.org/10.1016/S0956-053X\(96\)00072-4](https://doi.org/10.1016/S0956-053X(96)00072-4).
- [89] CLARK, S. M., et al. Effect of pressure on the crystal structure of ettringite. *Cement and Concrete Research*, 2008, 38.1: 19–26. Available from: <https://doi.org/10.1016/j.cemconres.2007.08.029>.
- [90] MANTELLATO, S., PALACIOS, M., FLATT, R. J. Impact of sample preparation on the specific surface area of synthetic ettringite. *Cement and Concrete Research*, 2016, 86: 20–28. Available from: <https://doi.org/10.1016/j.cemconres.2016.04.005>.
- [91] HARTMAN, M. R., et al. The evolution of structural changes in ettringite during thermal decomposition. *Journal of Solid State Chemistry*, 2006, 179.4: 1259–1272. Available from: <https://doi.org/10.1016/j.jssc.2006.01.038>.
- [92] RENAUDIN, G., et al. A comparative structural study of wet and dried ettringite. *Cement and Concrete Research*, 2010, 40.3: 370–375. Available from: <https://doi.org/10.1016/j.cemconres.2009.11.002>.
- [93] BAQUERIZO, L. G., MATSCHEI, T., SCRIVENER, K. L. Impact of water activity on the stability of ettringite. *Cement and Concrete Research*, 2016, 79: 31–44. Available from: <https://doi.org/10.1016/j.cemconres.2015.07.008>.
- [94] GRUSCZCINSKI, E., BROWN, P. W., BOTHE JR, J. V. The formation of ettringite at elevated temperature. *Cement and concrete research*, 1993, 23.4: 981–987. Available from: [https://doi.org/10.1016/0008-8846\(93\)90052-B](https://doi.org/10.1016/0008-8846(93)90052-B).
- [95] ZHOU, Q., LACHOWSKI, E. E., GLASSER, F. P. Metaettringite, a decomposition product of ettringite. *Cement and Concrete Research*, 2004, 34.4: 703–710. Available from: <https://doi.org/10.1016/j.cemconres.2003.10.027>.
- [96] ZHANG, Jie., SCHERER, G. W. Comparison of methods for arresting hydration of cement. *Cement and Concrete Research*, 2011, 41.10: 1024–1036. Available from: <https://doi.org/10.1016/j.cemconres.2011.06.003>.
- [97] LIU, M., et al. Influence of water removal techniques on the composition and microstructure of hardened calcium sulfoaluminate cement pastes. *Materials and Structures*, 2020, 53: 1–11. Available from: <https://doi.org/10.1617/s11527-020-01527-3>.
- [98] KHOSHNAZAR, R., et al. Solvent exchange in sulfoaluminate phases. Part II: monosulfate. *Advances in cement research*, 2013, 25.6: 322–331. Available from: <https://doi.org/10.1680/adcr.12.00055>.
- [99] GALAN, I., et al. Impact of drying on pore structures in ettringite-rich cements. *Cement and Concrete Research*, 2016, 84: 85–94. Available from: <https://doi.org/10.1016/j.cemconres.2016.03.003>.

- [100] JIMÉNEZ, A., PRIETO, M. Thermal stability of ettringite exposed to atmosphere: Implications for the uptake of harmful ions by cement. *Environmental Science & Technology*, 2015, 49.13: 7957–7964. Available from: <https://doi.org/10.1021/acs.est.5b00536>.
- [101] PERKINS, R. B., PALMER, C. D. Solubility of ettringite ($\text{Ca}_6 [\text{Al}(\text{OH})_6]_2 (\text{SO}_4)_3 \cdot 26\text{H}_2\text{O}$) at 5–75° C. *Geochimica et Cosmochimica Acta*, 1999, 63.13–14: 1969–1980. Available from: [https://doi.org/10.1016/S0016-7037\(99\)00078-2](https://doi.org/10.1016/S0016-7037(99)00078-2).
- [102] ZHOU, Q., GLASSER, F. P. Thermal stability and decomposition mechanisms of ettringite at < 120 C. *Cement and Concrete Research*, 2001, 31.9: 1333–1339. Available from: [https://doi.org/10.1016/S0008-8846\(01\)00558-0](https://doi.org/10.1016/S0008-8846(01)00558-0).
- [103] BROWN, P. W., BOTHE JR, J. V. The stability of ettringite. *Advances in Cement Research*, 1993, 5.18: 47–63. Available from: <https://doi.org/10.1680/adcr.1993.5.18.47>.
- [104] MISHRA, G., DASH, B., PANDEY, S. Layered double hydroxides: A brief review from fundamentals to application as evolving biomaterials. *Applied Clay Science*, 2018, 153: 172–186. Available from: <https://doi.org/10.1016/j.clay.2017.12.021>.
- [105] DIETMANN, K. M., et al. Layered double hydroxides with intercalated permanganate and peroxydisulphate anions for oxidative removal of chlorinated organic solvents contaminated water. *Minerals*, 2020, 10.5: 462. Available from: <https://doi.org/10.3390/min10050462>.
- [106] Pöllmann. H. Cementitious Materials: composition, properties, application. Germany, 2017. ISBN 9783110473728
- [107] BAQUERIZO, L. G., et al. Methods to determine hydration states of minerals and cement hydrates. *Cement and Concrete Research*, 2014, 65: 85–95. Available from: <https://doi.org/10.1016/j.cemconres.2014.07.009>.
- [108] PÖLLMANN, H. Characterization of different water contents of ettringite and kuzelite. In: *Proceedings of 12th International Congress on the Chemistry of Cement, Montreal, QC, Canada*. 2007. p. 8–13. Available from: <https://iccc-online.org/fileadmin/gruppen/iccc/proceedings/12/pdf/fin00355.pdf>.
- [109] ALLMANN, R. REFINEMENT OF THE HYBRID LAYER STRUCTURE $(\text{CA}_2\text{Al}(\text{OH})_6)^+ \cdot (12\text{SO}_4 \cdot 3\text{H}_2\text{O})$. 1977.
- [110] MELLER, N., KYRITSIS, K., HALL, C. The hydrothermal decomposition of calcium monosulfoaluminate 14-hydrate to katoite hydrogarnet and β -anhydrite: An in-situ synchrotron X-ray diffraction study. *Journal of Solid State Chemistry*, 2009, 182.10: 2743–2747. Available from: <https://doi.org/10.1016/j.jssc.2009.07.029>.
- [111] MATSCHEI, T., LOTHENBACH, B., GLASSER, F. P. Thermodynamic properties of Portland cement hydrates in the system $\text{CaO}-\text{Al}_2\text{O}_3-\text{SiO}_2-\text{CaSO}_4-\text{CaCO}_3-\text{H}_2\text{O}$. *Cement and Concrete Research*, 2007, 37.10: 1379–1410. Available from: <https://doi.org/10.1016/j.cemconres.2007.06.002>.

- [112] BAQUERIZO, L. G., et al. Hydration states of AFm cement phases. *Cement and Concrete Research*, 2015, 73: 143–157. Available from: <https://doi.org/10.1016/j.cemconres.2015.02.011>.
- [113] PÖLLMANN, H. Syntheses, properties and solid solution of ternary lamellar calcium aluminate hydroxi salts (AFm–phases) containing SO₄²⁻, CO₃²⁻ and OH. *Neues Jahrbuch für Mineralogie–Abhandlungen*, 2006, 182.2: 173–182.. Available from: <https://doi.org/10.1127/0077-7757/2006/0042>.
- [114] DAMIDOT, D., GLASSER, F. P. Thermodynamic investigation of the CaO – Al₂O₃ – CaSO₄ – H₂O system at 50° C and 85° C. *Cement and Concrete Research*, 1992, 22.6: 1179–1191. Available from: [https://doi.org/10.1016/0008-8846\(92\)90047-Y](https://doi.org/10.1016/0008-8846(92)90047-Y).
- [115] EDMONDS, R. N., MAJUMDAR, A. J. The hydration of monocalcium aluminate at different temperatures. *Cement and Concrete Research*, 1988, 18.2: 311–320. Available from: [https://doi.org/10.1016/0008-8846\(88\)90015-4](https://doi.org/10.1016/0008-8846(88)90015-4).
- [116] MOTZET, H., PÖLLMANN, H. Synthesis and characterisation of sulfite–containing AFm phases in the system CaO–Al₂O₃–SO₂–H₂O. *Cement and Concrete Research*, 1999, 29.7: 1005–1011. Available from: [https://doi.org/10.1016/S0008-8846\(99\)00082-4](https://doi.org/10.1016/S0008-8846(99)00082-4).
- [117] DILNESA, B. Z., et al. Stability of monosulfate in the presence of iron. *Journal of the American Ceramic Society*, 2012, 95.10: 3305–3316. Available from: <https://doi.org/10.1111/j.1551-2916.2012.05335.x>.
- [118] LEISINGER, S. M., et al. Thermodynamic modeling of solid solutions between monosulfate and monochromate 3CaO•Al₂O₃•Ca [(CrO₄)_x(SO₄)_{1-x}]•nH₂O. *Cement and Concrete Research*, 2012, 42.1: 158–165. Available from: <https://doi.org/10.1016/j.cemconres.2011.09.005>.
- [119] GASTALDI, D, et al. A chemical/mineralogical investigation of the behavior of sulfoaluminate binders submitted to accelerated carbonation. *Cement and Concrete Research*, 2018, 109: 30–41. Available from: <https://doi.org/10.1016/j.cemconres.2018.04.006>.
- [120] BRAHIM, M. N, et al. Early stage ettringite and monosulfoaluminate carbonation investigated by in situ Raman spectroscopy coupled with principal component analysis. *Materials Today Communications*, 2023, 35: 105539. Available from: <https://doi.org/10.1016/j.mtcomm.2023.105539>.
- [121] ZHANG, Y., ÇOPUROĞLU, O. The role of hydrotalcite–like phase and monosulfate in slag cement paste during atmospheric and accelerated carbonation. *Cement and Concrete Composites*, 2022, 132: 104642. Available from: <https://doi.org/10.1016/j.cemconcomp.2022.104642>.
- [122] SEO, J, et al. Carbonation of calcium sulfoaluminate cement blended with blast furnace slag. *Cement and Concrete Composites*, 2021, 118: 103918. Available from: <https://doi.org/10.1016/j.cemconcomp.2020.103918>.

- [123] SHAH, V, et al. Changes in microstructure characteristics of cement paste on carbonation. *Cement and Concrete Research*, 2018, 109: 184–197. Available from: <https://doi.org/10.1016/j.cemconres.2018.04.016>.
- [124] HARGIS, C. W., et al. Carbonation of calcium sulfoaluminate mortars. *Cement and Concrete Composites*, 2017, 80: 123–134. Available from: <https://doi.org/10.1016/j.cemconcomp.2017.03.003>.
- [125] BYRAPPA, K., YOSHIMURA, M. *Handbook of hydrothermal technology*. William Andrew, 2012. Secon edition. ISBN 9780123750907.
- [126] RIMAN, R. E., SUCHANEK, W. L., LENCKA, M. M. Hydrothermal crystallization of ceramics. In: *Annales de Chimie Science des Materiaux*. No longer published by Elsevier, 2002. p. 15–36. Available from: [https://doi.org/10.1016/S0151-9107\(02\)90012-7](https://doi.org/10.1016/S0151-9107(02)90012-7).
- [127] ISHIDA, H., SASAKI, K., MITSUDA, T. Highly Reactive β -Dicalcium Silicate: I, Hydration Behavior at Room Temperature. *Journal of the American Ceramic Society*, 1992, 75.2: 353–358. Available from: <https://doi.org/10.1111/j.1151-2916.1992.tb08186.x>.
- [128] SINGH, N. B., RAI, S., SINGH, N. Highly Reactive β -Dicalcium Silicate. *Journal of the American Ceramic Society*, 2002, 85.9: 2171–2176. Available from: <https://doi.org/10.1111/j.1151-2916.2002.tb00430.x>.
- [129] LI, C., HIRABAYASHI, D., SUZUKI, K. Synthesis of higher surface area mayenite by hydrothermal method. *Materials Research Bulletin*, 2011, 46.8: 1307–1310. Available from: <https://doi.org/10.1016/j.materresbull.2011.03.023>.
- [130] KHAN, K., et al. Low temperature synthesis of nano porous $12\text{CaO} \cdot 7\text{Al}_2\text{O}_3$ powder by hydrothermal method. *Journal of Wuhan University of Technology–Mater. Sci. Ed.*, 2016, 31.6: 1201–1205. Available from: <https://doi.org/10.1007/s11595-016-1512-7>.
- [131] MAZOUZI, W., et al. Properties of low temperature belite cements made from aluminosilicate wastes by hydrothermal method. *Cement and Concrete Composites*, 2014, 53: 170–177. Available from: <https://doi.org/10.1016/j.cemconcomp.2014.07.001>.
- [132] CYGAS, D., FROEHNER, K. D., BREZNIKAR, A (ed.). *Environmental Engineering: Selected Papers. Sustainable Urban Development. Roads and Railways. Technologies of Geodesy and Cadastre*. Vilnius Gediminas Technical University Press" Technika", 2011. ISBN 9955288299.
- [133] GOŃI, S., et al. Dehydration of pozzolanic products hydrothermally synthesized from flyash: microstructure evolution. *Materials research bulletin*, 2000, 35.8: 1333–1344. Available from: [https://doi.org/10.1016/S0025-5408\(00\)00326-3](https://doi.org/10.1016/S0025-5408(00)00326-3).
- [134] PIMRAKSA, K., HANJITSUWAN, S., CHINDAPRASIRT, P. Synthesis of belite cement from lignite fly ash. *Ceramics International*, 2009, 35.6: 2415–2425. Available from: <https://doi.org/10.1016/j.ceramint.2009.02.006>.

- [135] KACIMI, L., CYR, M., CLASTRES, P. Synthesis of α' L-C2S cement from fly-ash using the hydrothermal method at low temperature and atmospheric pressure. *Journal of Hazardous Materials*, 2010, 181.1–3: 593–601. Available from: <https://doi.org/10.1016/j.jhazmat.2010.05.054>.
- [136] BOUHA, F. N., KACIMI, L., ANGELES, G. Manufacture of rich-sulfoaluminate belite cement at low temperature from waste mixture by dry and hydrothermal processes. *Construction and Building Materials*, 2022, 314: 125641. Available from: <https://doi.org/10.1016/j.conbuildmat.2021.125641>.
- [137] RUNGCHET, A., et al. Hydrothermal synthesis of calcium sulfoaluminate–belite cement from industrial waste materials. *Journal of Cleaner Production*, 2016, 115: 273–283. Available from: <https://doi.org/10.1016/j.jclepro.2015.12.068>.
- [138] QUARCIONI, V. A., et al. Indirect and direct Chapelle's methods for the determination of lime consumption in pozzolanic materials. *Revista IBRACON de Estruturas e Materiais*, 2015, 8: 1–7. Available from: <https://doi.org/10.1590/s1983-41952015000100002>.
- [139] SANTOS, P. S., SANTOS, H. S., TOLEDO, S. P. Standard transition aluminas. Electron microscopy studies. *Materials Research*, 2000, 3: 104–114. Available from: <https://doi.org/10.1590/S1516-14392000000400003>.
- [140] HAFFER, S., WEINBERGER, C., TIEMANN, M. Mesoporous Al₂O₃ by nanocasting: Relationship between crystallinity and mesoscopic order. *European Journal of Inorganic Chemistry*, 2012, 2012.20: 3283–3288. Available from: <https://doi.org/10.1002/ejic.201200131>.
- [141] JAMES, S. L., et al. Mechanochemistry: opportunities for new and cleaner synthesis. *Chemical Society Reviews*, 2012, 41.1: 413–447. <https://doi.org/10.1039/c1cs15171a>.
- [142] KOSENKO, N. F., BELYAKOV, A. S., SMIRNOVA, M. A. Effect of mechanical activation procedure on the phase composition of gypsum. *Inorganic Materials*, 2010, 46: 545–550. Available from: <https://doi.org/10.1134/S0020168510050195>.
- [143] OLIVEIRA, E. G., et al. Moisture sorption characteristics of microalgae *Spirulina platensis*. *Brazilian Journal of Chemical Engineering*, 2009, 26: 189–197. Available from: <https://doi.org/10.1590/S0104-66322009000100018>.
- [144] JIAO, Y., et al. A new approach for measurement of the low-temperature specific heat capacity. *Measurement*, 2022, 203: 111892. Available from: <https://doi.org/10.1016/j.measurement.2022.111892>.
- [145] SCRIVENER, K., et al. (ed.). *A practical guide to microstructural analysis of cementitious materials*. Boca Raton, FL, USA: Crc Press, 2016. ISBN 9781498738675.
- [146] DAMBRAUSKAS, T., BALTAKYS, K., EISINAS, A. Formation and thermal stability of calcium silicate hydrate substituted with Al³⁺ ions in the mixtures

- with CaO/SiO₂ = 1.5. *Journal of Thermal Analysis and Calorimetry*, 2018, 131: 501–512. Available from: <https://doi.org/10.1007/s10973-017-6321-5>.
- [147] OLIVOTOS, S; ECONOMOU–ELIOPOULOS, Maria. Gibbs free energy of formation for selected platinum group minerals (PGM). *Geosciences*, 2016, 6.1: 2. Available from: <https://doi.org/10.3390/geosciences6010002>.
- [148] YANG, W., et al. Effect of Ni addition on the preparation of Al₂O₃–TiB₂ composites using high–energy ball milling. *Journal of Asian Ceramic Societies*, 2014, 2.4: 399–402. Available from: <https://doi.org/10.1016/j.jascer.2014.08.005>.
- [149] BLANC, Ph., et al. Chemical model for cement–based materials: Thermodynamic data assessment for phases other than C–S–H. *Cement and Concrete Research*, 2010, 40.9: 1360–1374. Available from: <https://doi.org/10.1016/j.cemconres.2010.04.003>.
- [150] LOTHENBACH, B., et al. Cemdata18: A chemical thermodynamic database for hydrated Portland cements and alkali–activated materials. *Cement and Concrete Research*, 2019, 115: 472–506. Available from: <https://doi.org/10.1016/j.cemconres.2018.04.018>.
- [151] STEINOUR, H. H. Rate of sedimentation. *Industrial & Engineering Chemistry*, 1944, 36.9: 840–847. Available from: <https://doi.org/10.1021/ie50417a018>.
- [152] KHAWAM, A., FLANAGAN, D. R. Solid–state kinetic models: basics and mathematical fundamentals. *The journal of physical chemistry B*, 2006, 110.35: 17315–17328. Available from: <https://doi.org/10.1021/jp062746a>.
- [153] NISHIKAWA, T., et al. Decomposition of synthesized ettringite by carbonation. *Cement and Concrete Research*, 1992, 22.1: 6–14. Available from: [https://doi.org/10.1016/0008-8846\(92\)90130-N](https://doi.org/10.1016/0008-8846(92)90130-N).
- [154] NARMLUK, M., NAWA, T. Effect of curing temperature on pozzolanic reaction of fly ash in blended cement paste. *International Journal of Chemical Engineering and Applications*, 2014, 5.1: 31. Available from: <https://doi.org/10.7763/ijcea.2014.v5.346>.
- [155] PROVIS, J. L. On the use of the Jander equation in cement hydration modelling. *RILEM Technical Letters*, 2016, 1: 62–66. Available from: <https://doi.org/10.21809/rilemtechlett.2016.13>.
- [156] AYTURK, M. E., et al. Isothermal nucleation and growth kinetics of Pd/Ag alloy phase via in situ time–resolved high–temperature X–ray diffraction (HTXRD) analysis. *Journal of Membrane Science*, 2008, 316.1–2: 97–111. Available from: <https://doi.org/10.1016/j.memsci.2007.09.038>.
- [157] STARINK, M. J. Kinetic equations for diffusion–controlled precipitation reactions. *Journal of materials science*, 1997, 32: 4061–4070. Available from: <https://doi.org/10.1023/A:1018649823542>.
- [158] DRI, M., SANNA, A., MAROTO–VALER, M. M. Dissolution of steel slag and recycled concrete aggregate in ammonium bisulphate for CO₂ mineral

- carbonation. *Fuel processing technology*, 2013, 113: 114–122. Available from: <https://doi.org/10.1016/j.fuproc.2013.03.034>.
- [159] AVRAMI, M. Granulation, phase change, and microstructure kinetics of phase change. III. *The Journal of chemical physics*, 1941, 9.2: 177–184. Available from: <https://doi.org/10.1063/1.1750872>.
- [160] AL'MYASHEVA, O. V., et al. Preparation of nanocrystalline alumina under hydrothermal conditions. *Inorganic materials*, 2005, 41: 460–467. Available from: <https://doi.org/10.1007/s10789-005-0152-7>.
- [161] MIRONENKO, R. M., et al. Effect of γ -Al₂O₃ hydrothermal treatment on the formation and properties of platinum sites in Pt/ γ -Al₂O₃ catalysts. *Applied Catalysis A: General*, 2014, 469: 472–482.. Available from: <https://doi.org/10.1016/j.apcata.2013.10.027>.
- [162] ANANTHAKUMAR, S., et al. Thermal decomposition characteristics of boehmite gels under microwave heating and associated microstructural features. *Materials Letters*, 1998, 35.1–2: 95–99. Available from: [https://doi.org/10.1016/S0167-577X\(97\)00228-0](https://doi.org/10.1016/S0167-577X(97)00228-0).
- [163] EISINAS, A., et al. The peculiarities of mayenite formation from synthetic katoite and calcium monocarboaluminate samples in temperature range 25–1150° C. *Journal of Thermal Analysis and Calorimetry*, 2019, 138: 2275–2282. Available from: <https://doi.org/10.1007/s10973-019-08482-4>.
- [164] SINGH, N. B., SINGH, N. P. Formation of CaO from thermal decomposition of calcium carbonate in the presence of carboxylic acids. *Journal of thermal analysis and calorimetry*, 2007, 89: 159–162. Available from: <https://doi.org/10.1007/s10973-006-7565-7>
- [165] SEO, J., et al. Local Al network and material characterization of belite–calcium sulfoaluminate (CSA) cements. *Materials and Structures*, 2022, 55.1: 12. Available from: <https://doi.org/10.1617/s11527-021-01842-3>.
- [166] TAMBARA JÚNIOR, L. U. D., et al. Effect of alkaline salts on calcium sulfoaluminate cement hydration. *Molecules*, 2021, 26.7: 1938. Available from: <https://doi.org/10.3390/molecules26071938>.
- [167] MACKENZIE, K. J. D., et al. Effect of mechanochemical activation on the thermal reactions of boehmite (γ -AlOOH) and γ -Al₂O₃. *Thermochimica acta*, 2000, 359.1: 87–94. Available from: [https://doi.org/10.1016/S0040-6031\(00\)00513-X](https://doi.org/10.1016/S0040-6031(00)00513-X).
- [168] SERRIS, E., et al. Study of the hydration of CaO powder by gas–solid reaction. *Cement and Concrete Research*, 2011, 41.10: 1078–1084.. Available from: <https://doi.org/10.1016/j.cemconres.2011.06.014>.
- [169] CHAROLA, A. E., PÜHRINGER, J., STEIGER, M. Gypsum: a review of its role in the deterioration of building materials. *Environmental geology*, 2007, 52: 339–352. Available from: <https://doi.org/10.1007/s00254-006-0566-9>.
- [170] SCHMIDT, A. *Technical thermodynamics for engineers*. Second edition. Springer Nature: Cham, Suisse, 2019. ISBN 9783030971502

- [171] VUCELIC, M., MOGGRIDGE, G. D., JONES, W. Thermal properties of terephthalate–and benzoate–intercalated LDH. *The Journal of Physical Chemistry*, 1995, 99.20: 8328–8337. Available from: <https://doi.org/10.1021/j100020a068>
- [172] BORRACHERO, M., et al. The use of thermogravimetric analysis technique for the characterization of construction materials: the gypsum case. *Journal of thermal analysis and Calorimetry*, 2008, 91.2: 503–509. Available from: <https://doi.org/10.1007/s10973-006-7739-3>
- [173] GUIMARÃES, D., DE A. OLIVEIRA, V., LEAO, V. A. Kinetic and thermal decomposition of ettringite synthesized from aqueous solutions. *Journal of Thermal Analysis and Calorimetry*, 2016, 124: 1679–1689. Available from: <https://doi.org/10.1007/s10973-016-5259-3>.
- [174] DUBINA, E., et al. Influence of water vapour and carbon dioxide on free lime during storage at 80 C, studied by Raman spectroscopy. *Spectrochimica Acta Part A: Molecular and Biomolecular Spectroscopy*, 2013, 111: 299–303. Available from: <https://doi.org/10.1016/j.saa.2013.04.033>.
- [175] J WANG, J., et al. Accelerated carbonation of hardened cement pastes: Influence of porosity. *Construction and Building Materials*, 2019, 225: 159–169. Available from: <https://doi.org/10.1016/j.conbuildmat.2019.07.088>.
- [176] GALAN, I., ANDRADE, C., CASTELLOTE, M. Natural and accelerated CO₂ binding kinetics in cement paste at different relative humidities. *Cement and Concrete Research*, 2013, 49: 21–28. Available from: <https://doi.org/10.1016/j.cemconres.2013.03.009>.
- [177] ZHANG, J., WANG, J., GAO, Y. Moisture movement in early–age concrete under cement hydration and environmental drying. *Magazine of Concrete Research*, 2016, 68.8: 391–408. Available from: <https://doi.org/10.1680/jmacr.15.00293>.
- [178] CHEN, B., et al. Comparative kinetics study on carbonation of ettringite and meta–ettringite based materials. *Cement and Concrete Research*, 2020, 137: 106209. Available from: <https://doi.org/10.1016/j.cemconres.2020.106209>.
- [179] BULLERJAHN, F., et al. Hydration reactions and stages of clinker composed mainly of stoichiometric ye'elimite. *Cement and Concrete Research*, 2019, 116: 120–133. Available from: <https://doi.org/10.1016/j.cemconres.2018.10.023>.
- [180] VIOLANTE, A., HUANG, P. M. Formation mechanism of aluminum hydroxide polymorphs. *Clays and Clay Minerals*, 1993, 41.5: 590–597. Available from: <https://doi.org/10.1346/CCMN.1993.0410509>
- [181] ZHANG, Y., CHANG, J., JI, J. AH₃ phase in the hydration product system of AFt–AFm–AH₃ in calcium sulfoaluminate cements: A microstructural study. *Construction and Building Materials*, 2018, 167: 587–596. Available from: <https://doi.org/10.1016/j.conbuildmat.2018.02.052>.

- [182] LOTHENBACH, B., et al. Thermodynamic properties and hydration behavior of ye'elimite. *Cement and Concrete Research*, 2022, 162: 106995. Available from: <https://doi.org/10.1016/j.cemconres.2022.106995>.
- [183] GARCÍA-MATÉ, M., et al. Hydration studies of calcium sulfoaluminate cements blended with fly ash. *Cement and Concrete Research*, 2013, 54: 12–20. Available from: <https://doi.org/10.1016/j.cemconres.2013.07.010>.
- [184] MARTIN, L. HJ., et al. Influence of fly ash on the hydration of calcium sulfoaluminate cement. *Cement and concrete research*, 2017, 95: 152–163. Available from: <https://doi.org/10.1016/j.cemconres.2017.02.030>.
- [185] BAERT, G., et al. Reactivity of fly ash in cement paste studied by means of thermogravimetry and isothermal calorimetry. *Journal of Thermal Analysis and Calorimetry*, 2008, 94.2: 485–492. Available from: <https://doi.org/10.1007/s10973-007-8787-z>
- [186] MARTIN, L. HJ., et al. Contribution of limestone to the hydration of calcium sulfoaluminate cement. *Cement and Concrete Composites*, 2015, 62: 204–211. Available from: <https://doi.org/10.1016/j.cemconcomp.2015.07.005>.
- [187] PELLETIER-CHAIGNAT, L., et al. Beneficial use of limestone filler with calcium sulphoaluminate cement. *Construction and Building Materials*, 2012, 26.1: 619–627. Available from: <https://doi.org/10.1016/j.conbuildmat.2011.06.065>.
- [188] HEWLETT, P., LISKA, M (ed.). *Lea's chemistry of cement and concrete*. Fifth edition. Butterworth-Heinemann, 2019. ISBN 978-0-08-100773-0.
- [189] VIOLANTE, A., HUANG, P. M. Formation mechanism of aluminum hydroxide polymorphs. *Clays and Clay Minerals*, 1993, 41.5: 590–597. Available from: <https://doi.org/10.1346/CCMN.1993.0410509>
- [190] JUENGER, M. CG; SNELLINGS, R., BERNAL, S.A. Supplementary cementitious materials: New sources, characterization, and performance insights. *Cement and Concrete Research*, 2019, 122: 257–273. Available from: <https://doi.org/10.1016/j.cemconres.2019.05.008>.
- [191] JUENGER, M. C., SIDDIQUE, R. Recent advances in understanding the role of supplementary cementitious materials in concrete. *Cement and concrete research*, 2015, 78: 71–80. Available from: <https://doi.org/10.1016/j.cemconres.2015.03.018>.
- [192] KOCAK, Y., NAS, S. The effect of using fly ash on the strength and hydration characteristics of blended cements. *Construction and Building Materials*, 2014, 73: 25–32. Available from: <https://doi.org/10.1016/j.conbuildmat.2014.09.048>.
- [193] BENTZ, D. P., FERRARIS, C. F. Rheology and setting of high volume fly ash mixtures. *Cement and Concrete Composites*, 2010, 32.4: 265–270. Available from: <https://doi.org/10.1016/j.cemconcomp.2010.01.008>.
- [194] DE WEERDT, K., et al. Hydration mechanisms of ternary Portland cements containing limestone powder and fly ash. *Cement and Concrete Research*,

- 2011, 41.3: 279–291. Available from: <https://doi.org/10.1016/j.cemconres.2010.11.014>.
- [195] PELLETIER, L; WINNEFELD, F; LOTHENBACH, B. The ternary system Portland cement–calcium sulphoaluminate clinker–anhydrite: hydration mechanism and mortar properties. *Cement and Concrete Composites*, 2010, 32.7: 497–507. Available from: <https://doi.org/10.1016/j.cemconcomp.2010.03.010>.
- [196] DE WEERDT, K., et al. The effect of temperature on the hydration of composite cements containing limestone powder and fly ash. *Materials and structures*, 2012, 45: 1101–1114. Available from: <https://doi.org/10.1617/s11527-011-9819-5>.
- [197] PELLETIER–CHAIGNAT, L., et al. Influence of the calcium sulphate source on the hydration mechanism of Portland cement–calcium sulphoaluminate clinker–calcium sulphate binders. *Cement and Concrete Composites*, 2011, 33.5: 551–561. Available from: <https://doi.org/10.1016/j.cemconcomp.2011.03.005>.
- [198] PARK, S., et al. Hydration characteristics of calcium sulfoaluminate (CSA) cement/portland cement blended pastes. *Journal of Building Engineering*, 2021, 34: 101880. Available from: <https://doi.org/10.1016/j.jobbe.2020.101880>.
- [199] PELLETIER, L., WINNEFELD, F; LOTHENBACH, B. The ternary system Portland cement–calcium sulphoaluminate clinker–anhydrite: hydration mechanism and mortar properties. *Cement and Concrete Composites*, 2010, 32.7: 497–507. Available from: <https://doi.org/10.1016/j.cemconcomp.2010.03.010>.
- [200] EL–DIADAMONY, H, et al. Hydration and characteristics of metakaolin pozzolanic cement pastes. *HBRC journal*, 2018, 14.2: 150–158. Available from: <https://doi.org/10.1016/j.hbrcj.2015.05.005>.
- [201] GOLEWSKI, G. L. The role of pozzolanic activity of siliceous fly ash in the formation of the structure of sustainable cementitious composites. *Sustainable Chemistry*, 2022, 3.4: 520–534. Available from: <https://doi.org/10.3390/suschem3040032>.
- [202] BISHNOI, S., SCRIVENER, K. L. μ ic: A new platform for modelling the hydration of cements. *Cement and concrete research*, 2009, 39.4: 266–274. Available from: <https://doi.org/10.1016/j.cemconres.2008.12.002>.
- [203] SIAUCIUNAS, R., SMALAKYS, G; DAMBRAUSKAS, T. Porosity of calcium silicate hydrates synthesized from natural rocks. *Materials*, 2021, 14.19: 5592. Available from: <https://doi.org/10.3390/ma14195592>.
- [204] G SMALAKYS, G., SIAUCIUNAS, R. The hydrothermal synthesis of 1.13 nm tobermorite from granite sawing powder waste. *Ceramics–Silikaty*, 2020, 64.3: 239–248. Available from: <https://doi.org/10.13168/cs.2020.0013>.

- [205] MU, Y., et al. Carbonation characteristics of γ -dicalcium silicate for low-carbon building material. *Construction and Building Materials*, 2018, 177: 322–331. Available from: <https://doi.org/10.1016/j.conbuildmat.2018.05.087>.
- [206] BROWN, P. W. Early-age cement hydration reactions. *Transportation Research Record*, 1990, 1284. Available from: <https://onlinepubs.trb.org/Onlinepubs/trr/1990/1284/1284-007.pdf>
- [207] WINNEFELD, F., LOTHENBACH, B. Hydration of calcium sulfoaluminate cements—Experimental findings and thermodynamic modelling. *Cement and Concrete Research*, 2010, 40.8: 1239–1247. Available from: <https://doi.org/10.1016/j.cemconres.2009.08.014>.
- [208] LONDONO-ZULUAGA, D., et al. Clinkering and hydration of belite-alite-yeielimite cement. *Cement and Concrete Composites*, 2017, 80: 333–341. Available from: <https://doi.org/10.1016/j.cemconcomp.2017.04.002>.
- [209] KLIMESCH, D. S., RAY, A., GUERBOIS, J. P. Differential scanning calorimetry evaluation of autoclaved cement based building materials made with construction and demolition waste. *Thermochimica acta*, 2002, 389.1–2: 195–198. Available from: [https://doi.org/10.1016/S0040-6031\(02\)00058-8](https://doi.org/10.1016/S0040-6031(02)00058-8)
- [210] SVIDRÓ, J., DIÓSZEGI, A., SVIDRÓ, J. T. The origin of thermal expansion differences in various size fractions of silica sand. *International Journal of Cast Metals Research*, 2020, 33.6: 242–249. Available from: <https://doi.org/10.1080/13640461.2020.1838078>
- [211] GIRAUDO, N., et al. Dehydration and dehydroxylation of CSH phases synthesized on silicon wafers. *Applied Surface Science*, 2018, 433: 589–595. Available from: <https://doi.org/10.1016/j.apsusc.2017.10.039>
- [212] TIGHARE, P., SINGH, Mr RC. Study of different methods of curing of concrete & curing periods. *International Journal for Research in Applied Science & Engineering Technology (IJRASET)*, 2017, 5: 444–447. Available from: <https://www.scribd.com/document/467785101/downloads-papers-n590608be7e6d0-pdf>.

CURRICULUM VITAE

Dovilė Rubinaitė

dovile.rubinaite@ktu.lt

Education:

2012 – 2014 Secondary education at Telšiai Žemaitės Gymnasium, Telšiai, Lithuania

2014 – 2018 Bachelor's degree in Applied Chemistry, Kaunas University of Technology, Kaunas, Lithuania

2018 – 2020 Master's degree in Chemical Engineering, Kaunas University of Technology, Kaunas, Lithuania

2020 – 2024 PhD candidate in Chemical Engineering, Kaunas University of Technology, Kaunas, Lithuania

Professional experience:

2018 – 2019 Student internship in the project *Synthesis and Hydration of Belite-Sulfoaluminate Cement*.

2019 – 2020 Research internship at the *Centre for Building Materials* of the *Technical University of Munich*, Germany.

2020 – present Engineer at Kaunas University of Technology.

2020 Junior researcher in the project *Synthesis of Calcium Silicates with Intercalated Metal Ions and Their Application in Production of Alternative Cementitious Materials* (METSIL).

2020 – 2023 Junior researcher in the project *Centre of Excellence in Chemical Engineering and Bioprocesses* (CIBKC)".

2021 – 2022 Research internship at the *Centre for Building Materials* of the *Technical University of Munich*, Germany.

2021 – 2024 Junior researcher in the project *Two-step synthesis of low-lime cement, its structure and properties* (LIMECEM).

2022/06/29-07/02 Module *Characterization Methods of Blended Cements* was studied at the international LC3 doctoral school at the *Swiss Federal Institute of Technology* in Lausanne, Switzerland.

Scientific interests:

Ms. Dovilė Rubinaitė focuses on developing alternative binder materials, by investigating the utilization of industrial by-products, while adopting sustainable production technologies.

LIST OF SCIENTIFIC PUBLICATIONS:

Articles published in journals indexed in the *Clarivate Analytics Web of Science with Impact Factor*:

1. Rubinaite, Dovile; Dambrauskas, Tadas; Baltakys, Kestutis; Siauciuonas, Raimundas. Influence of water vapour pressure on the carbonation process of calcium monosulfoaluminate 12-hydrate // *Journal of Thermal Analysis and Calorimetry*. Dordrecht: Springer. Confirmed acceptance of the manuscript for publication (DOI: 10.1007/s10973-024-13233-1).
2. Rubinaite, Dovile; Dambrauskas, Tadas; Baltakys, Kestutis; Siauciuonas, Raimundas. Effect of hydrothermal curing on the hydration and strength development of belite cement mortar containing industrial wastes // *Sustainability*. Basel: MDPI. ISSN 2071-1050. 2023, Vol. 15, iss. 12, art. No. 9802, p. 1–13. DOI: 10.3390/su15129802.
3. Rubinaite, Dovile; Dambrauskas, Tadas; Baltakys, Kestutis; Hilbig, Harald; Siauciuonas, Raimundas. Thermal stability assessment of calcium monosulfoaluminate 12-hydrate by applying the in-situ X-ray diffraction method at 25–1250 °C // *Scientific Reports*. Berlin: Nature Portfolio. ISSN 2045-2322. eISSN 2045-2322. 2023, Vol. 13, iss. 1, art. No. 3782, p. 1–11. DOI: 10.1038/s41598-023-30919-y.
4. Rubinaite, D.; Dambrauskas, T.; Baltakys, K.; Siauciuonas, R. Investigation on the hydration and strength properties of belite cement mortar containing industrial waste // *Journal of Thermal Analysis and Calorimetry*. Dordrecht: Springer. ISSN 1388–6150. eISSN 1588-2926. 2023, Vol. 148, iss. 4, p. 1481–1490. DOI: 10.1007/s10973-022-11556-5.
5. Baltakys, K.; Dambrauskas, T.; Rubinaite, D.; Siauciuonas, R.; Grineviciene, A. Formation and hydration of ecofriendly cement using industrial wastes as raw materials // *Scientific Reports*. London: Springer. ISSN 2045–2322. 2021, Vol. 11, iss. 1, art. No. 14742, p. 1–12. DOI: 10.1038/s41598-021-94148-x.

Presentation of research results at conferences:

1. Rubinaite, D.; Machner, A.; Heisig, A. Early age hydration behaviour of synthetic ye'elinite blended with fly ash // *2nd International Workshop on Calcium Sulfoaluminate Cements*. Rome, Italy, 2–4 October 2023.
2. Rubinaite, D.; Dambrauskas, T.; Eisinas, A. Role of water vapour pressure in the carbonation process of calcium monosulfoaluminate 12-hydrate // *Chemistry and Chemical Technology: international conference CCT–2023*, March 10, 2023, Vilnius: conference book. Vilnius: Vilnius University Press, 2023, P 070. ISBN 9786090708330. p. 107.
3. Rubinaite, Dovile; Dambrauskas, Tadas; Baltakys, Kestutis; Machner, Alisa; Heisig, Anne. Impact of water vapour pressure on the stability of calcium monosulfoaluminate 12-hydrate // *Chemistry and Chemical Technology*:

- proceedings of international scientific conference, Kaunas, 2022. Kaunas: Kaunas University of Technology. ISSN 2538–7359. 2022, p. 119.
4. Rubinaite, Dovile; Dambrauskas, Tadas; Baltakys, Kestutis; Siauciunas, Raimundas. Two-stage approach for the synthesis of ye'elinite // *13th European symposium on Thermal Analysis and Calorimetry*, 19–22 September 2022, Palermo, Italy: book of abstracts. Palermo: University of Palermo. 2022, p. 183.
 5. Rubinaite, Dovile; Dambrauskas, Tadas; Baltakys, Kestutis; Siauciunas, Raimundas. Synthesis and characterisation of calcium monosulfoaluminate 12–hydrate // *1st Central and Eastern European Conference on Physical Chemistry and Materials Science (CEEC–PCMS1)*, 26–30 July 2022, Split, Croatia: book of abstracts / editors: M. Erceg, A. Rotaru, L. Vrsalovic. Craiova: Sitech, 2022, PS2.20. ISBN 9786061181643. p. 162.
 6. Rubinaite, Dovile; Baltakys, Kestutis; Dambrauskas, Tadas; Siauciunas, Raimundas. Thermal stability of synthetic kuzelite in the temperature range of 30–1250 °C // *6th Central and Eastern European Conference on Thermal Analysis and Calorimetry (CEEC–TAC6)* and *15th Mediterranean Conference on Calorimetry and Thermal Analysis (Medicta2021)*, 20–24 July 2021, Split, Croatia: book of abstracts / A. Rotaru, M. Erceg (eds.). București: SITECH, 2021, PS3.013. ISBN 9786061178612. p. 209.

ACKNOWLEDGEMENTS

I want to express my most sincere appreciation to my supervisor, Prof. Dr. Raimundas Šiaučiūnas, for his respect, knowledge, understanding, and support throughout my PhD studies. I also want to express my gratitude to my long-time advisors, Prof. Dr. Kęstutis Baltakys and Associate Professor Dr. Tadas Dambrauskas, who have been guiding and supporting me since the very beginning of my scientific journey. Furthermore, I am genuinely thankful to Prof. Dr. Alisa Machner and Dr. Anne Heisig for their advice and assistance during the internship period at the *Technical University of Munich*. The collective expertise and insightful advice from each individual have played a pivotal role in shaping both this thesis and my personal development as a researcher.

I express profound gratitude to *Kaunas University of Technology* for providing the resources, facilities, and conducive research environment, all of which are essential for the successful completion of this study. I am grateful to all my friends and colleagues from the Department of Silicate Technology, especially Gabrielė and Inga, for their help, discussions, and support.

Lastly, I want to give a huge thanks to my close friends and family, especially my mom and dad, for believing in me and for encouraging me to pursue what I really want in life. I am sincerely thankful for this opportunity and to all those who contributed to its realization. My heartfelt gratitude to everyone!

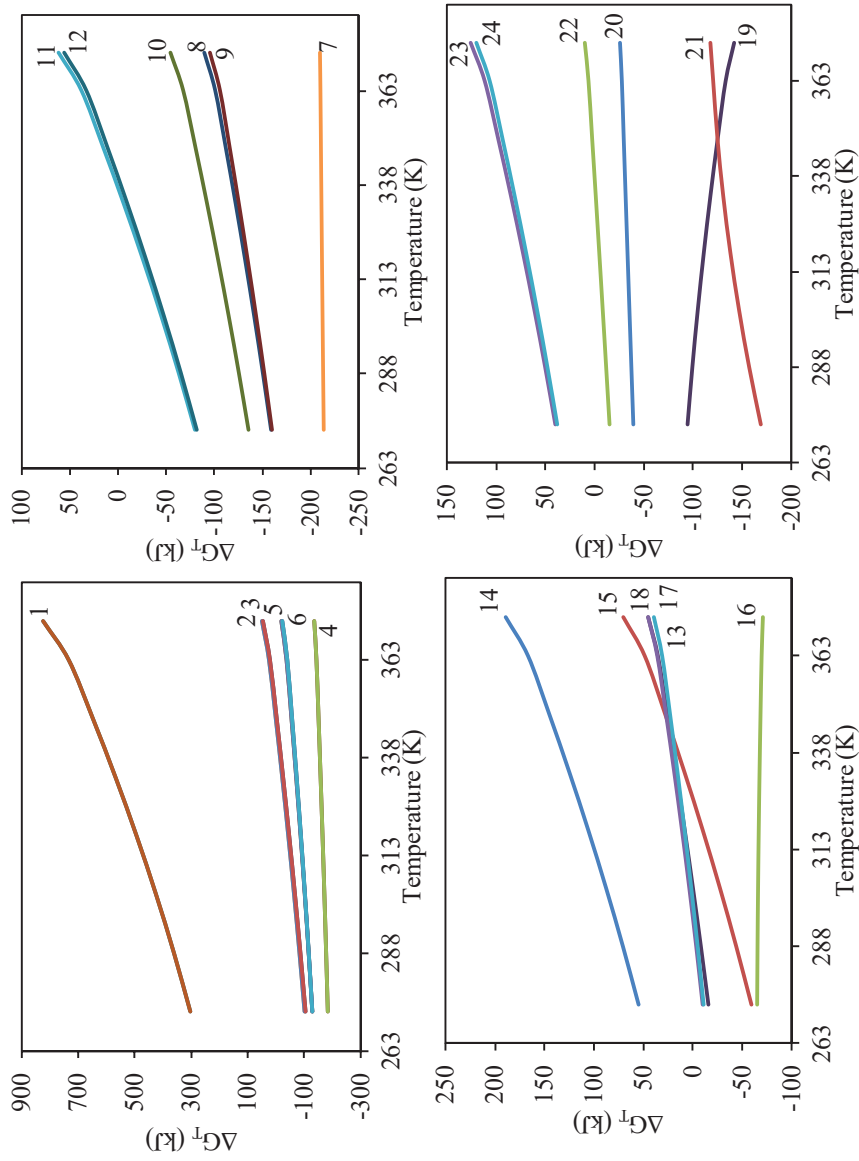


Fig. 1. Dependence of Gibbs free energy on temperature (<100 °C) for calcium monosulfaluminate hydrate formation based on Equations 1–

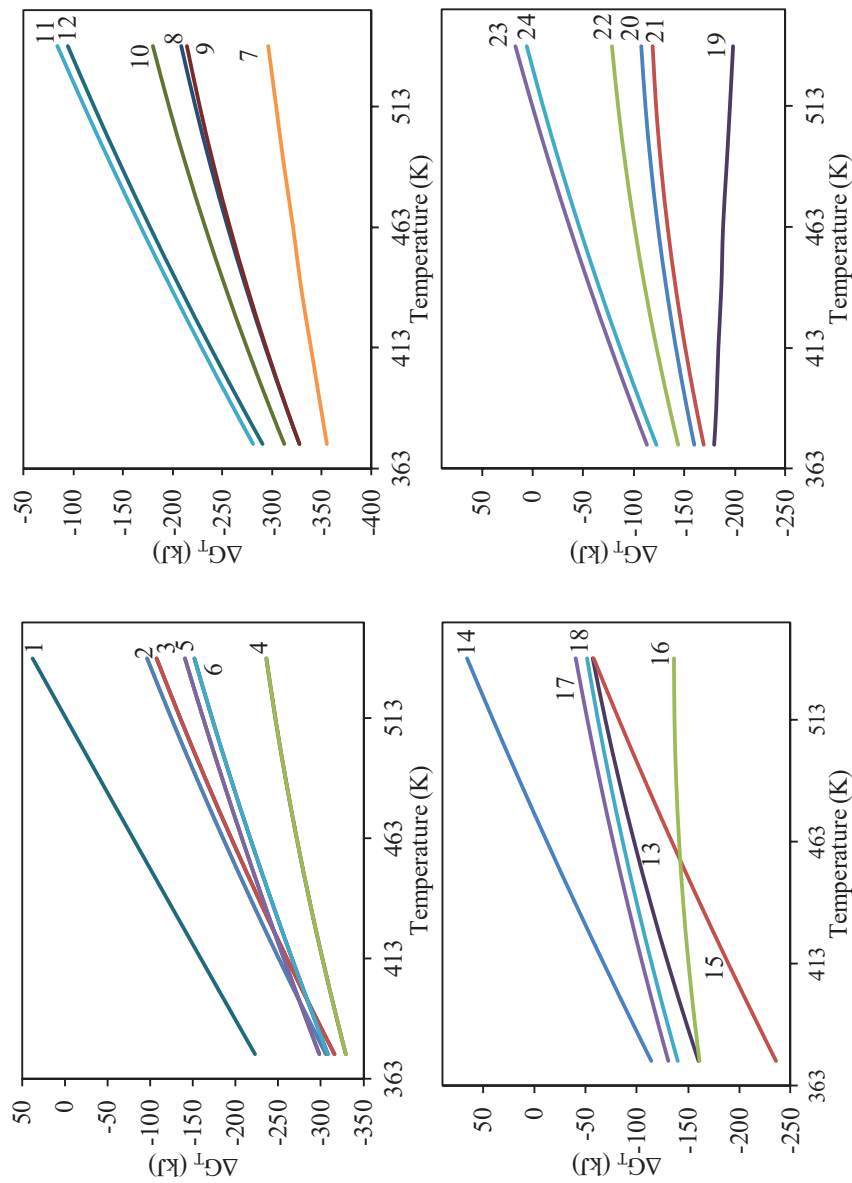


Fig. 2. Dependence of Gibbs free energy on temperature (>100 °C) for calcium monosulfoaluminate hydrate formation based on Equations 1–24

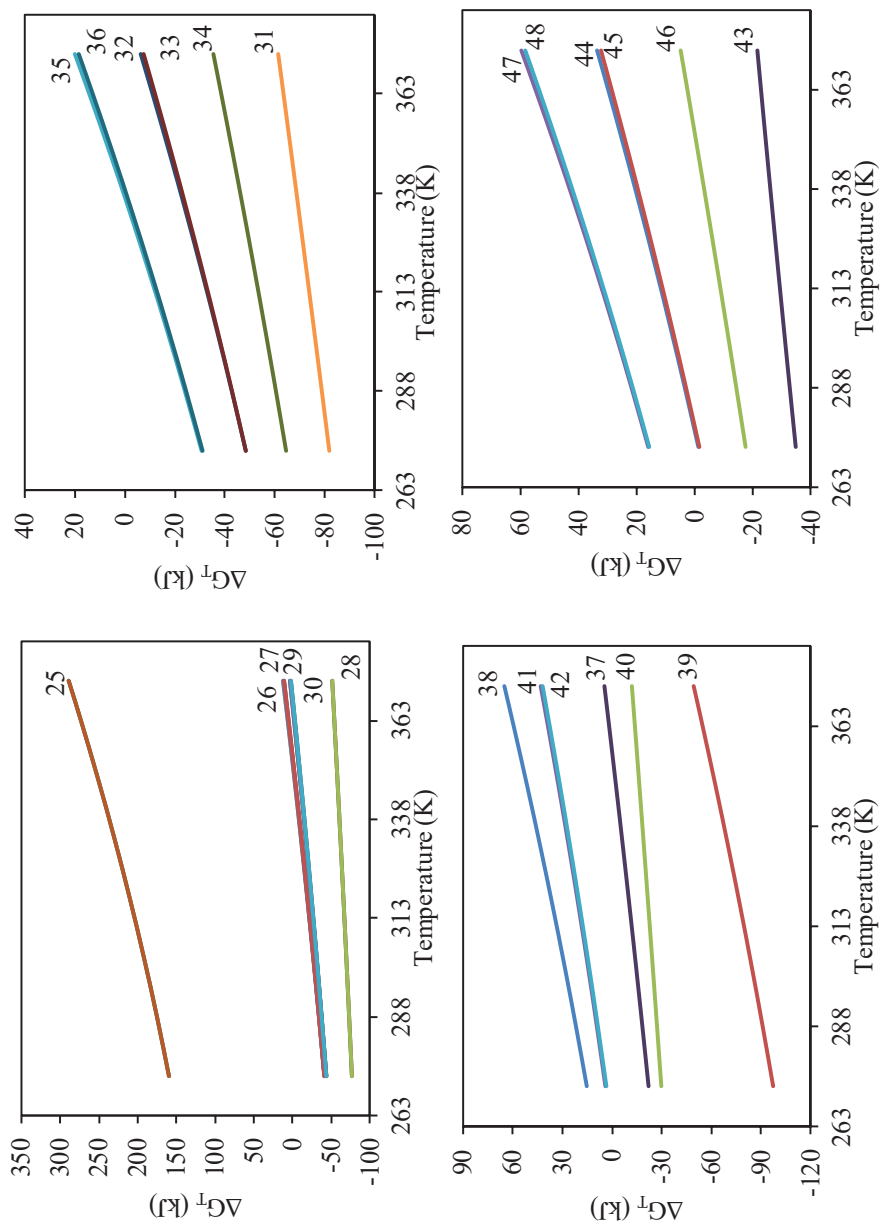


Fig. 3. Dependence of Gibbs free energy on temperature (<100 °C) for ettringite formation based on Equations 25–48

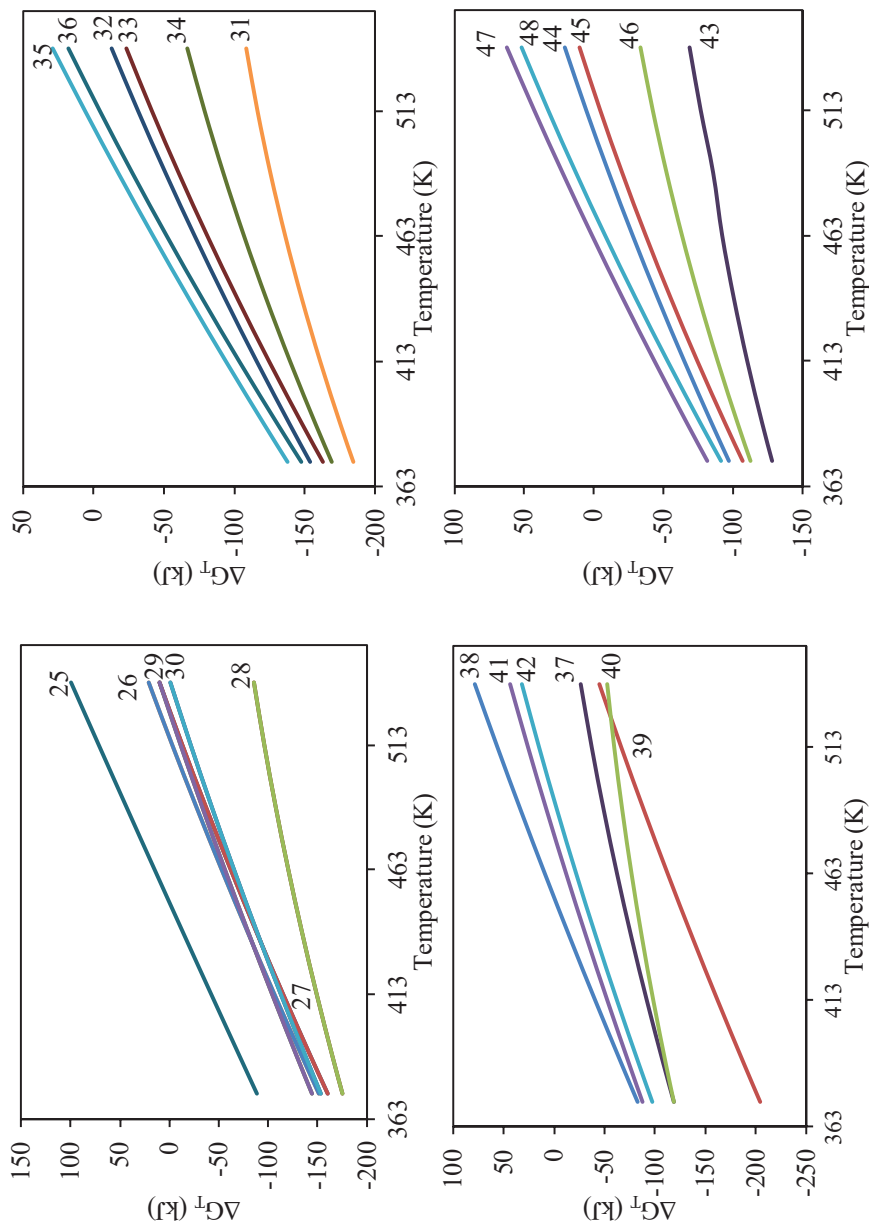


Fig. 4. Dependence of Gibbs free energy on temperature (> 100 °C) for ettringite formation based on Equations 25–48

The possible formation reactions of hydrates from the initial compounds are presented in the equations below:

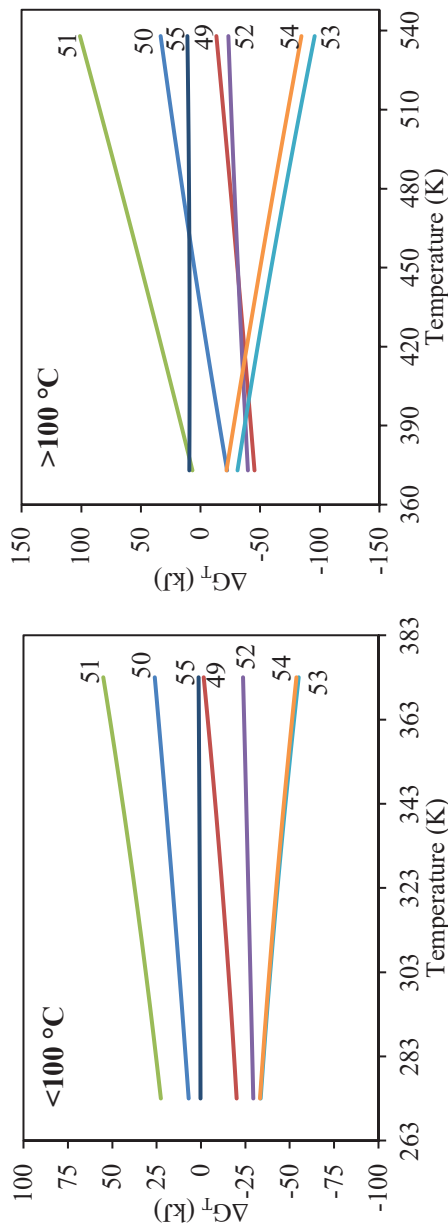
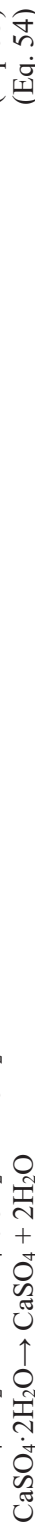


Fig. 5. Dependence of Gibbs free energy on temperature for the feasible formation of hydrates from the initial compounds based on Equations 49–55

UDK 666.965+666.946](043.3)

SL344. 2024-07-31, 23,75 leidyb. apsk. I. Tiražas 14 egz. Užsakymas 132.
Išleido Kauno technologijos universitetas, K. Donelaičio g. 73, 44249 Kaunas
Spausdino leidyklos „Technologija“ spaustuvė, Studentų g. 54, 51424 Kaunas

